

# Powder Pulse Plating

Thesis submitted for the degree of  
Doctor of Philosophy  
at the University of Leicester

by

Salih Cihangir  
Department of Chemistry  
University of Leicester

Supervisors

Prof Andrew P. Abbott

Prof Karl S. Ryder

January 2018



UNIVERSITY OF  
**LEICESTER**

## **Abstract**

### **Powder Pulse Plating**

Salih Cihangir  
University of Leicester  
2017

Electroplating is a common method of obtaining metallic coatings on a surface. Generally, the metal salt is introduced into solution and a direct current is applied to the material that is to be coated. In this thesis, an alternative approach is investigated, namely the metal is introduced onto the metal surface as a powder and a pulsed current is applied to firstly dissolve some of the powder and the polarity is reversed so that the metal is then deposited. This fuses the powder to itself and to the substrate.

In the current study, deep eutectic solvents were used as the electrolytes and two metals were chosen; zinc and copper. Initially the dissolution and deposition of the pure metals were investigated. It was found that far from being simple dissolution and deposition processes insoluble films were formed on the electrode surface during both deposition and dissolution for zinc and during dissolution for copper.

Powder pulse plating was successfully demonstrated if the current pulse characteristics were kept within a window of size and duration which avoided these insoluble films. It was found that large metallic particles could be used when the substrate was held in a horizontal orientation and small particles were best when the electrode was held vertically. For both metals it was demonstrated that super-efficient deposition could be obtained (Faradaic current efficiency in the cathodic pulse  $> 100\%$ ). It was also shown that composite materials could be produced by mixing inert particles with the metallic powder.

## Publications

### A) Paper (submitted):

Andrew P. Abbott\* Salih Cihangir and Karl Ryder, Effect of Film Formation During Electrodeposition and Electrodissolution of Zinc using Deep Eutectic Solvents, *Phys.Chem.Chem.Phys.*

### B) Conference:

#### 1- Talk

Salih Cihangir, Andrew P. Abbott and Karl S. Ryder, *Powder Pulse Plating, 21st meeting of the ELECTROCHEM conference series*, (August 17-19, 2016), University of Leicester, Leicester, UK.

#### 2- Talk

Salih Cihangir, Andrew P. Abbott and Karl S. Ryder, *Super-Efficient Powder Pulse Electrodeposition for Possible Additive Manufacturing Applications, 68th ISE Meeting*, (27 August-1 September, 2017), Providence, RI, USA.

#### 3- Talk

Salih Cihangir, Andrew P. Abbott and Karl S. Ryder, *Initially Placed Solid Particle Deposition for Super Efficient Systems and Possible Additive Manufacturing Applications, 232nd ECS Meeting*, (October 1-6, 2017), Washington, D.C, USA.

#### 4- Poster

Salih Cihangir, Andrew P. Abbott and Karl S. Ryder, Powder Pulse Plating, The Midlands Electrochemistry Group, (June 22, 2015), Warwick, Leicester, UK

## **Statement of originality**

All the work described in this thesis for the degree of Ph.D entitled “Powder Pulse Plating” was conducted by the author in the Department of Chemistry at the University of Leicester mainly during the period between January 2014 and August 2017.

The work in this thesis is original unless otherwise acknowledged in the text or by references and none of the work has been submitted for another degree at this or any other university.

.....  
Salih Cihangir  
23th August 2017

## Acknowledgements

I would like to express my deep sense of gratitude to my supervisor, *Professor Andrew Abbott* for his skilful guidance, encouragement, patience, support, and great concern, which drove this work to a successful stage.

I would also like to thank my second supervisor *Professor Karl Ryder* for his support, and suggestions in our discussions.

I am also thankful to Asuman Unal, Abdulcabbar Yavuz, Kevser Sevim, and specially to Ramy Mesalam for their helpful discussions, and great company during my study.

I also would like to thank to my colleagues from the Leicester ionic liquid group both past and present for their individual contributions.

Special thanks to my parents Turan and Leyla Cihangir, and brother Serhat Cihangir for their endless support.

I would like to express my great love to my wife Sibel, for her patience and for staying up with me through most difficult stage of my study.

Last, but not least, I also wish to express my deep sense of gratitude to the Ministry of National Education in Turkey for providing financial support throughout my PhD project.

# Contents

## Chapter I: Introduction

1.1	Electrodeposition	2
1.2	Nucleation and Growth of Nuclei	3
1.3	Zinc Electroplating from Aqueous Solutions	9
1.4	Copper Deposition from Aqueous Solutions	11
1.5	Non-aqueous Electrodeposition Systems	13
1.5.1	Ionic Liquids	14
1.5.2	Deep Eutectic Solvents	17
1.6	Applications of ionic liquids and deep eutectic solvents	21
1.7	Electrodeposition using ILs and DESs	22
1.8	Zinc Deposition from ILs and DESs	25
1.9	Copper Deposition from ILs and DESs	28
1.1	Research Aims	30
1.11	References	32

## Chapter II: Experimental Procedure

2.1	Materials	39
2.2	Preparation of solutions	39
2.3	Preparation of the Electrochemical Cells	39
2.4	Electrochemical Techniques	40
2.4.1	Reference Electrodes in RTILs and DES	40
2.4.2	Cyclic Voltammetry	43
2.4.3	Chronoamperometry and Chronocoulometry	46
2.4.4	Pulse Reverse Electrodeposition	48
2.4.5	Electrochemical Impedance Spectroscopy	51
2.4.6	Electrochemical Quartz Crystal Microbalance	55
2.5	Non-Electrochemical Techniques	56
2.5.1	Spectroscopic Techniques	56
2.5.2	Surface Imaging Techniques	56
2.5.3	Scanning Electron Microscopy	56
2.5.4	3D Optical Profiler	58
2.5.5	X-ray Diffraction	59
2.6	Electrodeposition Devices	61

2.6.1	AC/DC Power Supply	61
2.6.2	Pulse Reverse Electrodeposition	62
2.7	References	63

### **Chapter III: Basics**

3.1	Introduction	65
3.1.1	Passivation	65
3.1.2	Oxidation Mechanisms in Aqueous Solutions	67
3.1.3	Anodic dissolution in ionic liquids and DESs	69
3.2	Zinc Electrodeposition	71
3.2.1	Cyclic Voltammetry and EIS for Zinc-based DESs	73
3.2.2	3D Optical Profiler Study of Zinc Reduction and Oxidation	80
3.2.3	Electrochemical Impedance Spectroscopy	81
3.2.4	SEM and XRD Results of Bulk Electrolysis	91
3.3	Anodic Dissolution of Zinc	96
3.4	Conclusions	100
3.5	References	102

### **Chapter IV: Zinc Powder Deposition**

4.1	Introduction	107
4.2	Pulse Electrodeposition (PED) and Pulse Reverse Deposition (PRD)	107
4.3	Results and Discussion - Zinc Powder Pulse Plating	111
4.3.1	Cyclic Voltammetry of Zinc Particles	112
4.3.2	Single Particle Pulse Plating	115
4.4	Bulk Powder Deposition	119
4.4.1	Electrode Geometry - Vertical	120
4.4.2	Electrode Geometry - Horizontal	122
4.4.3	Bulk Powder Deposition -Stirred Systems	129
4.4.4	Current Efficiency	133
4.5	Electrochemical Quartz Crystal Microbalance	134
4.6	Electrodeposition of Composite Coatings	135
4.7	Conclusion	138
4.8	References	139

## **Chapter V: Copper Powder Deposition**

5.1	Introduction	142
5.2	Project Aims and Objective	143
5.3	Result and Discussion	143
5.3.1	Cyclic Voltammetry Studies	143
5.4	Anodic Dissolution of Copper	145
5.4.1	LSV of Copper under 3D Optical Profiler	148
5.4.2	Electrochemical Impedance Study of Copper Metal	150
5.4.3	Chronoamperometric Studies of Copper Dissolution and Deposition	153
5.5	Deposition with Copper Powder	157
5.5.1	Single Powder Deposition	157
5.5.2	Bulk Deposition of Copper Powder	160
5.5.3	Horizontal Powder Pulse Plating	163
5.5.4	Electroforming of a Copper Film	165
5.6	XRD Analysis	169
5.7	Electrodeposition of Composite Coatings	175
5.8	Conclusions	177
5.9	References	179

## **Chapter VI: Future Work**

6.1	Conclusions	182
6.2	Suggestions for Future Work	184
6.2.1	Metal Deposition and Electropolishing	184
6.2.2	Powder Pulse Plating	185
6.3	References	187

## **Chapter VII: Appendix**

7	Appendix	188
7.1	Nucleation Mechanism	188
7.1.1	Zinc	188
7.1.2	Copper	190
7.2	Mass Transport Modelling	191
7.3	References	197

# Symbols

$\Delta E$	Potential difference	Volt (V)
$E_{pa}$	Oxidation peak Potential	Volt (V)
$E_{ca}$	Reduction peak Potential	Volt (V)
$n$	Electron number	(-)
$i_{pa}$	Anodic peak current	Ampere (Coulomb s <sup>-1</sup> )
$i_{pc}$	Cathodic peak current	Ampere (Coulomb s <sup>-1</sup> )
$\nu$	Scan rate	Volt per second (V s <sup>-1</sup> )
$t$	Time	Seconds
$I$	Current	Ampere (Coulomb s <sup>-1</sup> )
$S$	Surface area	cm <sup>2</sup>
$r$	Plating rate	cm s <sup>-1</sup>
$C_0$	Initial concentration	mol dm <sup>-3</sup>
$T_{ON}$	Current flow in pulse deposition	Ampere s <sup>-1</sup>
$T_{OFF}$	No current flow in pulse deposition	Zero Ampere s <sup>-1</sup>
$I_L$	Limiting current density in pulse	Ampere cm <sup>-2</sup>
$I_G$	Limiting current density in DC	Ampere cm <sup>-2</sup>
$I_A$	Average current density	Ampere cm <sup>-2</sup>
$I_P$	Peak current density	Ampere cm <sup>-2</sup>
$R$	Resistance	Ampere V <sup>-1</sup>
$V$	Potential	V
$E_t$	Excitation signal (EIS)	mV
$\varphi$	Phase shift (EIS)	$I_0 \cdot \sin \varphi$ in angular frequency
$ Z $	Quantity vector (EIS)	$[(Z_0 \cos \varphi)^2 + (Z_0 \sin \varphi)^2]^{1/2}$

$R_s$	Solution resistance	$\mu S^{-1} (\Omega)$
$R_p$	Charge transfer resistance	$\mu S^{-1} (\Omega) \text{ cm}^{-2}$
CPE	Constant phase element	$s^n \mu S(F) \text{ cm}^{-2} [1 / Z=Y=Q^\circ (j \omega)^n, 0 \leq n \leq 1]$
$C_{dl}$	Capacitance	When $n=1$ , $s \mu S (F) \text{ cm}^{-2}$
$Z_w$	Warburg impedance	$S^{-1} (f_{O(s)}) \text{ at } \text{rad}^{-1/2}$
$\sigma$	Warburg coefficient	$RTn^{-2}F^{-2}A^{-1}2^{-1/2}(D_0^{-1/2}C_{O}^{b_{O-1}} + D_0^{-1/2}C_{R}^{b_{R-1}})$
F	Faraday constant	96485.33289 (C mol <sup>-1</sup> )
A	Electrode surface area	cm <sup>2</sup> / mm <sup>2</sup>
$D_0$	Diffusion constant	cm s <sup>-1</sup>
$Z_F$	Faradic impedance	$R_p + Z_{mt}$
$Z_{mt}$	Mass transfer impedance	$A 2^{1/2} \sigma s^{-1/2} [(1+e^{-\zeta}) (f_{O(s)} + f_{R(s)})] (\Omega)$
$E_{SS}$	Stationary state potential	V
$k_f$	Heterogenous rate constant	rate $[(A)^n]^{-1}$
Rate	Change in molarity over time	mol dm <sup>-3</sup> s <sup>-1</sup>
$(A)^n$	Reaction degree related molarity	(mol dm <sup>-3</sup> s <sup>-1</sup> ) <sup>n</sup> , n: reaction order
$\theta$	Surface coverage	$A_{SUB} N_{ADS} A_{ADS}^{-1}$
$A_{SUB}$	Area of the unit cell of the substrate	
$N_{ADS}$	Number of atoms in $A_{ADS}$	
$A_{ADS}$	Area of adsorbate unit cell	
$J_c$	Cathodic pulse density	$I_c (As^{-1}) \text{ cm}^{-2}$
$J_A$	Anodic pulse density	$I_A (As^{-1}) \text{ cm}^{-2}$
$f$	Frequency	s <sup>-1</sup>
$t_a$	Anodic pulse time	$I_A s^{-1} (As^{-1})$
$t_c$	Cathodic pulse time	$I_c s^{-1} (As^{-1})$
T	Duty cycle	

$J_{AV}$	Average current density	$As^{-1} cm^{-2}$
$M_{RMM}$	Relative molar mass	$g mol^{-1}$
$\Gamma$	Surface coverage	$mol cm^{-2}$
$\tau$	Crystal size	nm
$\rho$	Density	$gr cm^{-3}$

## Abbreviations

ABS	Acrylonitrile Butadiene Styrene
AC	Alternating current
Ag/ AgCl	Silver in 0.1 M AgCl in 1ChCl: 2EG
ChCl	Choline chloride
EDX	Energy-dispersive X-ray spectroscopy
EG	Ethylene Glycol
EIS	Electrochemical impedance spectroscopy
EQCM	Electrochemical quartz crystal microbalance
DC	Direct current
LSV	Linear sweep voltammetry
M	Metal
PAM	Pulse amplitude modulation
PCM	Pulse code modulation
PED	Pulse electrodeposition
PDM	Pulse density modulation
PPM	Pulse position modulation
PRC	Pulse reverse current
PRD	Pulse reverse deposition

QCM	Quartz crystal microbalance
RE	Reference electrode
SEM	Scanning electron microscope
Uv-vis	Ultraviolet-visible
WE	Working electrode

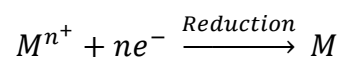
**Chapter I**  
**INTRODUCTION**

## 1.1 Electrodeposition

Electrodeposition is a process whereby metal ions in solution are electroreduced at a polarised interface and nucleate to form a metallic film on the electrode surface. This enables metals to be coated with a layer of another metal which can impart anti-corrosion, anti-wear, aesthetic, or catalytic properties to the substrate. The metals which are deposited on a commercial scale are Cr, Ni, Cu, Au, Ag, Zn, and Cd together with several copper and zinc-based alloys. Electroplating is used extensively to produce decorative reflective coatings such as chromium, nickel, gold, and silver on household items such as jewellery, plumbing, cutlery, and ornaments. It can also be used for automotive or aerospace application to impart a protective surface e.g. chromium, cadmium, zinc. Finally, the other major application is in electrics where it is used to produce tracking in printed circuit boards e.g. copper, silver, and gold.

Electrodeposition has its roots in the early work of Davy and Faraday who used the newly discovered voltaic piles to electrolyse molten salts. Through electroreduction, many of the elements were isolated for the first time. One of the first commercial processes was developed by John Wright in 1840s to deposit silver and gold. This relied on the use of cyanide based electrolytes to obtain bright metallic deposits. Since this time most commercial electroplating baths have been based on aqueous solutions.<sup>1</sup>

The process of electrodeposition is in principle trivial and given as;



However, the reduction process is very complex and numerous additives must be included. The bath needs to contain a source of the metal usually in the form of a metal salt, a ligand to solubilise the metal ions, ions to enable conductivity, additives to stabilise the solution, salts to buffer the solution pH, additives to control deposit morphology e.g. brighteners and compounds to control the anodic reaction.

The main industries served by electroplating are: Automotive (34%); Heavy Industrial (30%); Aerospace (27%); Tools & Fasteners (28%). Also, the products are widely used in the production of items for domestic and commercial use. The function of coatings

produced in the sector is split between corrosion (42%), decorative (31%), abrasion (22%), other (5%).

Pan-European statistics for electroplating are not available but the total size of the surface-finishing sector in the EU can be inferred from the good statistical data available in Germany. There are about 2,100 businesses in the surface treatment industry with about 56,000 employees and a total market volume of 4 billion Euros. The total size of the market in France has been estimated as 6 billion Euros. Electroplating has been estimated to employ around 1 million people in Europe.<sup>2</sup>

In this thesis, the electrodeposition of two metals will be studied, Zn and Cu. It is therefore useful to review their deposition from aqueous solutions.

## 1.2 Nucleation and Growth of Nuclei

The rate of nuclei formation on a metal electrode can be given by *Equation 1.1*.<sup>3</sup>

$$N = N_0[1 - \exp(-At)] \quad \text{Equation 1.1}$$

Where  $N_0$  is total number of sites, in other words, maximum possible number of nuclei on the unit surface,  $t$  is the time,  $A$  is the nucleation rate constant. *Equation 1.1* represents the first order kinetic model of nucleation. The rate of 2D nucleation  $Z$  is given by *Equation 1.2*.<sup>3</sup>

$$Z = k_l \exp\left(-\frac{bs\varepsilon^2}{zekT\eta}\right) \quad \text{Equation 1.2}$$

Where  $k$  is the Boltzmann constant,  $\varepsilon$  is specific edge energy,  $s$  is the area occupied by one atom on the surface of the cluster,  $b$  is the geometric factor which depends on the shape of the 2D cluster,  $k_l$  is the rate constant; the other symbols have their usual meaning. When *Equation 1.1* is investigated, there are two limiting cases for the initial stages of nucleation (when  $t$  is low).<sup>3</sup>

- If the nucleation constant,  $A$ , is large, **Equation 1.1** reduces to  $N \approx N_0$ . This outcome indicates that all electrode sites are converted to the nuclei instantaneously. Therefore, it is referred to as **instantaneous nucleation**.
- If the nucleation constant,  $A$ , is small, the term  $-e^{-At}$  in **Equation 1.1** can become representable in the form of  $-e^{-At} \approx -1 - At$  as a linear approximation. Therefore, **Equation 1.1** reduces to  $N \approx AN_0t$ . This outcome indicates that number of nuclei,  $N$ , is a function of time,  $t$ , and it is referred to as **progressive nucleation**.

It is possible to distinguish between these two types of nucleation growth mechanisms by analysing the experimental data obtained from potentiostatic current-time transients. The rate of nuclei growth can be determined by either of two steps if the charge transfer step in an electrodeposition reaction is fast.<sup>3</sup>

- Lattice incorporation step
- Diffusion of electrodepositing ions into the nucleus

In the lattice incorporation step, there are four types of simple models of nuclei which are usually considered, and these are given in **Figure 1.1**.<sup>3</sup>

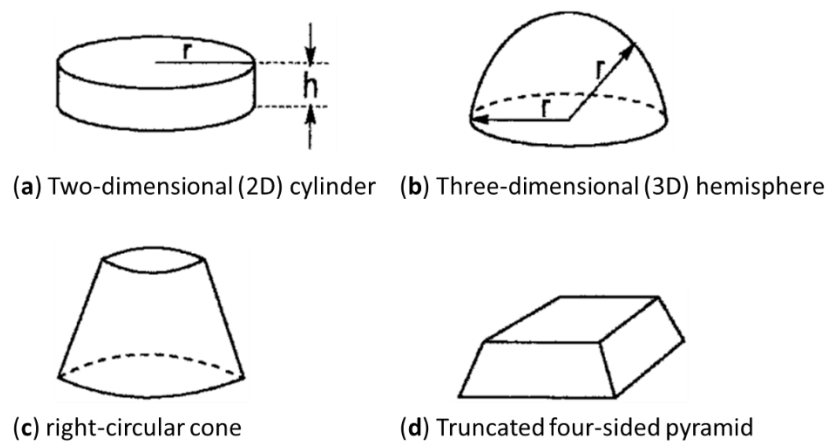


**Figure 1.1** Models of surface nuclei.

Independent and interacting growth of nuclei are the sub cases of growth of surface nuclei. In the initial stages of nuclei growth, the case of nuclei growth can be assumed to be

independent of each other. In this case, the current results only from lateral growth of a single (free) 2D cylindrical nucleus is given by **Equation 1.3**.<sup>3</sup>

$$i = \frac{nFk^2 2\pi hM}{\rho} t \quad \text{Equation 1.3}$$

Where  $\rho$  is the density of deposit,  $M$  is molecular weight,  $h$  is the height of a cylindrical nucleus (a height of monolayer), and  $k$  is the rate constant of 2D nucleus growth ( $\text{mol cm}^{-2} \text{s}^{-1}$ ).

Similarly, the current for a single 3D hemispherical nucleus is given by **Equation 1.4**.

$$i = \frac{nFk^3 2\pi M^2}{\rho^2} t^2 \quad \text{Equation 1.4}$$

In **Equation 1.3** and **Equation 1.4** it is assumed that nuclei growth is independent neighbours, and this is only valid for the initial stages of the growth. In successive stages, it is inevitable that overlapping will take place as shown in **Figure 1.2** due to local concentration and overpotential distribution in the neighbourhood of the growing nuclei (clusters). At this point, the growing nuclei process will not proceed freely in all directions as they will impinge each other.<sup>3</sup>

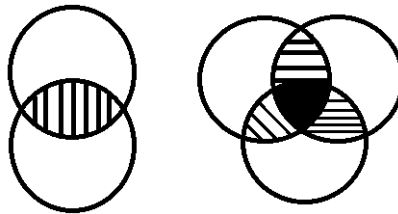


**Figure 1.2** Overlap of diffusion zones of cylindrical nuclei growing on a surface.

Shaded regions show two zones overlapping; and black region, three zones overlapping.<sup>3</sup>

The overall current-time relationships for the simultaneous nucleation and growth of nuclei are of the form  $i \propto t^p$ , and the value of  $p$  depends primarily on whether nucleation is 2D or 3D and if it is instantaneous or progressive.<sup>3</sup>

**Equation 1.3** and **Equation 1.4** are for a single nucleus, and these can be combined with **Equation 1.1** and **Equation 1.2** to provide the overall current-time relationship. If simultaneous two-dimensional (2D) cylindrical growth is taken as a reference to investigate instantaneous and progressive nucleation types, overlapping and non-overlapping cases given in **Figure 1.2** should be used.<sup>3</sup>

The current-time relationship for simultaneous two-dimensional (2D) cylindrical growth is given in **Equation 1.5** and **Equation 1.6** for instantaneous nucleation without overlapping and instantaneous nucleation with overlapping respectively.<sup>3</sup>

$$i = \frac{2n\pi FMhN_0k^2}{\rho} t \quad \text{Equation 1.5}$$

$$i = \frac{2n\pi FMhN_0k^2}{\rho} t \exp\left(-\frac{\pi M^2 t^2 N_0 k^2}{\rho^2}\right) \quad \text{Equation 1.6}$$

Similarly, **Equation 1.7** and **Equation 1.8** is given for progressive nucleation without overlapping and progressive nucleation with overlapping respectively for simultaneous two-dimensional (2D) cylindrical growth.

$$i = \frac{n\pi FMhAN_0k^2}{\rho} t^2 \quad \text{Equation 1.7}$$

$$i = \frac{nF\pi hMAk^2}{\rho} t^2 \exp\left(-\frac{\pi M^2 A t^3 k^2}{3\rho^2}\right) \quad \text{Equation 1.8}$$

In **Equation 1.6** and **Equation 1.8**, the exponential term represents the overlap effect correction.<sup>3</sup>

This model of simultaneous nucleation and growth of nuclei, given in **Equation 1.6** and **Equation 1.8**, predicts an initial increase in current, reaching a maximum, and then a decrease in current. As shown in **Figure 1.3**, progressive nucleation shows an

asymptotical decrease of current to the zero, and this model of nucleation and growth agrees with experimental data of  $I = f(t)$ .<sup>3</sup>

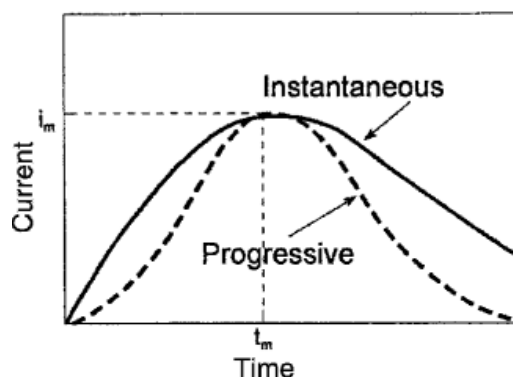


**Figure 1.3** Theoretical current–time transients for instantaneous and progressive nucleation.<sup>3</sup>

Monolayer formation occurs by one of these nucleation types. In the instantaneous nucleation mechanism, according to the **Equation 1.6** with the monolayer spreading out on the substrate from the initial nuclei at time,  $t=0$ . In the progressive nucleation mechanism, according to the **Equation 1.8**, nuclei appear randomly in space and time. Current-time trends for these two mechanisms are shown in **Figure 1.3**.<sup>3</sup>

The theoretical potentiostatic current-time transient which also includes the overlap effect is shown in **Figure 1.4**. The potentiostatic transient is divided into three-time intervals. Current decays during the process of nucleation and growth in the first-time interval, and this is the double layer charging,  $i_{dl}$ . In the second-time interval the current increases, and this increase can be due to the growth of either independent nuclei alone or independent nuclei together with an increase in the number of nuclei forming. This is the current transferred for deposition without overlapping,  $i_{free}$ . Depending on  $i_{free}$ , the nucleation type can be determined; if  $i_{free}$  increases linearly with time, nucleation is instantaneous, and if  $i_{free}$  increases as  $t^2$ , nucleation is progressive. In the third-time interval, growth of independent nuclei and overlap are two opposing effects which causes an initial increase in current, a maximum, and then a decrease in the current in the third-time interval,  $i_{overlap}$ . The increase in current stops when the growth centres begin to overlap, and a decrease in the current starts when the diffusion zones around the nuclei overlap and the growth centres impinge on the each other.<sup>3</sup>

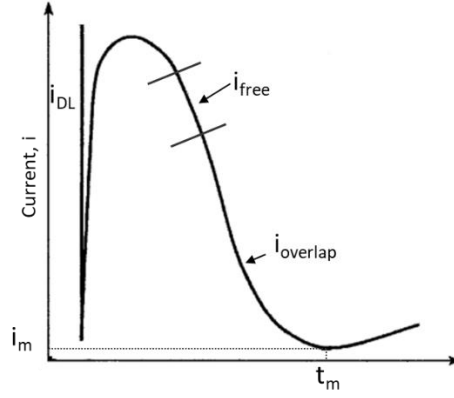


**Figure 1.4** Theoretical potentiostatic current–time transient, including the effect of overlap.<sup>4</sup>

Theoretical diagnostic relationships of current and time for 2D nucleation are given in **Equation 1.9** and **Equation 1.10** for instantaneous and progressive nucleation.<sup>3</sup>

$$\ln \frac{i}{t} = a - bt^2 \quad \text{Equation 1.9}$$

$$\ln \frac{i}{t^2} = c - dt^3 \quad \text{Equation 1.10}$$

Where  $a, b, c,$  and  $d$  are theoretically derived constants. Similarly, Scharifker and Hills,<sup>5</sup> developed a theory for 3D nucleation with diffusion-controlled growth by adding maximum current and time values to the theoretical diagnostic relationship given in **Equation 1.9** and **Equation 1.10**. According to this theory, the theoretical diagnostic relationship in a non-dimensional form are given in **Equation 1.11** and **Equation 1.12** for instantaneous and progressive nucleation respectively.<sup>3</sup>

$$\frac{I^2}{I_m^2} = \frac{3.8181}{\frac{t}{t_m}} \left[ 1 - \exp \left[ -1.2654 \left( \frac{t}{t_m} \right) \right] \right]^2 \quad \text{Equation 1.11}$$

$$\frac{I_m}{I_m^2} = \frac{1.2254}{\frac{t}{t_m}} \left[ 1 - \exp \left[ -2.3367 \left( \frac{t}{t_m} \right)^2 \right] \right]^2 \quad \text{Equation 1.12}$$

In conclusion, it can be seen that theoretical current transients ( $i/i_m$ ) for *Equation 1.11* and *Equation 1.12* shows the same trend as those given in *Figure 1.3*.

### 1.3 Zinc Electroplating from Aqueous Solutions

Electrochemical deposition of zinc is commonly applied on a large scale to steel as an anti-corrosion coating.<sup>6</sup> However, the electrodeposition of zinc from aqueous electrolytes shows relatively low current efficiency due to hydrogen evolution<sup>7</sup>, which can result in hydrogen embrittlement of the substrate.<sup>8</sup> The standard redox potential of zinc is -0.76 V vs. SHE. This potential is more negative than that for iron ( $\text{Fe}/\text{Fe}^{+2}$ ) which is -0.44 V so the Zn provides a sacrificial coating.<sup>9</sup> There are different kind of electrolytes used to deposit zinc and each produces a different deposit morphology. If the deposition medium is acidic with a sulfate anion, the deposit grain size is relatively coarse. If the deposition medium is chloride based, the crystallite diameter is generally larger.<sup>10, 11</sup> For cyanide based electrolytes, two distinct phenomena can be observed. One is a field-oriented texture with finer grains deposited perpendicular to the substrate, whereas the other is un-oriented dispersion finish with small crystals that tend to show three-dimensional nucleation throughout the deposition processes. Although pH is an important factor, the zinc reduction potential is always more negative than that of hydrogen evolution.<sup>12</sup> As a result, zinc deposition is always accompanied by hydrogen evolution.

While the electrodeposition of zinc is a common technique, hot-dip galvanizing is an alternative method for applying zinc to surfaces, although it only works with low carbon steels. These two method which on the face of it carry out the same process tend not to compete as they have different properties and applications. Electroplating produces thinner, smoother, and less adherent coatings and are used on any substrate typically when appearance or tolerance are important. Hot dip galvanising produces an alloy with steel which therefore has better adherence, but the thickness is more difficult to control. This tends to be used for more complicated shapes particularly on small components such as nails and bolts.

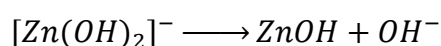
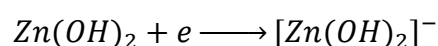
There are three common zinc plating baths; cyanide zinc baths, alkaline non-cyanide zinc baths and acid chloride zinc baths. In cyanide zinc baths, there are two types of plating methods; rack and barrel. In the rack plating, materials are hung, and dip into plating

solutions. The current density of rack plating is between 2 and 5 A dm<sup>-2</sup> (typically with 3 - 6 V). In barrel plating, small objects, such as screws or bolts, are put into a moving barrel which is rotated so that the small pieces keep a contact with an inert cathode. Current density for barrel plating is typically 0.6 A.dm<sup>-2</sup> with a higher applied potential (15 - 25 V). This method is cost effective with small components while ensuring the even current distribution, and so much more even deposition. The average current density in barrel plating is lower than rack plating. There are different electrolyte compositions used in cyanide baths and some of these are listed in **Table 1.1**.<sup>9</sup>

**Table 1.1** Composition (in mol dm<sup>-3</sup>) of cyanide zinc electrolytes.

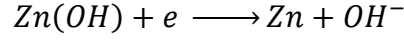
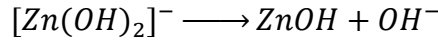
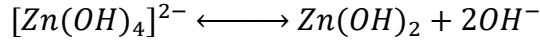
Constituent	Regular	Mid	Low
Zn(CN) <sub>2</sub>	0.51	0.27	0.85
NaCN	0.82	0.41	0.16
NaOH	2	1.9	1.6
Na <sub>2</sub> CO <sub>3</sub>	0.14	0.14	0.14
Na <sub>x</sub> Sy/g L <sup>-1</sup>	2	2	—
Brightener/g L <sup>-1</sup>	1-4	1-4	1-4

The general reaction mechanism for cyanide baths are;<sup>13</sup>

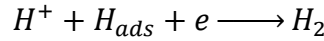
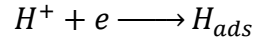


Cyanide baths are obviously quite toxic and for this reason, companies which use them are closely monitored. It is expected, in the near future, that cyanide baths will be prohibited in most electrodeposition processes by EU legislation.<sup>14</sup>

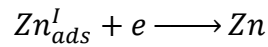
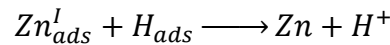
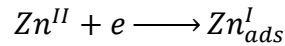
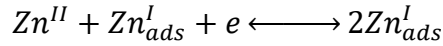
As an alternative method of cyanide zinc baths, alkaline non-cyanide zinc baths were developed. However, the resulting deposit was dendritic in structure.<sup>15</sup> For this reason, most research was focused on controlling deposit morphology with organic and inorganic additives.<sup>16-22</sup> The general reactions of zinc deposition in non-cyanide alkaline zinc baths occurs in four steps.<sup>9</sup>



When alkaline non-cyanide zinc baths and cyanide zinc baths are compared, current efficiency and zinc metal content are lower in the former case. The current densities in non-cyanide baths can range between 2 and 31 A.dm<sup>-2</sup>. Non-cyanide zinc baths are a greener alternative for deposition, but they still cannot compete on the deposit quality of cyanide bath. Acid chloride zinc baths have also been studied as an alternative method to cyanide zinc baths. Current densities are typically in the region of 30 A dm<sup>-2</sup>, as a result of hydrogen evolution reactions;<sup>19</sup>



It has been proposed that zinc electro-crystallization starts with a Zn<sup>I</sup><sub>ads</sub> adions that is weakly bound to the metal surface and diffuse. The proposed reaction processes are;<sup>19</sup>



In order to have better surface properties without dendritic or powdery finishes, proper hydrodynamic control or organic additives are required as it was required in non-cyanide alkaline zinc baths.<sup>23-25</sup>

#### 1.4 Copper Deposition from Aqueous Solutions

Copper is very commonly electrodeposited from aqueous solutions particularly to make electrical interconnects on printed circuit boards. The plating solutions commonly contain inorganic or organic additives such as thiourea,<sup>26</sup> sodium chloride, sodium bromide,

sodium iodide,<sup>27</sup> and ethylenediamine<sup>28</sup> to improve current efficiency, levelling and grain refinement.

In the 18<sup>th</sup> century, copper plating was performed on steel castings by immersing them in copper sulphate solution on a zinc tray.<sup>29</sup> Jacobi obtained the first patent in 1839 for an electrolytic process, for copper deposition and the next 70 years were dominated by acidic electrolytes.<sup>30</sup> These include sulfate-sulfuric acid solutions, sulfate-oxalate-boric acid, benzene disulfonic acid, alkane sulfonic acid, sulfamic acid and fluosilicate-silicic acids. Currently, sulphate and fluoborate solutions are commonly used for copper deposition.<sup>29</sup> The reason behind this is the ionization of  $\text{Cu}^{2+}$  salts in either sulphate or fluoborate solutions are higher than other solutions.<sup>31</sup> The solution resistance of acidic solutions which made of either by sulfate or fluoborate solutions are less than alkaline ones, so they require a lower cell voltage. The solubility of copper fluoborate is twice as high as copper sulfate.

Cyanide based plating baths have been, and to some extent are still, extensively used for copper electrodeposition. This is because cyanide baths produce high quality coatings due in part to their ability to aid anodic corrosion keeping a constant concentration of metal ions in solution. Cyanide base formulations of  $\text{CuCN}$ ,  $\text{NaCN}$  or  $\text{KCN}$  result in stable complexes such as  $\text{CuCN}_{(\text{aq})}$ ,  $[\text{Cu}(\text{CN})_2]^-$ ,  $[\text{Cu}(\text{CN})_3]^{2-}$ ,  $[\text{Cu}(\text{CN})_4]^{3-}$  in water. These are used to increase adhesion, brightness, surface improvement, buffing, soldering. However, usage of cyanide base formulations is decreased approximately 50% in today's plating industry when compared the industrial usage in the 1970s. The alkaline thiocyanate copper bath was introduced by Wernlund in 1941 to increase the smoothness and brightness of the deposits.

Just as observed with zinc, there has been a movement away from cyanide based baths since the beginning of mid-1980s. Alkaline non-cyanide copper plating solutions have now taken over and are used extensively in barrel plating, where they allow faster plating rates and lower sludge generation and provide easier wastewater treatment although they are sensitive to impurities have higher operating costs, and can only be used over a much more limited copper concentration range.

Copper pyrophosphate solutions ( $\text{Cu}_2\text{P}_2\text{O}_7 \cdot 3\text{H}_2\text{O}$ ) with either pyrophosphate ( $\text{K}_4\text{P}_2\text{O}_7$ ) or sodium salt nitrate ( $\text{Na}_4\text{P}_2\text{O}_7$ ) with ammonia have also been extensively used but are less common now. They do yield a significant phosphorous content in the copper deposit which makes the deposit harder and more wear resistant although there are now moves to limit phosphorous emissions into the environment.

While water is an ideal solvent in terms of its availability, high solubility of salts and high conductivity of electrolyte solutions, there are significant issues with its use for electroplating. Firstly, its potential window is relatively narrow (c.a. 1.5 V) which makes it unsuitable for electronegative metals such as aluminium, chromium and zinc. Electroreduction of water leads to poor current efficiencies and hydrogen embrittlement.<sup>32</sup> It also means that electrodeposition onto water sensitive substrates such as aluminium and magnesium is difficult. Finally, it must be remembered that whatever is put into an aqueous solution must be removed before it can be returned to the watercourse. This means that acids and bases must be neutralised, and heavy metals and toxic ligands must also be removed. This can be costly and can lead to environmental damage if not completed correctly.

## **1.5 Non-aqueous Electrodeposition Systems**

The above issues with aqueous solutions have led to significant interest in non-aqueous solutions in the last few decades although few of these alternatives have penetrated the market. There is growing pressure to decrease the use of environmentally hazardous processes such as chromium and nickel plating and EU and US legislation is attempting to limit the use of some of these chemicals. There is also a move to eradicate the use of some metal coatings such as cadmium which is extensively used as an anti-corrosion coating in the aerospace industry. Because of this, there has been a long-standing interest in the electrodeposition of metals such as aluminium. There are a variety of alternative solvents that could be utilized, both ionic and molecular; polar and non-polar. Polar solvents can dissolve electrolytes and result in high conductivities. In general, small solvent molecules will usually offer a high fluidity. However, all polar molecules possess electronegative elements, such as oxygen. This phenomenon comes from their nature which makes them good electron donors and results in strongly coordinated metal ions. This tends to move the reduction potential to more negative values which may again

compete with solvent decomposition. Thus, some of the positive metals can be electrodeposited from polar solvents but with no significant advantages compared to aqueous solutions. Non-polar organic solvents, generally aromatic hydrocarbons have been utilized in electrodeposition of metals. Although they can provide wide potential windows, conductivity of these solvents is poor. One example of these non-polar deposition from the late 1980s is aluminium plating from toluene, and this is a technologically advanced technique for its era called Alumiplate process.<sup>33, 34</sup> However, it is difficult to operate due to the use of triethyl aluminium used as a source of aluminium. This is pyrophoric which is dangerous when used in combination with a highly flammable solvent such as toluene. Other metals have also been plated using aromatic solvents including Pb, Cr, Ti, Cd, Cu, and Sn.<sup>35, 36</sup> The topic of electrochemistry in non-aqueous solutions has been extensively reviewed by Izutsu.<sup>37</sup>

### 1.5.1 Ionic Liquids

High temperature molten salts have been used since the early 1800s for metal reduction but their use for metal plating has been limited by the practical difficulties of working at high temperatures. It should be stressed, however, that one of the largest electroreduction reaction is the Hall–Héroult process for the smelting of aluminium. This is carried out 940–980°C on the millions of tonnes p.a. scale and uses a molten salt based on Al<sub>2</sub>O<sub>3</sub> in Na<sub>3</sub>AlF<sub>6</sub>. The discovery of low and even room temperature molten salts (termed ionic liquids) has, with hindsight, been credited to several groups and was initially used for Friedel and Crafts aromatic substitution reactions<sup>38</sup> using Lewis acid catalysts such as AlCl<sub>3</sub>. During the reaction process a red-coloured oil was formed which has subsequently been identified as an early ionic liquid with a stable cationic intermediate. Walden, at about the same time made ethylammonium nitrate with a melting point 12 °C.<sup>39, 40</sup>

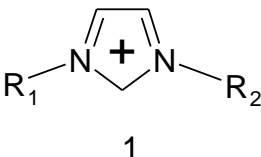
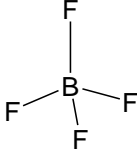
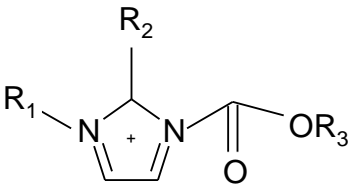
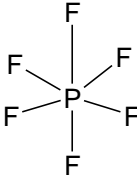
The first recognised attempts to purposefully form low temperature molten salts were made in the 1950s using LiCl/ KCl/ AlCl<sub>3</sub> eutectics. Seminal work at the end of that decade used ethylpyridinium chloride/ AlCl<sub>3</sub> eutectics and later N-butylpyridinium cations. These liquids were quite viscous and resistive but work by Hussey et al. used 1-ethyl-3-methyl-imidazolium as a cation led to the first truly room temperature ionic liquid. The liquid has been extensively used to study aluminium deposition and the area has recently been reviewed.<sup>41</sup>

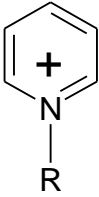
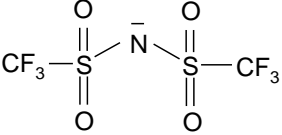
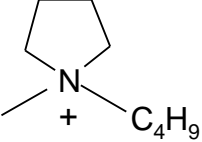
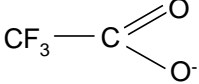
The mixtures of ammonium halides with aluminium chloride form a range of complex anions which in this case are mostly  $[\text{AlCl}_4]^-$  and  $[\text{Al}_2\text{Cl}_7]^-$ . They have been used to study the electrodeposition of aluminium alloys together with the deposition of more electropositive metals but the issue with them is that they hydrolyse in contact with moisture and are therefore difficult to use. Wilkes and Zaworotko made an ionic liquid that was air- and water-stable by incorporating tetrafluoroborate or ethanoate anions with imidazolium cations.<sup>42</sup> These do not contain a very electroactive element and so should have a wider potential window. The  $\text{BF}_4^-$  anion has a delocalised charge which brings down the melting point and decreases the viscosity.

Since this initial description of ionic liquids using discrete anions and cations a wide variety of salts have been synthesised and characterised. Some of the most common cations and anions are listed in **Table 1.2**.

By far the largest body of work has been carried out using 1-alkyl 3-methyl imidazolium cations (Compound 1 in **Table 1.2** lowest viscosity). There is a lot of inconsistencies in the literature, but they are usually abbreviated to a \*mim or \*MIM where \* is the alkyl group i.e. Bmim or BMIM is 1-butyl 3-methyl imidazolium. The nomenclature which has recently been adopted for this cation is C<sub>4</sub>mim. Ethyl- and butyl- substituted cations are the most commonly used as they have the lowest melting points and the lowest viscosity.

**Table 1.2** Commonly used cations and anions in ionic liquids.

Nitrogen based Cations	Discrete Anions
 <p style="text-align: center;">1</p>	
	

	
	$(\text{CN})_2\text{N}^-$
$\text{R}_1\text{R}_2\text{R}_3\text{R}_4\text{N}^+$	

By comparing various chloride salts, the influence of the cationic component can be seen. Alkali metal chlorides such as NaCl and KCl have high melting points (801°C and 772 °C respectively). Substituting the cation with a suitable organic cation for example [EMIM]<sup>+</sup> or [BMIM]<sup>+</sup>, the melting point decreases significantly (87 °C and 65 °C respectively). Factors involving the cation that form lower melting ionic liquids are low symmetry, weak intermolecular bonding, for example the avoidance of hydrogen bonding, and a good distribution of charge in the cation.

The cationic component is not the only factor that controls the melting point of the system. The anion also plays a role. By keeping the cation constant, in this case [EMIM]<sup>+</sup> altering the size of the anion whilst maintaining the same charge alters the melting point for example [EMIM]Cl has a melting point of 87 °C, but the melting point lowers when the Cl<sup>-</sup> anion is replaced with for example [NO<sub>3</sub>]<sup>-</sup> (38 °C), [AlCl<sub>4</sub>]<sup>-</sup> (7 °C), [CF<sub>3</sub>CO<sub>2</sub>]<sup>-</sup> (-14 °C) etc. As anion size is increased there is a further decrease in the melting point of the system. Additionally, presence of several anionic species has been shown to reduce the melting point of the system. The molar ratio of Lewis acid species added to the halide salt can alter the anionic species. This mixture of anionic species results in a decrease in the melting point of the system.

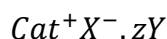
Ionic liquids have no measurable vapour pressure, and this is often misreported as indicating that they are “Green” solvents. This property does mean that it is possible to separate the reaction mixture by distillation effectively and it is possible to work with these liquids under high vacuum conditions. The thermal stability of an ionic liquid is

directly related to the strength of the heteroatom-carbon and heteroatom-hydrogen bonds. Ionic liquids formed from alkylation of amines or phosphanes show higher thermal stability but do show a tendency to undergo retro-quaternization at temperatures nearer 150 °C. It has been shown that certain ionic liquids however show very high thermal stability for example [EMIM][BF<sub>4</sub>] has a liquid stability range of 300 °C and [EMIM][(CF<sub>3</sub>SO<sub>2</sub>)<sub>2</sub>N] has been shown to have a liquid range of 400 °C.

The viscosity of ambient temperature molten salts is several orders of magnitude higher than high temperature molten salts due partially to the difference in size of the ions, but also due to the increased void volume. The viscosity can be tuned but the lowest value is thought to be about 10 cP. Ionic liquids with the lowest viscosity tend to have highly fluorinated anions.

### 1.5.2 Deep Eutectic Solvents

Some of the first ionic liquids were mixtures of quaternary ammonium salts with aluminium chloride forming a low melting point eutectic. A eutectic is the composition that has the minimum melting point in a two-component phase diagram. For a significant decrease in melting point to occur a strong complex needs to be formed between the two components. One of these components is usually a halide salt and these can form ionic or hydrogen bonds with the other component. Abbott has classified the types of compounds that form ionic eutectics into four categories. They can be described by the general formula given by the general formula.



where  $Cat^+$  is usually any ammonium, phosphonium or sulfonium cation although in eutectic type 4 systems it can also be a metal ion,  $X^-$  is normally a halide anion (usually  $Cl^-$ ). The halide anion interacts with a Lewis or Brønsted acid  $Y$  and  $z$  refers to the stoichiometric constant.

Type 1  $Y = MCl_x$ ,  $M = Zn$ ,<sup>43-45</sup>  $Sn$ ,<sup>46</sup>  $Fe$ ,<sup>47</sup>  $Al$ ,<sup>48</sup>  $Ga$ ,<sup>49</sup>  $In$ <sup>50</sup>

Type 2  $Y = MCl_x \cdot yH_2O$ ,  $M = Cr$ ,<sup>14</sup>  $Co$ ,  $Cu$ ,  $Ni$ ,  $Fe$

Type 3  $Y = RZ$ ,  $Z = CONH_2$ ,<sup>51</sup>  $COOH$ ,<sup>52</sup>  $OH$ <sup>53</sup>

Type 4  $Cat+X^- = ZnCl_2, AlCl_3$   $Y = RZ$ ,  $Z = CONH_2$

Several of these given eutectic systems above will be used in Chapter 3 to investigate the role of speciation and Lewis acidity in controlling deposit morphology.

Type 1 eutectics simply extended the concept used initially for aluminium chloride to other Lewis acid metal salts such as  $ZnCl_2$ ,  $SnCl_2$  and  $FeCl_3$ . These all formed room temperature eutectic mixtures which could be used for metal deposition and Lewis acid catalysis. In these mixtures, a covalent/ionic bond is formed between the metal salt and the chloride forming a complex anion of the form  $ZnCl_3^-$  or  $Zn_2Cl_5^-$  depending upon the ratios of the two components.

Type 2 eutectics were primarily studied for chromium electrodeposition. In Type 3 eutectics the chloride anion forms complexes with compounds able to form a hydrogen bond. This included a variety of amides, alcohols, and carboxylic acids. The so-called deep eutectic solvents (DES) have been extensively used for a wide variety of applications including metal deposition and dissolution.<sup>54</sup>

In these DESs, the lattice energy of salts is decreased by the formation of a complex. One advantage of these liquids is that the hydrogen bond donors are simple compounds. Many are non-toxic and inexpensive. These can include simple compounds such as glycerol, fructose, urea, and oxalic acid. They are made by simply mixing the two compounds with moderate heat. Recent work has even shown that they can be prepared in continuous flow mode using an extruder.<sup>55</sup> These liquids are generally stable with atmospheric moisture, many are biodegradable and some have negligible toxicity.

Metal halide and quaternary ammonium ionic liquids have higher depression of freezing points when compared hydrogen bonding types, such as amides and acids. This is because the covalent bonds are stronger than the hydrogen bonds.

**Table 1.3** shows the Melting points of mixtures of complexes formed with choline chloride compared to the melting point of the pure complexing agent  $T_m^*$ . The  $\Delta T_f$  value is related to how strongly the anion and complexing agent interact with each other. **Table 1.3** shows that  $\Delta T_f$  is larger for Type 1 eutectics than for the other eutectics. This is logical

as the covalent/ionic bond formed with the metal salt will be bigger than the hydrogen bond formed in a Type 3 eutectic. Recently Abbott et al. used calorimetry to determine the enthalpy of interaction between the anion and HBD. They measured the heat capacity of the two components and the heat capacity of the mixture and used a Hess cycle to determine the enthalpy of interaction between the components. The HBDs used were all phenolic compounds and substituted benzoic acids. It was found that the enthalpy of interaction was -10 to -20 kJ mol<sup>-1</sup> which is typical of hydrogen bond formation. It was shown that  $\Delta T_f$  values correlated strongly with the depression of freezing point.<sup>56</sup>

**Table 1.3** Freezing temperature data for a variety of metal salts and amides when mixed with choline chloride in 2:1 ratio.<sup>57</sup>

		$T_f/^\circ\text{C}$	$T_f^*/^\circ\text{C}$	$\Delta T_f/^\circ\text{C}$
Type 1	ZnCl <sub>2</sub>	24	283	259
	SnCl <sub>2</sub>	37	246	209
	FeCl <sub>3</sub>	65	306	241
Type 2	CrCl <sub>3</sub> . 6H <sub>2</sub> O	4	83	79
	MgCl <sub>2</sub> .6H <sub>2</sub> O	10	117 <sup>a</sup>	107
	CoCl <sub>2</sub> .6H <sub>2</sub> O	16	86	70
	LaCl <sub>3</sub> .6H <sub>2</sub> O	6	91	85
	CuCl <sub>2</sub> .2H <sub>2</sub> O	48	100 <sup>a</sup>	52
Type 3	Urea	12	134	122
	1, Methyl urea,	29	93	64
	1,3 Dimethyl urea	70	102	32
	1,1 Dimethyl urea	149	180	31
	Thiourea	69	175	106
	Acetamide	51	80	29
	Benzamide	92	129	37

<sup>a</sup>Denotes decomposition temperatures.

Hydrogen bonding in Type 3 eutectics was also studied using NMR spectroscopy<sup>58</sup> Heteronuclear Overhauser effect spectroscopy (HOESY) was used to investigate the interaction between the fluoride anion of choline fluoride, HOCH<sub>2</sub>CH<sub>2</sub>N<sup>+</sup> (CH<sub>3</sub>)<sub>3</sub> F<sup>-</sup> and urea. Intense cross-correlation were observed between protons on urea and the fluoride

anion. Fast atom bombardment mass spectrometry also shows evidence of clusters of  $[\text{Cl} \cdot 2\text{urea}]^-$  and  $[\text{Cl} \cdot 1\text{urea}]^-$ .

The factors affecting the physical properties of DESs are like those for ionic liquids discussed above. They are tuneable not only in terms of the components used but also in terms of the composition. In most practical cases Type 3 eutectics often have more than one HBD to tune both the physical and chemical properties of the liquid.

The DES with the lowest viscosity and highest conductivity is that with  $\text{ChCl}$  and ethylene glycol as shown in **Table 1.4**. This liquid known by its trade name of Ethaline is for this reason one of the most commonly used. The glycol and the chloride anion have relatively weak interactions which probably results in some ‘free’ glycol which can freely move, decreasing the viscosity of the liquid. The glycol-based liquids have been used for the deposition of zinc and zinc alloys<sup>59</sup> as well as the electropolishing of stainless steel.<sup>53</sup>

**Table 1.4** Viscosity and conductivity of a variety of ionic liquids at 298 K.

Cation Anion	$\kappa / \text{mS cm}^{-1}$	$\eta / \text{cP}$
EMIM $\text{BF}_4$	14	32
EMIM $\text{N}(\text{CF}_3\text{SO}_2)_2$	8.4	28
BMIM $\text{BF}_4$	3.5	180
BuMePy $\text{N}(\text{CF}_3\text{SO}_2)_2$	2.2	85
choline $\text{Zn}_2\text{Cl}_5$	0.02	76 000
choline $\text{CrCl}_4 \cdot 6\text{H}_2\text{O}$	0.37	2346
choline $\text{CoCl}_3 \cdot 6\text{H}_2\text{O}$	1.7	392
choline $\text{Cl} \cdot 2\text{urea}$	0.75	632
choline $\text{Cl} \cdot 2\text{propanediol}$	2.2	89
acetylcholine $\text{Cl} \cdot 2\text{propanediol}$	0.51	117
choline $\text{Cl} \cdot \text{malonic acid}$	0.36	3340
choline $\text{Cl} \cdot 2\text{ethylene glycol}$	7.6	36
$\text{ZnCl}_2 \cdot 3.5 \text{ urea}$	0.06	11 340
$2\text{CrCl}_3 \cdot 6\text{H}_2\text{O} : \text{urea}$	5	2602

The type 4 eutectics are slightly different from the other three types, in that they do not have quaternary ammonium salts. Instead, the complex is formed between a metal salt and a HBD<sup>58</sup> which is a glycol or amide. Some examples of this type of eutectic include ZnCl<sub>2</sub>-urea,<sup>58</sup> AlCl<sub>3</sub>- acetamide, and SbCl<sub>3</sub>/TeCl<sub>4</sub>- acetamide<sup>60</sup>. In most cases the metal salt disproportionates forming a metal containing anion and cation e.g. ZnCl<sub>2</sub> and urea forms [ZnCl<sup>+</sup>.urea] and [ZnCl<sub>3</sub><sup>-</sup>]. In an analogous manner the same happens with aluminium chloride and a range of amides.<sup>61</sup>



A similar approach was used by Fang et al using dipropyl sulfide to complex AlCl<sub>3</sub>.<sup>62</sup> What is interesting about these systems is that the metal is present in a cationic form which will change the concentration of metal ions present in the double layer.

Type 4 eutectics are useful as they produce cationic metal complexes, ensuring that the double layer close to the electrode surface has a high metal ion concentration. Abbott et al. have also produced non-halide containing eutectics using nitrate salts e.g. Zn(NO<sub>3</sub>)<sub>2</sub>.6H<sub>2</sub>O. 2propylene glycol. This has a very high conductivity and low viscosity ( $\kappa = 20 \text{ mS cm}^{-1}$  at 25 °C). Binnemans et al, used a similar approach to create a complex between Cu((CF<sub>3</sub>SO<sub>2</sub>)<sub>2</sub>N)<sub>2</sub> and acetonitrile<sup>63</sup> forming the complex cation [Cu(CH<sub>3</sub>CN)<sub>4</sub>]<sup>2+</sup>.

## 1.6 Applications of ionic liquids and deep eutectic solvents

ILs and DESs have been commercialised for a variety of applications as summarised below. These are covered in a variety of reviews although there is little discussion of the economics of the processes.<sup>53, 56, 58-65</sup> The main areas of study include;

<b>Active liquids</b>	Lubricants, plasticisers, dispersing agents
<b>Electrochemistry</b>	Metal deposition, electropolishing, electrolytes in batteries, photovoltaic devices, fuel cells
<b>Synthetic chemistry</b>	Phase transfer catalysts, Lewis acid catalysis, natural product extraction
<b>Analysis</b>	HPLC and gas chromatography stationary phases

Probably the most successful process that has been commercialised to date is BASF's BASIL process. This is a classic case study of Green Chemistry as it decreases the volume of material used and optimises the space-time yield of a process by designing a base which remains a liquid when it neutralises the acid. This greatly simplifies phase separation.

Alkoxyphenylphosphines are precursors for the synthesis of photoinitiators that are used in the manufacture of printing inks and wood coatings. The phosphines are prepared by the reaction of phenyl-chlorophosphines with alcohols. State-of-the-art conventional acid scavengers such as triethylamine produce solids that are difficult to separate from product and require large amounts of organic solvents to keep in suspension. The BASIL process is one of the best success stories for the use of an ionic liquid as it provides a significantly simpler process than the previous technology.

### **1.7 Electrodeposition using ILs and DESs**

There is an extensive literature on the electrodeposition of metals and the topic has been covered in a series of reviews and books.<sup>32, 45, 57, 59, 61, 66-76</sup>

While there is little point in re-reviewing this extensive topic here, it is important to recap on the reasons why ionic liquids are different to aqueous solutions for electrodeposition and why there are some inconsistencies in previous ionic liquid studies.

Most metals have been electrodeposited from ambient temperature ionic liquids. and extensive review have been written by Abbott<sup>32, 77</sup> and Endres.<sup>78, 79</sup> These suggest that the most suitable ionic liquid to use depends upon the metal being deposited. Ionic liquids with discrete anions are the most appropriate for reactive metals such as Al, Li, Ti, V and W. Type 1 eutectics are more suitable for metals like Al, Ga and Ge whereas Cr is most suitable for Type 2 eutectics. Lower value metals such as Zn, Cu, Ag, and their alloys are better suited to Type 3 eutectics.

Although ionic liquids can be used for the electroreduction of most metals there are technical and economic reasons why they will not be used everywhere. It is probably easier to focus on the unique reasons why they should be used.

**Deposition of novel-architectures:** Probably the most important reason for this thesis, is that ionic liquids enable novel deposit morphologies to be obtained. Aqueous solutions tend to deposit metals with large crystallites as compared to nanocrystalline deposits with ionic liquids. The double layer structure could be one cause of this and the cation used has been shown to significantly affect the deposit morphology.<sup>80, 81</sup> Larger aromatic cations, have been shown to produce smaller grain sizes than small aliphatic ones.<sup>82</sup>

A variety of microstructures have been deposited using masks and templates to produce pores, tubes, and wires. Endres et al. created a variety of 3D Cu<sup>83</sup> and Si<sup>84</sup> surfaces creating photonic devices with different colours. A variety of well-defined silver<sup>85</sup> and aluminium<sup>86</sup> nano wires were deposited through polymer templates. These have recently been reviewed.<sup>57</sup>

It is the ability to deposit novel architecture for novel materials such as metal foams, composite materials, novel semiconductors and photocatalysts that ionic liquids show the most potential.

**Replacement of toxic solutions:** As described above, a significant issue with aqueous electroplating is that toxic compounds such as NaCN, CrO<sub>3</sub>, NiSO<sub>4</sub> and CoCl<sub>2</sub> must be removed from the water before it can be disposed of. The use of these compounds is controlled by legislation such as REACH.<sup>87-89</sup> Work by Abbott et al. has used ionic liquids to produce the first chromium plating system based on Cr(III) rather than Cr (VI). This has been scaled up in Belgium to the tonne scale by OCAS.<sup>14, 90</sup> Nickel is another metal under threat as most of the compounds are classed as sensitizers. It has recently been shown that if deposition is carried out under the same conditions of temperature and concentration that are used in aqueous solutions then the same deposition rate can be achieved using ionic liquids. The deposit does however have a higher hardness and a smaller crystallite size when deposited using an ionic liquid.<sup>91</sup>

**Electrodeposition of electronegative metals:** Water has a relatively small potential window compared to ionic liquids. This is the area which has received most research attention particularly for the electrodeposition of aluminium. This is one of the main goals for corrosion resistant coatings, particularly in the aerospace industry as a replacement

for cadmium electrodeposition. This area has been reviewed by Endres et al.<sup>92</sup> and Alemany et al.<sup>93</sup> Ionic liquids have been shown to have potential windows  $> 5$  V which enables the deposition of reactive metals such as magnesium<sup>94</sup> and sodium<sup>95, 96</sup> Ta and Ru.<sup>97-99</sup>

Ionic liquids also enable the redox potentials of metals to be changed significantly which enables novel alloys to be electrodeposited. Some of the ones deposited include Al-Zn,<sup>100</sup> Ti-Al,<sup>101</sup> Al-Mn<sup>102</sup> and Al-Li<sup>103</sup> alloys. Again, these are interesting from an anti-corrosion perspective.

**Electrodeposition of semiconductors:** The electrodeposition thin film semiconductors means that they can be used for inexpensive photovoltaic devices. LED materials, photonic devices, and p-n junctions. Comparatively little work has been carried out in this area from aqueous solutions because many of the elements are water sensitive. The electrochemistry of pure semiconductor materials has been studied in-depth particularly by Endres et al. and they and others have shown the deposition of Si, Ge, Ga and In.<sup>104-106</sup> The deposition of compound semiconductors has also been studied including CdTe,<sup>107</sup> CdS,<sup>108</sup>  $\text{Si}_x\text{Ge}_{1-x}$ <sup>109</sup> Bi-Te and Sb-Te.<sup>110</sup> Some three and four component semiconductors have also been produced including  $\text{AlInSb}$ <sup>111</sup> and  $\text{Cu}_2\text{ZnSnS}_4$ .<sup>112</sup> Semiconductor electrodeposition has recently been thoroughly reviewed.<sup>57</sup>

**Coating reactive metals:** In addition to being able to electrodeposit electronegative metals onto substrates ionic liquids have been used to deposit metals onto electronegative substrates. This is particularly interesting for coating metals such as aluminium and magnesium and their alloys.<sup>113, 114</sup>

Electrodeposition of electronegative elements in aqueous solutions results in hydrogen evolution from the electrochemical reduction of water as a competing reaction. This decreases the current efficiency of the process but more importantly it can lead to incorporation of hydrogen in the matrix of the substrate metal. This can lead to a process known as hydrogen embrittlement which can lead to mechanical failure of the item at stresses below the ultimate tensile strength of the material. Carrying out electrodeposition in an aprotic solvent should stop hydrogen embrittlement. Hydrogen evolution can also

lead to cracking of the coating which decreases the corrosion protection offered by the electrodeposit.

## 1.8 Zinc Deposition from ILs and DESs

Zinc is one of the most commonly studied metals for electrodeposition in ionic liquids. Most of the studies have involved Type 1 chlorozincate based ionic liquids which are analogous to the haloaluminates studies. The chlorozincate liquids are easy to make and handle although they have lower conductivities and higher viscosities. It was initially thought that these liquids were water stable but Hsiu et al. studied EMIMCl: ZnCl<sub>2</sub> mixtures and showed using FAB MS that some hydrolysis does occur.<sup>115</sup> It was also found by the same group that the potential window of this mixture was significantly affected by the Lewis acidity. This is because the reduction of zinc appears to be more difficult in Lewis basic liquids.

Sun *et al.* studied the 1:1 EMIMCl: ZnCl<sub>2</sub> system on glassy carbon (GC), nickel and platinum electrodes.<sup>116</sup> The anodic dissolution process showed one peak on GC, but there were two peaks on Ni separated c.a. 0.6 V. They suggested that the more positive oxidation process corresponded to the dissolution of an inter-metallic compound formed during electrodeposition. This is a topic that will be discussed in more detail in this thesis and it is a topic that we have carried out in collaboration with Zhang who has confirmed this mechanism of intermetallic formation.<sup>117</sup>

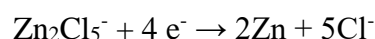
Sun used chronoamperometry on a variety of surface with and without diluents and found that the electrodeposition of zinc proceeds under mixed diffusion and kinetic control. The zinc grain size was about 4-5 μm without a diluent but increased when propylene carbonate was added. Grain size also increased when the temperature was increased.<sup>83</sup> These are important observations which will hopefully be addressed in this thesis.

A similar study was performed by Iwagishi who used the Lewis basic C<sub>2</sub>mim Br: ZnBr<sub>2</sub> using ethylene glycol as a diluent.<sup>118</sup> Sharifker-Hills analysis of the chronoamperometric data suggested progressive nucleation with diffusion controlled growth. The addition of ethylene glycol increased the reduction current despite the zinc being diluted which shows that mass transport is important in the rate of metal deposition.

Abbott *et al.* used a 1: 2 choline chloride (ChCl): ZnCl<sub>2</sub> to study the electrodeposition of zinc.<sup>119</sup> This produced relatively large crystallites which were similar in size to those obtained using EMIMCl: ZnCl<sub>2</sub>. It was found that high current densities resulted in non-adherent deposits. The current efficiency for deposition was almost 100 % and the charge for deposition and stripping were almost equal although it was noted that a layer of underpotential deposited zinc remained on the surface.

Chlorozincate liquids have also been studied for the deposition of several zinc-based alloys including Pt–Zn, Zn–Fe, Sn–Zn and Cd–Zn alloys. Zinc alloys, which are not dealt within this thesis, were recently reviewed by Sun.<sup>57</sup>

The changes in zinc morphology with composition, diluents and temperature discussed above, could be due to changes occurring close to the electrode surface during electrodeposition. As the chlorozincate anions are reduced chloride anions are released into the liquid making it Lewis basic.



which will affect the speciation of the zinc;

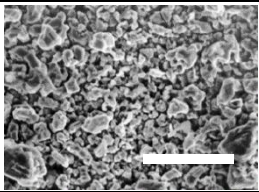
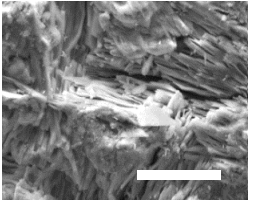
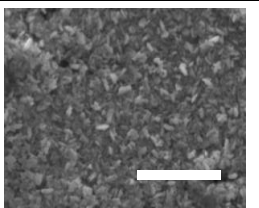
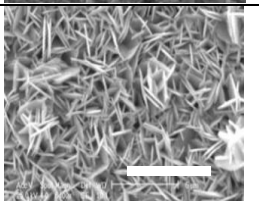
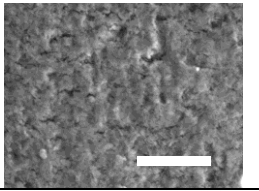
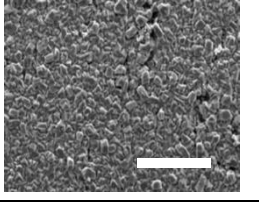


The effect will be made worse because the chlorozincate liquids are particularly viscous, so the diluents will decrease the viscosity and allow the chloride ions to diffuse into the bulk solution.

Zinc and zinc alloy deposition has been studied in choline chloride based Type 3 eutectics using ethylene glycol and urea as the HBDs.<sup>59</sup> The HBDs were found to affect the electrochemistry of the metals presumably due to differences in speciation. In urea, the only zinc containing species is ZnCl<sub>3</sub><sup>-</sup> whereas in EG ZnCl<sub>3</sub><sup>-</sup>, Zn<sub>2</sub>Cl<sub>5</sub><sup>-</sup> and Zn<sub>3</sub>Cl<sub>7</sub><sup>-</sup> were detected and this is because urea will act as a far stronger ligand for ZnCl<sub>3</sub><sup>-</sup> than ethylene glycol. The zinc deposits obtained were different in morphology to each other and different to that obtained in the Type 1 eutectic (See **Table 1.3**). The zinc-tin system is of great importance due to its superior corrosion protection properties. The deposition using these eutectics was scaled up to pilot scale and used for the electrodeposition onto water sensitive magnesium alloys and in a barrel plating configuration for coating nuts and bolts.<sup>120, 121</sup>

The HBD also affects the way in which alloys form. Voltammetry and XRD showed that when both Zn and Sn were present in the same melt a homogeneous Zn-Sn alloy phase was formed when urea was used as the HBD whereas ethylene glycol caused separate zinc and tin phases to form.<sup>59</sup>

**Table 1.5** Morphologies of zinc deposits obtained from different types of DESs at 25 °C. Scale bar is 5 μm.

Type	SEM	Viscosity/ cP	DES	[Zn] / mol dm <sup>-3</sup>
1		72,000	1 ChCl: 2 ZnCl <sub>2</sub>	8.24
2		18	1 ChCl: 1.5 Zn(NO <sub>3</sub> ) <sub>2</sub> ·6H <sub>2</sub> O	4.09
3		200	1 ChCl: 2 Urea	0.30
3		20	1 ChCl: 2 EG	0.30
4		46.3	2 PG: 1 Zn(NO <sub>3</sub> ) <sub>2</sub> ·6H <sub>2</sub> O	4.63
4		11,340	1 ZnCl <sub>2</sub> : 4 Urea	9.92

Studies of zinc deposition in Type 3 eutectics showed that the adsorption of chloride on zinc poisons the metals surface and can lead to platelet shaped deposits.<sup>122</sup> Strong HBDs

can complex the chloride ions and these brighten the deposits resulting in nodular grains. *Table 1.5* shows the zinc morphologies obtained from different DESs. The first aim of this thesis will be to understand the deposition of zinc in these different liquids and explain how the Lewis acidity of the liquid affects the deposit morphology.

This thesis also deals with pulse plating, so it is important to understand the electrodisolution process. For zinc, this is almost unstudied. Karim<sup>123</sup> did study the dissolution of zinc using impedance spectroscopy and voltammetry and found that it was the easiest metal to dissolve and there were no apparent films formed on the electrode surface during dissolution which was in contrast to most of the other metals studied. This finding will be challenged later in this thesis.

## 1.9 Copper Deposition from ILs and DESs

In comparison to zinc, copper has been studied in far less detail in ionic liquids. This is partially for the obvious reason that it works so well from aqueous solutions so why study it in an ionic liquid. Chen and Chang studied the electrodeposition of copper in 1-butyl-3-methylimidazolium salicylate. They found that copper halides were soluble in them and they found that the deposit morphology was extremely potential dependent.<sup>124</sup>

El-Abedin et al studied Cu<sup>I</sup> in a [BMP][Tf<sub>2</sub>N] liquid. Copper salts were found to be poorly soluble so the copper(I) species was introduced into the liquid by anodic dissolution. Electrodeposition resulted in nanocrystalline copper with crystallites of about 50 nm in diameter.<sup>106</sup> The same group were also able to deposit highly ordered macroporous copper films using 1-butyl-3-methylimidazolium dicyanamide with a polystyrene template. The copper electrodeposited around the polystyrene spheres resulting in an ordered hexagonal structure with regular interstitial voids once the polymer sphere had been dissolved with an organic solvent. The deposits resulted in photonic devices where the colour of the film depended on the size of the voids and the angle at which the material was viewed.<sup>83</sup> Brooks et al.<sup>63</sup> used a copper bistriflamide complex with acetonitrile to electrodeposit copper and got a smooth deposit at a current density of 25 A dm<sup>-2</sup>. This was a good method of overcoming the solubility issues of some copper salts in some ionic liquids.

Most of the rest of the work was carried out using deep eutectic solvents. Copper deposition was studied by Abbott et al, in 1 ChCl: 2 urea, and 1 ChCl: 2 ethylene glycol liquids. It was found that bright deposits could be obtained in both liquids. Composite materials could also be deposited using SiC and Al<sub>2</sub>O<sub>3</sub> particles.<sup>125</sup> Chronoamperometry at a high copper concentration showed that nucleation occurred through a progressive mechanism and resulted in a nanostructured deposit. The incorporation of particles was studied using electrochemical quartz crystal microbalance (EQCM) and it enabled in-situ measurement of particulate incorporation. The particles formed stable colloids in the ionic liquid this resulted in an even distribution of the composite particles throughout the coating.

The electrodeposition of copper and indium were studied in a 1 ChCl: 2 urea eutectic using InCl<sub>3</sub> and CuCl<sub>2</sub>. The deposition of numerous phases could be seen using cyclic voltammetry and XRD was used to identify the alloys formed. The intermetallic formed was thermally annealed with gaseous selenium under pressure to form the intermetallic CuInSe<sub>2</sub>.<sup>126</sup>

Abbott et al studied the electrodeposition of copper-tin alloys from DESs at room temperature using EQCM, XRD, SEM and EDX. They found that numerous phases were deposited, and that the composition of the deposit was dependent on the solution composition and the current density. The HBD (urea or ethylene glycol) had a significant effect on the deposit composition. The study also showed that classical aqueous brighteners for copper deposition were also effective for DESs.<sup>127</sup>

## 1.10 Research Aims

This project aims to investigate a fundamentally different process to incorporate metal onto a substrate. This can be best illustrated by the schematic diagram in *Figure 1.5*.

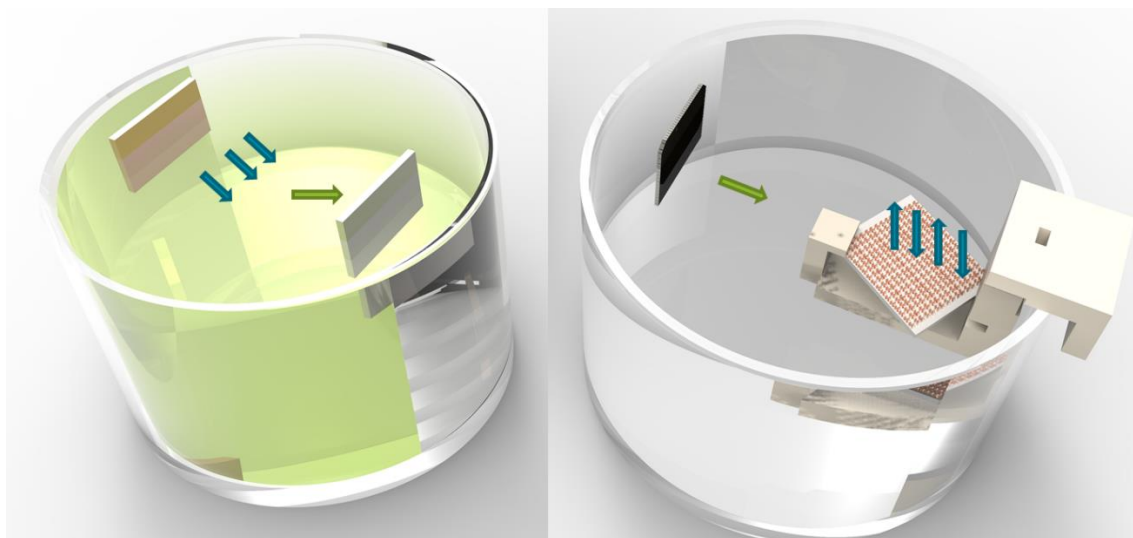


*Figure 1.5* Traditional plating system is represented in the left which cations are provided from solution and dissolved anode as well. The process applied in this thesis aims to provide cations from the powders of target metal desired to be deposited placed onto substrate.

In traditional aqueous solutions, metal ions from solution are electrodeposited onto the cathode surface usually using a constant, direct current supply. To maintain the metal ion concentration in solution a soluble anode is used. If there are no alternative side reactions such as solvent decomposition, then in principle the overpotential required for deposition should be relatively small and the process just takes metal from the anode and deposits it on the cathode. The aim behind the proposed project is to coat the cathode with a fine powder of the metal to be coated and then to apply potential pulses to the electrode surface to bring about partial dissolution followed by deposition in between the particle grains.

This, if successful, this should enable the metal powder to be “stuck” to the electrode surface and potentially enable metal to be deposited with >100 % current efficiency. For the purposes of this study, two metals were chosen; zinc and copper. These have significantly different reduction potentials zinc is reduced at about -1.4 V and copper at -0.5 V. It was also chosen to try this experiment in DESs because it had a greater possibility of obtaining high current efficiency than in aqueous solutions.

Several outcomes were envisaged for this project;

The electrochemistry of zinc and copper will be studied in detail to understand the reversibility of the dissolution and deposition processes. Recent work in the group has suggested that the electro dissolution process may not be a trivial solubilisation process and film formation may be involved.

Both deposition and dissolution of copper and zinc will be studied using a combination of *in-situ* 3D microscopy and impedance spectroscopy to look at film formation. Cyclic voltammetry and chronoamperometry will also be used to determine the reversibility of the deposition/ dissolution process.

Attempts will be made to demonstrate super-efficient deposition (current efficiency > 100 %) for both metals. Plating experiments will be demonstrated using pulse reverse power supply as well as DC or AC power supplies This will also be demonstrated as a function of the metal particle size and the concentration of metal ions in solution. The optimum conditions of pulse length and size will be determined to let the powder fused on the electrode.

Finally, attempts will be made to produce composite materials of metallic and non-metallic particles on the electrode surface.

## 1.11 References

1. M. Schlesinger and M. Paunovic, *Modern Electroplating*, John Wiley & Sons, Inc., New Jersey, 4th edn., 2000.
2. E. L. Smith, C. Fullarton, R. C. Harris, S. Saleem, A. P. Abbott and K. S. Ryder, *Transactions of the IMF*, 2010, **88**, 286-293.
3. M. Paunovic and M. Schlesinger, in *Fundamentals of Electrochemical Deposition*, John Wiley & Sons, Inc., USA, 2006, ch. 7, pp. 113-127.
4. H. Bort, K. Juttner, W. J. Lorenz, G. Staikov and E. Budevski, *Electrochimica Acta*, 1983, **28**, 985-991.
5. B. Scharifker and G. Hills, *Electrochimica Acta*, 1983, **28**, 879-889.
6. F. C. Porter, in *Corrosion Resistance of Zinc and Zinc Alloys*, ed. P. A. Schwietzer, Markel Dekker, Inc., New York, 5th edn., 1994, vol. 5, ch. 371-375, p. 523.
7. X. Gregory Zhang, *Corrosion and Electrochemistry of Zinc*, Springer, Boston, 1996.
8. H. Geduld, *Zinc Plating*, Asm Intl, USA, 1988.
9. R. Winand, in *Modern Electroplating*, eds. M. Schlesinger and M. Paunovic, John Wiley & Sons, Inc., Pennigton, New Jersey, 2010, vol. 10, pp. 285-307.
10. A. Frumkin, O. Petrii, B. Damaskin, J. Bockris, B. Conway and E. Yeager, *Comprehensive Treatise of Electrochemistry*, Plenum, , New York, 1980.
11. A. Vagramyan and M. Zhamagortsyants, *Electrodeposition of metals and inhibiting adsorption*, U.S. Dept. of Commerce, Springfield, USA, 1974.
12. M. Pourbaix, *Atlas of electrochemical equilibria in aqueous solutions*, National Association of Corrosion Engineers, Texas, USA, 1974.
13. A. R. Despic, B. Conway, J. O. M. Bockris, E. Yeager, S. U. M. Khan and R. E. W. (Eds.), *Comprehensive Treatise of Electrochemistry*, Plenum Press, New York, 1983.
14. A. P. Abbott, G. Capper, D. L. Davies and R. K. Rasheed, *Chemistry – A European Journal*, 2004, **10**, 3769-3774.
15. J. W. Diggle, A. R. Despic and J. O. M. Bockris, *J. Electrochem. Soc.*, 1969, **116**, 1503-1514.
16. I. Epelboin, M. Jousselein and R. Wiart, *Journal of Electroanalytical Chemistry and Interfacial Electrochemistry*, 1979, **101**, 281-284.

17. A. R. Despić, D. Jovanović and T. Rakić, *Electrochimica Acta*, 1976, **21**, 63-77.
18. J. N. Jovićević, D. M. Dražić and A. R. Despić, *Electrochimica Acta*, 1977, **22**, 589-595.
19. J. Bressan and R. Wiart, *J Appl Electrochem*, 1979, **9**, 43-53.
20. C. Cachet, U. Ströder and R. Wiart, *J Appl Electrochem*, 1981, **11**, 613-623.
21. M. Y. Abyaneh, J. Hendrikx, W. Visscher and E. Barendrecht, *J. Electrochem. Soc.*, 1982, **129**, 2654-2659.
22. C. Cachet, U. Ströder and R. Wiart, *Electrochimica Acta*, 1982, **27**, 903-908.
23. R. Winand, *Hydrometallurgy*, 1992, **29**, 567-598.
24. R. Winand, *Electrochimica Acta*, 1994, **39**, 1091-1105.
25. R. Winand, *Electrochimica Acta*, 1998, **43**, 2925-2932.
26. K. S. Kumar, K. Biswas and R. Balasubramaniam, *J Nanopart Res*, 2011, **13**, 6005-6012.
27. J. J. Kelly and A. C. West, *Journal of The Electrochemical Society*, 1998, **145**, 3477-3481.
28. R. H. Watanabe, M. C. Gois and B. S. Lima-Neto, *Surface and Coatings Technology*, 2009, **204**, 497-502.
29. J. W. Dini and D. D. Snyder, in *Modern Electroplating*, John Wiley & Sons, Inc., 2010, DOI: 10.1002/9780470602638.ch2, pp. 33-78.
30. W. Safranek, F. Dahle and C. Faust, *Plating*, 1948, **35**, 39-49.
31. M. Schlesinger and M. Paunovic, in *Modern Electroplating*, John Wiley & Sons, Inc., New Jersey, 5th edn., 2010, pp. 33-78.
32. A. P. Abbott and K. J. McKenzie, *Physical chemistry chemical physics : PCCP*, 2006, **8**, 4265-4279.
33. E. Peled and G. E., *Journal of The Electrochemical Society*, 1976, **123**, 15-19.
34. S. Simanavicius, *Chemija*, 1990, **3**, 178.
35. G. Geblewicz, R. Potter and D. Schriffrin, *Trans. Inst. Met. Finish.*, 1986, **64**, 134-136.
36. A. Abbott, *Chemical Society Reviews*, 1993, **22**, 435-440.
37. K. Izutsu, *Electrochemistry in Non-aqueous Solutions*, Wiley-VCH, Verlag GmbH, 2002.

38. C. Friedel and J. M. Crafts, *Compt. Rend.*, 1877, **84**, 1392 & 1450.
39. P. Walden, 1914, **68**, 405-408.
40. P. Walden, 1914, **85**, 1800-1801.
41. T. Schubert, S. Zein, E. Abedin, A. P. Abbott, K. J. McKenzie, K. S. Ryder and F. Endres, in *Electrodeposition from ionic liquids 2nd Edition*, eds. F. Endres, A. Abbott and D. R. MacFarlane, John Wiley & Sons, Weinheim, 2nd edn., 2017, pp. 83-120.
42. J. S. Wilkes and M. J. Zaworotko, *Journal of the Chemical Society, Chemical Communications*, 1992, DOI: 10.1039/C39920000965, 965-967.
43. N. Koura, T. Endo and Y. Idemoto, *Journal of Non-Crystalline Solids*, 1996, **205**, 650-655.
44. L. Simanavicius, A. Stakenas and A. Starkis, *Electrochimica Acta*, 1997, **42**, 1581-1586.
45. Y. Lin and I. Sun, *Electrochimica acta*, 1999, **44**, 2771-2777.
46. A. P. Abbott, G. Capper, D. L. Davies, H. L. Munro, R. K. Rasheed and V. Tambyrajah, *Chemical Communications*, 2001, DOI: 10.1039/b106357j, 2010-2011.
47. M. S. Sitze, E. R. Schreiter, E. V. Patterson and R. G. Freeman, *Inorg Chem*, 2001, **40**, 2298-2304.
48. J. S. Wilkes, *Green Chemistry*, 2002, **4**, 73-80.
49. W.-G. Xu, X.-M. Lü, Q.-G. Zhang, J.-S. Gui and J.-Z. Yang, *Chinese Journal of Chemistry*, 2006, **24**, 331-335.
50. J.-Z. Yang, P. Tian, L.-L. He and W.-G. Xu, *Fluid Phase Equilibria*, 2003, **204**, 295-302.
51. A. P. Abbott, G. Capper, D. L. Davies and R. Rasheed, *Chem. Commun.*, 2003, **70**.
52. A. P. Abbott, D. Boothby, G. Capper, D. L. Davies and R. K. Rasheed, *Journal of the American Chemical Society*, 2004, **126**, 9142-9147.
53. A. P. Abbott, G. Capper, B. G. Swain and D. A. Wheeler, *Transactions of the IMF*, 2005, **83**, 51-53.
54. A. P. Abbott, G. Capper, D. L. Davies, R. K. Rasheed and V. Tambyrajah, *Chem comm*, 2003, 70-71.

55. D. Crawford, L. Wright, S. James and A. Abbott, *Chem comm*, 2016, **52**, 4215-4218.
56. A. P. Abbott, E. I. Ahmed, K. Prasad, I. B. Qader and K. S. Ryder, *Fluid Phase Equilibria*, 2017, **448**, 2-8.
57. F. Endres, A. Abbott and D. MacFarlane, *Electrodeposition from ionic liquids 2nd Edition*, John Wiley & Sons, Weinheim, 2017.
58. A. P. Abbott, J. C. Barron, K. S. Ryder and D. Wilson, *Chemistry – A European Journal*, 2007, **13**, 6495-6501.
59. A. P. Abbott, G. Capper, K. J. McKenzie and K. S. Ryder, *Journal of Electroanalytical Chemistry*, 2007, **599**, 288-294.
60. H. P. Nguyen, X. Peng, G. Murugan, R. J. M. Vullers, P. M. Vereecken and J. Fransaer, *Journal of The Electrochemical Society*, 2013, **160**, D75-D79.
61. A. P. Abbott, R. C. Harris, Y.-T. Hsieh, K. S. Ryder and I.-W. Sun, *Physical chemistry chemical physics : PCCP*, 2014, **16**, 14675-14681.
62. Y. Fang, X. Jiang, X.-G. Sun and S. Dai, *Chemical Communications*, 2015, **51**, 13286-13289.
63. N. R. Brooks, S. Schaltin, K. Van Hecke, L. Van Meervelt, K. Binnemans and J. Fransaer, *Chemistry – A European Journal*, 2011, **17**, 5054-5059.
64. N. V. Plechkova and K. R. Seddon, *Chemical Society Reviews*, 2008, **37**, 123-150.
65. S. Aparicio, M. Atilhan and F. Karadas, *Industrial & Engineering Chemistry Research*, 2010, **49**, 9580-9595.
66. William R. Pitner and C. L. Hussey, *J. Electrochem. Soc.*, 1997, **144**, 3095-3103.
67. R. T. Carlin, C. Hugh, J. Fuller and P. C. Trulove, *Journal of The Electrochemical Society*, 1998, **145**, 1598-1607.
68. B. J. Tierney, W. R. Pitner, J. A. Mitchell, C. L. Hussey and G. R. Stafford, *Journal of The Electrochemical Society*, 1998, **145**, 3110-3116.
69. F. Endres and A. Schweizer, *Physical Chemistry Chemical Physics*, 2000, **2**, 5455-5462.
70. J.-J. Lee, B. Miller, X. Shi, R. Kalish and K. A. Wheeler, *Journal of The Electrochemical Society*, 2001, **148**, C183-C190.
71. T. Iwagishi, H. Yamamoto, K. Koyama, H. Shirai and H. Kobayashi, 2002, **70**, 671-675.

72. F. Endres, *Chemphyschem : a European journal of chemical physics and physical chemistry*, 2002, **3**, 144-154.
73. J. Dogel and W. Freyland, *Physical Chemistry Chemical Physics*, 2003, **5**, 2484-2487.
74. T. Jiang, M. C. Brym, G. Dubé, A. Lasia and G. Brisard, *Surface and Coatings Technology*, 2006, **201**, 10-18.
75. A. P. Abbott, K. El Ttaib, G. Frisch, K. S. Ryder and D. Weston, *Physical chemistry chemical physics : PCCP*, 2012, **14**, 2443-2449.
76. A. B. Andriana Ispas, *Electrochem. Soc. Interface*, 2014, **23**, 47-51.
77. A. P. Abbott, G. Frisch, J. Hartley, W. O. Karim and K. S. Ryder, *Progress in Natural Science: Materials International*, 2015, **25**, 595-602.
78. F. Endres and S. Zein El Abedin, *Physical Chemistry Chemical Physics*, 2006, **8**, 2101-2116.
79. Z. F. Endres, *Chem. (Muenchen Ger.)* 2004, **218**, 255 – 283.
80. Q. X. Liu, S. Zein El Abedin and F. Endres, *Journal of The Electrochemical Society*, 2008, **155**, D357-D362.
81. S. Zein El Abedin, E. M. Moustafa, R. Hempelmann, H. Natter and F. Endres, *Chemphyschem : a European journal of chemical physics and physical chemistry*, 2006, **7**, 1535.
82. P. Eiden, Q. Liu, S. Zein El Abedin, F. Endres and I. Krossing, *Chemistry – A European Journal*, 2009, **15**, 3426-3434.
83. S. Zein El Abedin, A. Prowald and F. Endres, *Electrochemistry Communications*, 2012, **18**, 70-73.
84. X. Liu, Y. Zhang, D. Ge, J. Zhao, Y. Li and F. Endres, *Physical Chemistry Chemical Physics*, 2012, **14**, 5100-5105.
85. I. Kazeminezhad, A. C. Barnes, J. D. Holbrey, K. R. Seddon and W. Schwarzacher, *Applied Physics A*, 2007, **86**, 373-375.
86. M. B. Pomfret, D. J. Brown, A. Epshteyn, A. P. Purdy and J. C. Owrutsky, *Chemistry of Materials*, 2008, **20**, 5945-5947.
87. H. Adelkhani and M. R. Arshadi, *Journal of Alloys and Compounds*, 2009, **476**, 234-237.
88. A. P. Abbott, K. E. Ttaib, K. S. Ryder and E. L. Smith, *Transactions of the IMF*, 2008, **86**, 234-240.

89. Y.-L. Zhu, Y. Kozuma, Y. Katayama and T. Miura, *Electrochimica Acta*, 2009, **54**, 7502-7506.
90. F. C. Smith EL, Harris R, Saleem S, Abbott AP, Ryder KS., *Trans. Inst. Met. Finish.*, 2010, **88**, 285-293.
91. A. P. Abbott, J. C. Barron and K. S. Ryder, *Transactions of the IMF*, 2009, **87**, 201-207.
92. S. Zein El Abedin and F. Endres, *Accounts of Chemical Research*, 2007, **40**, 1106-1113.
93. M. I. Alemany A., Vagt U., Maase M., O'Meara M., *Plating and Surface Finishing*, 2010, **97**, 34-37.
94. G. T. Cheek, W. E. O'Grady, S. Z. El Abedin, E. M. Moustafa and F. Endres, *Journal of The Electrochemical Society*, 2008, **155**, D91-D95.
95. P. C. Howlett, N. Brack, A. F. Hollenkamp, M. Forsyth and D. R. MacFarlane, *Journal of The Electrochemical Society*, 2006, **153**, A595-A606.
96. R. Wibowo, L. Aldous, R. M. J. Jacobs, N. S. A. Manan and R. G. Compton, *Chemical Physics Letters*, 2011, **509**, 72-76.
97. A. Ispas, B. Adolphi, A. Bund and F. Endres, *Physical Chemistry Chemical Physics*, 2010, **12**, 1793-1803.
98. N. Borisenko, A. Ispas, E. Zschippang, Q. Liu, S. Zein El Abedin, A. Bund and F. Endres, *Electrochimica Acta*, 2009, **54**, 1519-1528.
99. O. Raz, G. Cohn, W. Freyland, O. Mann and Y. Ein-Eli, *Electrochimica Acta*, 2009, **54**, 6042-6045.
100. S.-J. Pan, W.-T. Tsai and I. W. Sun, *Electrochemical and Solid-State Letters*, 2010, **13**, D69-D71.
101. D. Pradhan, R. G. Reddy and A. Lahiri, *Metall and Materi Trans B*, 2009, **40**, 114-122.
102. J. Chen, B. Xu and G. Ling, *Materials Chemistry and Physics*, 2012, **134**, 1067-1071.
103. N. S. Hudak and D. L. Huber, *Journal of The Electrochemical Society*, 2012, **159**, A688-A695.
104. N. Borisenko, S. Zein El Abedin and F. Endres, *The Journal of Physical Chemistry B*, 2006, **110**, 6250-6256.

105. L. H. S. Gasparotto, N. Borisenko, O. Höfft, R. Al-Salman, W. Maus-Friedrichs, N. Bocchi, S. Zein El Abedin and F. Endres, *Electrochimica Acta*, 2009, **55**, 218-226.
106. S. Zein El Abedin, A. Y. Saad, H. K. Farag, N. Borisenko, Q. X. Liu and F. Endres, *Electrochimica Acta*, 2007, **52**, 2746-2754.
107. P. J. Dale, A. P. Samantilleke, D. D. Shivagan and L. M. Peter, *Thin Solid Films*, 2007, **515**, 5751-5754.
108. A. Izgorodin, O. Winther-Jensen, B. Winther-Jensen and D. R. MacFarlane, *Physical Chemistry Chemical Physics*, 2009, **11**, 8532-8537.
109. R. Al-Salman, S. Z. El Abedin and F. Endres, *Physical Chemistry Chemical Physics*, 2008, **10**, 4650-4657.
110. F. GOLGOVICI, A. COJOCARU, M. NEDELICU and T. VISAN, *Chalcogenide Letters*, 2009, **6**, 323 – 333.
111. T. Tsuda and C. L. Hussey, *Thin Solid Films*, 2008, **516**, 6220-6225.
112. C. P. Chan, H. Lam and C. Surya, *Solar Energy Materials and Solar Cells*, 2010, **94**, 207-211.
113. A. Bakkar and V. Neubert, *Electrochemistry Communications*, 2007, **9**, 2428-2435.
114. J.-K. Chang, S.-Y. Chen, W.-T. Tsai, M.-J. Deng and I. W. Sun, *Electrochemistry Communications*, 2007, **9**, 1602-1606.
115. S.-I. Hsiu, J.-F. Huang, I. W. Sun, C.-H. Yuan and J. Shiea, *Electrochimica Acta*, 2002, **47**, 4367-4372.
116. Y.-W. Lin, C.-C. Tai and I. W. Sun, *Journal of The Electrochemical Society*, 2007, **154**, D316-D321.
117. Q. B. Zhang, A. P. Abbott and C. Yang, *Physical Chemistry Chemical Physics*, 2015, **17**, 14702-14709.
118. T. Iwagishi, H. Yamamoto, K. Koyama, H. Shirai and H. Kobayashi, *Electrochem*, 2001, **70**, 178-183.
119. A. P. Abbott, G. Capper, D. L. Davies, H. Munro, R. K. Rasheed and V. Tambyrajah, in *Ionic Liquids as Green Solvents*, American Chemical Society, 2003, vol. 856, ch. 35, pp. 439-452.
120. E. L. Smith\*, *Transactions of the IMF*, 2013, **91**, 241-248.
121. A. P. Abbott, K. S. Ryder and U. König, *Transactions of the IMF*, 2008, **86**, 196-204.

122. A. P. Abbott, J. C. Barron, G. Frisch, S. Gurman, K. S. Ryder and a. Fernando Silva, *Physical chemistry chemical physics : PCCP*, 2011, **13**, 10224-10231.
123. W. O. Karim, PhD thesis, University of Leicester, 2016.
124. P.-Y. Chen and Y.-T. Chang, *Electrochimica Acta*, 2012, **75**, 339-346.
125. K. El ttaib, *University of Leicester PhD Thesis*, 1-Jun-2011.
126. J. C. Malaquias, M. Steichen, M. Thomassey and P. J. Dale, *Electrochimica Acta*, 2013, **103**, 15-22.
127. A. P. Abbott, A. I. Alhaji, K. S. Ryder, M. Horne and T. Rodopoulos, *Transactions of the IMF*, 2016, **94**, 104-113.

**Chapter-II**  
**EXPERIMENTAL**

## 2.1 Materials

The chemicals, and pure metals used during the experiments are listed in **Table 2.1**.

**Table 2.1** List of compounds used through to projects. All chemicals were used as obtained

Compound	Abbreviation	MW g mol <sup>-1</sup>	Purity
Choline chloride (ChCl)	HOC <sub>2</sub> H <sub>4</sub> N(CH <sub>3</sub> ) <sup>+</sup> Cl <sup>-</sup>	139.63	Aldrich, >98%
Ethylene glycol (EG)	C <sub>2</sub> H <sub>4</sub> (OH) <sub>2</sub>	62.07	Aldrich, >99%
Boric Acid	H <sub>3</sub> BO <sub>3</sub>	61.83	Aldrich, >99%
Zinc chloride	ZnCl <sub>2</sub>	136.30	Aldrich, >99%
Copper(II) chloride dihydrate	CuCl <sub>2</sub> .2H <sub>2</sub> O	170.48	Aldrich, >99%
Zinc powder	Zn	65.39	Aldrich, >99%
Copper powder	Cu	65.55	Aldrich, >99%

## 2.2 Preparation of solutions

The deep eutectic solvents used throughout the projects were mixtures of hydrogen bond donors with/without metal salts; a) ZnCl<sub>2</sub> and b) CuCl<sub>2</sub>.2H<sub>2</sub>O. Ethylene glycol was used as the H-bond donor for most experiments. The deep eutectic solvent was prepared by heating the mixture of the two components at approximately 60°C with continuous stirring until a homogeneous liquid formed. In this study, mostly Ethaline 200 was used. Mixture ratio was 1:2 as one choline chloride and two ethylene glycol at 60 °C ends up a clear deep eutectic solvent. Boric acid was used as additive in copper depositions to increase the electroplating efficiency and throwing power during deposition.

## 2.3 Preparation of the Electrochemical Cells

Various novel cell designs were used for use during the experiments due to the unique way in which the electrode needed to be coated. Generally, it was important to keep cathode in the horizontal plane. The cells were designed using Solid Works, Autodesk software. The files were exported to a 3D printer in STL file format and the cells were printed using either ABS (acrylonitrile butadiene styrene) or PLA (polylactic acid). ABS was chosen as it can be used at higher temperatures (c.a. 100 °C) while PLA can only be used effectively up to 50-60 °C. The printing times depended on the size and complexity

of the mesh that needed to be drawn but generally did not exceed 3 hours. The cell designs used are presented in the Appendix section.

A FLASHFORGE Creator 3D printer was used throughout. It has dual extruders with positioning precision of 2.5  $\mu\text{m}$  on the Z axis, 2.5  $\mu\text{m}$  on XY plane and a resolution of 10  $\mu\text{m}$ . The maximum build volume was 22.3 x 14.5 x 14.5 cm.

## 2.4 Electrochemical Techniques

Electrochemical techniques are *iVt* techniques, and are based on controlling the current by measuring the potential with respect to time or each other. In this study, an Autolab PGSTAT20 potentiostat (Ecochemie, Holland) controlled by GPES2 software, and Autolab PGSTAT302N were used for the analysis of cyclic voltammetry, chronoamperometry, and electrochemical impedance spectroscopy respectively. During the experiments 1 mm diameter platinum, 1 mm gold, 1 mm copper, and 1 mm zinc disc electrodes were used as working electrodes. The reference electrode was made up by immersing a silver wire in a glass tube with a frit tip, and electrode was filled with 0.1 M Ag/AgCl prepared in 1ChCl: 2EG. The counter electrode was a platinum flag with an area of 4  $\text{cm}^2$ . Before starting each experiment, the working electrode was cleaned mechanically with 0.05-0.3  $\mu\text{m}$  alumina powder until a mirror finish was obtained.

### 2.4.1 Reference Electrodes in RTILs and DES

When a generalized electrode process is considered for a reaction:  $A \pm ne \rightarrow B$ , in which B is formed at a suitable electrode as a result of electrolytic conversion of A. The rate of the reaction is related to the current which is controlled by the magnitude of the electrical potential applied to the electrode of interest (commonly referred to as the “*working electrode*”). The current is directly proportional to the number of electrons transferred, the electrode area, and the flux of material.<sup>1</sup>

$$I = nFAJ \qquad \text{Equation 2.1}$$

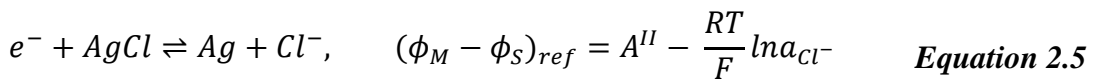
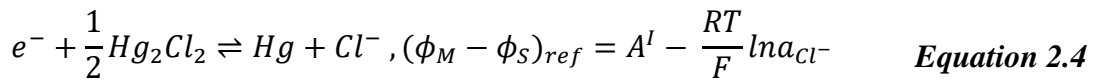
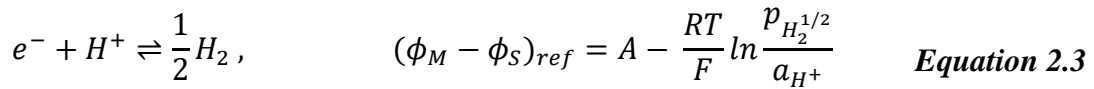
$F$  is the *Faraday constant* (96485  $\text{C mol}^{-1}$ ),  $A$  is the electrode area, and  $J$  is the flux of species A to the electrode ( $\text{mol cm}^{-2} \text{s}^{-1}$ ) averaged over its surface. The applied potential

needs to be reference to a system which has a fixed potential, i.e. one through which negligible current flows. This is called as reference electrode.<sup>2</sup> The potential between the electrode and the electrolytic solution ( $\phi_M - \phi_S$ ) needs to remain constant and the potential difference for the reaction  $\text{Ox} + e \leftrightarrow \text{Red}$  is given by the Nernst equation given in **Equation 2.2**.<sup>3</sup>

$$(\phi_M - \phi_S)_{ref} = a \text{ constant} - \frac{RT}{F} \ln \frac{a_{red}}{a_{ox}} \quad \text{Equation 2.2}$$

where  $R$  is the universal gas constant,  $T$  is the temperature in Kelvin, and  $a_{red}$  and  $a_{ox}$  are the activities of the reduced and oxidized species, respectively.

The reference electrode against which all standard potentials are determined is based in the  $\text{H}^+/\text{H}_2$  redox couple which arbitrarily has a reference potential of 0.00 V. It uses a platinized platinum electrode immersed in a  $1 \text{ mol kg}^{-1}$  strong acid solution through which hydrogen gas at 1 bar pressure is bubbled. This redox electrode is difficult to set up and so the silver/silver chloride and mercury/mercurous chloride redox couples are also used.<sup>1</sup>



In practice, a third electrode, known as counter or auxiliary, is connected to the potentiostat to eliminate current passage through the reference electrode (only negligible amount current will be passed) to complete the circuit.<sup>1</sup>

Reference electrode is divided three classes in the conventional solvent media.<sup>4</sup> The first kind of electrodes is based on a potential determining equilibrium such as  $\text{Ag}^+ + e^- \rightleftharpoons \text{Ag}$  or  $\frac{1}{2} \text{Cl}_2 + e^- \rightleftharpoons \text{Cl}^-$  between atoms or molecules and their corresponding cations for cationic electrodes in solution or anionic electrodes with their corresponding anions. The

second kind of electrodes consist of three phases in which a metal is covered by a layer of its sparingly soluble salt, and immersed into solution containing the anion of this metal salt. The  $\text{Ag}/\text{AgCl}/\text{Cl}^-$  and  $\text{Hg}/\text{Hg}_2\text{Cl}_2/\text{Cl}^-$  electrodes are examples. The third kind of electrodes are known as redox electrodes in which an inert, non-reactive metal such as platinum or gold, is immersed in a solution containing both species contributing to a redox couple of the electrolyte. For example, benzoquinone in water,  $\text{BQ} + 2\text{e}^- + 2\text{H}^+ \rightleftharpoons \text{H}_2\text{Q}$ , where BQ is benzoquinone and H<sub>2</sub>Q is hydroquinone or, in acetonitrile,  $\text{Cp}_2\text{Fe} + \text{e}^- \rightleftharpoons \text{Cp}_2\text{Fe}^+$ , where Cp<sub>2</sub>Fe is ferrocene and Cp<sub>2</sub>Fe<sup>+</sup> the ferrocenium cation.<sup>1</sup>

According to the Butler's suggestion,<sup>5</sup> a satisfactory reference electrode must follow one of the given properties.

- RE should have a potential stable with time.
- RE should return to the same potential after polarization.
- RE should obey the Nernst equation with respect to some species in the electrolyte.
- RE's solid phase must not be appreciably soluble in the case of using second kind reference electrode.

Maintaining a stable potential with time is particularly important as it is also critical condition to sustain stable potential after a polarization, and having an insoluble solid phase. Thus, a satisfactory reference electrode needs not only to have a stable potential with time, but it should also have fast electrode kinetics to establish the potential determining equilibrium. While exchange current densities for metal-solution interfaces cover the range  $10^{-2}$  to  $10^{-18}$  A cm<sup>-2</sup> the range of reference electrodes is normally much more restricted.<sup>1</sup>

#### 2.4.1.1 Pseudo-reference Electrodes

Butler states that “*If one is not too critical, many metal electrodes show relatively stable potentials in various electrolyte solutions*”.<sup>5</sup> Accordingly, ‘pseudo reference’ electrode, also commonly known as ‘quasi reference electrodes’ have been used in many voltammetric studies. It is basically a metal wire, commonly silver or platinum which is immersed in the solution and it is expected to sustain a constant potential throughout the voltammetric experiment. This expectation may be realistic if the composition of the bulk

solution is essentially constant during the period of experiments as Bard and Faulkner pointed out.<sup>6</sup> When a pseudo-reference electrode is used, its actual potential should be calibrated by measuring formal potential of an electrochemically reversible couple.<sup>6</sup> One of the IUPAC recommended couple is the use of ferrocene/ferrocenium,  $\text{Cp}_2\text{Fe}/\text{Cp}_2\text{Fe}^+$ .<sup>7</sup> In the experimental practice, selected couple voltammogram against the pseudo reference electrode, metal wire, is recorded that of species of interest in the same medium.

#### 2.4.1.2 Reference Electrode Choice

Throughout this thesis a Ag/AgCl (0.01M) in 1 ChCl: 2EG reference electrode was used. This was found to give a stable potential. The only issue with this reference electrode is that the glass frit has a relatively high resistance and can produce artefacts when large currents are used. In one experiment a Ag wire pseudo-reference was used. This was found to have a reference potential of approximately 130 mV more positive of Ag/AgCl. Hartley showed that that the Ag/Ag<sup>+</sup> couple behaved in a Nernstian manner in 1 ChCl: 2EG in the concentration range  $10^{-6}$  to 0.1 mol kg<sup>-1</sup>.<sup>8</sup> Given that each order of magnitude change in the activity of silver corresponds to a shift in redox potential of approximately 60 mV at ambient temperature then this corresponds to an effective concentration of  $10^{-4}$  to  $10^{-5}$  mol kg<sup>-1</sup> which would see appropriate.

#### 2.4.2 Cyclic Voltammetry

Cyclic voltammetry is one of the most commonly applied electrochemical measurement techniques. A standard electrochemical cell requires three-electrodes; a working electrode (WE), counter electrode (CE), and reference electrode (RE) placed in electrolyte solution. In a standard CV measurement, the potential is cycled from the starting potential to the upper limit, then down to the lower limit and generally back to the starting potential. This is generally carried out at a steady scan rate ( $v / \text{Vs}^{-1}$ ). This is shown schematically in **Figure 2.1 (a)**. A potentiostat is used to apply the potential to the working electrode, WE with respect to the reference electrode (RE). While the potential is swept at a steady scan rate between WE and RE the current flow between the WE and CE is measured. The current is presented as a function of potential  $I(E)$ . This so-called cyclic voltammogram can provide information about the mechanism of the reaction, the rate of reaction, and the process of adsorption.<sup>9, 10</sup> Cyclic voltammetry is carried out in a solution of high ionic

strength to suppress the migration of ions and ensure that diffusion is the main mechanism of mass transport. The experiments are also generally carried out at a relatively low concentration of electroactive species to ensure that diffusion dominates mass transport.

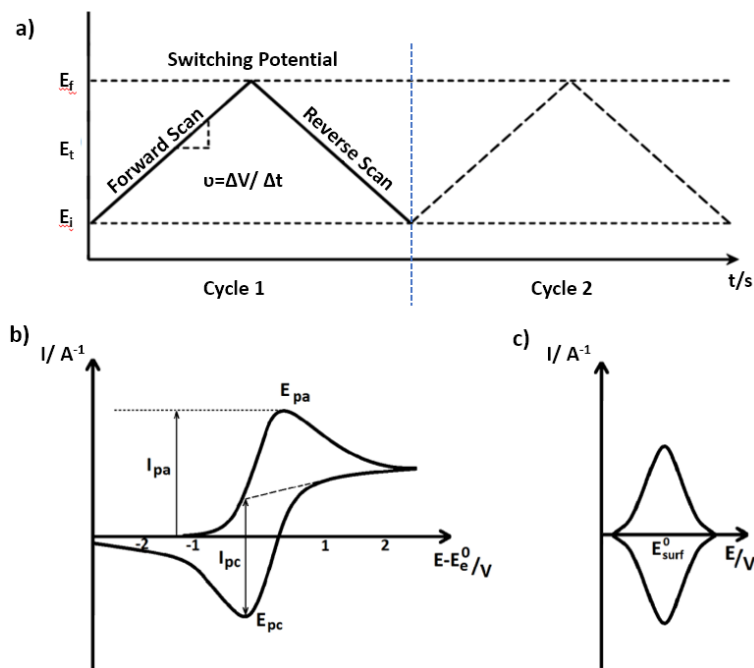


**Figure 2.1** a) potential-time profile for a cyclic voltammogram b) CV of a reversible process which is under diffusion control, c) CV of an immobilized redox couple in a diffusionless system.

**Figure 2.1** shows the CV responses expected for a reversible electron transfer process of a soluble species where mass transport is controlled (**Figure 2.1, b**). It also shows the response expected for an electron transfer process when the electroactive species is confined to the electrode surface (**Figure 2.1, c**). The forward sweep is continued until the pre-programmed potential value, when the sweep direction is reversed. Cycles can be partial, full, or repetitive depending on the nature of the experiment. Cyclic voltammogram of a reversible process is shown in **Figure 2.1, b**.  $E_i$  is the initial potential value of the electrode, and it is lower than the  $E^0$  in which non-Faradic currents flow until  $E_i$  approaches  $E^0$ . Once  $E_i$  is close to  $E^0$ , oxidation of the reagent begins at the electrode, and the current increases exponentially until the concentration of reduced species approaches zero close to the electrode. Following this, electrochemical consumption of the reduced species becomes limited by mass transfer and diffusion governs the voltammetric response. A similar process occurs during the reverse potential sweep.

There are several factors affecting the electrode reaction rate and current, such as rate of the electron transfer at the electrode surface, rate of the mass transfer of species between the bulk solution and electrode surface, homogenous/heterogeneous chemical reactions, and further surface processes: electrodeposition, adsorption/desorption.

Cyclic voltammogram responses can be different depending on the reversibility of the redox processes. In a reversible electron transfer system, the voltammogram given in **Figure 2.1 (b)**, should have the following characteristics:

The potential difference between the peak currents should be as given in **Equation 2.6**.

$$\Delta E = E_{pa} - E_{pc} = \frac{59}{n} \text{ (mV)} \quad \text{Equation 2.6}$$

The ratio of peak currents should be equal to 1 as given in **Equation 2.7**.

$$\left( \frac{i_{pa}}{i_{pc}} = 1 \right) \quad \text{Equation 2.7}$$

Peak currents should be proportional to the square root of the scan rate in **Equation 2.8**.

$$I_p \propto \sqrt{v} \quad \text{Equation 2.8}$$

If the electrochemical reaction taking place is fully reversible, electron transfer is faster than the rate of mass transport. Thus, the general control mechanism of the system is diffusion.

The Nernst equation is given in **Equation 2.9** describes the relation formal potential and cell potential by accounting temperature and concentration of species.

$$\Delta E = E^{0'} + \frac{RT}{nF} \ln \frac{C_{OX}}{C_{RED}} \quad \text{Equation 2.9}$$

If the electron transfer rate is slower than the mass transport rate, system becomes irreversible, and the shape of the cyclic voltammogram changes. In this kind of system, consumed current requires a greater driving force i.e. a greater potential for the driving force in an unstirred system is the potential gradient. As a result, hysteresis (increases in peak separation values) can be observed with increasing scan rate.

In the case of metal electroplating, it is possible to use Faraday's Law to calculate the theoretical mass ( $m$ ) of metal plated. Then, the thickness,  $T$ , of the deposit can be calculated knowing the density of the material by *Equation 2.10*.

$$m = \frac{I t A}{n F} \quad T = \frac{m}{\rho S} \quad \text{Equation 2.10}$$

Rate of the electrochemical deposition in microns per minute can be calculated using the current, atomic mass of the coated metal, surface area of the coated electrode, and density of the coated metal in grams for per cubic centimetre as given in *Equation 2.11*.

$$r = \frac{I A 600000}{n F \rho S} \quad \text{Equation 2.11}$$

In *Equation 2.10* and *Equation 2.11*,  $m$  = mass of plated metal,  $I$  = current,  $t$  = time,  $A$  = molar mass of the metal,  $n$  = valence of the dissolved metal,  $F$  = Faraday's constant,  $T$  = thickness,  $\rho$  = density,  $S$  = surface area, and  $r$  = plating rate.

### 2.4.3 Chronoamperometry and Chronocoulometry

Chronoamperometry and Chronocoulometry are two sub class of potential step experiments performed for various purposes. Chronoamperometry measures the rate of reaction, and this enables the diffusion coefficient as well as the current efficiency to be calculated. Chronocoulometry is much more sophisticated than chronoamperometry, and it is initially devised to work on species adsorbed on the surface of working electrode. Chronoamperometry is a powerful method for quantitative analysis of a nucleation process. By using chronoamperometry, it is possible to obtain various information about the nucleation and growth mechanism (see appendix).

For a reduction reaction, when an electrode is immersed into a solution which contains oxidised form of the redox couple with an initial concentration  $C_0$ , the electrode potential will be stepped from  $E_1$  which is more positive than  $E^{0'}$  to  $E_2$  which is more negative than  $E^{0'}$ . It is also assumed that the fluxes of species to the electrode is only controlled by diffusion. Initial time is represented as  $t_0$ , and proceeding times are represented as  $t_1, t_2, t_3$  etc. In a metal deposition process which is represented in **Figure 2.2**, metallic ions in the vicinity of the electrode will be immediately plated onto the electrode surface once the potential is shifted to  $E_2$ . During deposition on the electrode, the metallic ion concentration will be reduced to zero from its initial bulk concentration, and this leads to a decrease in concentration gradient of metallic ions at a given distance from the electrode as the time increases. The longer the electrode stays at the  $E_2$  value means the further away from the electrode the region depleted of cations extend, and this layer called diffusion layer.

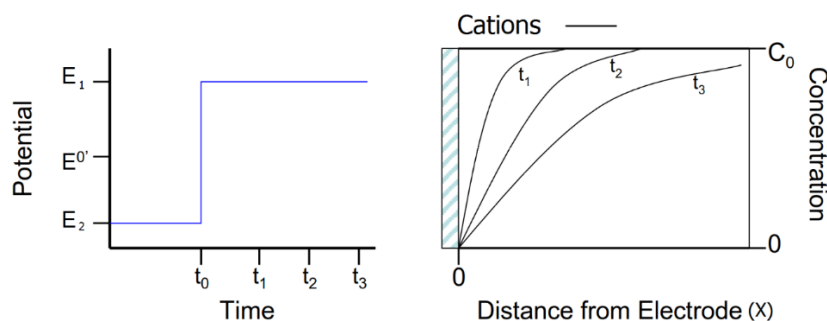


**Figure 2.2** Concentration-distance profile as a function of time for a potential step experiment.

In chronoamperometry, the current is measured with respect to time as a result of the potential pulse. The capacitive and Faradic currents dominate the signal at different time scales. For instance, capacitive currents are proportional to  $e^{-t/RC}$  so dominate at short time lengths, and for longer time periods, diffusion is limited, and the Faradic current dominates as it is proportional to  $t^{1/2}$ . The Faradic current is directly related to the concentration gradient,  $\partial C_i/\partial x$ , in a diffusion controlled system. According to the Nernst equation, it is required to have 118 mV more negative potential value than the  $E^{0'}$  in order to reduce 1/100<sup>th</sup> of the oxidised species at any potential. Chronoamperometry experiments are mostly performed in a single step.

The Cottrell equation given in *Equation 2.12* is commonly applied with chronoamperometry for a reversible electron transfer process where both the reagent and product are soluble in solution. The current should be proportional to  $t^{-1/2}$ . These data can be used to determine the diffusion coefficient for a species in solution.

$$i_t = \frac{nFAC_0D_0^{1/2}}{\pi^{1/2}t^{1/2}} \quad \text{Equation 2.12}$$

where,  $D_0$  is the diffusion constant at infinite dilution.

#### 2.4.4 Pulse Reverse Electrodeposition

In electrodeposition, control of nucleation and growth is important to control the morphology of the deposit. Pulsing the electrode potential can be used to control the density of grains on the electrode surface. Thus, it is possible to obtain much finer finishes than with DC power supplies.<sup>11</sup>

There are different types of pulse modulations accessible with these plating units as showed in *Figure 2.3*. Each modulation can be applied individually or as mixed forms of each for given time. However, mixing the types increases the complexity, and hence, understanding of the phenomenon for each specific study becomes enormously difficult due to increased entries with complex variations to the system.

One advantage of using PED is to be able to discharge a charged layer on the substrate during either  $T_{OFF}$  or short, and sudden change of the direction of current flow during electrodeposition. Continuously charging a layer of an ongoing deposition generally prevents to reach optimum transfer speed of the species in DC plating systems, and hence, the low density of grain formation likely to be observed.<sup>11</sup> There is a diffusion phenomenon on the target plating surface, and the migration of metal ions are related the current density of the region on cathode.

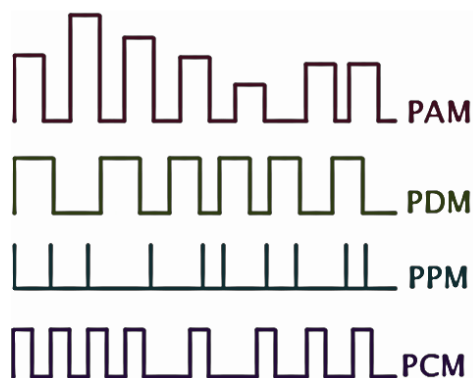


**Figure 2.3** Different types of pulse modulation: *PAM = pulse amplitude modulation, PDM = pulse density modulation, PPM = pulse position modulation and PCM = pulse code modulation.*

For this reason, in normal DC plating, depletion of ions is occurred due to locally observed high current density which results in non-even distribution of grain formation. On the other hand, using the PED these local high current density regions can be relaxed and filled with metal ions during the  $T_{OFF}$  period. When  $T_{on}$  turned back, available ions will be separated as uniform onto surface onto whole plating area. By doing so; evenly distribution, good final finish, and required porosity can be obtained without mixing the additives as normally required in many applications of DC plating.<sup>11</sup>

Another type of pulse electrodeposition known as pulse reverse current (PRC). PRC can create different sign of the current in millisecond timescale, and so; the change in direction of the current flow is occurred by polarization change. The advantage of this system to its relatives (PED) is the ability of the dissolution of protrusions on the plated surface by polarization change in short time scale. The time scale of course will be depending on the physical properties of solutions. For example, it requires longer times for viscous mediums. If the time for dissolution on plated metal is kept too long, the process becomes slower with lower efficiency due to extra time required to refill the lost part in the reverse current period. There is not an available perfect deposition model for ionic liquid based electrochemical deposition, and the introduction of pulse systems make it much harder to standardize a model due to introducing different variations to the whole system which make the things completely different from DC, such as long  $T_{OFF}$  time may cause the loss of charged layer on the cathode for a cathodic deposition, or the reverse current can cause a new formation of layer on the anode in a cathodic deposition.<sup>11</sup>

As it is known, the potential  $E$  appears in cyclic voltammetry or any other electrochemical application is the function of transform of metal ions to metal solid deposited on the plate ( $M^{z+}/M$ ) which comes from the Nernst equation.<sup>11</sup> This diffusion model has been changed in the PED due to availability of the metal ions along with relaxation of the charged layer.<sup>12, 13</sup> In general, pulse plating may decrease the required amount of additive up to 60%. This may be the reason of the notable increase possibility on the limiting current due to replacement of metal ions during the period of  $T_{OFF}$ .<sup>14</sup>

### Electrical Double Layer in Pulse Systems

EDL (electrical double layer) is formed following the change in potential to balance the change in charge on the electrode surface. Pulse peak current,  $I_P$ , is made of two constituents; the capacitive current,  $I_P$  and the Faradaic current,  $I_F$ . The capacitive current charges the double layer while Faradaic current,  $I_F$ , corresponds to the rate of electron transfer. In a pulsed experiment where the current is controlled there will be a lag in the Faradaic current while the electrode is charged.<sup>15</sup> This process has been studied for copper deposition from  $CuSO_4$  in a 1 M  $H_2SO_4$  solution. **Figure 2.4** shows that the peak current drops asymptotically to zero after the charge,  $t_c$ , and discharge,  $t_d$  periods are completed. When the current pulse is switched off or changed in polarity then the current does not immediately fall to zero due to capacitive decay. The time taken for the current to fall to 99% of its peak value can be set as the defining point for the  $t_c$  point. Value for charging and discharging time depend on the medium properties such as the conductivity, and viscosity.

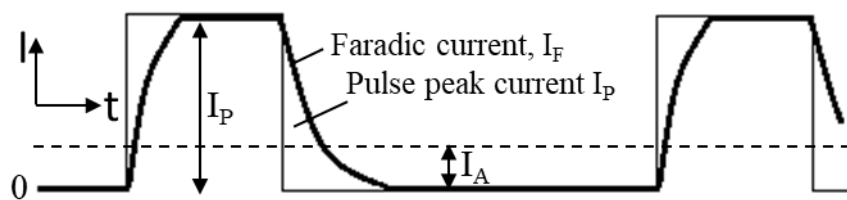


**Figure 2.4** The influence of the capacitance of the electrical double layer for medium effect.<sup>15</sup>

In the experiments performed with deep eutectic solvents, it was found that standard pulse conditions were different from those in aqueous solutions<sup>11, 15</sup> due to increased viscosity i.e., the charging and discharging times were higher than in water.

## Mass Transport in Pulsed Systems

An important limiting factor in the metal deposition rate is mass transport. Mass transport can also impact the deposit morphology. In a pulse experiment the pulse limiting current,  $I_L$ , will affect the mass transport of the electroactive species to the electrode surface. The value of  $I_L$  depends on the solution resistance, the liquid viscosity, the double layer capacitance and applied current ON time,  $T_{ON}$ . The value of  $T_{ON}$  should be sufficiently short to supply current below the limiting current, but also sufficiently long to fully charge the double layer and start the diffusion of the electroactive species to the working electrode. A study completed to analyse the limiting current densities in pulse and DC plating for copper deposition defined useful parameter space in terms of two dimensionless number  $N_m$  and  $N_p$  representing the steady state, DC, and transient, pulse, mass transfer limitations.<sup>16</sup>  $N_p = i_A/i_G$  and  $N_m = i_p/i_{PL}$ , where  $i_A$  and  $i_p$  are average and peak currents for DC and pulse systems,  $i_{PL}$  and  $i_m$ , are the limiting current densities for pulse and DC systems respectively.<sup>17</sup> The value of pulse the pulse current,  $I_{PL}$ , might far exceed DC limiting current density,  $I_G$ .<sup>18</sup> To obtain compact non-dendritic deposits, the conditions should be  $I_A/I_G < 1$  and  $I_p/I_L < 1$ .<sup>11</sup>

In DC plating, the deposit may be powdery if the applied current density is close to the limiting current density,  $I_G$ . Therefore, keeping the applied current density at 10-20% of  $I_G$  is recommended. However, in PED, applied current densities can be close to the limiting current density and still result with smooth deposits by keeping the pulsating diffusion layer very small. In PRC, preferential redissolution of dendrites is observed by applying short anodic pulses between cathodic pulses.<sup>11</sup>

### 2.4.5 Electrochemical Impedance Spectroscopy

Ohm's law defines the resistance in terms of a ratio between voltage,  $E$ , and current,  $I$ ;

$$R = \frac{V}{I} \quad \text{Equation 2.13}$$

However, Ohm's law of resistance is limited for only circuit element, and it follows some fundamentals to be valid as given below;

- All currents and voltages remain in ratio,
- Resistance,  $R$ , is independent from frequency,
- A.C current and voltage signals are in phase with each other.

When we consider the electrochemistry, resistance term turns into “impedance”, and it is a measure of the ability of an electrochemical cell to resist the flow of electrical current, but it does not simply follow the rule of Ohm’s law. Basically, the term “voltage and current are in phase is each other” is cancelled as schematically shown in **Figure 2.5**.

This sinusoidal excitation signal can be written as a function of time as given in **Equation 2.14**.

$$E_t = E_0 \sin(\omega t) \quad \text{Equation 2.14}$$

In this equation,  $\omega$  is known as radial or angular frequency which is a scalar measure of rotation rate. Radial frequency refers to angular displacement per second (unit time) in rotation or the rate of change of the phase created by the difference of sinusoidal waveforms of potential and current signal outputs.

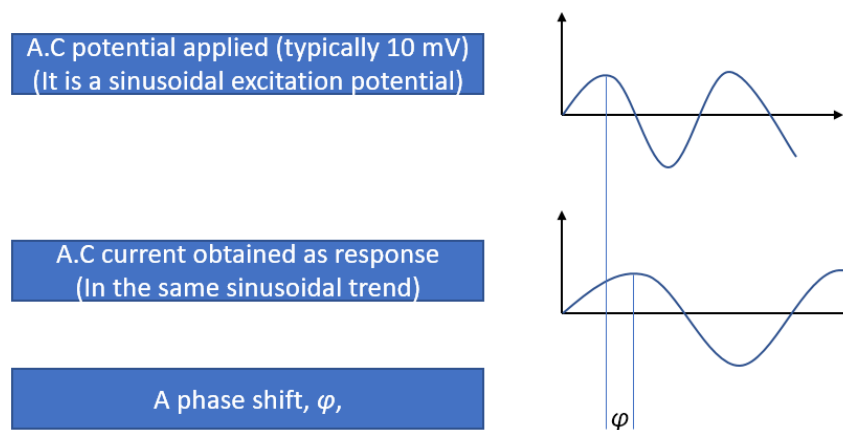


**Figure 2.5** In impedance systems, in a linear or pseudo-linear system, the current output to a sinusoidal potential will be a sinusoidal response at the same frequency but shift in  $\phi$  (phase).

One revolution is equal to  $2\pi$  radians, and thus,  $\omega = 2\pi/T = 2\pi f$ . In a linear system, response of  $I(t)$  shifts at certain phase  $\phi$  value, and it has different aptitude than  $I_0$ . The value of  $I_t$  is given in **Equation 2.15**.

$$I_t = I_0 \sin(\omega t + \phi) \quad \text{Equation 2.15}$$

Then, if an analogue is made for impedance by following the way of Ohm, **Equation 2.16** is obtained.

$$Z = \frac{E_t}{I_t} = \frac{E_0 \sin(\omega t)}{I_0 \sin(\omega t + \phi)} = Z_0 \frac{\sin(\omega t)}{\sin(\omega t + \phi)} \quad \text{Equation 2.16}$$

Thus, impedance now expressed in terms of a magnitude  $Z_0$ , and phase shift,  $\phi$ . If a plot is drawn by using the numerator, and denominator of the  $Z$  as “y”, and “x” axis, we obtain an oval shape which is known as Lissajous figure as shown in **Figure 2.6**.

As it is seen, the change in current and potential is demonstrated in differential change, and the function  $e^{ix}$  helps for simplifying solutions even if the final answer is a real function evolving sine and cosine.

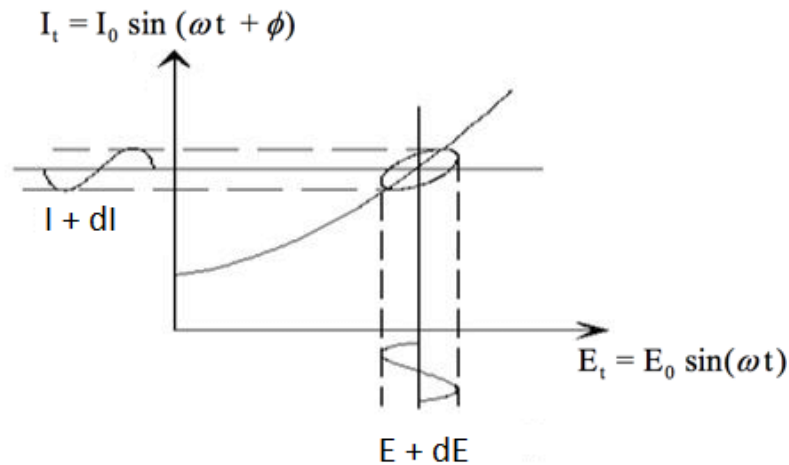


**Figure 2.6** Demonstration of obtaining Lissajous figure is shown.

In signal processing, signals vary periodically over time, and are often described as a combination of sinusoidal functions (Fourier analysis), and these are easy to express as a sum of exponential functions with imaginary exponents driven from Euler’s formula given in **Equation 2.17**.

$$e^{ix} = \cos x + i \sin x \quad \text{Equation 2.17}$$

Now, by using relation given in **Equation 2.17**, phase shift can be written with Euler’s formula by assuming that “j” as an imaginary part as given in **Equation 2.18**.

$$e^{j\varphi} = \cos\varphi + j\sin\varphi \quad \text{Equation 2.18}$$

If impedance is expressed as a complex function by applying Euler's relation to the potential, and current at time, t, another **Equation 2.19** is obtained.

$$\begin{aligned} E_t &= E_0 \cdot e^{j\omega t} \quad \text{and} \quad I_t = I_0 \cdot e^{j\omega t - \varphi} \\ Z(\omega) &= E/I = Z_0 \cdot e^{j\varphi} = Z_0 \cdot (\cos\varphi + j \cdot \sin\varphi) \end{aligned} \quad \text{Equation 2.19}$$

As it is applied to obtain Lissajous figure, if the values of real part,  $Z_0 \cdot \cos\varphi$ , are placed to the "y" axis, and values of imaginary part,  $Z_0 \cdot \sin\varphi$ , are placed to the "x" axis, Nyquist plot given in **Figure 2.7** obtained as shown below.

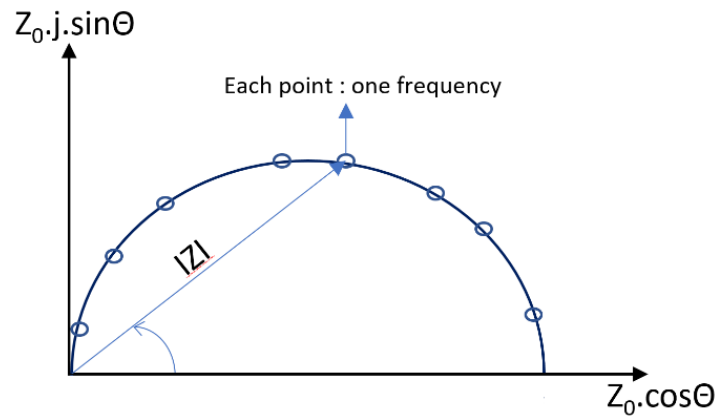


**Figure 2.7** Nyquist plot with impedance vector

In the Nyquist plot, frequency increased from left to right. Impedance for each frequency can be presented as a vector quantity,  $|Z|$ . The angle between each frequency point and real part axis known as phase angle. The argument of impedance or any complex number create the phase angle, and it is mainly demonstrating the difference between real and imaginary parts in impedance. While Nyquist plot helps to find specific frequency of a data point, it does not tell the existent relation between the data plot and frequency.

EIS can be used for many different purposes in various atmospheres from liquid to solid measurements. Resistance is the fundamental concept of EIS. Also, it is not wrong to say that there is no liquid medium with zero resistance, and so EIS turns into an important technique for electrochemistry. EIS can give quite useful data to analyse solid state semiconductors as well. The use of EIS makes it possible to analyse mechanisms of

electrochemical reactions by taking the advantage of existence of resistance. For example, formation of passivating layers on the electrode surface can be observed in the equivalent circuit. Depending on the obtained data, diffusion mechanisms can be studied by Warburg impedance analysis.

#### **2.4.6 Electrochemical Quartz Crystal Microbalance**

Hewlett Packard 87512A transmission/ reflectance unit was used during the experiment. Experimental setup consists a 50  $\Omega$  coaxial cable, an AT-cut polished quartz crystal (10 MHz), RE, CE, potentiostat. Throughout the experiment HP VEE program was used connected to network analyser for recovering the temporal resolution by recording the admittance spectra every 2-3 sec.

In a brief description, the electrochemical quartz crystal microbalance (EQCM) is based on piezoelectric effect which is occurring on the crystal itself in the presence of alternating voltage applied to the two side of electrodes carries AT-cut crystal between them. While on side of the crystal is in touch with the solution and works as WE, other side of the crystal was exposed to the air.<sup>19</sup> Mechanical oscillation takes place within the crystal lattice itself, but also creates certain frequency of vibration (10 MHz in our case) onto the touched electrode which can be various metals, such as platinum, gold, titanium, chromium, copper. When the deposition takes the place onto the part of the crystal which is used as working electrode, resonant frequency decrease with loaded mass due to carried current and so deposition occurs via redox reaction with current flow. The change in the frequency of the crystal face can be determined quantitatively, and it is proportional to mass change onto crystal surface.<sup>20</sup> Organized experimental setup allows to make in-situ studies by monitoring change of mass during redox switching onto the surface of quartz crystal electrode in real time. EQCM allows the measurement of mass changes up to  $10^{-9}$  g  $\text{cm}^{-2}$ . The change in amount of electroactive species loaded onto crystal surface can be determined by the combination of QCM and electrochemistry techniques.

Throughout the experiment, 10MHz AT-cut quartz crystal obtained by International Crystal Manufacturing Co., Oklahoma City, USA. Crystal has 0.211  $\text{cm}^2$  active area, and deposited with 900  $\text{\AA}$  polished platinum in vacuum conditions. Basically, quartz crystal has two side, and EQCM measures the each quartz vibration in which one exposed to the

air, and other side exposed to the solution for electrochemical purposes. Due to magnitude of the frequency, it has a great sensitivity to change in mass immersed in electroactive solution. Thus, it is possible to calculate amount of deposited species to the electrode surface of the QCM. EQCM/QCM will be given in much more detail with visual explanations in the electrochemical fundamentals chapter. A few articles were selected to give detailed information about the working mechanism of these techniques. Although selected articles are not directly related metal depositions onto crystals, they have extensive language along with detailed quantitative explanations which helps to understand how useful, and applicable techniques they are in general electrochemistry.

## **2.5 Non-Electrochemical Techniques**

### **2.5.1 Spectroscopic Techniques**

Information of surface coatings of deposited cathodes at the atomic and molecular level in response to electrochemical stimuli can be extracted by conventional spectroscopic techniques. One of the most common spectroscopic technique is Ultraviolet-visible (UV-vis) absorbance. This technique was applied in a part of thesis.

### **2.5.2 Surface Imaging Techniques**

The study of topographic and morphological properties of coated metals on different substrates can be studied by these techniques for acquiring data about deposition mechanisms as well as local structure changes. The most common applied surface imaging techniques: scanning electron microscopy and 3D optical profiler will be described in this section.

### **2.5.3 Scanning Electron Microscopy**

Phillips XL30 ESEM instrument was used to image the surface morphology. Measurements were performed with accelerating voltage between 15 keV and 20 keV, which supports an average beam current of ca. 120  $\mu$ A.

SEM uses electrons for surface imaging and all measurements are performed in a vacuum. The advantage of using electron beam for visualization is that surfaces can be viewed with a higher resolution than using visible light. **Figure 2.8** shows a schematic representation of the SEM set up. Electrons are generated from an electron gun called a thermionic gun through a positively charged anode. The positively charged anode pushes the electrons through a series of condenser lenses (which are ring-shaped electromagnets) to adjust the direction of the electrons, and concentrate them on to the specimen. Due to increase in astigmatism by non-uniform magnetic field, Stigmator is installed.<sup>21, 22</sup> Stigmator performs to reduce astigmatism of the beam by imposing a weak electric or magnetic quadrupole field on the electron beam in a spherical coordinate system. There are two detectors: one is positively charged and responsible to get signal from secondary electrons and backscattered electrons, and the other works as an X-ray detector. Secondary electrons released to the detector from atoms which absorb the energy (electrons) by releasing their own electron from K, L, or M shell of the atom. However, backscattered electrons are the electrons reflected from surface. They are not the electrons released by impact from electrons emitted by thermion gun. In the case of insufficient signal release to the scattering electron sensor for some surface constituents, backscattering sensor can be useful for obtaining higher resolutions. X-ray detector supports data for the quantitative analysis of the elements found on the surface, and it is called as EDX analysis. Secondary and backscattered electrons are the most commonly used electrons to obtain images of samples. By using SEM, it is possible to obtain morphology, chemical compositions, and crystalline structure of the samples.

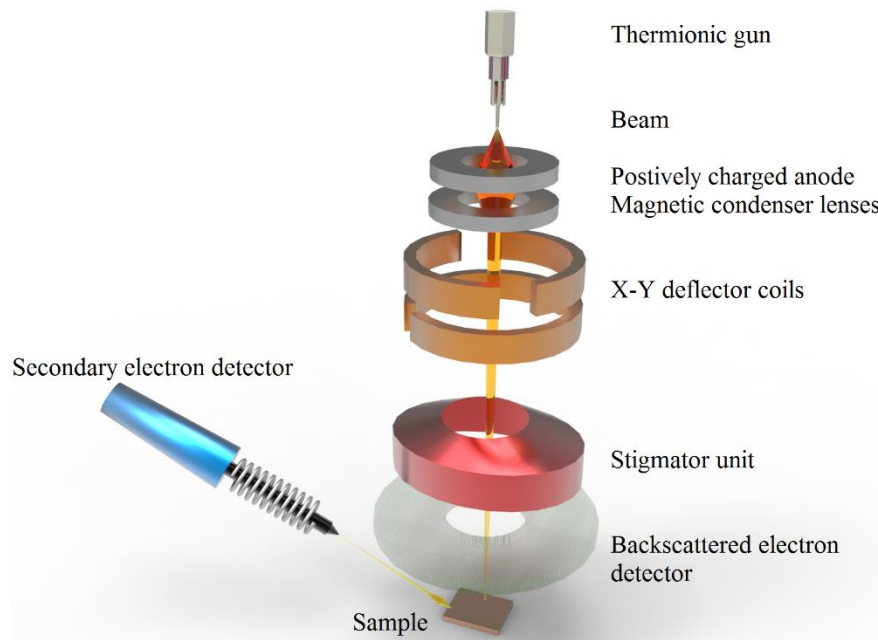


*Figure 2.8 A schematic demonstration of SEM*

#### 2.5.4 3D Optical Profiler

A Zeta instruments branded as Zeta-20 optical profiler using Zeta3D software version 1.8.5 was applied to create a 3-D colour image of the surface. The profiler carries a fully integrated microscope unit which provides 3D imaging and metrology capability in a single cost and space effective design. One of the most important property of the unit is to gaining surface image and data with quite low reflectivity, and very high roughness as well. The device is versatile, and capable of analysing different size features on samples of various types which cover smooth to rough, very low to very high reflectivity, transparent to opaque, single layer to multilayer, sub-nm to mm. Zeta optic modules performs to calculate accurate pixel data of adjusted sample position on X, Y, and Z directions. This data is used to obtain 3D true colour images, and 2D composite images of sample. These images are obtained with a protracted depth of focus resulted with clear wide surface image. The software of the Zeta-20 optical profiler can be used to calculate surface roughness along with dimensions, and so the volume. For instance, it is possible to calculate volume loss after a ball-friction test. To have reasonable data, two height set points are required to be adjusted by software. The first height the lowest surface height, and the second one the highest surface height, thereafter profiler scan each step

separately, and put one each other. Each step is the equal distance across the measurement height, divided by user preference. For example, if 1  $\mu\text{m}$  height will be scanned for a 200 step sizes, each step will be  $1/200 \mu\text{m}$ . Step sizes can be 200,400,600 and 1000. However, most measurements are performed at 200 step sizes. The highest magnification is 100X with Zeta-20 placed in material centre lab. However, it can be increased with 150X, and 200X optical magnifier kits.

### **2.5.5 X-ray Diffraction**

Throughout the experiments, Phillips model PW 1730 X-ray generator was used. Machine set up carries a PW 1716 diffractometer, and PW 1050/25 detector. The X-ray tube was a long fine focus Cu anode with Ni  $K\alpha$  filtered radiation. Analysis were generally performed at 40 KV, and 30 mA. Surface scanned with  $15^\circ$  and  $110^\circ$   $2\theta$  with a step size of  $0.02^\circ$   $2\theta$ . Synthetic Si sintered standard was used for angle calibration purposes.

X-rays with energies between 100 eV and 10 MeV are classified as electromagnetic waves. The difference of X-rays than the radio ways or gamma, and light rays is the wavelength, and energy. While visible light has wavelength 400-700 nm, X-rays have wavelengths 40-400 pm. X-ray waves are in the range of 10 to the  $10^{-3}$  nm.<sup>23</sup>

X-ray diffraction (XRD) is one of the most useful techniques for characterization. It is a powerful and non-destructive technique for characterizing the crystalline materials due to ability to gain data about phases, structures, preferred crystal orientations, and other structural parameters, such as crystallinity, average grain size, strain, and crystal defects. The way of X-ray production peaks is to collect constructive interference data of a monochromatic beam of scattered X-rays at specific angles from each set of lattice planes in a sample. Distribution of the atoms within the lattice generates peak intensity data.<sup>24</sup> As a result, X-ray diffraction pattern becomes a finger print pattern of the periodic atom arrangements in a given material. German physics Max von Laue and Co. discovered that crystalline substances responses to the X-rays as three-dimensional gratings for applied wavelengths in a crystal lattice of an element in 1912.<sup>25</sup> The idea that was taken a solid in crystalline structure it has lots of planes of atoms, and use each plane of

atom as kind of a slit. Briefly, Laue took an X-ray tube applied high voltage to produce X-rays, and condense them by using a lead slit with a narrow hole in which X-rays cannot pass throughout the lead slit except pre-opened small hole. Then, the condensed beam of X-rays hit the crystal solid. The pattern of scattering of crystalline solid creates an interesting pattern ray of dots, constructive interference of scattered X-rays (X-ray diffraction) on photographic plate. Thereafter, formulation of constructed interference, and its utilization for diagnosing the structure of crystal lattices was published by English scientist, William Bragg.<sup>26</sup> The background information of Bragg's theory is given in **Figure 2.9**. Incident X-rays comes into the lattice, and scattering from different planes of a crystal lattice. Each dot represents an atom of a lattice. **Figure 2.9** shows very regular ray of pattern, and there can be various patterns of different kinds of crystals, such as cubic crystals, tetragonal crystals, and hexagonal crystals. There are planes of atoms. These atoms found in the lattice structure are hit by electronic waves, and reflecting out of different planes. Once the electric light waves strike any of these planes, they can reflect all different planes of the lattice. The rays come to lattice in some angle, and they reflect out with the same angle due to the law of reflection. A ray scatters out from the second plane of atoms should proceed extra distance to reflect shown as orange arrow shown in **Figure 2.9**, and the ray must come back that extra distance to catch up with the ray that reflected out from the first plane of atoms. The detector gets the rays of signal which are the superposition of all raised rays that reflected, and come back out from the crystal. As a result, a right triangle shape can be defined as the rays coming in and reflecting out are the parallel rays to each other. The hypotenuse of right triangle is the distance,  $d$  between the atoms, and the perpendicular projection shows the distance of coming rays. The length of orange arrow of the right triangle shows the extra path the lower light of electric wave proceeded.

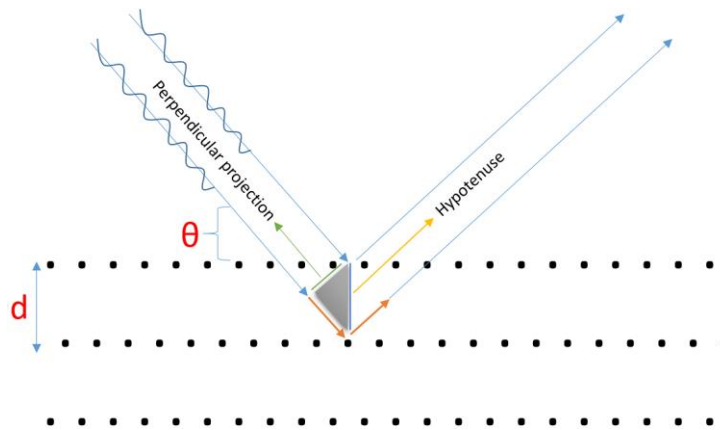


**Figure 2.9** Schematic presentation of Bragg's law

In conclusion,  $d\sin\theta$  shows the distance that second wave must travel, and  $2d\sin\theta$  is the total path of the ray which travels extra to catch up the first wave. Constructive interference can be obtainable if the extra path difference ends of being a multiple of the wavelength, ( $n\lambda$ ). In this case,  $n\lambda$  will be equal to  $2 d\sin\theta$ , which defines the Bragg law given in **Equation 2.20**.

$$2d \sin\theta = n\lambda \qquad \text{Equation 2.20}$$

## 2.6 Electrodeposition Devices

Throughout the study various electrodeposition devices were used. In a basic description. These devices have two power output in which one works as anode, another one is cathode. While AC/DC power supplies allow the user to change potential and current values, Pulse reverse electrodeposition devices are capable to change the duration of the current applied onto cathode in milliseconds.

### 2.6.1 AC/DC Power Supply

TTI EX355R model with 35 Volt, and 5 Ampere maximum outputs power supply was used during the experiments. It has a resolution of current up to 10 mA.

### **2.6.2 Pulse Reverse Electrodeposition**

The device was supplied from the Plating Electronics Company with model number of pe86cb. During the experiment, pulse reverse power supply was one of the most applied device due to purpose of main study. Pe86cb can create complex waveforms by performing a constant current regulation with the inaccuracy level less than 0.5 %. Pe86cb is a microprocessor controlled unit provides 3 A effective current, 9 A forward-backward pulse current, and 20 V effective voltage.

Pulse electrodeposition based on the change in flow-direction of current in time with respect to zero point. By using this technique, it is possible to apply different current amplitudes with different direction and periods as repetitive cycles.

## 2.7 References

1. D. S. Silvester, E. I. Rogers, R. G. Compton, K. J. McKenzie, K. S. Ryder, F. Endres, D. MacFarlane and A. P. Abbott, in *Electrodeposition from ionic liquids*, eds. F. Endres, A. Abbott and D. MacFarlane, John Wiley & Sons, Weinheim, 2 edn., 2017, pp. 287-345.
2. R. G. Compton and G. H. W. Sanders, *Electrode Potentials*, Oxford University Press, Oxford, UK, 1996.
3. W. Nernst, *Z. Phys. Chem.*, 1888, **2**, 613.
4. J. Kotyta, J. Dvorak and L. Kavan, in *Principles of Electrochemistry*, John Wiley & Sons, Inc., New York, 2 edn., 1993, pp. 169-184.
5. J. N. Butler, *Reference Electrodes in Aprotic Organic Solvents*, John Wiley & Sons, Inc., New York, 1970.
6. A. J. Bard and L. R. Faulkner, in *Electrochemical Methods: Fundamentals and Applications*, John Wiley & Sons, Inc., New York, 2001, vol. 38, ch. 2, p. 53.
7. G. Gritzner and J. Kuta, *Pure Appl. Chem.*, 1982, **54**, 1527–1532.
8. J. M. Hartley, PhD thesis, University of Leicester, 2013.
9. D. Pletcher, *A first course in electrode processes*, RSC Publishing, Cambridge, UK, 2009.
10. A. J. Bard and L. R. Faulkner, in *Electrochemical Methods: Fundamentals and Applications*, John Wiley & Sons, Inc., New York, 2001, vol. 1, p. 23.
11. M. S. Chandrasekar and M. Pushpavanam, *Electrochimica Acta*, 2008, **53**, 3313-3322.
12. A. Ispas and A. Bunda, *Electrochem. Soc. Interface*, 2014, **23**, 47-51.
13. P. A. Kohl, in *Modern Electroplating*, eds. M. Schlesinger and M. Paunovic, John Wiley & Sons, Inc., New Jersey, 5th edn., 2010, p. 125.
14. S. Roy, A. Connell, M. Ludwig, N. Wang, T. O'Donnell, M. Brunet, P. McCloskey, C. ÓMathúna, A. Barman and R. J. Hicken, *Journal of Magnetism and Magnetic Materials*, 2005, **290–291**, Part 2, 1524-1527.
15. N. Ibl, *Surface Technology*, 1980, **10**, 81-104.
16. O. Chène and D. Landolt, *J Appl Electrochem*, 1989, **19**, 188-194.
17. S. Roy and D. Landolt, *J Appl Electrochem*, 1997, **27**, 299-307.
18. H. Y. Cheh, *Journal of The Electrochemical Society*, 1971, **118**, 551-557.

19. S. Bruckenstein and M. Shay, *Electrochimica Acta*, 1985, **30**, 1295-1300.
20. G. Sauerbrey, *Zeitschrift für Physik*, 1959, **155**, 206-222.
21. J. Hillier and E. Ramberg, *Journal of Applied Physics*, 1947, **18**, 48-71.
22. B. Lencová, in *Handbook of Charged Particle Optics*, ed. J. Orloff, CRC Press, 2 edn., 2009, pp. 162-201.
23. Y. Waseda, K. Shinoda and E. Matsubara, in *X-Ray Diffraction Crystallography*, Springer Heidelberg Dordrecht London New York, 2011, DOI: DOI 10.1007/978-3-642-16635-8, ch. 1, p. 1.
24. A. A. Bunaciu, E. G. Udristioiu and H. Y. Enein, *Critical Reviews in Analytical Chemistry*, 2015, **45**, 289-299.
25. W. Friedrich, P. Knipping and M. Laue, *Verl. der Kgl. Bayer. Akad. der Wiss.*, 1913, **5**, 303-322.
26. W. L. Bragg, *Proceedings of the Royal Society of London. Series A*, 1913, **89**, 248.

# **Chapter III**

## **BASICS**

### **3.1 Introduction**

This thesis aims to study a novel method for copper and zinc deposition using deep eutectic solvents. While these metals have been studied in-depth in these liquids it became apparent during subsequent studies that the previously assumed simple mechanism of metal deposition and dissolution was an over-simplification. The information gathered in this chapter, in fact, was obtained at the end of the project but it helps to explain the work presented in chapters 4 and 5.

An important part of this thesis is the use of pulse plating to dissolve and the redeposit the metal onto the surface. Although electrodeposition processes have been studied in detail in deep eutectic solvents, not much work has been carried out to investigate the anodic dissolution process. To date it was assumed that electrodeposition occurs as a simple electron transfer and nucleation/growth process. The presence of films on the electrode surface has previously been largely ignored.

A recent study has shown that films do form on the electrode surface during electro-dissolution of the electrode in DESs.<sup>1</sup> To some extent this is not surprising since anodic processes in aqueous solutions commonly end up in electrolyte breakdown and the formation of surface films but it was felt that the high chloride concentration in DESs might circumvent this. Ultimately it was shown that the film formation in DESs was due to insoluble chloride films and this will be discussed in greater depth in this chapter. Film formation is important as it can control mass transport, electron transfer, surface morphology as well as the throwing power of the cell.<sup>2</sup>

#### **3.1.1 Passivation**

Passivation is observed especially during anodic dissolution processes, and it is an important characteristic of some metals. The subject is very important for micromachining, electropolishing, batteries, and corrosion.<sup>3, 4</sup>

Pulse reverse deposition has been studied intensively, particularly where powdery deposits are obtained, as a method to acquire dense deposits.<sup>5-12</sup> By using a pulsed power supply in a deposition process, it is possible to increase the current efficiency as well as

change the morphology of the deposit as will be shown in chapter 3 and 4. However, passivation plays a vital role to explain phenomena encountered in other chapters, and thus, it is explained in this chapter.

The growth and dissolution of films depend upon the medium, pulse time and magnitude of the current pulse. In aqueous solutions, the growth and dissolution of films is critically pH dependent as this controls the oxide and hydroxide films which form on metal surfaces. Throughout the studies, speciation of various metal ligand systems have been characterized in aqueous solutions using Pourbaix diagrams which show the most stable phase which forms as a function of pH and potential.<sup>13</sup> Pourbaix diagrams characterise the species as being immune, passive or corroding. An example of a Pourbaix diagram is shown in *Figure 3.1*.

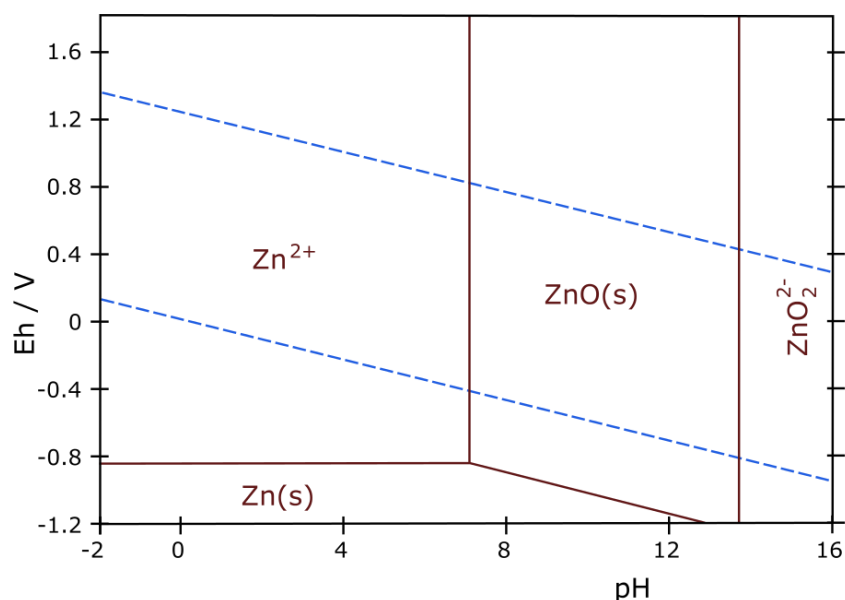


*Figure 3.1* Pourbaix diagram for zinc in aqueous solutions. Blue dashed lines show the potential for the hydrogen evolution process (lower) and oxygen reduction process (upper).

While these diagrams are useful in predicting species that form there are some limitations associated with their use; they provide no kinetic information about the corrosion/dissolution process, they are only derived for pure metals under standard condition assuming a metal ion concentration of  $10^{-6}$  mol dm<sup>-3</sup>. They also make no assumptions about where the passive film forms and whether it is electrically insulating or conducting and tend to only be well defined for H<sup>+</sup> and OH<sup>-</sup> ions. No Pourbaix

diagrams exist for non-aqueous solutions due to the lack of information about thermodynamic parameters or the meaning of pH in aprotic media.

### 3.1.2 Oxidation Mechanisms in Aqueous Solutions

There are two main oxidation mechanisms in aqueous solutions; the duplex salt mechanism, and the adsorbate-acceptor mechanisms.

The duplex salt mechanism assumes a compact but porous film forms on the electrode surface. It was originally proposed by Grimm et al. and is shown schematically in **Figure 3.2**.<sup>14</sup>

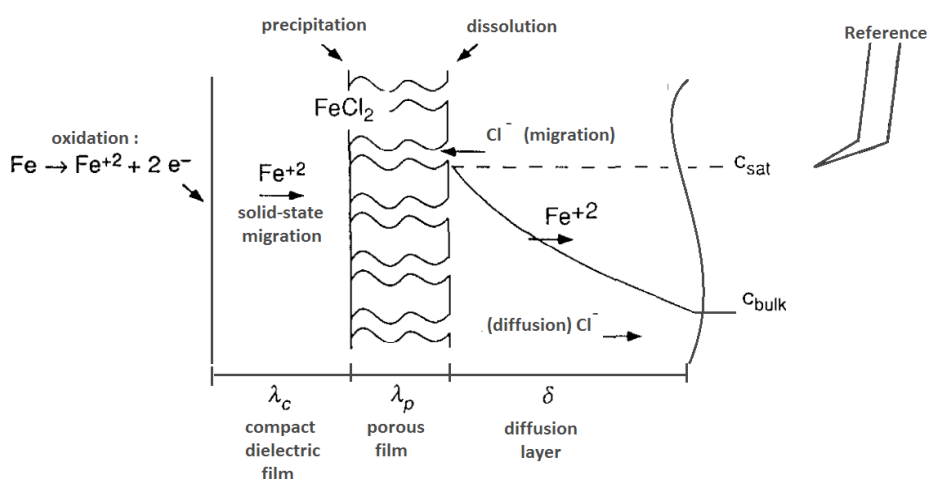


**Figure 3.2** Schematic representation of duplex salt film model.<sup>14</sup>

This model, assumes that the film is made up of two layers; a dense layer close to the metal surface which forms a solid dielectric and an outer region which is porous. The dense layer limits the transport of cations from the metal surface and most of the potential drop is across this layer. It is usually assumed that there is no movement of anion or ligand through the dense layer which is typically about 10 nm thick and most the observed potential drop occurs across to this layer. It is assumed that the film formed has a constant thickness and that the precipitation and dissolution steps occur at a constant rate. The diffusion of cations through the compact dielectric film occurs at the same rate as the rate of anions diffusing through the porous film. The film thickness controls the potential drop across the film. The porous film is 100 to 1000 times thicker than the dense layer and is filled with electrolyte

whose concentration is thought to be constant. The metal dissolution kinetics are limited by metal ion mobility in most cases.<sup>15</sup>

The other mechanism is called as adsorbate-acceptor mechanism which assumes a constant rate of anodic dissolution. The model assumes that acceptors (ligands) solubilise in the bulk electrolyte region and adsorb on the electrode surface ready to react with the dissolving metal. The dissolution rate is limited by the amount of acceptor in solution which can complex the metal ion. A concentration gradient of both the acceptor and the acceptor metal complex are set up across the diffusion layer. No thick film forms on the electrode surface in this model.<sup>16, 17</sup> Therefore, mass transport in the electrolyte comes solely from solvated cations as shown schematically in **Figure 3.3**. The rate of anodic dissolution decreases with increasing surface coverage by the ligand from the bulk electrolyte region.

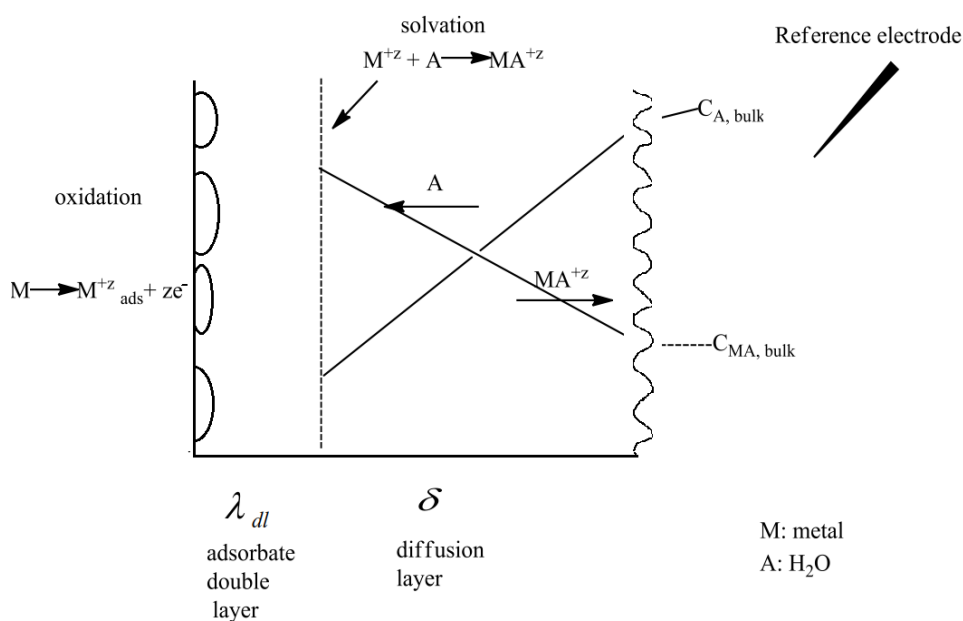


**Figure 3.3** Schematic representation of the adsorbate-acceptor model

The adsorption of ions on the electrode surface, can change the potential for metal dissolution which is often increased to overcome the blocking effect of adsorbed ions.<sup>17</sup>

In addition to differences in the structure of films formed at the electrode surface. It should also be noted that the double layer structure at the electrode-solution interface will also be significantly different in an ionic liquid to an aqueous solution. The double layer has received significant study recently. A review by Alam et al. summarises some ideas

of the topic.<sup>18</sup> In aqueous solutions the electrode charge is compensated by a strongly bound layer of counterions and a diffuse layer with a concentration gradient of counterions. In an ionic liquid, the commonly agreed model of the interfacial structure has layers of ions with alternating charges as given in **Figure 3.4**. The strength of these interactions weakens as a function of distance from the electrode surface and it is thought that up to 4 layers anions and cations are relatively strongly bound. Furthermore, the double layer structure of ionic liquids makes them suitable media for use in supercapacitors. It could, however, also be the cause of changing deposit morphology in electroplating. Changing the ions in the ionic liquid has a significant effect on deposit morphology and it has been shown that adding cations, such as lithium, can change the energetics of metal nucleation and growth. Endres et al. used AFM and showed how LiCl significantly disrupted metal deposition.<sup>19</sup> Compared to ionic liquids the double layer structure in DESs is almost unstudied. Silva et al studied the capacitance in 3 DESs and showed that the potential of zero charge was similar in all the liquids c.a. -200 mV vs Ag/Ag<sup>+</sup>.<sup>20</sup> A recent study by Atkin et al. showed that unlike most ionic liquids, the double layer structure in DESs only really extends over about two molecular layers from the electrode surface.<sup>21</sup>

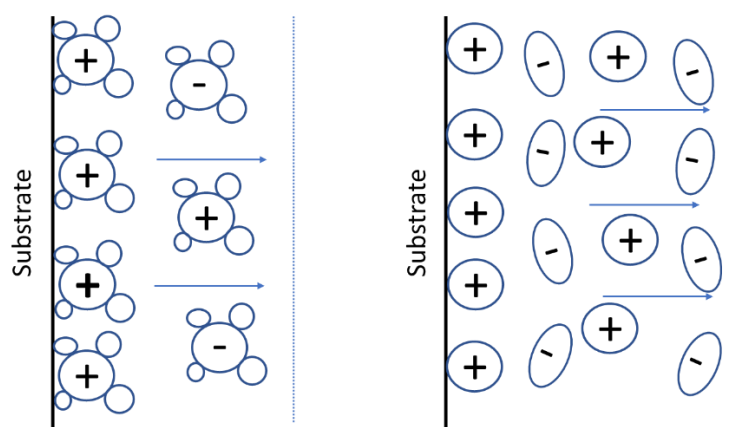


**Figure 3.4** Electrode electrolyte interface in an aqueous (left) and ionic liquid (right).

### 3.1.3 Anodic dissolution in ionic liquids and DESs

While deposition reaction has been studied in ionic liquids and DESs comparatively little is known about oxidation reactions. In ionic liquids pH is almost unstudied and the stability of passivating layers are unknown. Some qualitative evidence exists that trans-

passive corrosion occurs at positive over-potentials as metals such as aluminium and chromium can be readily oxidised in ionic liquids.<sup>22, 23</sup>

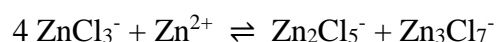
Electrooxidation was first studied by Abbott et al. for the electropolishing of stainless steels. This was studied using ChCl: EG eutectics with voltammetry and impedance spectroscopy.<sup>15, 24</sup> It was shown that the dissolution mechanism in the DES was different from that in acidic aqueous solutions. The authors suggested that diffusion in the viscous DES controlled electropolishing.<sup>25</sup> Polishing only occurred in the current density range 70 to 50 mA cm<sup>-2</sup> with an applied voltage of about 8 V which was narrower than that in aqueous phosphoric/ sulphuric acid mixtures, but the current density requirements were considerably lower using the DES. This was thought to be due to decreased gas evolution at the anode which increased the current efficiency from about 30 to 80 %. No dealloying of the steel took place.

Karim studied the anodic behaviour of 9 metals in 1ChCl: 2 EG and in BMIMCl.<sup>15</sup> In most cases the rate of anodic dissolution was found to be higher in 1 ChCl: 2 EG than BMIMCl which was thought to be due to mass transport. It was found that in most of the cases studied, film formation, or quasi-passivation of the metal surface occurred. In some cases, a clear coloured layer is formed at the electrode surface. This was thought to occur in some cases because an uncharged product was formed which was insoluble.

It had previously been assumed that, because most metal halide salts are very soluble in DESs, anodic dissolution should lead to soluble products. It has been shown that when copper chloride dissolves in DESs it forms  $[\text{CuCl}_4]^{2-}$ .<sup>1</sup> It should, however be noted that the dissolution of anhydrous  $\text{CuCl}_2$  is relatively slow and generally requires high temperatures and vigorous stirring to achieve due to its high lattice energy. The oxidation of copper metal could be limited by the diffusion of the ligand to the metal surface. If this were the case, then  $\text{CuCl}_2$  could form and if the concentration in the double layer exceeded the solubility limit then the material would precipitate out. This was found to be the case by Karim and it was shown that if the solution was stirred or the electrode rotated then passivation of the electrode surface did not occur.<sup>15</sup> This study showed that in metal deposition mass transport is vital in controlling deposit morphology and the efficiency of the anodic process.

The liquid has also been shown to affect passivation. Electrodissolution of nickel in 1 ChCl: 2 EG produces a blue/green solid on the electrode surface but in BMIMCl a soluble blue complex form. Ni can be electropolished in 1 ChCl: 2 EG but not in the latter. A Ni(II) complex is formed with two ethylene glycols and two chlorides in 1 ChCl: 2 EG, and this neutral complex has a low solubility.<sup>26</sup> Formation of the complex on the electrode surface decreases mass transport to and from the electrode surface and results in electropolishing.

It should also be appreciated that oxidation of metals in ionic liquids is very complex as the ligands while present in 2-4 mol.dm<sup>-3</sup> are quickly used up in the double layer and diffusion in the viscous liquids is very slow. It is more important in liquids where the metal is present in high concentration in the liquid. In type 1 zinc chloride eutectics, for example, the concentration of free chloride is very low such that electrooxidation can only occur by a mechanism such as;



This shows that electro-deposition and dissolution are complex processes and are different in DESs compared to aqueous solutions. It is unsurprising that the concentration and speciation of the electroactive species has such a strong effect on both processes. It is also unsurprising that the nature of the cation and the temperature of the system are also more complex than might be envisioned. These factors are discussed in more details in reviews by Abbott et al.<sup>27, 28</sup>

### 3.2 Zinc Electrodeposition

Metal deposition has been studied in-depth in a variety of ionic liquids and deep eutectic solvents.<sup>26, 29-34</sup> These novel solvents are of interest because they enable innovative structures to be formed on surfaces. They also permit oxide and hydroxide chemistry to be circumvented for oxophilic metals enabling deposition of metals such as aluminium.<sup>35-37</sup> It is thought that the electrochemistry of metals in these media is very dependent upon speciation.<sup>38</sup> The behaviour of metals in these ionic solutions is strongly dependent on metal ion concentration and temperature.

Zinc is one of the most commonly studied metals for electrodeposition in ionic liquids.<sup>39</sup> Most of the studies have involved Type 1 chlorozincate based ionic liquids which are analogous to the haloaluminates studies.<sup>41</sup> The chlorozincate liquids are easy to make and handle although they have lower conductivities and higher viscosities. It was initially thought that these liquids were water stable but Hsiu et al. studied C<sub>2</sub>mimCl: ZnCl<sub>2</sub> mixtures and showed that some hydrolysis does occur.<sup>42</sup> It was also found by the same group that the potential window of this mixture was significantly affected by the Lewis acidity. This is because the reduction of zinc appears to be more difficult in Lewis basic liquids. Zinc deposition has been studied in a variety of liquids as a function of composition, temperature and diluents.<sup>39, 43, 44</sup> The most in-depth study was by Baron who applied different techniques, such as SEM, EDX, EQCM, AFM, and XRD along with nucleation studies to study zinc deposition in Type 3 eutectics.<sup>20, 40, 45, 46</sup> There has, however, never been a holistic study of these systems to identify the factors controlling morphology changes.

Metal dissolution has been studied in much less detail. The first concerted study in this area showed that film formation occurred during electrodisolution for 9 common metals and this was due to the high viscosity of the medium and the relatively low ligand concentration.<sup>15</sup> This resulted in uncharged species forming at the electrode-solution interface which precipitated. Film formation can cause difficulties due to electrical resistance slowing down the anodic process or they can have advantages as is seen with electropolishing.<sup>47, 48</sup>

DESs can be made to contain zinc in a variety of ways. The original DESs were based on a quaternary ammonium salt and zinc chloride. These were found to contain a variety of zinc species; ZnCl<sub>3</sub><sup>-</sup>, Zn<sub>2</sub>Cl<sub>5</sub><sup>-</sup> and Zn<sub>3</sub>Cl<sub>7</sub><sup>-</sup>.<sup>39</sup> Eutectics made from a quaternary ammonium salt and a hydrogen bond donor have also been studied for metal deposition and very high concentrations of zinc could be obtained. Finally, it was found that zinc chloride disproportionated when mixed with hydrogen bond donors such as urea to form [ZnCl.urea]<sup>+</sup> and [ZnCl<sub>3</sub>]<sup>-</sup>. While electrodeposition has been studied in these media, the deposit morphology is very different depending on the conditions and a comparison at comparable conditions has never been carried out. The issue when trying to compare these liquids is that their physical properties and solute speciation change significantly. **Table**

3.1 lists the viscosity, zinc concentration and speciation for six eutectic mixtures which will be studied in greater detail below.

**Table 3.1** Viscosity, concentration and speciation for the eutectics used in this study.<sup>49-</sup>

52

Type	Composition	$\eta$ / cP	[M]/ mol dm <sup>-3</sup>	Speciation
1	1 ChCl: 2 ZnCl <sub>2</sub> <sup>49</sup>	72,000	8.24	[ZnCl <sub>3</sub> ] <sup>-</sup> / [Zn <sub>2</sub> Cl <sub>5</sub> ] <sup>-</sup>
2	1 ChCl: 1 CrCl <sub>3</sub> .6H <sub>2</sub> O <sup>53</sup>	5800	7.81	[CrCl <sub>4</sub> .2H <sub>2</sub> O] <sup>-</sup>
2	1 ChCl: 1.5 Zn(NO <sub>3</sub> ) <sub>2</sub> .6H <sub>2</sub> O	18	4.09	unknown
2	2 PG: 1 Zn(NO <sub>3</sub> ) <sub>2</sub> .6H <sub>2</sub> O	46	4.63	unknown
3	1 ChCl: 2 EG	20	0.40	[ZnCl <sub>3</sub> ] <sup>-</sup>
3	1 ChCl: 2 Urea <sup>51</sup>	200	0.40	[ZnCl <sub>3</sub> ] <sup>-</sup>
4	1 ZnCl <sub>2</sub> : 4 Urea <sup>50</sup>	11,340	9.92	[ZnCl <sub>3</sub> ] <sup>-</sup> / [ZnCl.urea] <sup>+</sup>

Part of the issue associated with the electrodeposition of metals from ionic liquids is that they are usually carried out at very different conditions from those employed in aqueous solutions. It was recently shown that the electrodeposition of nickel carried out under comparable conditions in a DES and in two aqueous solutions gave similar deposition rates despite an order of magnitude difference in the viscosity and conductivity.<sup>54</sup> It was concluded that electrodeposition in many aqueous solutions was carried out in very different conditions than those typically used in the literature for ionic liquids and DESs. Most aqueous plating solutions operate at high metal concentrations (0.5 to 2 mol dm<sup>-3</sup>) and generally at elevated temperatures (50 - 70 °C).

### 3.2.1 Cyclic Voltammetry and EIS for Zinc-based DESs

The voltammograms given in **Figure 3.5, a** and **b** are for 1: 2 ChCl: ZnCl<sub>2</sub> and 4: 1 urea: ZnCl<sub>2</sub>. Both show evidence of iR artefacts originating from the high viscosity and low conductivity of the liquids. It is, however still valid to analyse the onset potentials for Zn reduction. In the former, reduction begins at -0.55 V whereas in the latter it is at -0.95 V. This difference in reduction potential could occur due to; differences in Zn salt concentration, a liquid junction potential, blocking of the electrode surface or differences in zinc speciation. It has previously been shown that solutes in DESs show approximately Nernstian behaviour even at high solute concentration.<sup>3,55</sup> The difference in concentration

between the two liquids ( $4.8 \text{ mol kg}^{-1}$  vs.  $2.7 \text{ mol kg}^{-1}$ ) cannot account for the difference in reduction potential from a Nernstian perspective.

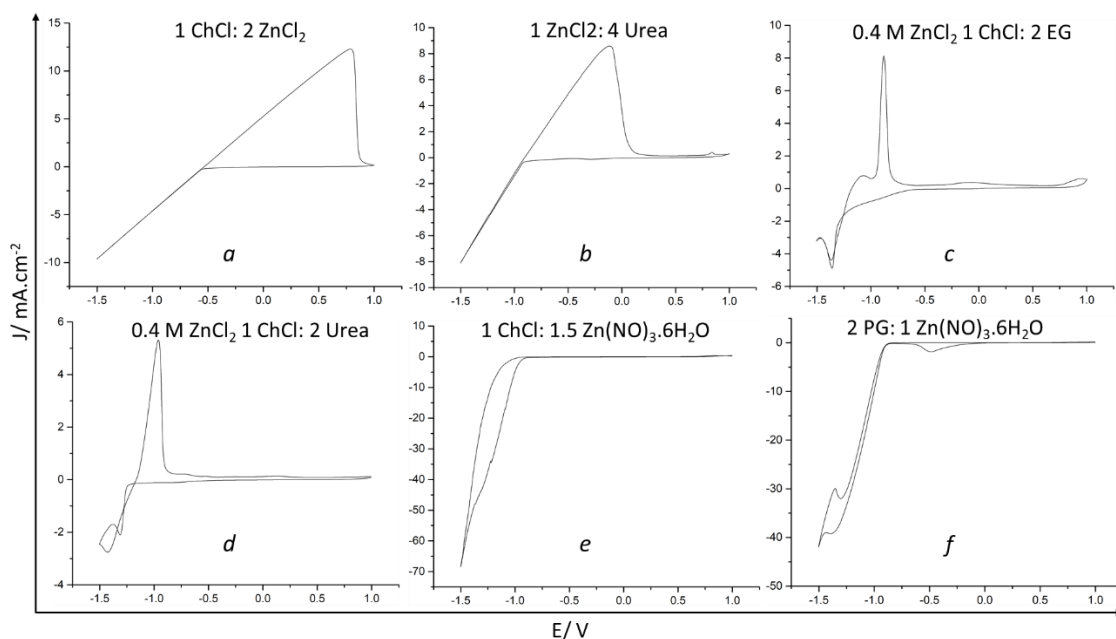


**Figure 3.5** Cyclic voltammogram (Pt WE, Ag/AgCl RE, and Pt CE) of 6 different DESs at  $50^\circ\text{C}$  at a sweep rate of  $20 \text{ mV s}^{-1}$ .

The liquid junction potentials (LJP) in DESs has recently studied and it was shown that even in extreme cases where the charge carrier changes from a choline cation to a proton then the difference in LJP was less than  $30 \text{ mV}$ .<sup>56</sup> It can therefore be concluded that the reference electrode cannot be the cause of the difference between the reduction potentials. It is known that speciation is different in the two liquids; in 1: 2 ChCl:  $\text{ZnCl}_2$ ,  $[\text{ZnCl}_3]^-$ ,  $[\text{Zn}_2\text{Cl}_5]^-$  and  $[\text{Zn}_3\text{Cl}_7]^-$  are all present whereas in 4: 1 urea:  $\text{ZnCl}_2$ ,  $[\text{ZnCl}\cdot\text{urea}]^+$  and  $[\text{ZnCl}_3]^-$  are formed.<sup>39</sup> In both liquids, the concentration of free chloride will be negligible so chloride adsorption will be less likely but it may be reticent to leave the zinc atom once it is reduced so chloride could still be adsorbed on the zinc surface. In both liquids, the cathodic charge was equal to the anodic charge showing that the deposition was reversible.

In the type 3 DESs; 1: 2 ChCl: EG and 1: 2 ChCl: urea, both containing approximately  $0.4 \text{ mol kg}^{-1} \text{ ZnCl}_2$ , (**Figure 3.5 c** and **d**) reversible deposition and stripping can be observed in their cyclic voltammograms. The reduction currents are less than that observed for 1: 2 ChCl:  $\text{ZnCl}_2$  and 4: 1 urea:  $\text{ZnCl}_2$ . This must be due to the lower

concentrations in 1: 2 ChCl: EG and 1: 2 ChCl: urea as they have significantly lower viscosities (**Table 3.1**). In the CVs for both liquids, the total cathodic charge was equal to the total anodic charge showing that the deposition was reversible. The onset potentials for reduction differ in the two liquids despite the speciation being essentially the same. The difference in LJP between the two liquids is known to be only 14 mV so can be discounted. What is clear from the images *c* and *d* given in **Figure 3.5**, that we have not commented on before, is the presence of a small current at between -0.2 and -0.5 V. These currents are small and as seen in **Figure 3.6** correspond to approximately a monolayer of charge.

The two eutectic mixtures based on zinc nitrate; 2: 1 PG: Zn(NO)<sub>3</sub>.6H<sub>2</sub>O and 1: 1.5 ChCl: Zn(NO)<sub>3</sub>.6H<sub>2</sub>O DESs, *e* and *f* respectively in **Figure 3.5** show large reduction currents but did not exhibit any significant current on the anodic sweep. This could mean that the electrodeposition of Zn is very inefficient or that the Zn passivates. These liquids have much lower viscosities and clearly contain quite high-water concentrations. The voltammograms also decrease their current on subsequent scans and appear to be prone to passivation. As will be shown in further paragraphs, this is due to the formation of zinc oxide or hydroxide on the electrode surface.

While the nucleation of zinc in these liquids has previously been studied, little has been reported about under-potential deposition, UPD. It has previously been assumed that zinc could easily dissolve on the anodic sweep and was simply deposited on the cathodic sweep. Although UPD regions were always there, they were never closely investigated as the currents were small compared to those for bulk deposition.

**Figure 3.6** shows the UPD regions of the cyclic voltammograms shown in **Figure 3.5** before bulk deposition occurs, for the zinc chloride based eutectics. In each case a small reversible current is observed. The potential for the onset of UPD is relatively similar in all four liquids showing that it is dominated by the interaction between the Pt substrate and the zinc species. UPD starts to occur in the 1: 2 ChCl: ZnCl<sub>2</sub> at about +0.6 V whereas it occurs at +0.2 V in 4: 1 urea: ZnCl<sub>2</sub>. In the more Lewis acidic liquid [Zn<sub>2</sub>Cl<sub>5</sub>]<sup>-</sup> dominates which is possibly easier to electrodeposit from. Integration of the charge under the peak shows that the amount of UPD material deposited varies in the four liquids. The lowest is in the ChCl: 2ZnCl<sub>2</sub> liquid and the highest is in the 4 urea: 1 ZnCl<sub>2</sub>. In the former,

$[\text{Zn}_2\text{Cl}_5]^-$  will be the dominant electroactive species whereas in the latter  $[\text{ZnCl.urea}]^+$  is the most likely electroactive species. Under-potential deposition is thought to occur when the deposition of the coating metal is easier on the substrate than on itself. It generally corresponds to a monolayer of metal but can sometimes produce up to 3 monolayers.

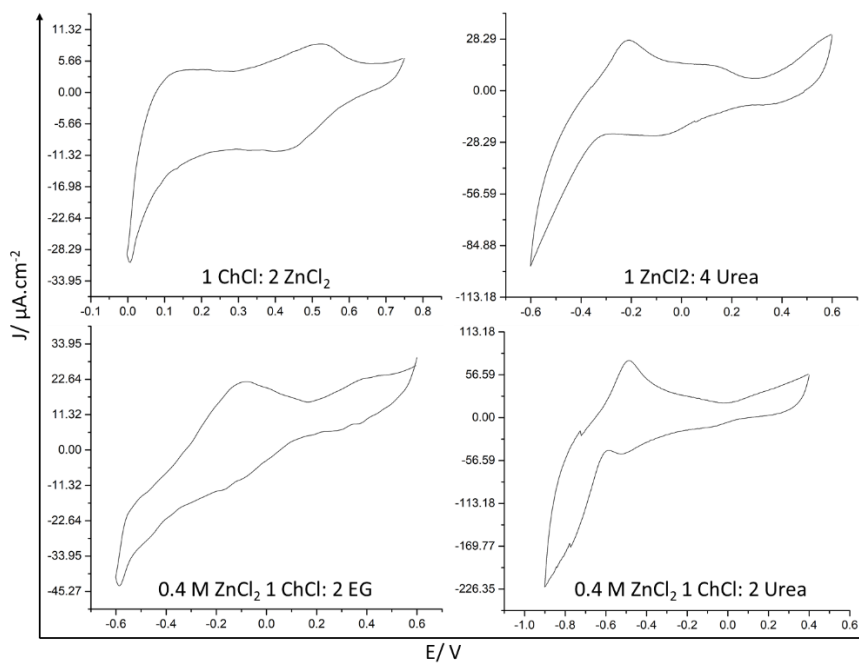


**Figure 3.6** Cyclic voltammograms ((Pt WE, Ag/AgCl RE, and Pt CE) operated at 50 °C, and a sweep rate of 20 mV s<sup>-1</sup> to investigate the UPD regions of cyclic voltammogram given in **Figure 3.5**.

In some cases, the ligand from the metal may be only partially labile and may remain adsorbed to the deposited ad-layers.<sup>57, 58</sup> If chloride was adsorbed on the zinc surface, then the partition coefficient between the surface and solution would depend upon the relative Lewis acidity of the liquid. The ChCl: 2 ZnCl<sub>2</sub> liquid is strongly Lewis acidic and would tend to complex adsorbed chloride from the surface. For the 1 ChCl: 2 EG and 1 ChCl: 2 urea systems UPD is prominent as might be expected as these are more Lewis basic liquids with a higher chloride concentration.

An unusual observation about the 1 ChCl: 2 EG and 1 ChCl: 2 urea systems is that bulk zinc electrodeposition cannot be achieved at metal salt concentrations below 0.05 mol dm<sup>-3</sup>. This is not the case for other metals such as copper and silver which can be deposited at concentrations below 5 mmol dm<sup>-3</sup>. It is clear from **Figure 3.6** that UPD is occurring which suggests that it is not speciation *per se* which is preventing metal reduction. One

cause for this could be that something is blocking the electrode surface at low metal concentrations which prevents nucleation from occurring. Endres *et al.* have previously studied metal deposition in ionic liquids and proposed that the cation affects the reduction of metal.<sup>52</sup> They showed that the morphology of the deposit could be changed in ionic liquids by changing an imidazolium- to a pyrrolidinium-based cation. Atkin *et al.* showed that in these ionic liquid, ions formed ordered alternating layers of anions and cations up to 4 layers thick and it was inferred that this could affect the morphology of deposits forming on the substrate. Atkin *et al.* repeated this study for the DESs 1 ChCl: 2 EG and 1 ChCl: 2 urea and unlike the imidazolium and pyrrolidinium-based liquids, only one layer was seen at the electrode DES interface and in both cases, this was similar in size to the solvated chloride anion.

Several groups have also studied UPD of metals in ionic liquid and found that a range of metals exhibit this phenomenon. Few groups have noted the minimum concentration needed to deposit metals except in the case of the chloroaluminate ionic liquids. Here it has been noted that aluminium can only be deposited once a Lewis acidic mixture is used ( $x \text{ AlCl}_3 > \text{halide salt}$ ). This has been explained in terms of an inability to reduce  $[\text{AlCl}_4]^-$  but it could be due to chloride adsorption (UPD is observed in this system) and the chloride is only removed once the liquid becomes Lewis acidic.

An alternative explanation could be due to the structure at the electrode-solution interface. Given that the structure is most probably dominated by alternating anion and cationic layers a low metal complex concentration will mean that the double layer is dominated by  $\text{Cl}^-$  rather than  $[\text{ZnCl}_3]^-$ . At  $0.05 \text{ mol dm}^{-3} \text{ ZnCl}_2$  the concentration of free chloride will be more than 100 times larger than that of  $[\text{ZnCl}_3]^-$  which many mean that the metal ion is too slow to reduce and nucleate. If that were the only reason, then the same claim could be made for copper which can still be deposited at low copper chloride concentrations which suggests that this is also not the reason.

The experiment shown in **Figure 3.5** was repeated as a function of zinc chloride concentration in the 1 ChCl: 2EG system and the results are shown in **Figure 3.7**. At low zinc concentration ( $0.05 \text{ mol.dm}^{-3}$ ) there is a reduction current which is at the cathodic limit of the potential window of the eutectic mixture. On the anodic sweep, there is a small peak at  $-0.9 \text{ V}$  and a larger peak at  $0.0 \text{ V}$ . Increasing the  $\text{ZnCl}_2$  concentration to  $0.2$

and then  $0.4 \text{ mol.dm}^{-3}$  causes the cathodic current to decrease and the anodic peak at  $-0.9 \text{ V}$  to increase in height while that at  $0.0 \text{ V}$  decreases. The peak at  $0.0 \text{ V}$  is in approximately the same area as UPD Zn dissolution but the charge is considerably greater than a monolayer suggesting that it has a different origin.

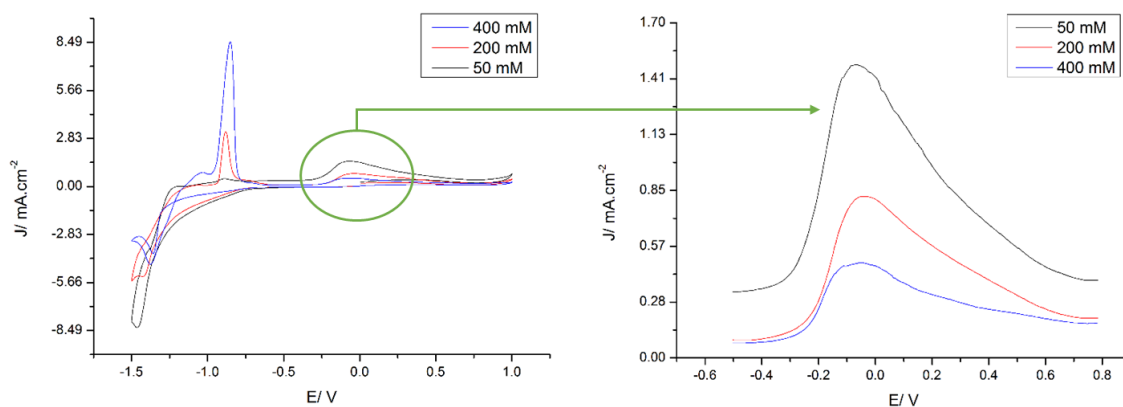


**Figure 3.7** Cyclic voltammograms (Pt WE, Ag/AgCl RE, and Pt CE) of  $\text{ZnCl}_2$  at  $40 \text{ }^\circ\text{C}$ , and a sweep rate of  $20 \text{ mV s}^{-1}$  in 1 ChCl: 2 EG as a function of concentration.

It could also be argued that the different concentrations of  $\text{ZnCl}_2$  change the physical properties of the eutectics. In most cases adding a metal salt to a Type 3 eutectic would normally be expected to increase the viscosity. **Table 3.2** shows the viscosity and conductivity for different concentrations of zinc chloride in 1 ChCl: 2 EG at  $50 \text{ }^\circ\text{C}$ .

**Table 3.2** Viscosity and conductivity measurements of zinc chloride in 1 ChCl: 2 EG at different molarities at  $50 \text{ }^\circ\text{C}$ .

Conc. $\text{ZnCl}_2 / \text{mol dm}^{-3}$	0.1	0.2	0.3	0.4
Viscosity/ cP	20.8	19.9	19.9	19.0
Conductivity/ $\text{mScm}^{-1}$	15.5	15.8	15.9	16.1

It can be seen that the metal salt has only a small effect on the solvent properties. Barron studied the effect of  $\text{ZnCl}_2$  on the viscosity and conductivity of 1 ChCl: 2 EG at different molarities at  $25 \text{ }^\circ\text{C}$ , and while the data were slightly different, the trends were the same.<sup>40</sup> Barron did, however, note that in the 1 ChCl: 2 urea system  $\text{ZnCl}_2$  had a much more significant effect decreasing viscosity and increasing conductivity as the concentration was increased.

Repeating the experiment in **Figure 3.7** for different cathodic limits shows a different response. **Figure 3.8** shows the cyclic voltammogram of ZnCl<sub>2</sub> in 1 ChCl: 2 EG as a function of cathodic sweep limit and when the cathodic limit is less negative, both peaks at -0.9 V and 0.0 V increases in height. In the absence of ZnCl<sub>2</sub> there is no oxidation peak at 0.0 V.

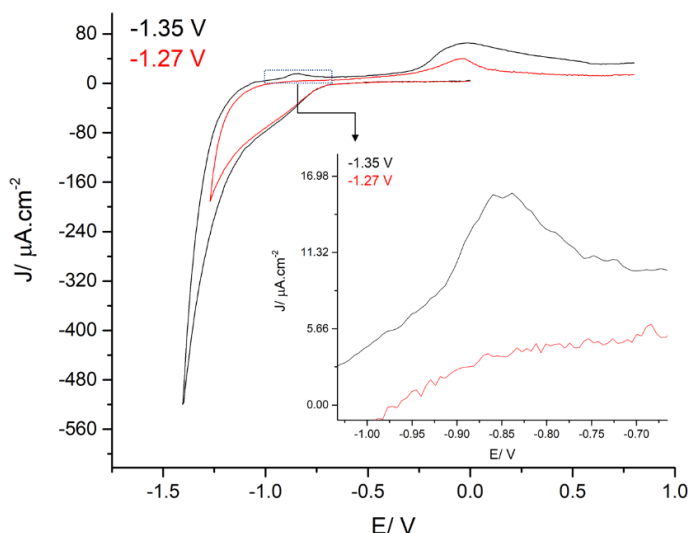
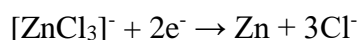


**Figure 3.8** Cyclic voltammograms (Pt WE, Ag/AgCl RE, and Pt CE) of ZnCl<sub>2</sub> at 40 °C, and a sweep rate of 20 mV s<sup>-1</sup> in 1 ChCl: 2 EG as a function of cathodic limit.

Analysis of the nucleation and growth mechanism for zinc deposition for ZnCl<sub>2</sub> in 1 ChCl: 2 EG on Pt at 40 °C using the Sharifker-Hills model shown that it grows by an instantaneous mechanism (See appendix 7.1 for data and fit). This does not fit wholly with the deposit morphology but is the mechanism proposed in **Figure 3.15 (IV)** then it could be approximated that the surface grows out radially beneath a glycolate film.

The data in **Figure 3.8** suggests that the two processes are related. It is proposed that the peak at 0.0 V is related to the dissolution of zinc which is covered with a quasi-passivating layer of oxygen containing species (oxide, hydroxide or glyxide). At negative potentials, occurring processes;



is in competition with the reduction of traces of water



Close to the electrode surface this could react with zinc species to form an insoluble layer. This would explain why the bulk deposition of zinc was not reversible in the 1ChCl: 2EG liquid.

It would also explain the behaviour of Zn in  $\text{Zn}(\text{NO}_3)_2$  eutectics. When 6 mole eq. of water are present, hydrogen evolution will be prevalent, and the double layer will become more basic during electrolysis. The formation of an oxide/hydroxide would prevent the dissolution of any zinc deposited during a pulse experiment. The formation of an insoluble layer would also affect the mechanism of metal deposition.

### 3.2.2 3D Optical Profiler Study of Zinc Reduction and Oxidation

The voltammogram in *Figure 3.6* was repeated with the working electrode under a 3D optical microscope. A 3D printed cell was used, and electrodes are placed so that the electrode could be imaged just below the solution air interface using a 3D optical microscope is given in *Figure 3.9*.

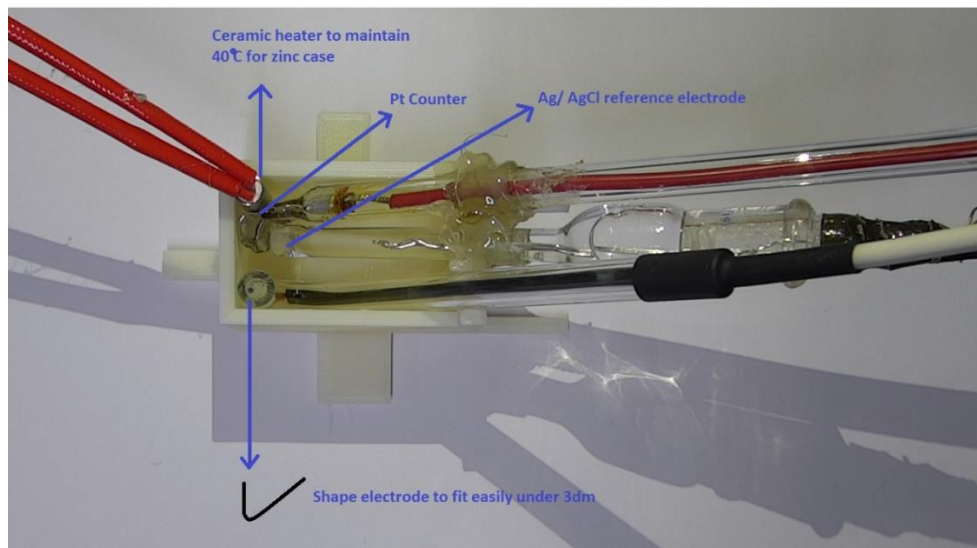


*Figure 3.9* Experimental set up for experiments performed under 3D optical profiler.

*Figure 3.10* shows images taken at different potentials during the scan. At -1.0 V on the cathodic sweep a matt platinum surface is observed with polishing grooves showing. At -1.27 V the surface becomes brighter and more grey-coloured as zinc is deposited but by

-1.4 V the surface has become dull potentially from the formation of a surface layer. At -1.5 V bubble nucleation and growth is observed.

On the anodic sweep, the solution close to the electrode becomes cloudy as the solution saturates with a Zn complex. It has recently been shown that the anodic dissolution of most metals in DESs leads to film formation on the electrode surface.<sup>15</sup> This is due to the high viscosity and the relatively low ligand concentration available to solubilise the metal ion. If insoluble complexes form from anodic dissolution, then this will affect the rate of the anodic process of a soluble zinc anode is used during the electrodeposition process. The effect of the anodic reaction on the rate of the cathodic process has not really been considered previously in DESs.

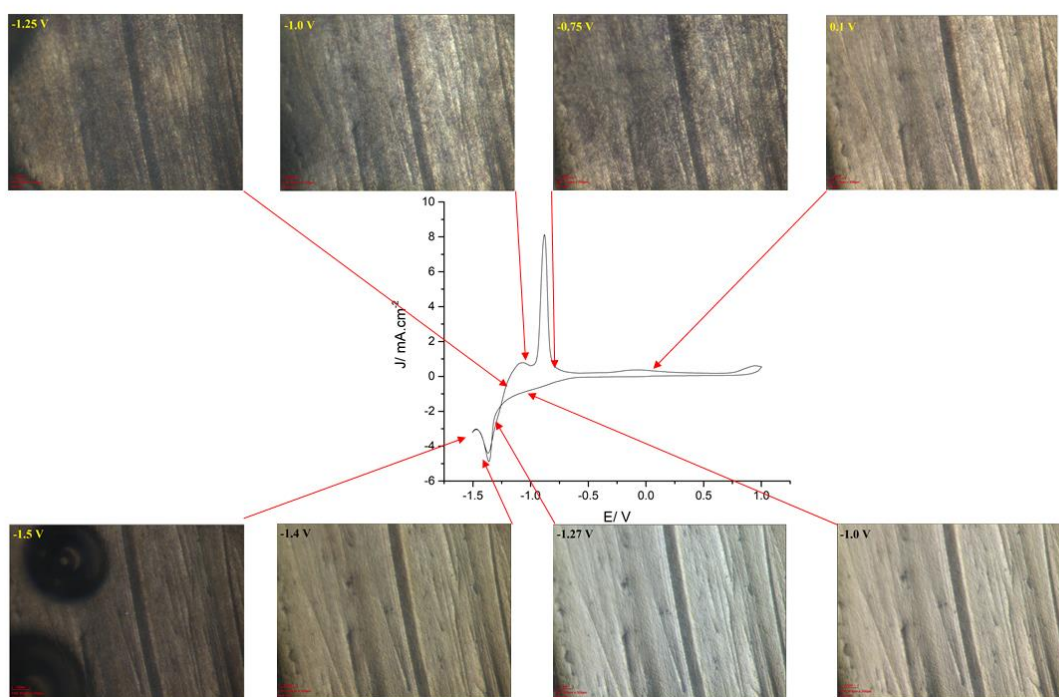


**Figure 3.10** Optical microscope images of the Pt electrode surface (Ag/AgCl RE, and Pt CE) during electrochemical polarisation of  $0.4 \text{ mol dm}^{-3} \text{ ZnCl}_2$  in 1 ChCl: 2 EG at  $40^\circ\text{C}$  and a sweep rate of  $20 \text{ mV s}^{-1}$ .

### 3.2.3 Electrochemical Impedance Spectroscopy

Fundamentally, there are three types of mass-transfer; diffusion under a concentration gradient, ionic migration under an electric field, and convection.<sup>59</sup> By using electrochemical impedance spectroscopy, one can relate these mass transfer phenomena

to an equivalent electrical circuit analogy in order to obtain data for mainly diffusion and migration controlled transport systems.

The simplified Randles cell is one of the most common cell models. Randles circuit is made up of three elements known as a solution resistance, a double layer capacitor and a charge transfer resistance. Randles cell is the starting point for any other more complex models which represented as a semicircle as given in **Figure 3.11 (I)**, and it is also often seen with an added Warburg element as represented in **Figure 3.11 (II)**.<sup>60</sup>

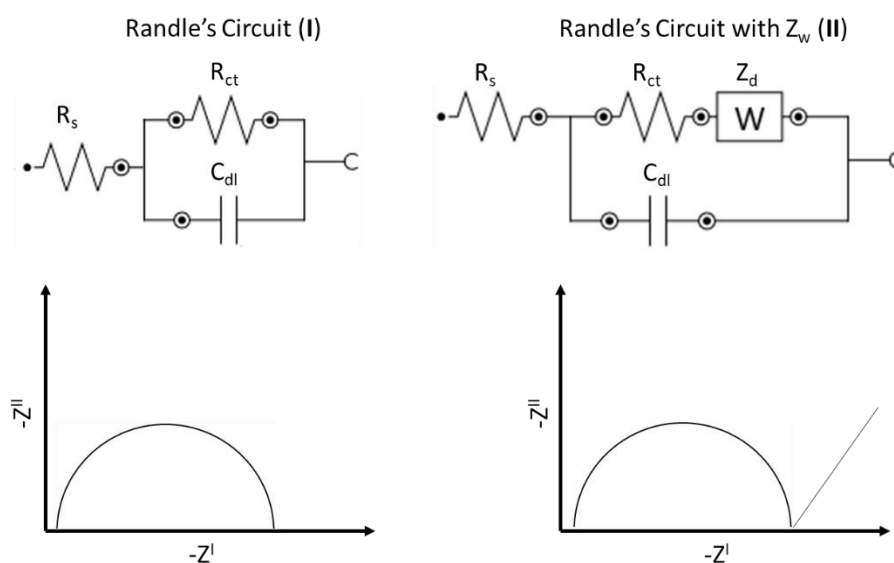


**Figure 3.11** Randles circuit (I) and Randles circuit with Warburg (diffusion) element with their Nyquist plots.

The circuit shown in **Figure 3.12** to model the data in **Figure 3.13** is similar to a study which investigates the film transfer resistance of a formed conducting polymer which also includes diffusion of charge carries, and redox reactions at electrode surface.<sup>61</sup> In the polymer case, a model circuit was prepared as given (A) in **Figure 3.12**, and it assumes a film formation on the substrate along with ionic charged species at the outer part of the substrate (working electrode). The model in A includes many elements, which may not necessarily be appropriate as increasing element complexity can lead to a false improvement in the fit to the data. The model in A was simplified to that in B which is in effect a modified version of Randle's circuit given in C.<sup>61</sup>

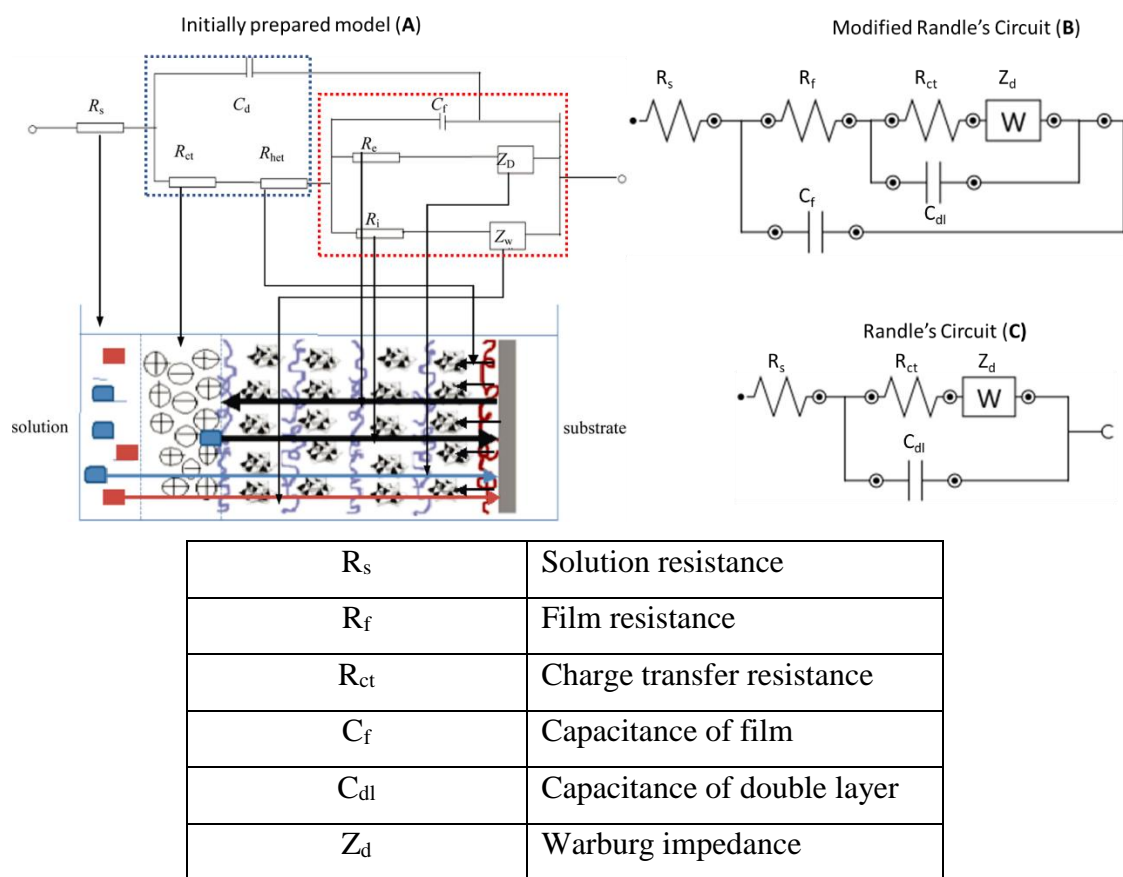


**Figure 3.12** Model used in Vyas to study conducting polymer growth (A), red squares show circuit elements in film region, and blue square represents the circuit elements for moving redox species.<sup>61</sup> Modified Randle's circuit used to fit data in this study.

To study film formation during electrodeposition, electrochemical impedance spectroscopy was used. Zinc deposition was studied at two different molarities as  $0.1 \text{ mol dm}^{-3}$  and  $0.4 \text{ mol dm}^{-3}$  in 1 ChCl: 2 EG. If the reaction mechanisms proposed in reactions in **section 3.2.1** is correct then two processes should be seen using EIS and the size of these responses should change with concentration.

To understand the processes occurring in the deposition of zinc from the 1 ChCl: 2 EG system, a series of electrochemical impedance spectroscopy studies were performed. **Figure 3.13** shows the EIS data for an experiment performed using an applied DC potential of  $-0.4 \text{ V}$  and an AC modulation of  $\pm 10 \text{ mV}$  for two different  $\text{ZnCl}_2$  concentrations;  $0.1$  and  $0.4 \text{ mol.dm}^{-3}$ . At this potential, it is known that UPD occurs in both systems ethylene glycol is not electrochemically reduced.

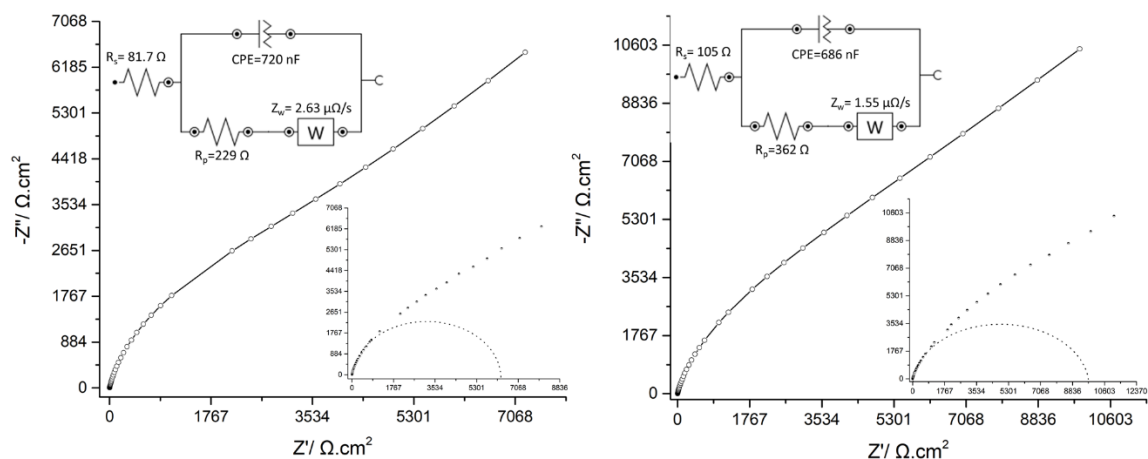


**Figure 3.13** EIS studies of  $0.1 \text{ mol.dm}^{-3} \text{ ZnCl}_2$  in  $1 \text{ ChCl}: 2 \text{ EG}$  (left with  $\chi^2 = 8.9 \times 10^{-2}$  Nyquist fitting error value) and  $0.4 \text{ mol.dm}^{-3} \text{ ZnCl}_2$  in  $1 \text{ ChCl}: 2 \text{ EG}$  (right with  $\chi^2 = 1.3 \times 10^{-2}$  Nyquist fitting error value). Applied potential is  $-0.4 \text{ V}$  at  $40^\circ \text{C}$ . Each graph shows fitted data as the main image, and equivalent circuit with measured values on the left top, and non-fitted data on the right bottom.

**Table 3.3** Quantitative data obtained from fitting the data to the equivalent circuits given in **Figure 3.12 (C)**.

Solution at $-0.4 \text{ V}$	$R_s$ ( $\Omega$ )	$R_p$ ( $\text{k}\Omega$ )	$C_{dl}$ ( $\text{nF.cm}^{-2}$ )	$Z_w$ ( $\mu\Omega.\text{s}^{-0.5}$ )
$0.1 \text{ M ZnCl}_2$ in $1 \text{ ChCl}: 2 \text{ EG}$	81.7	229.0	720.0	2.63
$0.4 \text{ M ZnCl}_2$ in $1 \text{ ChCl}: 2 \text{ EG}$	105.0	362.0	686.0	1.55

The Nyquist plots in **Figure 3.13** show that the responses at the two different concentrations are relatively similar; they both appear to fit a standard model of a parallel RC circuit with an associated Warburg element is due to diffusional impedance. This so-called, Randle's circuit is used as an equivalent circuit to study many simple electrochemical processes. A Randle's circuit consists of an active electrolyte resistance,  $R_s$ , in series with the parallel combination of the double-layer capacitance,  $C_{dl}$ , and an impedance of a Faradaic reaction known as Warburg element. Using an unmodified Randle's circuit is well known for deposition experiments, and in **Figure 3.13**, a good fit is obtained at an applied potential of  $-0.4 \text{ V}$ . This is shown diagrammatically in **Figure 3.13**. **Table 3.3** shows the values for the different elements when the data were fitted to the equivalent circuits. The magnitudes of the different variable are all the correct order of magnitude for these sorts of processes and the values are relatively similar at both

concentrations. This could be interpreted as implying that UPD occurs in the liquid and the rate at which the process occurs is relatively independent of the concentration of electroactive species which would seem logical.

**Figure 3.14** shows the EIS data for an experiment performed using an applied DC potential of -1.1 V and an AC modulation of  $\pm 10$  mV for two different  $\text{ZnCl}_2$  concentrations; 0.1 and 0.4  $\text{mol}\cdot\text{dm}^{-3}$ . At this potential, it is thought that ethylene glycol decomposes concurrently with zinc electrodeposition.

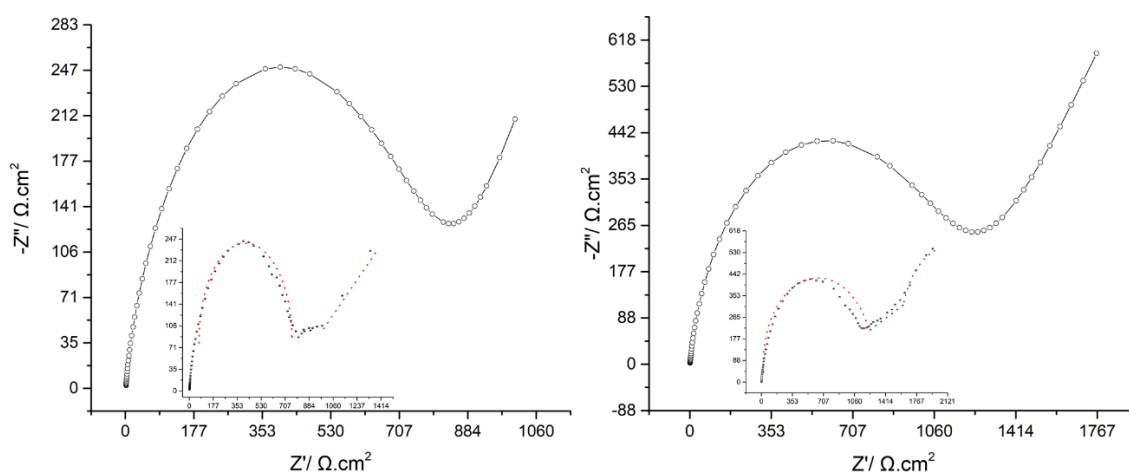


**Figure 3.14** EIS data of left 0.1  $\text{mol}\cdot\text{dm}^{-3}$   $\text{ZnCl}_2$  in 1 ChCl: 2 EG on the left with  $\chi^2 = 0.17$  Nyquist fitting error value, 0.4  $\text{mol}\cdot\text{dm}^{-3}$   $\text{ZnCl}_2$  in 1 ChCl: 2 EG on the right with  $\chi^2 = 5 \times 10^{-2}$  Nyquist fitting error value Applied potential is -1.1 V at 40 °C. Each graph shows fitted data as main image with unfitted graph in the inset.

The Nyquist plots in **Figure 3.14** show that the responses at the two different concentrations are again relatively similar although there is a larger difference in the magnitudes of the x and y axis maxima.

The Nyquist plots in **Figure 3.14** do not fit well to a standard Randle's circuit and there is clearly a second Faradaic process occurring in parallel. An alternative equivalent circuit is proposed as shown in **Figure 3.12 (B)**.<sup>61</sup> The values obtained data by fitting the data in **Figure 3.14** to the circuit in **Figure 3.12 (B)** are given in **Table 3.4**.

**Table 3.4** Calculated circuit elements for the fits of the data in **Figure 3.14** to the circuit in **Figure 3.12 (B)** at two  $ZnCl_2$  concentrations with an applied potential of -1.1 V.

Values	0.1 M	0.4 M
$R_s$	120 $\Omega$	-514 $\Omega$
$R_{(GF)}$	-1620 $\Omega$	707 $\Omega$
$C_{dl(GF)}$	0.41 $\mu F\ cm^{-2}$	1.39 $\mu F\ cm^{-2}$
$R_{ct(Zn)}$	49.7 k $\Omega$	71.7 k $\Omega$
$Z_w$	237.0 $\mu\Omega\ s^{-0.5}$	86.1 $\mu\Omega\ s^{-0.5}$
$C_{dl(Zn)}$	2.36 $\mu F\ cm^{-2}$	0.51 $\mu F\ cm^{-2}$

The magnitudes of the different variable are all of the correct order of magnitude for these sorts of processes.<sup>62</sup> The capacitances of the equivalent circuit can arise due to a double layer charge resulting from a separation of charge at the interface or the build-up of a dielectric film on the electrode surface. The value of the capacitance,  $C$  given in **Equation 3.1**.

$$C = \frac{\epsilon\epsilon_0 A}{d} \quad \text{Equation 3.1}$$

Where  $\epsilon$  is the dielectric constant,  $\epsilon_0$  is a constant and  $d$  is the distance of separation (or the film thickness). It is difficult to know the dielectric constant of a film but given that most transition metal oxides and halides are in the range of 5.3 to 11.2,<sup>63</sup> and value of 8 was assumed for the purposes of this study to be able to determine the magnitude of the film thickness. Using this assumption and the capacitance data from **Table 3.4**, film thicknesses were calculated approximately 8 nm.

The charge transfer resistances in **Table 3.4** are larger for both processes than for the process in **Table 3.3** meaning that the reactions are slower. This would be logical as UPD is generally considered a fast process. Examining the Warburg impedances at -0.4 V and -1.1 V, it can be seen in **Table 3.3** for -0.4 V applied system that 0.1 M has a higher Warburg impedance. It is reasonable because Warburg impedance given in **Equation 3.2** increases with increasing Warburg coefficient given in **Equation 3.3** which is also inversely proportional to the diffusion coefficient. Thus, an increasing Warburg

impedance represents a decrease in diffusion coefficient for same angular frequency system which is the case here. The diffusion coefficient can be related to the Warburg impedance through **Equation 3.2** and **Equation 3.3**.<sup>59</sup>

$$|Z_w| = \frac{\sqrt{2}\sigma}{\sqrt{\omega}} \quad \text{Equation 3.2}$$

$$\sigma = \frac{RT}{n^2 F^2 A \sqrt{2}} \left( \frac{1}{\sqrt{D_O} C_O^b} + \frac{1}{\sqrt{D_R} C_R^b} \right) \quad \text{Equation 3.3}$$

The Warburg impedances were  $237 \mu\Omega \text{ s}^{-0.5}$  in  $0.1 \text{ mol dm}^{-3}$  system and  $86.1 \mu\Omega \text{ s}^{-0.5}$  in the higher concentration system. Assuming all other factors are constant the difference in Warburg impedance can be explained through the difference in concentration which means that the Warburg is not controlled by diffusion through a viscous film on the electrode surface, but rather by diffusion through the same solution with effectively the same viscosity.

In impedance spectroscopy, constant phase elements (CPE) behave as a non-ideal capacitor, and it differs from an ideal capacitor ( $C_{dl}$ ). The electric double layer at the electrode-electrolyte interface almost never shows the behaviour of a pure capacitor, due to frequency dispersion in the EIS response.<sup>64</sup> The main difference between a capacitor  $C$ , and a constant phase element CPE is an additional parameter,  $a$ , as given in **Equation 3.4**. which can have the value between 0 and 1. Clearly its value is 1 for a pure capacitor. This can be as a result of surface roughness or other internal forces ( $C$  is for a pure capacitor and  $Q$  is the capacitor of CPE).<sup>65</sup>

$$Z_Q(f) = \frac{1}{Q(j2\pi f)^a}, \quad Z_C(f) = \frac{1}{Cj2\pi f}, \quad 0 \leq a \leq 1 \quad \text{Equation 3.4}$$

In DESs, and other ionic liquids, the Warburg impedance is thought to result from non-Debye behaviour that these liquids exhibit. Several studies prove the deviation of Debye-Hückel approximations on the ionic liquids.<sup>66, 67</sup>

In the equivalent circuit of EIS study for -1.1 V potential applied system, a film based model was assumed with a glycolate layer on the electrode surface and this occurs simultaneously with the electroreduction the zinc species. The processes occurring at the electrode surface are probably complex and can best be summarised in the schematic diagram in **Figure 3.15**.

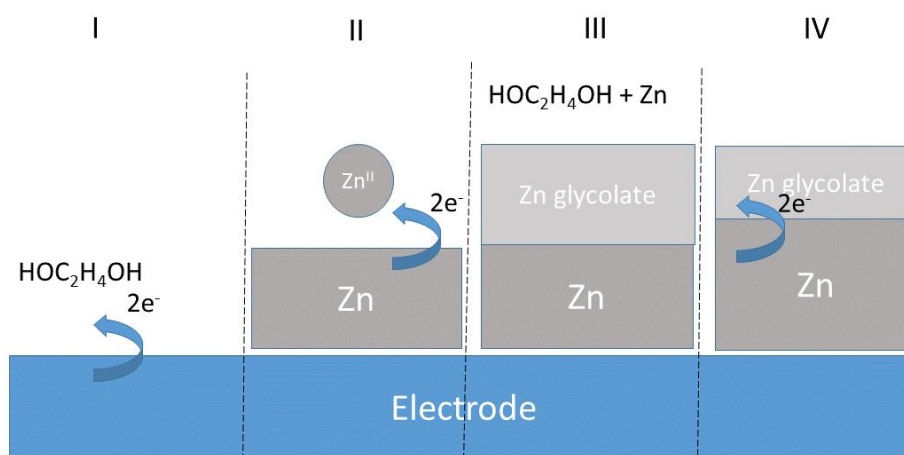


**Figure 3.15** Schematic diagram for the process that could be occurring on the electrode surface during electroreduction of  $\text{ZnCl}_2$  in  $1\text{ChCl}: 2\text{EG}$

Firstly, (I) the electroreduction of ethylene glycol competes with the electroreduction of the zinc species (II). The electroreduction of ethylene glycol will be faster on platinum than on zinc as it is a more electrocatalytic surface. Once the surface is covered with zinc, hydrogen evolution and glycolate production will be comparatively slow.

Zinc glycolate must form on the zinc surface (III). This can either be through reaction of the glycolate anion produced in (I) with zinc in solution or through the reaction of deposited zinc with ethylene glycol. While the former is more likely, then it would result in the complex forming away from the electrode surface, the solution would appear cloudy and the surface would not passivate so it is more likely that it is the latter case.

Once the zinc glycolate has formed there must be a mechanism by which it can be electroreduced (IV). If this did not occur, then the zinc films would be extremely thin. The results from the bulk electrolysis experiments show that zinc platelets with thicknesses  $> 1\ \mu\text{m}$  can be formed. If the zinc growth is occurring through a glycolate film then it would be expected that the process would be relatively slow. Using the

capacitance data in **Table 3.4**, the film thickness is approximately 17 nm for the lower concentration solution, and only 5 nm for the more concentrated solution. This latter value would correspond to a few molecular dimensions (10 to 20) which would seem reasonable.

For the final part of impedance discussion, it is important to comment on the negative  $R_s$  value in the 0.4 mol.dm<sup>-3</sup> system. In general, negative impedance values from steady-state polarization should not be possible. However, in dynamic systems, such as a voltammetric potential sweep, this effect can occur. They are frequently observed in corrosion studies or the systems which exhibit active-passive transitions or transpassivity. They can also appear in steady state systems in which one applied potential corresponds to various current responses.<sup>65</sup> They can also appear for systems which show an increase in potential after the value of peak current ( $di/dE < 0$ ).<sup>68, 69</sup> Studies performed by Koper<sup>70</sup>, Koper and Sluyters,<sup>71</sup> and Krischer and Varela<sup>72</sup> clarified the conditions of negative Faradic impedance with the result of negative resistance which directly support this study. Thus, it is helpful to elaborate on the conditions that result in an apparent negative solution resistance.

The steady state current at an electrode is described by equation **Equation 3.5**.<sup>70</sup>

$$i_f = nFAk_fC \quad \text{Equation 3.5}$$

where,  $A$  is the available electrode area,  $C$  is concentration of the electroactive species, and  $k_f$  represents heterogenous rate constant.

The Faradic impedance is described by equation **Equation 3.6**.<sup>70</sup>

$$Z_F^{-1} = \left( \frac{di_f}{dE} \right)_{E=E_{ss}} \quad \text{Equation 3.6}$$

where  $E_{ss}$  is the stationary state potential. By substituting **Equation 3.5** into equation **Equation 3.6**, **Equation 3.7** is obtained.<sup>70</sup>

$$Z_F^{-1} = nF \left( AC_0 \frac{dk_f(E)}{dE} + Ak_f(E) \frac{dC_0}{dE} + k_f(E)C_0 \frac{dA}{dE} \right) \quad \text{Equation 3.7}$$

In order to have a negative Faradic impedance, and so the negative resistance, the expression in the parentheses should be negative, and this can only happen if one of three conditions is met.<sup>70</sup>

- i. (a) where  $dk_f(E)/dE$  is negative i.e. a heterogenous rate constant decreases with increasing polarization at some potential intervals. For example, if the heterogenous rate constant changes as given below;

$$k_f(\theta, E) = [1 - \theta(E)] k_f(\theta=0, E) + \theta(E) k_f(\theta=1, E)$$

$\theta$  represents the surface coverage which is in effect an inhibitor which can be a passivation film or other side reactions, and in the case of  $k_f(\theta=0, E) \gg k_f(\theta=1, E)$  which means when potential at zero surface coverage is much higher than the potential at the full coverage of surface, so  $dk_f(E)/dE$  becomes negative.

(b) if during the potential dependent-desorption of a catalyst, reaction rate decreases with potential.

- ii. The condition where  $dC(0)/dE < 0$  can also be observed when the electrostatic repulsion of ions in the double layer proceeds strongly because of the Frumkin effect.<sup>73</sup> This effect is explained by the existence of high potential at the outer Helmholtz plane, usually because of low supporting electrolyte concentrations.
- iii.  $dA/dE < 0$ , this case only appears when the available surface area of electrode decreases with increasing polarization due to the formation of a passivation or strongly inhibiting film.

All three of these cases could occur for DESs and result in a negative Faradic impedance as passivation of the zinc is suggested from the results above and would support the data observed here.

### 3.2.4 SEM and XRD Results of Bulk Electrolysis

Bulk electrolysis was carried out in all 6 liquids under comparable temperature, and current density conditions. Morphologies of the deposits were analysed using scanning electron microscopy. A zinc cathode was electrolysed at a constant current density of  $4 \text{ mA cm}^{-2}$  for 120 minutes at  $50 \text{ }^\circ\text{C}$  using a zinc anode. Bulk deposition was carried out using the cell shown in **Figure 3.16** which was made from ABS using a 3D printer.

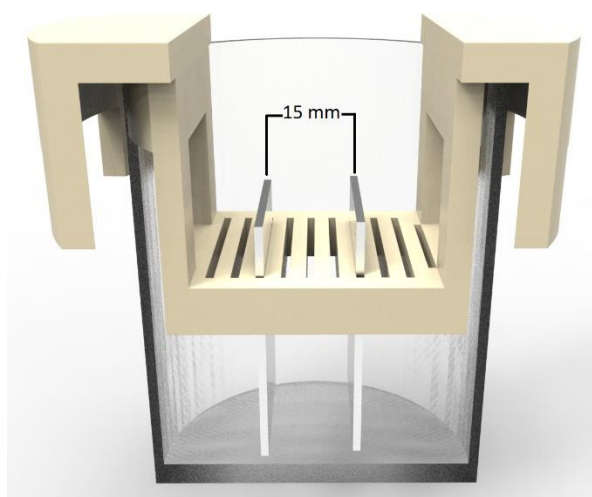


**Figure 3.16** Schematic diagram of the cell used for the bulk electrolysis experiments.

**Figure 3.17** show the SEM images and photographs of zinc coated cathodes. The figure also presents the morphology of the soluble zinc anodes used in the experiments. If an adsorbed layer is affecting the deposit morphology then it could also affect the morphology of the soluble zinc anode. It can be seen from the images in **Figure 3.17** that the zinc morphology is very different in each of these liquids. In the liquids where there is a high chloride activity (1 ChCl: 2 EG and 1 ChCl: 2 urea) the zinc grows as either platelets or small grains. In the liquids with a low or no chloride activity (1 ChCl: 2  $\text{ZnCl}_2$  and  $\text{ZnCl}_2$ : 4 urea) then large nodular crystals form.

The zinc nitrate-based eutectics both produced diffuse deposits made up of much smaller crystallites which were different in appearance to the deposits from any of the  $\text{ZnCl}_2$  based DESs. EDX analysis of the deposits in **Figure 3.18**, show there is a high oxygen content with clear signs of zinc oxide forming by reaction with the water or nitrate. Analysis of the zinc anode also shows the formation of zinc oxide on the anode surface.

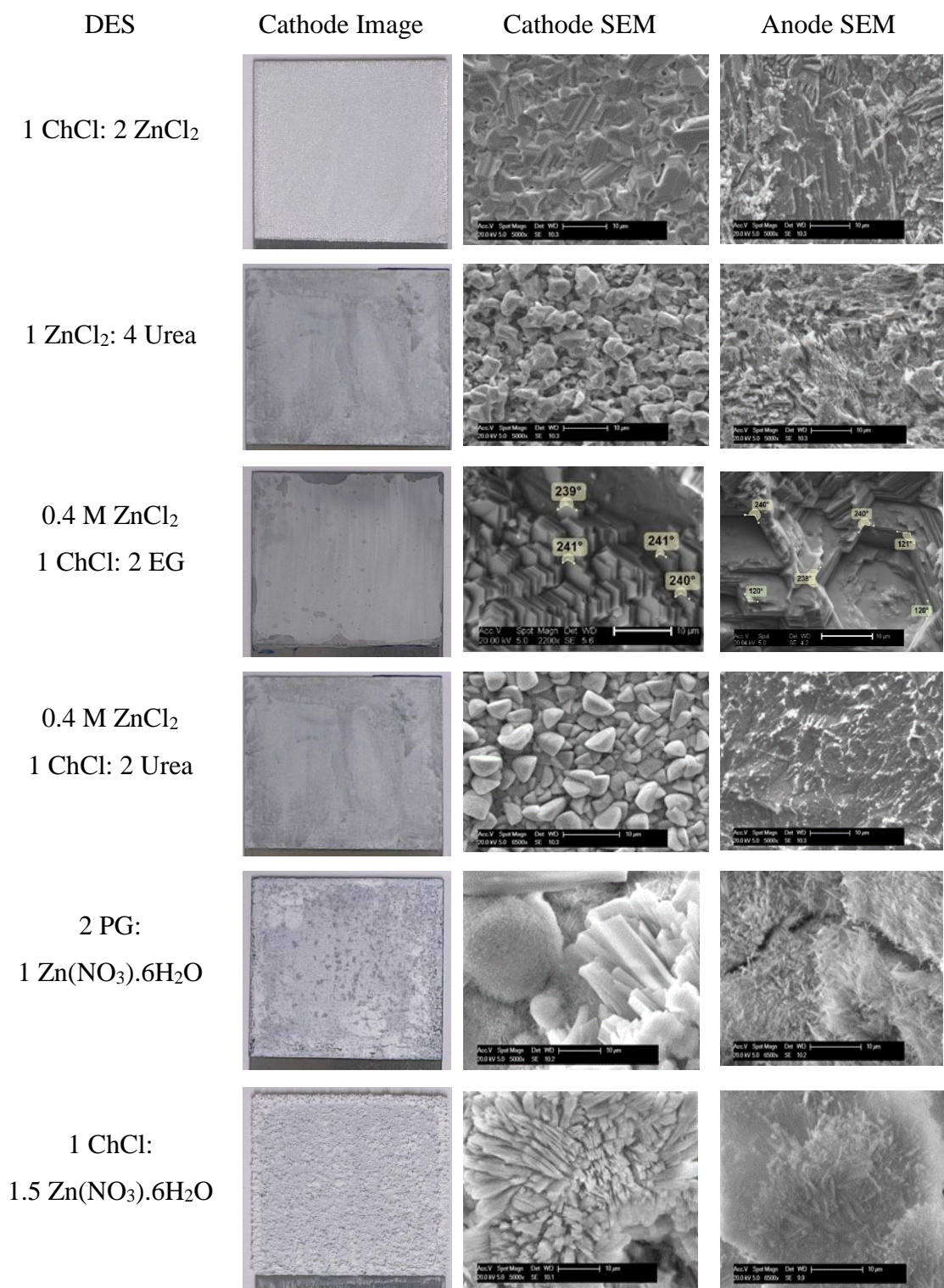


**Figure 3.17** Optical images of 2cm x 2cm samples, and SEM images of the morphology of the cathode and anode after deposition using a constant current density of 3.0 mA cm<sup>-2</sup> at 40 °C for 120 minutes.

XRD analysis of the zinc deposits given in *Figure 3.17* shows that different crystal growth is supported in different liquids as shown in *Figure 3.19*. There are numerous crystal faces that form but the three dominants in most deposits are the (002), (100) and (101) faces.

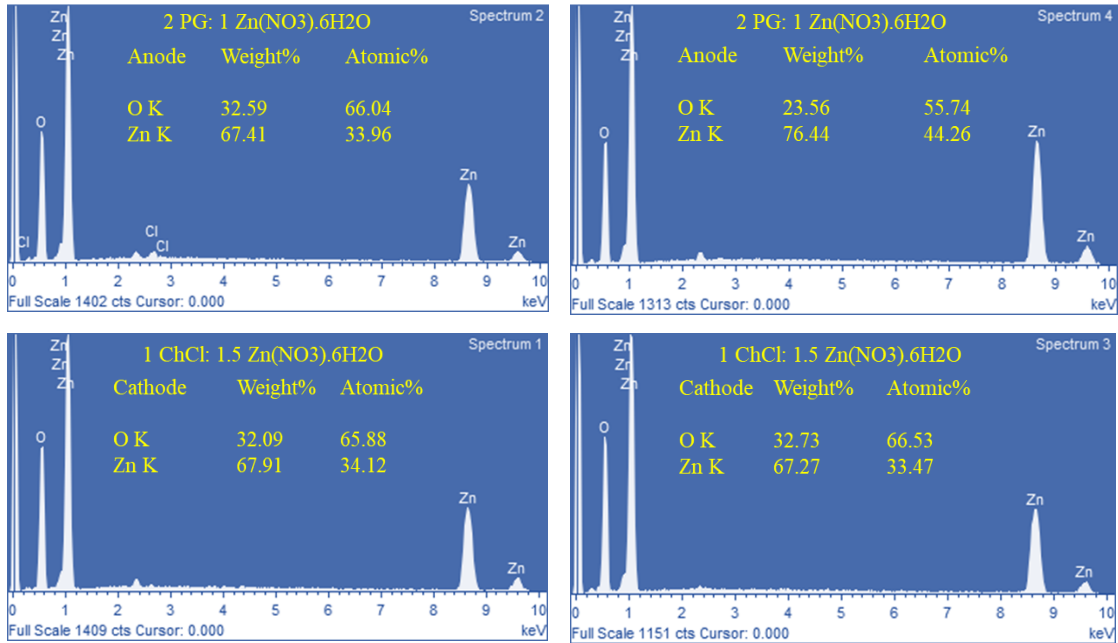


**Figure 3.18** EDX analysis of 2 PG: 1 Zn(NO<sub>3</sub>).6H<sub>2</sub>O and 1 ChCl: 1.5 Zn(NO<sub>3</sub>).6H<sub>2</sub>O for samples given in *Figure 3.17*.

In 1 ChCl: 2EG, and 1 ChCl: 2 urea the (101) faces dominate and there is almost no (002) present whereas in 1 ChCl: 2 ZnCl<sub>2</sub> (002) is dominant with some (101) present. The deposit obtained from ZnCl<sub>2</sub>: 4 urea has (002), (100) and (101) all present.

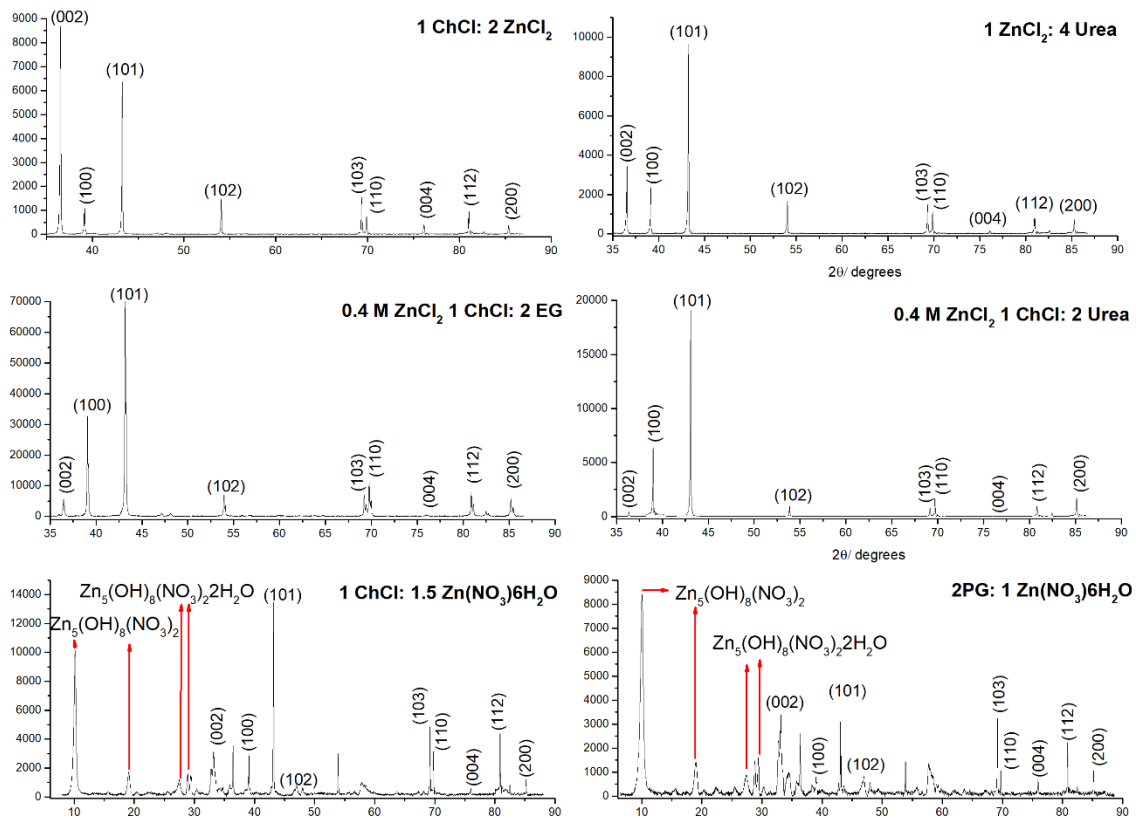


**Figure 3.19** XRD analysis results of the Zn deposits of those SEM images are shown in **Figure 3.17**, using a constant current density of  $3.0 \text{ mA cm}^{-2}$  at  $40^\circ\text{C}$  for 120 minutes.

The results for 1 ChCl: 2EG, and 1 ChCl: 2 urea tend to suggest that the film formation is anisotropic and not just due to a precipitation on the electrode surface. If an insoluble film is being formed on the cathode surface, then it would be expected that increasing the temperature would increase solubility and decrease film formation and accordingly change the deposit morphology.

**Figure 3.20** shows the photographs and SEM images of the zinc deposits obtained using  $0.4 \text{ mol dm}^{-3} \text{ ZnCl}_2$  in 1 ChCl: 2EG with a current density of  $3 \text{ mA.cm}^{-2}$  after electrolysis for 120 min at  $40$ ,  $65$  and  $90^\circ\text{C}$ . It can clearly be seen that the deposit morphology changes significantly as the temperature is increased. At low temperatures,  $40^\circ\text{C}$ , the hexagonal platelet morphology is obtained presumably due to the formation of an insoluble layer on the electrode surface. At higher temperatures, the morphology changes. At  $65^\circ\text{C}$  larger, irregular grains are formed. At  $90^\circ\text{C}$  the deposit becomes less crystalline. The deposit is darker, presumably because more light is scattered from the surface.

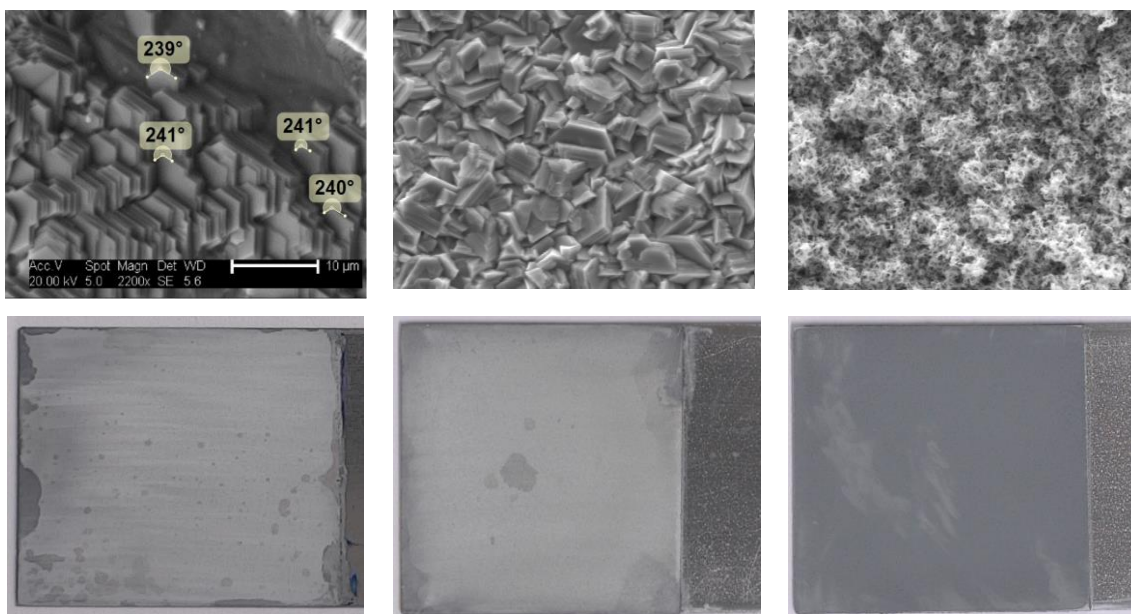


**Figure 3.20** Photographs and SEM images of the zinc deposits obtained using  $0.4 \text{ mol dm}^{-3} \text{ ZnCl}_2$  in  $1 \text{ ChCl} : 2 \text{ EG}$  with a current density of  $3 \text{ mA.cm}^{-2}$  after electrolysis for 120 min at 40, 65 and 90 °C.

**Figure 3.21** shows the XRD data of zinc deposited in **Figure 3.20** at three temperatures. In all the systems, the (101) signal dominates.

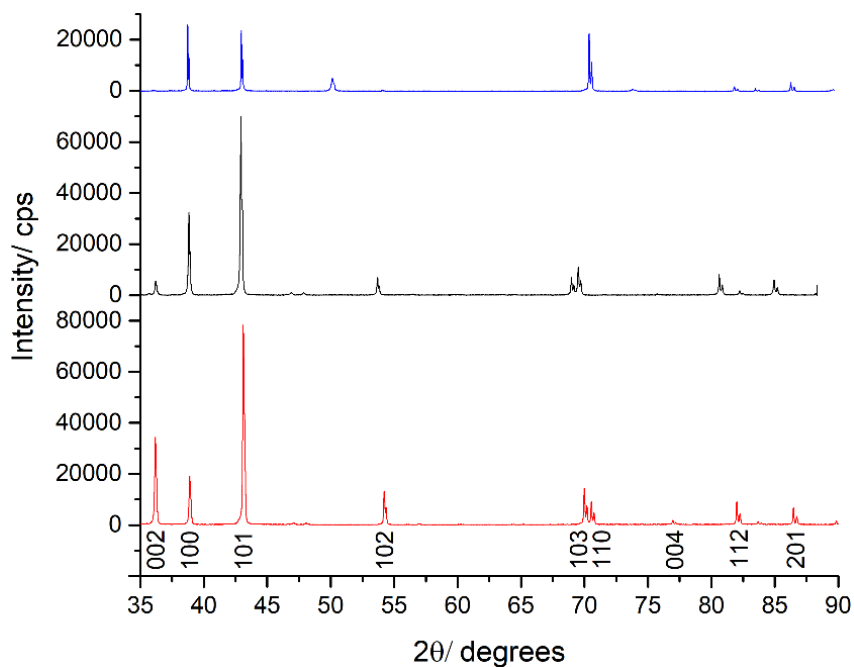


**Figure 3.21** XRD analysis of zinc deposited samples given in **Figure 3.20** red represents the system deposited at 90 °C, black that at 65 °C and blue that at 40 °C.

If these ideas are translated to other metals which have recently been studied in these liquids, there are several general trends that can be concluded.

- Non-oxophilic metals such as copper, silver and gold are reduced at potentials which do not compete with eutectic decomposition. There is no film formation on metal reduction and the deposit morphology is relatively unaffected by the eutectic chosen.
- More oxophilic metals such as Zn, Fe, Co and Ni behave similarly and there is the potential to form films on the metal surface particularly where water or ethylene glycol are involved. At low metal concentrations, decomposition of the eutectic can compete with the metal deposition and film formation affects the morphology and deposition rate of the metal.
- Film formation can be decreased by working at higher temperatures and higher metal ion concentrations. This increases the rate of the deposition process with respect to the eutectic decomposition and the increased temperature increases the solubility of any film formed.
- Brighteners appear to work if they form a solvophobic layer at the electrode-solution interface which can decrease the rate of the eutectic decomposition and decrease film formation.
- While this study may seem specific to eutectic formulations, the same is valid for metal deposition from aqueous solutions and the main aim to obtaining bright, thick deposits is to increase the rate of metal deposition and decrease the rate of competing reactions leading to film formation.

### **3.3 Anodic Dissolution of Zinc**

In Chapter 4 of this thesis powder pulse plating will attempt to dissolve zinc powder and then plate it back on to the electrode surface. For this to be successful the zinc dissolution will need to be reversible. *Figure 3.21* suggests that all the zinc chloride based eutectics are reversible although the results in section 3.2 suggest that the 1ChCl: 2EG system may be only partially reversible.

Studying the redox chemistry of zinc on a Pt electrode is different to how a zinc particle will behave as there is a far larger reservoir of zinc in the latter. **Figure 3.22** shows the electrochemistry of a zinc working electrode at in 1ChCl: 2EG, and (right) a Pt electrode in 1ChCl: 2EG containing  $0.3 \text{ mol dm}^{-3} \text{ ZnCl}_2$  both at  $45^\circ \text{C}$ .

With a zinc working electrode in 1ChCl: 2EG, on the anodic sweep oxidation starts to occur at  $-1.25 \text{ V}$ , there is an increase in the current at  $-0.8 \text{ V}$  and a peak is observed at  $-0.6 \text{ V}$ . The decrease in current is characteristic of a passivation process and following a minimum at  $-0.5 \text{ V}$  the current increases to a maximum at  $+0.75 \text{ V}$ . The increase in current after  $-0.5 \text{ V}$  is characteristic of what is known as trans-passive corrosion where dissolution occurs through a passive film. This has been observed for a variety of metals in DESs but was not seen for zinc.<sup>1</sup>

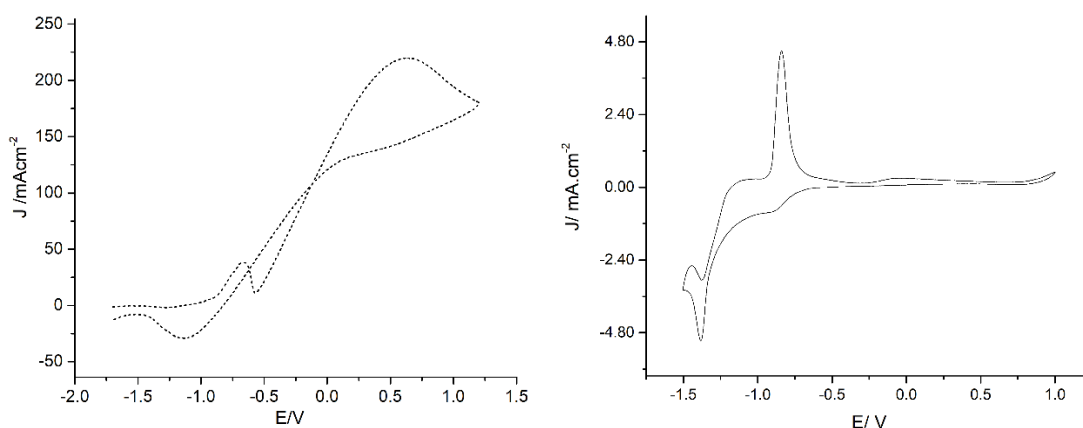


**Figure 3.22** Cyclic voltammograms of (left) zinc working electrode (Ag/AgCl RE, and Pt CE) at  $45^\circ \text{C}$  with sweep rate of  $50 \text{ mVs}^{-1}$  in 1 ChCl: 2 EG, and (right) Pt electrode (Ag/AgCl RE, and Pt CE) in 1 ChCl: 2 EG containing  $0.3 \text{ mol dm}^{-3} \text{ ZnCl}_2$  in 1 ChCl: 2 EG at  $45^\circ \text{C}$  with sweep rate of  $20 \text{ mV.s}^{-1}$ .

The anodic dissolution was previously studied by Karim<sup>15</sup> in 1ChCl: 2 EG using linear sweep voltammetry and EIS. **Figure 3.23** shows the EIS and LSV data from Karim's study. It was originally concluded that unlike the other 8 metals studied the anodic current from the LSV was not characteristic of a passivation process, so it was assumed that the zinc complex was soluble.

The published study was carried out at  $5 \text{ mV s}^{-1}$  but analysing the data obtained at higher sweep rates ( $50 \text{ mV s}^{-1}$ ) a response more typical of passivation is obtained. The result in **Figure 3.22** is like that reported in **Figure 3.23** and the significant dependence of the current on sweep rate is what would be expected for a slow film formation.

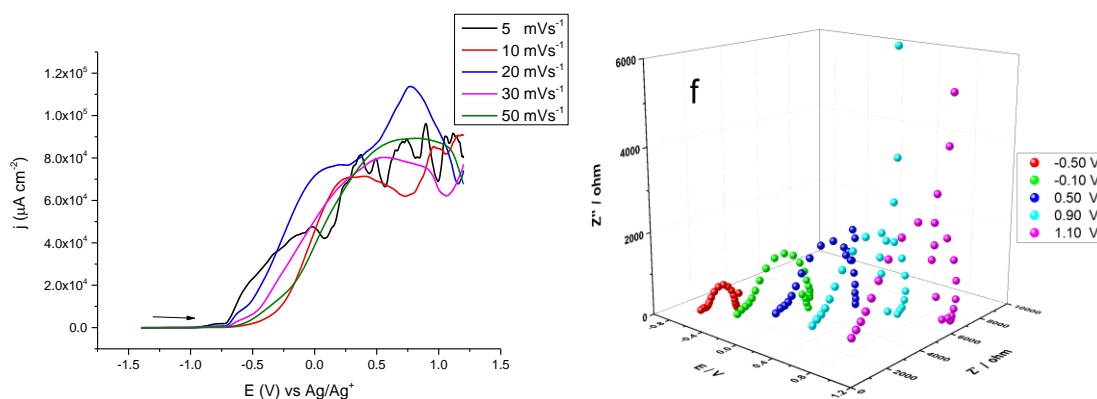


**Figure 3.23** LSV (left) and EIS (right) for the electro-dissolution of Zn in  $1\text{ChCl}: 2\text{EG}$  at  $25^\circ\text{C}$  taken from the literature.<sup>1</sup>

In hindsight, it is evident that a resistive film is forming on the zinc surface during anodic polarisation. This will affect the anodic pulse size and duration that can be applied in the next chapter. If a passivation film grows on the electrode during the anodic pulse, then it will affect the growth of metal on the cathodic pulse.

The anodic dissolution of zinc was studied using optical microscopy. **Figure 3.24** shows optical images of a zinc working electrode following a potential step of 1 V as a function of time.

Initially the zinc surface brightens as zinc dissolves but after about 2 s the electrode turns white and then after 10 s the solution above the electrode becomes cloudy. This is because the zinc concentration has exceeded the solubility.

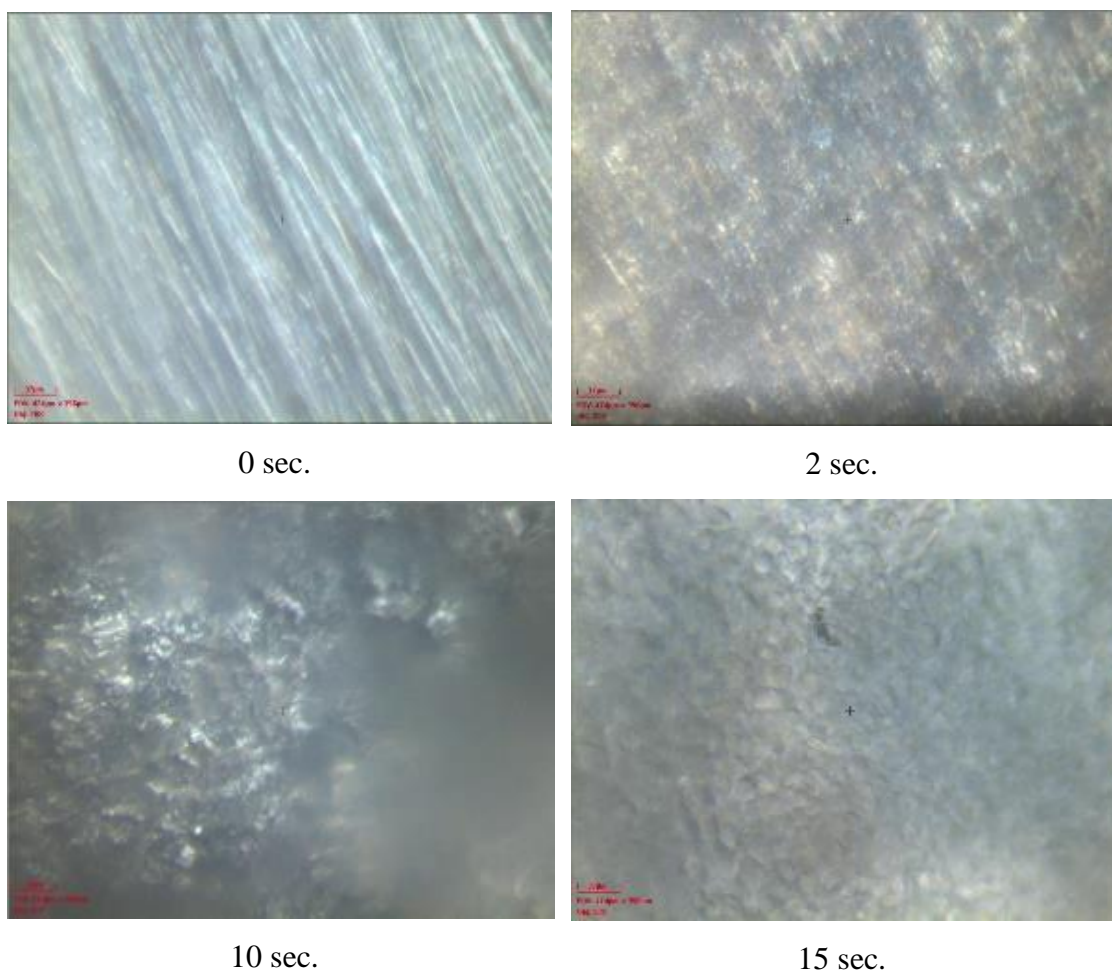


**Figure 3.24** Optical images of a zinc working electrode (Ag/AgCl RE, and Pt CE) at 45 °C following a potential step of 1.0 V as a function of time.

The amount zinc dissolved can be approximate from the charge passed. A pulse of 5 s consumes approximately 0.00892 C charge on 1mm diameter electrode which results in  $5.885 \times 10^{-6}$  moles  $\text{cm}^{-2}$  of Zn being oxidised. The exact diffusion coefficient of the complex is not known, but it should have a value similar to that of  $\text{CuCl}_4^{2-}$  which was found to be  $2.47 \times 10^{-7} \text{ cm}^2\text{s}^{-1}$  using cyclic voltammetry (see appendix). The zinc species can diffuse a maximum of 6.269  $\mu\text{m}$  in that time. ( $\langle x \rangle = (Dt/\pi)^{1/2}$ ). That makes an average concentration of zinc in the layer close to the electrode surface of  $9.38 \times 10^{-3} \text{ mol cm}^{-3}$  or  $9.38 \text{ mol dm}^{-3}$ . This exceeds the solubility for  $\text{ZnCl}_2$  and it is therefore not surprising that after this time the solution becomes cloudy and the electrode surface turns white. This is important for the next chapter as it means that the anodic pulse for the dissolution of zinc must not be too long so that the solution becomes saturated otherwise the deposition step will become irreversible.

### 3.4 Conclusions

This study has shown that the deposits formed from the electroreduction of zinc based eutectics differ significantly depending upon the composition of the liquid. The morphology can range from large nodular grains through flat planar hexagonal structures to small, almost amorphous structures. The structures appear to be strongly influenced by the type of ionic liquid. It was shown that film formation appears to be a significant issue when oxygen containing ligands are available to react with the zinc surface.

In  $\text{ChCl}:\text{ZnCl}_2$  deposition is reversible and large granular deposits are obtained. For the  $\text{ZnCl}_2:4$  urea eutectic smaller but still angular deposits were observed. In both cases the (002) crystal phase is prevalent. There was negligible carbon or oxygen content in the deposits.

The system  $1\text{ChCl}:2$  EG was studied in detail as this showed the largest changes in deposit morphology. This was thought to be due to the formation of zinc glycolate films. EDX shows the presence of both carbon and oxygen in the deposit. The (002) phase is suppressed and the (101) phase dominates resulting in flat, hexagonal crystals. The morphology is strongly affected by the temperature and this is thought to be due to changes in the film solubility. Increasing the temperature increases the (002) phase with respect to the (101) phase and results in a change in the size and shape of the crystallites. The zinc nitrate based eutectics had a different type of passivating film which is much thicker, resulting in an irreversible deposition.

Voltammetry shows that the onset potential for reduction is affected by speciation. The electrodeposition is fully reversible in eutectics which do not have an oxygen donating ligand for the metal. Oxygen containing films significantly affect the reversibility of the deposition process. This will be seen to be important in the next chapter where pulse plating is used.

Anodic polarisation of a zinc electrode shows that zinc dissolves readily, but the high viscosity of the liquid means that the solution close to the electrode surface rapidly becomes saturated in zinc. An insoluble complex form on the electrode surface which passivates the zinc surface. This is also important for the next chapter as it is important

that the anodic pulses are not too long so that the surface will become coated. This will affect the reversibility of the pulse and the morphology of the deposit. Optical microscopy shows that the solution becomes saturates in less than 5 s. This will clearly depend upon the operating temperature and any forced mass transport in the liquids.

### 3.5 References

1. A. P. Abbott, G. Frisch, J. Hartley, W. O. Karim and K. S. Ryder, *Progress in Natural Science: Materials International*, 2015, **25**, 595-602.
2. D. S. Silvester, E. I. Rogers, R. G. Compton, K. J. McKenzie, K. S. Ryder, F. Endres, D. MacFarlane and A. P. Abbott, in *Electrodeposition from ionic liquids*, eds. F. Endres, A. Abbott and D. MacFarlane, John Wiley & Sons, Weinheim, 2 edn., 2017, pp. 287-345.
3. A. P. Abbott, G. Frisch, J. Hartley and K. S. Ryder, *Green Chemistry*, 2011, **13**, 471.
4. A. P. Abbott, G. Frisch, S. J. Gurman, A. R. Hillman, J. Hartley, F. Holyoak and K. S. Ryder, *Chemical Communications*, 2011, **47**, 10031-10033.
5. A. C. West, C. C. Cheng and B. C. Baker, *Journal of The Electrochemical Society*, 1998, **145**, 3070-3074.
6. S. Roy, A. Connell, M. Ludwig, N. Wang, T. O'Donnell, M. Brunet, P. McCloskey, C. ÓMathúna, A. Barman and R. J. Hicken, *Journal of Magnetism and Magnetic Materials*, 2005, **290–291, Part 2**, 1524-1527.
7. A. Gomes and M. I. da Silva Pereira, *Electrochimica Acta*, 2006, **51**, 1342-1350.
8. M. S. Chandrasekar and M. Pushpavanam, *Electrochimica Acta*, 2008, **53**, 3313-3322.
9. H. Adelkhani and M. R. Arshadi, *Journal of Alloys and Compounds*, 2009, **476**, 234-237.
10. Y. Boonyongmaneerat, S. Saenapitak and K. Saengkiattiyut, *Journal of Alloys and Compounds*, 2009, **487**, 479-482.
11. K. S. Kumar, K. Biswas and R. Balasubramaniam, *J Nanopart Res*, 2011, **13**, 6005-6012.
12. M. S. P. Chandrasekar, Malathy, *J Solid State Electrochem*, 2014, **53**, 3313-3322.
13. M. Pourbaix, *Atlas of electrochemical equilibria in aqueous solutions*, National Association of Corrosion Engineers, Texas, USA, 1974.
14. M. Matlosz, *Electrochimica Acta*, 1995, **40**, 393-401.
15. W. O. Karim, PhD thesis, University of Leicester, 2016.
16. M. I. Ismail, *J Appl Electrochem*, 1979, **9**, 471-473.
17. B. Du and I. Ivar suni, *J Appl Electrochem*, 2004, **34**, 1215-1219.

18. M. T. Alam, M. M. Islam and T. Ohsaka, in *Electrochemical Properties and Applications of Ionic Liquids*, eds. A. A. J. Torriero and M. J. A. Shiddiky, Nova Science Publishers, USA, 2011, ch. 47-124.
19. R. Hayes, N. Borisenko, M. K. Tam, P. C. Howlett, F. Endres and R. Atkin, *The Journal of Physical Chemistry C*, 2011, **115**, 6855-6863.
20. A. P. Abbott, J. C. Barron, G. Frisch, S. Gurman, K. S. Ryder and a. Fernando Silva, *Physical chemistry chemical physics : PCCP*, 2011, **13**, 10224-10231.
21. S. J. Bryant, R. Atkin and G. G. Warr, *Langmuir*, 2017, **33**, 6878-6884.
22. B. Dilasari, Y. Jung, J. Sohn, S. Kim and K. Kwon, *International Journal of Electrochemical Science*, 2016, **11**, 1482-1495.
23. M. R. Ali, A. Nishikata and T. Tsuru, *Electrochimica Acta*, 1997, **42**, 2347-2354.
24. A. P. Abbott, G. Capper, K. J. McKenzie and K. S. Ryder, *Electrochimica Acta*, 2006, **51**, 4420-4425.
25. A. P. Abbott, G. Capper, K. J. McKenzie, A. Glidle and K. S. Ryder, *Physical Chemistry Chemical Physics*, 2006, **8**, 4214-4221.
26. A. P. Abbott, A. Ballantyne, R. C. Harris, J. A. Juma and K. S. Ryder, *Physical Chemistry Chemical Physics*, 2017, **19**, 3219-3231.
27. A. P. Abbott and K. J. McKenzie, *Physical chemistry chemical physics : PCCP*, 2006, **8**, 4265-4279.
28. G. F. Andrew P. Abbott, and Karl S. Ryder, *Annual Review of Materials Research*, 2013, **43**, 1-24.
29. X. Xie, X. Zou, X. Lu, C. Lu, H. Cheng, Q. Xu and Z. Zhou, *Applied Surface Science*, 2016, **385**, 481-489.
30. L. Vieira, Schennach, R, Gollas, B., *Electrochimica Acta*, 2016, **197**, 344-352.
31. J. A. Juma, PhD thesis, University of Leicester, 2016.
32. A. P. Abbott, A. I. Alhaji, K. S. Ryder, M. Horne and T. Rodopoulos, *Transactions of the IMF*, 2016, **94**, 104-113.
33. S. Ghosh and S. Roy, *Surface and Coatings Technology*, 2014, **238**, 165-173.
34. A. Ispas and A. Bunda, *Electrochem. Soc. Interface*, 2014, **23**, 47-51.
35. A. P. Abbott, R. C. Harris, Y.-T. Hsieh, K. S. Ryder and I.-W. Sun, *Physical chemistry chemical physics : PCCP*, 2014, **16**, 14675-14681.

36. T. Jiang, M. C. Brym, G. Dubé, A. Lasia and G. Brisard, *Surface and Coatings Technology*, 2006, **201**, 10-18.
37. Q. Zhang, Q. Wang, S. Zhang and X. Lu, *Journal of Solid State Electrochemistry*, 2013, **18**, 257-267.
38. A. Abdullah, PhD thesis Doctor of Philosophy, University of Leicester, 2014.
39. A. P. Abbott, G. Capper, K. J. McKenzie and K. S. Ryder, *Journal of Electroanalytical Chemistry*, 2007, **599**, 288-294.
40. J. C. Barron, PhD thesis, University of Leicester, 2009.
41. Z. Liu, S. Z. E. Abedin and F. Endres, *Electrochimica Acta*, 2013, **89**, 635-643.
42. S.-I. Hsiu, J.-F. Huang, I. W. Sun, C.-H. Yuan and J. Shiea, *Electrochimica Acta*, 2002, **47**, 4367-4372.
43. Y. Lin and I. Sun, *Electrochimica acta*, 1999, **44**, 2771-2777.
44. A. P. Abbott, G. Capper, D. L. Davies, H. Munro, R. K. Rasheed and V. Tambyrajah, in *Ionic Liquids as Green Solvents*, American Chemical Society, 2003, vol. 856, ch. 35, pp. 439-452.
45. A. P. Abbott, J. C. Barron and K. S. Ryder, *Transactions of the IMF*, 2009, **87**, 201-207.
46. A. P. Abbott, J. C. Barron, G. Frisch, K. S. Ryder and A. F. Silva, *Electrochimica Acta*, 2011, **56**, 5272-5279.
47. A. P. Abbott, G. Capper, B. G. Swain and D. A. Wheeler, *Transactions of the IMF*, 2005, **83**, 51-53.
48. E. L. Smith, A. P. Abbott and K. S. Ryder, *Chemical Reviews*, 2014, **114**, 11060-11082.
49. A. P. Abbott, G. Capper, D. L. Davies and R. Rasheed, *Inorganic chemistry*, 2004, **43**, 3447-3452.
50. A. P. Abbott, J. C. Barron, K. S. Ryder and D. Wilson, *Chemistry – A European Journal*, 2007, **13**, 6495-6501.
51. A. P. Abbott, G. Capper, D. L. Davies, R. K. Rasheed and V. Tambyrajah, *Chem comm*, 2003, 70-71.
52. F. Endres, A. Abbott and D. MacFarlane, *Electrodeposition from ionic liquids*, John Wiley & Sons, Weinheim, 2 edn., 2017.
53. A. P. Abbott, G. Capper, D. L. Davies and R. K. Rasheed, *Chemistry – A European Journal*, 2004, **10**, 3769-3774.

54. A. P. Abbott, A. Ballantyne, R. C. Harris, J. A. Juma, K. S. Ryder and G. Forrest, *Electrochimica Acta*, 2015, **176**, 718-726.
55. A. P. Abbott, G. Frisch, H. Garrett and J. Hartley, *Chemical communications (Cambridge, England)*, 2011, **47**, 11876-11878.
56. A. P. Abbott, S. S. M. Alabdullah, A. Y. M. Al-Murshedi and K. S. Ryder, *Farad Discuss*, 2017, **in press**.
57. A. Hubin, D. Gonnissen, W. Simons and J. Vereecken, *Journal of Electroanalytical Chemistry*, 2007, **600**, 142-150.
58. C. Zhu, A. Osherov and M. J. Panzer, *Electrochimica Acta*, 2013, **111**, 771-778.
59. A. J. Bard and L. R. Faulkner, in *Electrochemical methods: fundamentals and applications*, John Wiley & Sons, Inc., New York, 2001, pp. 28-29.
60. Andrzej Lasia, in *Electrochemical Impedance Spectroscopy and its Applications*, Springer, New York, USA, 2014, vol. 4, pp. 94-106.
61. R. N. Vyas and B. Wang, *International Journal of Molecular Sciences*, 2010, **11**.
62. M. Lyons, *Electroactive Polymer Electrochemistry: Part 1: Fundamentals*, Springer Science & Business Media, New York, 2013.
63. W. M. Haynes, *CRC Handbook of Chemistry and Physics*, CRC Press, 91st edn., 2010.
64. P. Córdoba-Torres, T. J. Mesquita and R. P. Nogueira, *The Journal of Physical Chemistry C*, 2015, **119**, 4136-4147.
65. A. Lasia, *Electrochemical Impedance Spectroscopy and its Applications*, Springer New York Heidelberg Dordrecht London, New York, 2014.
66. A.A. Lee, D. Vella, S. Perkin and A. Goriely, *The Journal of Physical Chemistry Letters*, 2015, **6**, 159-163.
67. L. M. Varela, M. García and V. c. Mosquera, *Physics Reports*, 2003, **382**, 1-111.
68. A. Sadkowsky, M. Dolata and J. P. Diard, *Journal of The Electrochemical Society*, 2004, **151**, E20-E31.
69. A. Sadkowsky, J.-P. Diard and C. Montella, *Journal of The Electrochemical Society*, 2009, **156**, F7-F13.
70. M. Koper, *Electrochimica Acta*, 1992, **37**, 1771-1778.
71. M. Koper and J. Sluyters, *Journal of Electroanalytical Chemistry*, 1993, **352**, 51-64.
72. K. Krischer and H. Varela, in *Handbook of Fuel Cells*, eds. W. Vielstich, A. Lamm and H. A. Gasteiger, John Wiley & Sons, Inc., New York, 2003, vol. 2, p. 2.

73. A. J. Bard and L. R. Faulkner, in *Electrochemical Methods: Fundamentals and Applications*, John Wiley & Sons, Inc., New York, 2001, vol. 38, ch. 2, p. 53.

**Chapter-IV**  
**Zinc Powder Deposition**

## 4.1 Introduction

This chapter aims to demonstrate a unique idea for the electrodeposition of zinc. By placing a zinc powder in electrical contact with an electrode and pulsing the potential, the aim is to fuse the metal powders layer by layer onto the substrate. The project will also use DC power supplies to electrodeposit zinc metal from the bulk solution to compare the two techniques. The aim is to ascertain whether super-efficient electrodeposition (current efficiency  $> 100\%$ ) can be obtained. In this study the term current efficiency is a measure of the mass of metal deposited with respect to the charge passed (Faradaic efficiency). While other aspects need to be considered (anodic charge). This current efficiency measure gives a useful comparison with the standard electrochemical efficiency.

The project will focus on the DES 1ChCl: 2EG, despite the issues raised in the previous chapter. It should be appreciated that this section of work was carried out at the start of the project. This chapter investigates the electrochemistry of a single zinc crystal using cyclic voltammetry and shows its similarities to bulk zinc dissolution and deposition. It also determines the optimum conditions for pulse dissolution and deposition. The bulk of this section investigates practical methods of contacting the powder with the electrode and highlights how novel cell design has been a significant challenge in this project. Once the optimum cell configuration was produced super-efficient deposition could be demonstrated. The final part used alumina and silicon carbide as model dispersed phases to demonstrate how composite materials can be deposited by this technique.

## 4.2 Pulse Electrodeposition (PED) and Pulse Reverse Deposition (PRD)

Electroplating is usually carried out with a direct current, DC source. This can either be applied using a constant potential or a constant current. In most practical plating systems, a constant current is used. An alternative approach is to use a modulation of the DC source. This is usually referred to as a pulsed current, (PC). There are a wide variety of pulsed forms which have been studied and some of these are shown schematically in *Figure 4.1*. Although modulated current techniques have been used for long time, pulse reverse current, PRC plating, (example F) has been the most commonly studied due to its better levelling results. It was occasionally applied for cyanide, and sulphate baths in the 1940s and 1960s.<sup>1, 2</sup> Unfortunately, in spite of PRC being a promising technique, the lack

of appropriate current sources as well as prohibitive costs hampered further widespread use for the next 50 years.<sup>3</sup>

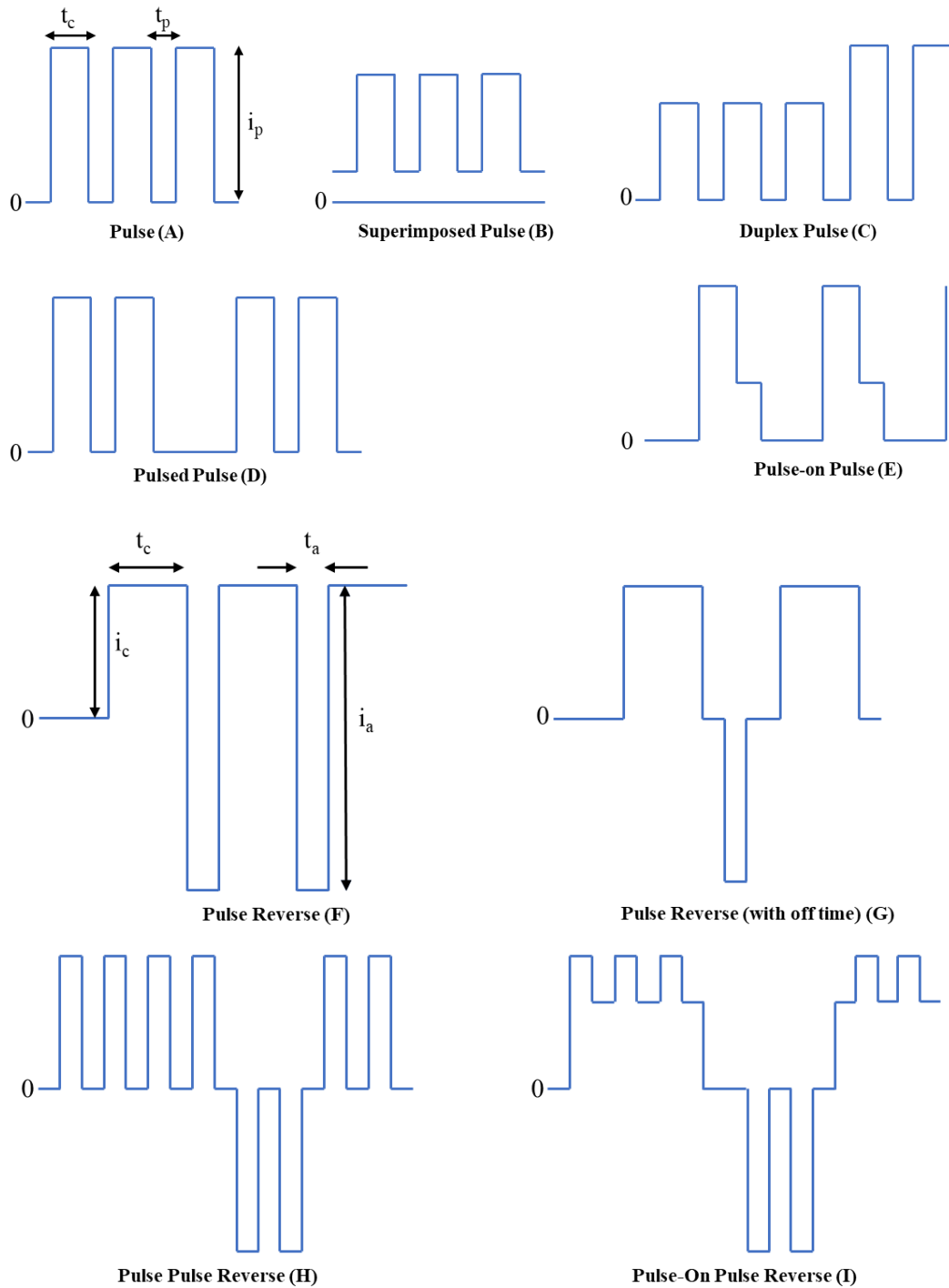


**Figure 4.1** Unipolar PC (up), and bipolar PRC (down) waveforms

Periodically reversed, and pulsed current received increased interest when it was shown to be superior for gold deposition in certain applications by decreasing porosity,<sup>4-6</sup> increasing adhesion,<sup>7-9</sup> brightness,<sup>10, 11</sup> and improving hardness.<sup>12, 13</sup> Along with

development in microprocessor technology, programming of applied current waves in complex forms became easier. Although square waves are the simplest waveforms to produce, sequences of pulses can be programmed to obtain quite complex waveforms.<sup>3</sup> <sup>14</sup> Applied waveforms can be divided into two major groups as unipolar pulses, and bipolar pulses. While bipolar pulses allow cathodic and anodic pulses to be arranged separately, unipolar pulses flow only in one direction. While complex waveforms can be created, it is difficult to understand the outcomes of waveforms, and therefore, most of the literature has mainly focused on unipolar or bipolar waveforms.<sup>3</sup>

In pulse electrodeposition (PED), either potential or current can be alternated between two different values with the result of equal amplitude pulse series in which zero current separates potential and current, and known  $t_{OFF}$  time.<sup>15-17</sup> Pulse amplitude and width make it possible to control deposit film composition and thickness on the atomic order.<sup>18-21</sup> By applying pulse sequences, initiation of grain nuclei can be favoured with the result of increased number of grains per unit area.<sup>22-24</sup> Thus, the properties of the deposit can be enhanced when it is compared to the conventionally plated systems. While current density is sufficient for characterization of deposited samples by DC plating, three parameters known as cathodic peak current density,  $J_c$ , cathodic pulse length,  $t_c$ , and the interval between pulses,  $t_p$ , are required to characterize materials deposited with PC. Additionally, the anodic current density,  $J_a$ , and anodic pulse length,  $t_a$ , are required to be known for PRC. **Equation 4.1**, **Equation 4.2** and **Equation 4.3** define the average current density,  $J_{AV}$ , duty cycle,  $T$ , and frequency,  $f$ , for PC, and PRC.<sup>3</sup>

$$J_{AV} = \frac{J_c \times t_c}{t_c + t_p} \text{ for PC, } J_{AV} = \frac{J_c \times t_c + J_a \times t_a}{t_c + t_a} \text{ for PRC} \quad \text{Equation 4.1}$$

$$T = \frac{t_c}{t_c + t_p} \text{ for PC, } T = \frac{J_c \times t_c - J_a \times t_a}{t_c + t_a} \text{ for PRC} \quad \text{Equation 4.2}$$

$$f = \frac{1}{t_c + t_p} \text{ for PC, } f = \frac{1}{t_c + t_a} \text{ for PRC} \quad \text{Equation 4.3}$$

Unipolar pulsed current systems (PC) have been used in practical applications mainly through its ability to affect the mechanisms of electrocrystallization, in other words, the physical and mechanical properties. This allows the use of higher current densities for PC systems resulting in reduced porosity and finer grain sizes. In detail,  $t_p$ , plays an important role, allowing desorption of impurities, and encouraging nucleation with the formation of fresh, smaller crystal grains. Grain size can be increased or decreased depending on the duty cycle. In gold-cobalt acidic plating media, a significant increase in ductility, electrical conductivity, density, and decrease in porosity, can be achieved using pulse plating which means thinner gold deposits can be applied resulting in significant cost saving.<sup>3</sup>

It is important to note here, that the majority the theoretical optimisation of PRC and PC techniques were determined for aqueous media where fast polarization response times with high diffusion rates are prevalent. These will not be the same for DESs, as will be discussed later. Studies conducted for aqueous media for PC and PRC techniques show some limitations. There is no doubt that the metal deposition rate is controlled by the applied current density or average current density in pulse systems. Thus, to have the same average deposition rates with DC as in PC or PRD, either peak current densities need to be increased while the duty cycle is reduced, or average current density need to be increased with increasing cathodic periods in case of applied higher duty cycles. A duty cycle of 33% to 50% is probably the minimum practical value if the rectifier capacity is available. For applications using high currents or in resistive media, 50% to 75% may be the lowest duty cycle which can be used. The frequency also has an impact on PC and PRC depositions. At high frequencies, the double layer does not have sufficient time to be fully charged after relaxation or the anodic pulse period, and this causes a smoothing effect on the applied waveform which begins to approximate DC plating. The suggested optimum higher and lower frequency ranges in aqueous solutions range from 500 Hz to 50 Hz to ensure it is far from the DC regime,<sup>3, 25</sup> There are, however some studies published for aqueous solutions which used much lower frequencies than 50 Hz with notable results.<sup>26</sup> These suggested limits are theoretically related with the capacitance of the double layer at the interface between the plating electrolyte and the article being plated.<sup>3</sup> However, the capacitance of the double layer is also related to the polarization rate of the substrate in the PRC technique, the diffusion coefficient of the ionic species in the medium and the solution resistivity. Thus, it is unreasonable to rely on one single

model studied for aqueous solutions if the plating process is performed in any other type of media, such as organic solvents, ionic liquids or DESs. In pulse plating the primary parameter affecting current distribution is cell geometry. Therefore, current distribution is incorporated as a variable of PC or PRC. There are various reported practical applications of pulse current for electrodeposition with smoother deposits of copper, nickel, and zinc from sulfate solutions,<sup>27-29</sup> and gold and copper from cyanide solutions.<sup>29-31</sup> These all kept the average current densities and plating times equal to the corresponding DC study. Additionally, it was reported that equal or better-quality deposits could be obtained for copper, gold and zinc even at higher current densities than those normally used with DC plating.<sup>23, 29, 32-35</sup> It is also important to highlight that decreased hydrogen evolution can be obtained and current efficiencies can be increased due to improved double layer response times. Periodically reversed current is the main method used for these studies, and it is basically bipolar electrodeposition process in which DC current is continuously changing its polarity (direction). It has been used not long before as a levelling technique in hot cyanide copper plating baths, but was not widely adopted due to environmental issues.<sup>36</sup>

### 4.3 Results and Discussion - Zinc Powder Pulse Plating

The concept of powder pulse plating is shown schematically in *Figure 4.2*. When the target metal powder is physically contacted on the surface, it is possible to dissolve it and then redeposit it using pulsed waveforms. Briefly, changing the direction of current flow periodically by using pulse reverse deposition is called PRC *Figure 4.1 (F)*. There are numerous feasible benefits to this approach including potentially obtaining super-efficient deposition (current efficiency > 100 %), deposition of heterogeneous alloys,<sup>37-39</sup> fast deposition of thick layers and deposition of composite materials.<sup>40, 41</sup>

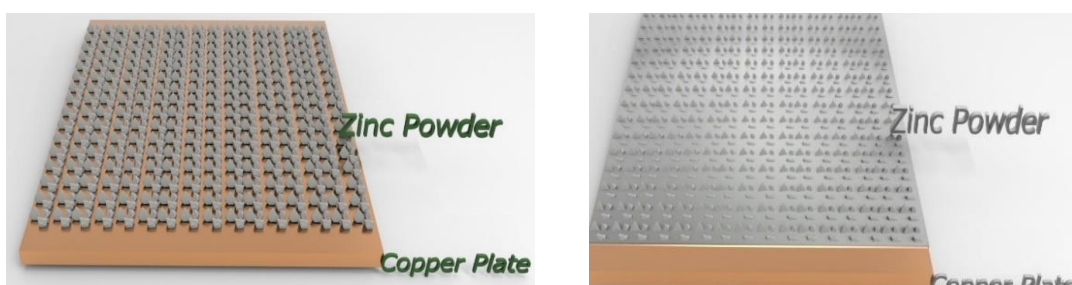


*Figure 4.2* Zinc particles placed onto copper cathode (left). Zinc particles fuse with the surface through repeated pulsed cycling (right)

### 4.3.1 Cyclic Voltammetry of Zinc Particles

Previously, zinc was studied from dissolved zinc salt in 1ChCl: 2EG, and it was found as almost fully reversible, and diffusion controlled.<sup>42-44</sup> In the previous chapter the electrochemical response of a zinc electrode was demonstrated and it was shown that dissolution and re-deposition could be achieved but the process was not fully reversible. In this experiment, the aim was to start with a zinc particle in contact with the electrode surface and then observe if the particle could be electrochemically dissolved through just a physical contact.

A single zinc particle was placed on a gold working electrode immersed in 1ChCl: 2EG. Gold working electrode was chosen instead of platinum in initial experiments since physical colour change was recorded. Experiment temperatures were kept at  $50 \pm 5$  °C to increase the rate of zinc dissolution and deposition. The zinc particle was approximately 1 mm<sup>3</sup> to enable clear visual inspection of the sample.

It was expected that a cyclic voltammogram like that observed for a zinc electrode in Chapter 3 would be observed, but *Figure 4.3* shows that an almost linear resistive artefact is revealed instead. This is due to the large current, for zinc dissolution and the high resistance of the solution.

Repeated cycling showed that small bubbles formed on the anodic and cathodic cycles. It was thought at the time that the liquid was stable in the region of the voltammogram and the reactivity between zinc and EG was unknown.

To study this phenomenon in more detail the cell was placed under a microscope and the experiment was repeated. *Figure 4.4* shows the microscope image of the zinc grain (dark area in the inset images), and the zinc grain moves during the experiment.

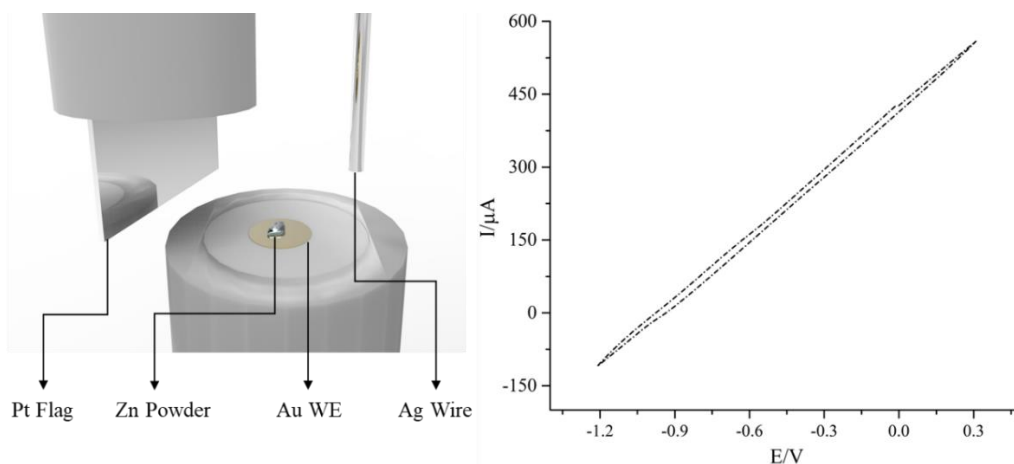


**Figure 4.3** CV was studied between 0.4 V and -1.2 V. Pt flag CE, silver wire reference electrode, and 150-micron size zinc particle on top of gold working electrode in 1ChCl: 2EG. The scan rate was  $30 \text{ mVs}^{-1}$ .

This movement was caused by microbubbles forming on the underside of the zinc particle, lifting away from physical contact with the gold substrate as proven in **Figure 4.4**.

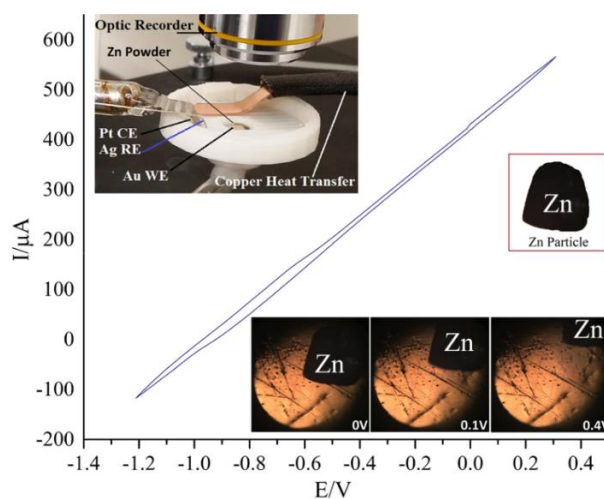


**Figure 4.4** Experimental set up for observing zinc particle during cyclic voltammetry experiment. Lower inset image shows movement of zinc particle.

After the problem was identified, a solution was developed to prevent movement of the Zn particle on the working electrode. To hinder the particle moving, a non-conductive spring was used to press the zinc particle down onto the Au working electrode surface as shown schematically in **Figure 4.5**. For the ease of experimental set up, a relatively big zinc particle was chosen to make contact between the point and the particle easier. This

experiment was repeated several times changing the tension on the spring until noise free voltammogram was obtained.

The cyclic voltammogram in **Figure 4.5** shows that a response characteristic of zinc dissolution and deposition is obtained which is similar with the one shown in **Figure 3.20** for bulk zinc dissolution from a zinc electrode. This shows that the Zn particle remained in contact with the electrode during the experiment. The oxidation and reduction charges were calculated as 23.5  $\mu\text{C}$  and 23.8  $\mu\text{C}$  respectively, which shows that the process is largely reversible. At low scan rates, on the anodic cycle, a white cloud was formed around the zinc particle. This is thought to result from either exceeding the solubility of zinc chloride in the double layer or due to the formation of an insoluble zinc glycolate complex. The results in chapter 3 suggest that it is the latter of these which is more likely.

The CV in **Figure 4.5** shows two anodic stripping potentials at c.a  $E_{p^1} = -0.8 \text{ V}$ ,  $E_{p^2} = -0.6 \text{ V}$ . The same observation was made by Barron<sup>44</sup> who used atomic force microscopy (AFM) to show that  $E_{p^1}$ , was assigned to the removal of the small scale, nanodeposits whereas the anodic peak,  $E_{p^2}$ , was due to the dissolution of bulk zinc. The formation of two stripping peak requires very sensitive conditions as it was not repeatable at every scan which is most probably due to the surface roughness.<sup>44</sup>

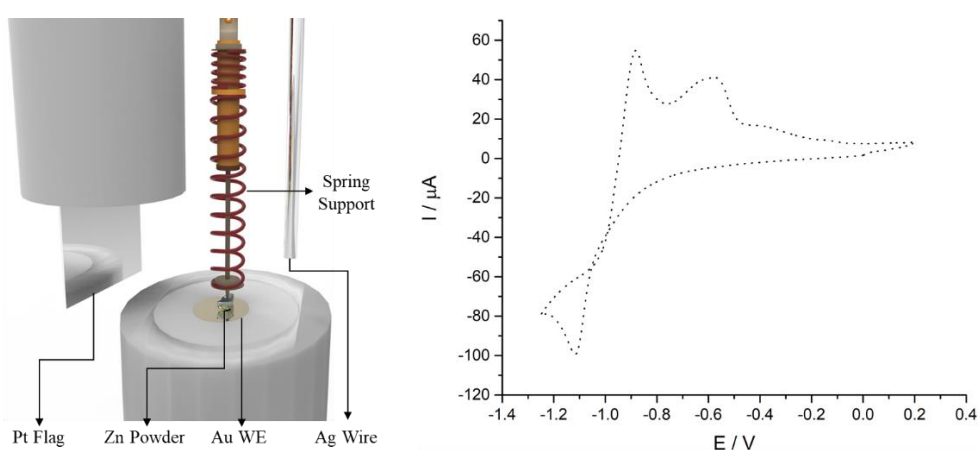


**Figure 4.5** Schematic diagram of the experimental set up (left) and resulting cyclic voltammogram (right), CV was studied (Ag wire RE, Pt CE) between 0.2 V and -1.25 V at sweep rate of 30  $\text{mVs}^{-1}$ . 150-micron size zinc particle on top of gold working electrode in 1ChCl: 2EG.

During the cycling of the zinc particle in **Figure 4.5** the area on the gold electrode around the zinc particle changed from a yellow colour to grey as it was expected to be seen before starting the experiment.

### 4.3.2 Single Particle Pulse Plating

In the previous section it was shown that zinc from a single particle could be dissolved and electrodeposited and in this section the concept of powder pulse plating is tested using a single zinc particle. The experiment was carried out using alternating current pulses to determine the feasibility of fusing the zinc particle to the substrate. In the experiment, the particle used was big enough so that pressure did not need to be applied to keep the zinc particle stable on the substrate. The experiment was set up with a 25 mm diameter O-ring glued to the 3 cm x 3 cm copper substrate. An iridium oxide coated titanium mesh was used as the counter electrode and the experiment was run in by electrodes as anode and cathode. **Figure 4.6** shows a schematic representation of the experimental set up. The electrolyte was 1ChCl: 2EG at  $47.5 \pm 2.5$  °C with no added  $ZnCl_2$ . A 3D optical profiler unit was used to observe the volume change of the zinc particle. Then, 1ChCl: 2EG filled the space inside the O-ring. Several pulse variables were tried as given in **Table 4.1**.

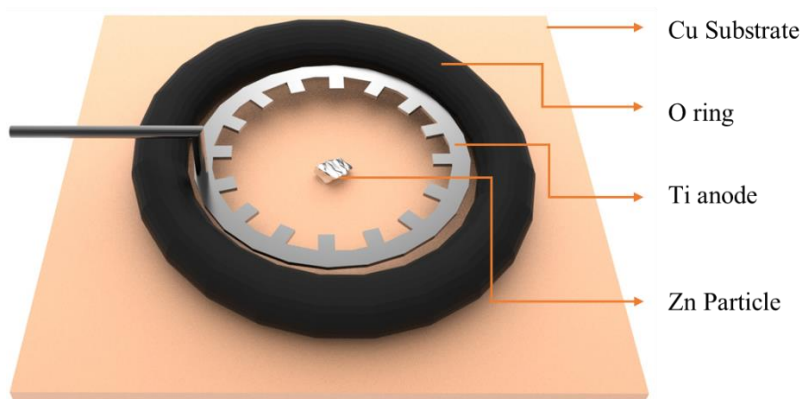


**Figure 4.6** Schematic diagram showing the experimental set-up used for deposition and dissolution of single c.a 600  $\mu m$  zinc particle placed on a copper plate.

**Table 4.1** Experimental conditions for the pulse sequences applied to fuse the zinc particles onto a copper substrate in 1ChCl: 2EG at 45°C for the experimental procedure shown in **Figure 4.6**.

Exp.	$I_c$ / mA	$t_c$ / s	$I_a$ / mA	$t_a$ / s	$t_{total}$ / s	$T$ / %	$f$ / Hz
<b>A</b>	50	0.001	10	0.001	0.002	50	500.00
<b>B</b>	50	0.006	15	0.002	0.008	75	125.00
<b>C</b>	40	0.01	10	0.004	0.012	71	71.43
<b>D</b>	35	0.02	10	0.01	0.03	66	33.33
<b>E</b>	35	0.08	10	0.03	0.13	73	9.09
<b>F</b>	35	0.8	10	0.3	1	73	0.91
<b>G</b>	35	1.5	10	0.5	2	75	0.50
<b>H</b>	35	3	10	1	4	75	0.25
<b>J</b>	35	6	10	2	10	75	0.13

The pulse trials initially chosen were similar with those used in the literature for aqueous solutions. In the experiment, labelled as **A**, the applied cathodic current and anodic currents were chosen to be 50 mA and 10 mA respectively with 80% ductility, and a 500 Hz frequency rate. However, at the end of the experiment no deposit was observed and only etching of the copper substrate was observed as shown in **Figure 4.7**.



**Figure 4.7** Photograph of the 3 cm x 3 cm copper substrate after 3h experiment **A** with applied +50 mA for 1 ms, and -10 mA for 1 ms  $47.5 \pm 2.5$  °C.

In experiment, **B**, while the anodic current and anodic pulse time increased, the frequency was decreased compared to experiment **A**. However, deposition was still not observed. In experiment, **C**, the cathodic current was decreased but the time was increased but the result did not differ significantly from **A**, **B**. Experiments **D**, **E**, **F**, and **G** also failed to stick zinc particles on to the surface as shown in **Figure 4.8**.



**Figure 4.8** Deposited 3 cm x 3 cm substrate images for experiments with applied +35 and -10 mA at  $47.5 \pm 2.5$  °C for deposition pulses of 80 ms, 800 ms, 1.5 s, and for dissolution pulses of 30 ms, 300 ms, and 500 ms, labelled as **E**, **F** and **G** respectively.

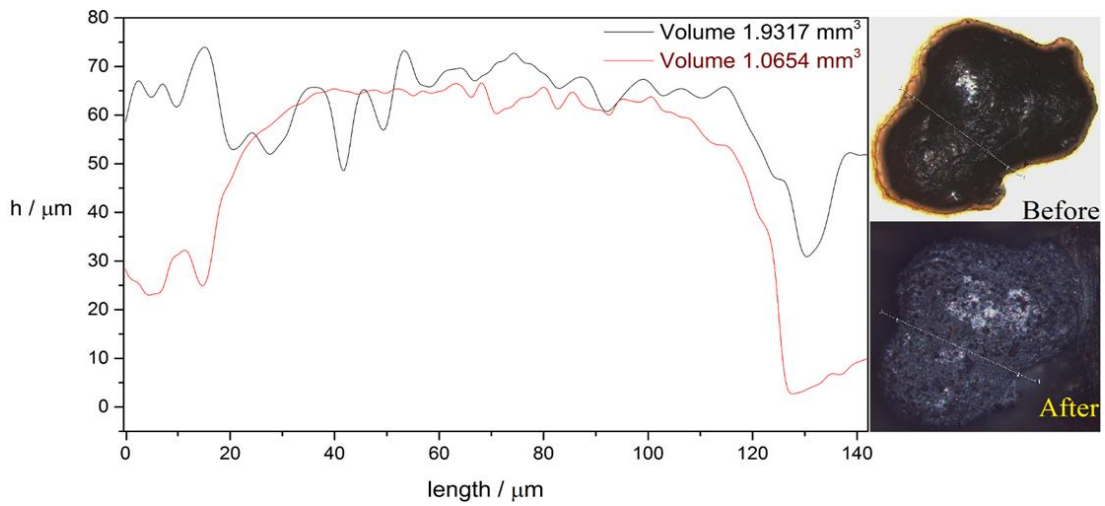
In experiment **H**, it was possible for the first time to fuse the single zinc particle to the copper surface with an applied deposition current of 35 mA, and an applied dissolution current of 10 mA values and a 0.25 Hz frequency ratio. As further decrease in frequency to 0.25 Hz produced a successful result. Decreasing the frequency to 0.13 Hz in experiment **J**, decreased the adhesion of the particle. It appears that the pulse plating parameter choice appears to be critical.

Consequently, it was found that the optimum effective duty cycle value was 75% while the optimum frequency value was 0.25 Hz for the case of single particle deposition process. The applied frequency is much lower than that would be used for aqueous plating. There are probably two reasons for this; the viscosity is significantly higher in DESs than in water and the distance that ions must travel are much larger for the large particles. For powder pulse plating the ions must move distances in the order of  $\mu\text{m}$  whereas for conventional electroplating it is in the order of nm. It is therefore not surprising that the frequency is several orders of magnitude lower than would be expected for aqueous pulse plating.

**Figure 4.9**, shows the zinc particle before and after the current pulses. The applied currents 35 mA for deposition, and 10 mA for dissolution. The pulse periods were 1 s for dissolution and 3 s for deposition. **Figure 4.9 a** and **e** show clearly that the particle is fused at the base to the copper substrate. The particle is clearly smoothed during the dissolution and deposition steps. It should be noted that the apparent volumes will be inaccurate as the 3DM profiler cannot image all around the 600  $\mu\text{m}$  sized particle, and so it assumes that everything under the topographical image is solid. Although the measure

volume appears to decrease by about a half, the material that is being removed from the top is simply being deposited not only at the base of the particle but also in the area surrounding the particle.

Qualitatively analysing the grain in **Figure 4.9**, this appears to be an appropriate estimate of the change in volume of the particle.



**a**



**b**



**c**



**d**



**e**

**Figure 4.9 a** Profilometry of the zinc particle before and after the pulse plating experiment Current density is  $7 \text{ mA}\cdot\text{cm}^{-2}$  for deposition, and  $2 \text{ mA}\cdot\text{cm}^{-2}$  for dissolution. Pulse periods are 1 s dissolution and 3 s deposition. **b** is particle before experiment, **c** is experiment in progress, **d**, and **e** show fusion of the particle to the substrate.

**Figure 4.9 (e)** shows that a layer of zinc which is approximately 10% of the height of the particle is needed to fuse the particle to the substrate which appears to be reasonable. As will be seen later using EQCM there is a critical time in the experiment before the particle fuses with the substrate.

**Figure 4.9** shows that the zinc did not completely coat the copper substrate but instead it coated only in the area around the zinc particle. This is because the current pulse was relatively short, and the zinc could not diffuse far before it was stripped from the solution. The short anodic pulse also ensures that the solution close to the zinc particle did not become saturated with zinc.

The aim of the experiment is to get as much zinc into solution as possible without saturating the solution and then to deposit it in the area between the particle and the substrate and ultimately, in the volume between the particles. This is shown schematically in **Figure 4.10**.

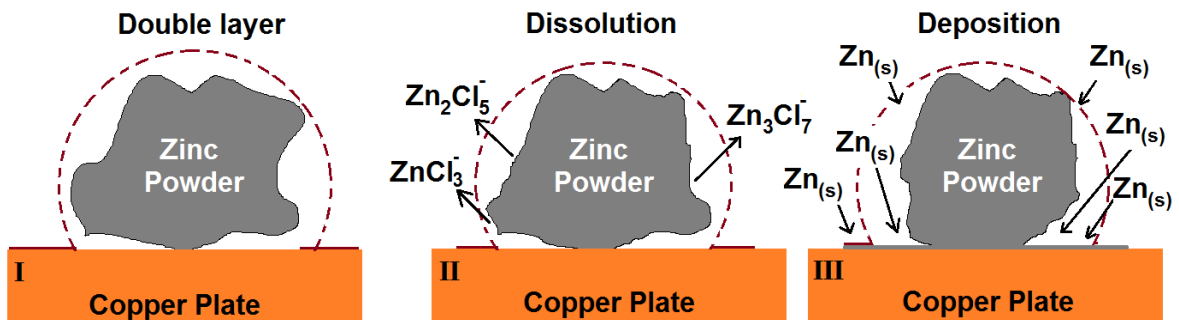


**Figure 4.10** Schematic diagram to show the dissolution and redeposition of Zn fusing a particle to a substrate.

#### 4.4 Bulk Powder Deposition

In an attempt to go from a single particle to a practical plating system the main issue is how to keep the zinc particles in contact with the substrate. Initial cell designs relied on gravity to ensure a contact between the substrate and the zinc particles. The optimised current density, dissolution and deposition times will need to be changed slightly to ensure particle fusion as presented in the following sections. It is a fact that required current is related surface area of the powder. While dedication of a fixed current density for a single powder was easy, it is difficult to measure for a bulk powder system as

placement of particles and their contact area with solution will be changed depending on placement. However, it is certain that current density will required to be increased for the same cathode plate used for single particle due to additional increase of surface area coming from each powder that contact with cathode.

#### 4.4.1 Electrode Geometry - Vertical

For a practical plating system, it must be possible to deal with a variety of electrode shapes and orientations. One approach would be to use a packed bed of zinc particles around the vertically oriented electrode.

*Figure 4.11* shows a schematic diagram of an ABS cell made using a 3D printer. The electrodes are separated by a filter paper membrane which just forms a physical barrier keeping the zinc/DES slurry in contact with the electrode. A plastic grill slots into the cell to keep filter paper flat and in place. A coarse filter paper was used to produce a set-up which was easy to adapt. The paper had to be carefully cut to ensure no leakage of the zinc/DES slurry into the counter electrode compartment.

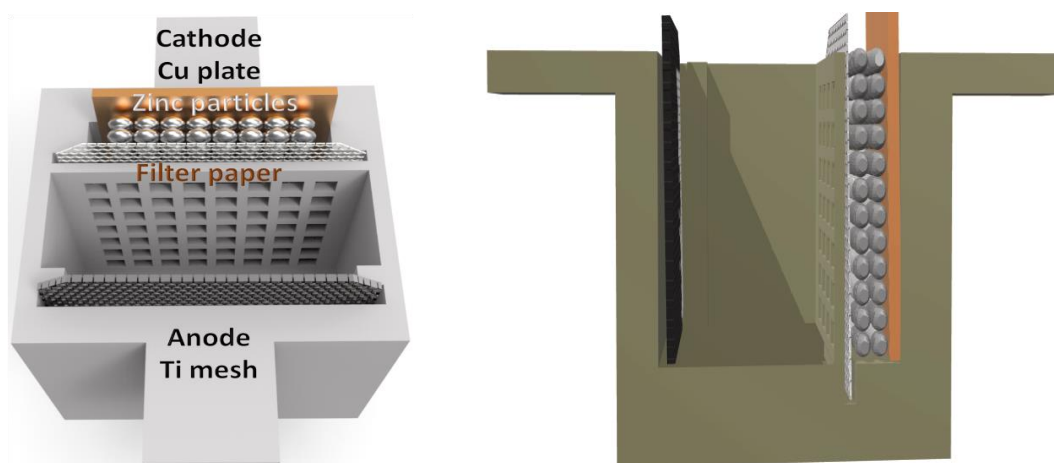


*Figure 4.11* plan view (left) and profile cross section view (right) of the packed zinc bed system.

The cell shown in *Figure 4.11* was used for the electrodeposition of zinc onto a copper substrate at first without dissolved zinc salt with no deposition, and later tried with 0.3 M  $\text{ZnCl}_2$  in 1  $\text{ChCl}$ : 2 EG solution for 180 minutes. The process conditions are shown in

**Table 4.2.** The zinc particles sizes were in the range 20-50  $\mu\text{m}$  packed on a copper substrate of approximate area 4.5  $\text{cm}^2$ . With a single particle, it is not difficult to discuss the current density, however, with the packed bed of particles the surface area will greatly increase. Due to the unknown surface area, the following experiments present total current rather than the current density.

**Table 4.2** Experimental conditions used for the sample in **Figure 4.12**

$T/^\circ\text{C}$	$I_c/\text{mA}$	$t_c/\text{s}$	$I_d/\text{mA}$	$t_d/\text{s}$	$t_{\text{total}}/\text{h}$	$T/\%$	$f/\text{Hz}$
50 $\pm$ 5	50	5	14	1	3	0.94	0.17

**Figure 4.12** shows a photograph of the deposit morphology of the zinc formed by this process. A thin, but patchy zinc deposit was obtained but no particles were fused to the electrode surface.

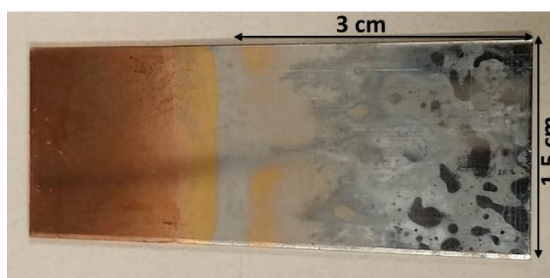


**Figure 4.12** is an optical photograph of a copper plate that deposited with zinc using the cell shown in **Figure 4.11** and the conditions described in **Table 4.2**.

This could result from the slurry density being insufficient to maintain contact with the electrode or because gassing is creating a gas pocket lifting the particles away from the electrode. As the zinc layer is thicker and more homogeneous at the bottom of the sample it is probable that a concentration profile is set up in the cell and the zinc complex formed on dissolution has a higher concentration at the base of the cell than at the air-solution interface. As was shown in Chapter 3, there appears to be a critical zinc concentration below which zinc cannot be electrodeposited and this would explain the results in this experiment. It was noted that gas was produced during the experiment and this resulted in fluctuation of the cell potential. Additionally, a mathematical modelling was used to

check the possible drawbacks of using filter paper and this analysis is given in appendix section. The simulation shows localised high current densities leading to vigorous gas production, and decreasing particle adhesion.

#### 4.4.2 Electrode Geometry - Horizontal

The issue in the previous section was that the zinc particles were not sticking to the electrode surface as there was insufficient force maintaining the in contact with the electrode. An alternative approach was tried where the electrode was maintained in a horizontal orientation. The cell in **Figure 4.13** was constructed using a 3D printer with ABS polymer. Before starting each experiment, the copper substrate was cathodically polarised for 10 minutes in a 0.3 M ZnCl<sub>2</sub> 1ChCl: 2 EG at a DC current density of 50 mA cm<sup>-2</sup> to create an initial layer of zinc which will prevent the copper dissolution during applied anodic pulses. The seed layer also ensures a reservoir of zinc to keep the zinc concentration high close to the bottom of the close packed zinc layer The working electrode was a square (3 cm x 3 cm) copper plate which was spring loaded to ensure a constant pressure with the edges of the holder. In this experiment, first, a paste made up of Zn powder (diameter 30-50 μm) with 1 ChCl: 2 EG, and this was spread on the copper substrate using a spatula. PRC was applied for 180 minutes, and experimental conditions are listed in **Table 4.3**.

**Table 4.3** Experimental conditions used for the sample in **Figure 4.14**.

<i>T</i> / °C	<i>I<sub>c</sub></i> / mA	<i>t<sub>c</sub></i> / s	<i>I<sub>a</sub></i> / mA	<i>t<sub>a</sub></i> / s	<i>t<sub>total</sub></i> / h	<i>T</i> / %	<i>f</i> / Hz
47.5±2.5	63	5	18	1	2	94	0.17

Consequently, the application method by which the powder was deposited onto the substrate is important. In initial trials of the horizontally placed substrate, a powder-paste was made up where a mixture of zinc powder and 1ChCl: 2EG containing 0.3 M ZnCl<sub>2</sub> was distributed on the surface using a spatula.

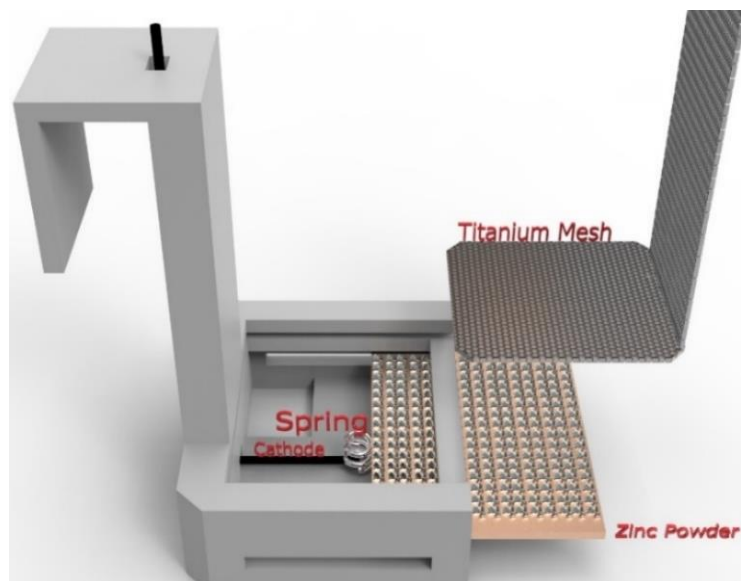


**Figure 4.13** Schematic diagram showing the electrode arrangement with a copper cathode which is supported by a spring from bottom to maintain a seal with the ABS.

An advantage of this cell to the previous design was that no filter paper separator was required which could decrease the potential drop across the cell.

When the experiment was performed using the conditions given in **Table 4.3** in the cell shown in **Figure 4.13** the deposit shown in **Figure 4.14** was obtained. The deposit showed poor adhesion and was easily wiped off the surface.



**Figure 4.14** photograph (left) and 3DM image (right) obtained using the cell shown in **Figure 4.13** by pasting zinc powder with 63 mA for 10 seconds deposition current, and 18 mA for 1 seconds dissolution current as given condition in **Table 4.3**. Powder applied with spatula onto substrate.

Consequently, it was found that regardless of how carefully the powder-paste was placed on the surface, fusion of particles did not occur efficiently as they were poorly packed on the surface meaning the distance between them was too great to allow zinc to be deposited between them and for them to fuse together. Also, if electrical contact did not occur between the particles then dissolution and deposition could not occur efficiently. To overcome this issue, larger zinc particles sized between 80-150  $\mu\text{m}$  were used with a new technique which is shown schematically in *Figure 4.15*.

The increased size and mass of particle meant that the particles easily settle down onto the electrode surface within 10 min. The experiment described in *Table 4.4* was used for 150 minutes at  $47.5 \pm 2.5$  °C with larger particles. This proved to be a successful method to achieve a fused zinc film and *Figure 4.16* shows the photograph, and 3DM images of the deposit obtained while *Figure 4.17* shows the SEM images.

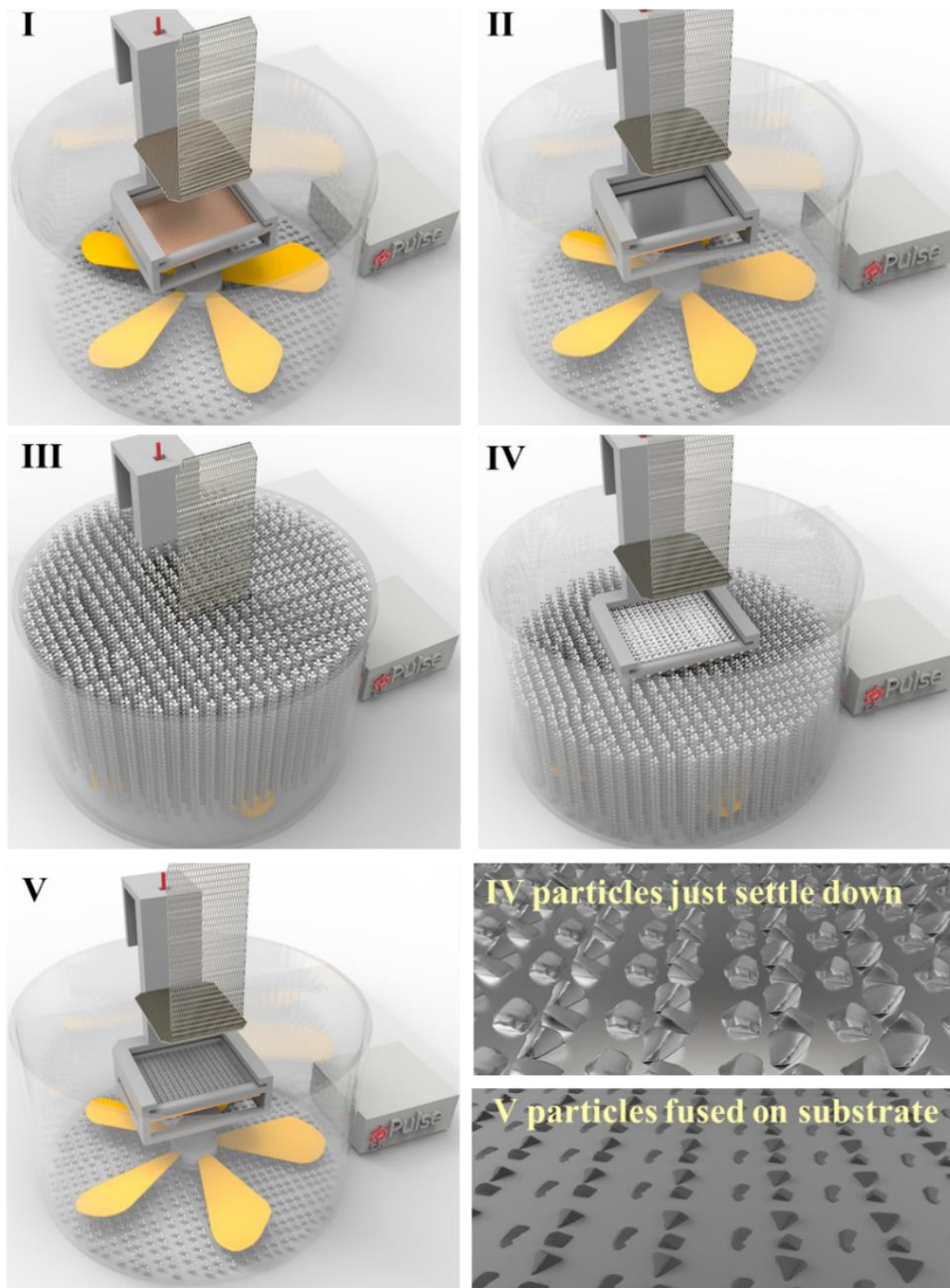


**Figure 4.15** Copper plate is placed into 0.3 M  $\text{ZnCl}_2$  containing DES (I), the initial zinc layer was deposited for 10 min (II). The particles were added to the beaker and stirred vigorously for 5 s (III), the particles settled onto substrate (IV), and pulse deposition is performed to fuse particles onto substrate (V)

As shown in **Figure 4.16**, particles are fused together and demonstrate for the first time that the concept of powder pulse plating can work but it is clear from the photograph alone that the particles are patchy and there are clearly void or holes that are present in the film.

**Table 4.4** Experimental conditions used for the sample in **Figure 4.15**

$T/^\circ\text{C}$	$I_c/\text{mA}$	$t_c/\text{s}$	$I_a/\text{mA}$	$t_a/\text{s}$	$t_{total}/\text{s}$	$T/\%$	$f/\text{Hz}$
$50\pm 5$	63	5	18	1	9000	94	0.17

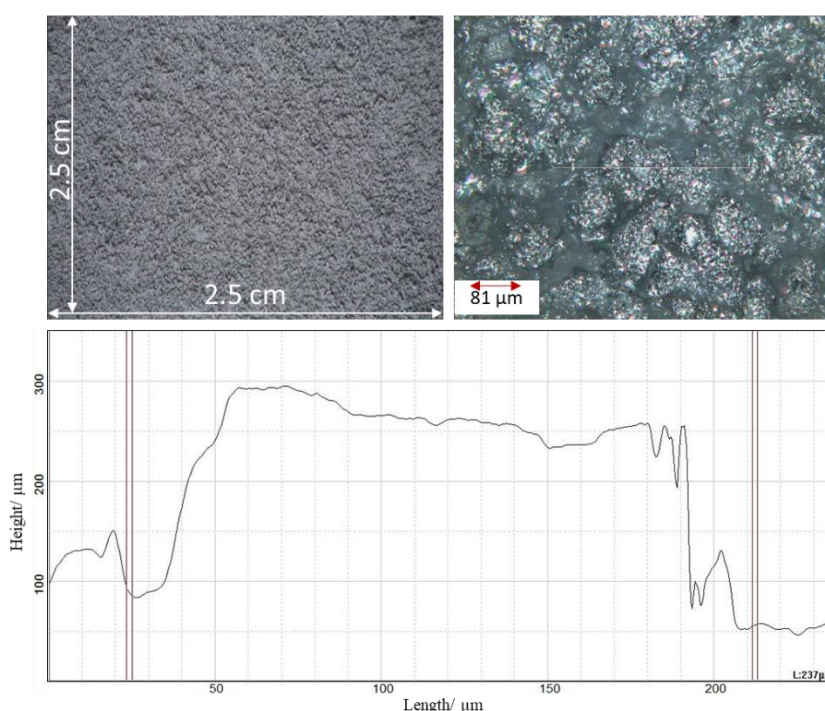


**Figure 4.16** photograph, and 3DM profile and image obtained using the cell shown in **Figure 4.13** with the conditions listed in **Table 4.4** in 0.3 M dissolved  $\text{ZnCl}_2$  1 ChCl: 2 EG solution.

The porosity of the film affects the adhesion of the film and act as sites where gas bubbles can stick. This certainly results from the way in which the slurry is applied to the electrode surface and the way that the particles pack on the surface. It can also be seen **Figure 4.16** that surface has become smoothed in the dissolution process. One issue may be that the small zinc particles form a stable colloid as noted previously by Ettaib so they do not settle properly on the electrode surface to form a dense packed layer.<sup>45</sup>

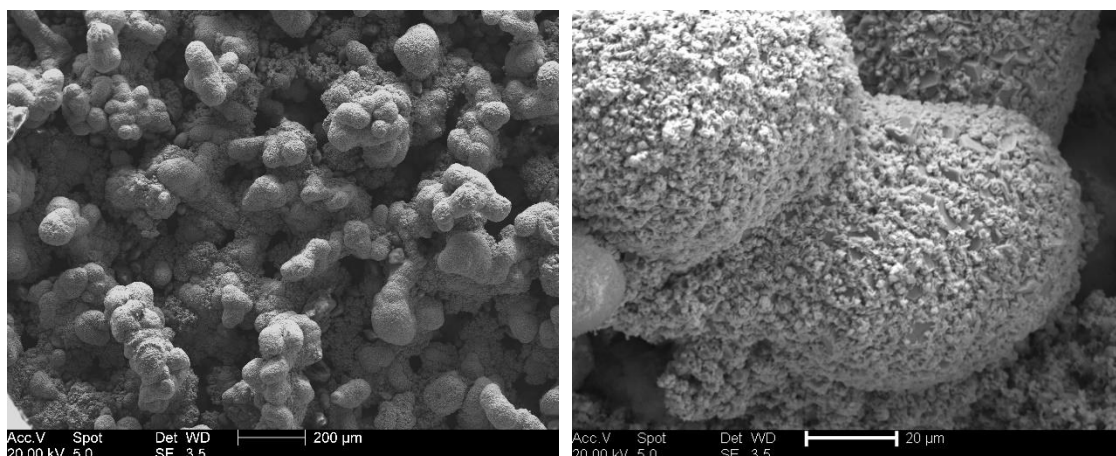


**Figure 4.17** SEM images of obtained sample given in **Figure 4.16** which the conditions given in **Table 4.4** is applied.

The SEM image given in **Figure 4.17**, however shows that there are macroscopic holes in the zinc film, so the technique can be used to make high surface area materials.

It could be questioned why a pulse technique is needed if there is  $\text{ZnCl}_2$  in the solution, it should be possible to simply coat in between the particles. A DC plating experiment was performed to observe the differences from the pulse reverse current deposition. Medium was the same with previous pulse experiment given above, 0.3 M  $\text{ZnCl}_2$  dissolved in Ethaline at  $50 \pm 5$  °C. Copper substrate was placed horizontally in the same cell used in PRC experiment given in **Figure 4.15**. Applied current was adjusted to 48 mA DC which is a little lower when compared to cathodic pulse current,  $I_c$ : 63 mA. The lower current pulse should decrease bubble formation. Similarly, as previously, an initial zinc layer was deposited for 10 minutes. Zinc powder was mixed, and a DC bulk electrolysis was carried for the same length of time as the PRC experiment described above.

**Figure 4.18** shows a photograph and 3DM image of the deposit obtained from the DC electrolysis. The darker grey is the substrate zinc which was initially deposited before the particles were added and the brighter parts are poorly adhered particles from the powder DC plating. This shows that DC plating yields a poorly adhered layer. The reason behind this can be clearly seen from the schematic diagram in **Figure 4.19**. When a DC source is used the  $\text{ZnCl}_2$  between the grains is rapidly used up and is insufficient to fuse the grains together. The  $\text{ZnCl}_2$  from the bulk solution will first be deposited on the interface between the solution and the grains. This zinc layer will fuse together the outer surface,

but it will not fuse the particles to the electrode. When pulse plating is used the zinc from the primed surface will maintain a high  $Zn^{II}$  concentration between the grains and lead to a fused mass. It will, however, be difficult to get sufficient Zn between the grains to prevent pores.

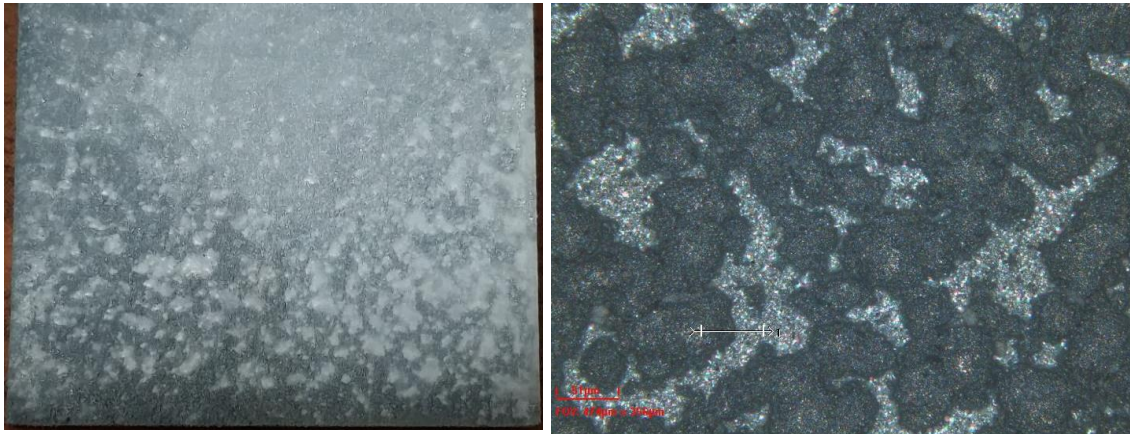


**Figure 4.18** Photograph (top left) and 3DM image (top right) of the deposit obtained with a DC source. Conditions were approximately same with **Table 4.4** as those used for the sample in **Figure 4.16**.

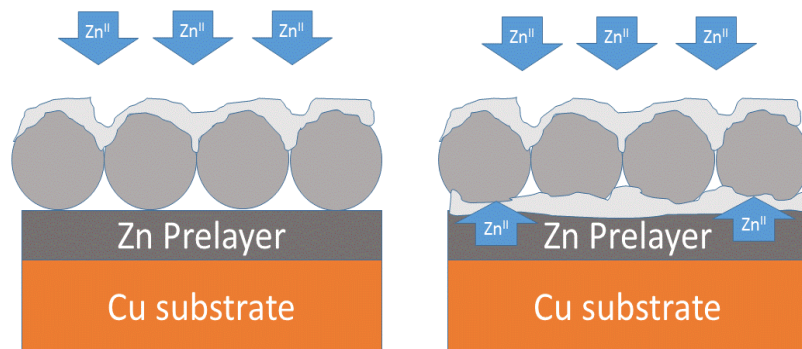


**Figure 4.19** Schematic diagram showing the difference between deposition using a pulsed current (right) and that with a DC (left).

Therefore, the PRC technique is essential for particle fusing. While DC provides the zinc nucleation around the particles and fills the holes between the particles, it does not provide enough metal between the particles to fuse them together. The PRC plating technique has a reservoir of metal close to the electrode surface so that during dissolution a high zinc concentration is maintained between the particles to fuse them together on the deposition cycle.

#### 4.4.3 Bulk Powder Deposition -Stirred Systems

The previous attempts to have a vertical electrode orientation failed to adhere the zinc particles to the surface but this orientation will still be the most important way in which pieces will be jigged in the plating bath. In an endeavour to coat particles onto the cathode an alternative approach was attempted.

The approach used was similar with those aqueous solutions to produce composite materials. In this case, fine zinc particles were distributed in a DES and zinc was plated from a 1ChCl: 2EG DES containing  $0.3 \text{ mol.dm}^{-3} \text{ ZnCl}_2$ . The cathode was placed vertically, and a pulse reverse signal was applied. An Arduino-UNO logic board was used to control the magnetic stirrer. The zinc powder sizes were between  $6 \mu\text{m}$  and  $9 \mu\text{m}$ . The temperature was set between  $47.5 \pm 2.5 \text{ }^\circ\text{C}$ . A schematic representation of the experimental set up is shown in **Figure 4.20**.

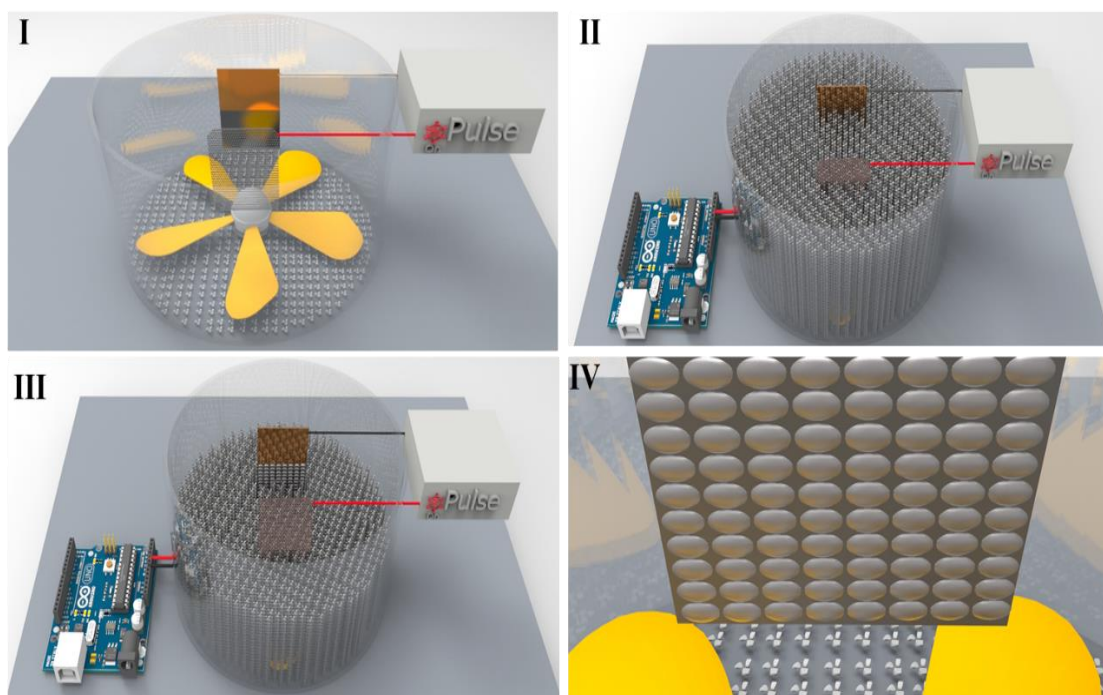


**Figure 4.20** Schematic diagram for the experimental set up for the pulsed powder deposition where the electrode was maintained in the vertical position. The electrodes are parallel to each other (I). The particles are mixed with the 1 ChCl: 2 EG solution (II) The stirrer is switched off (III) and the reverse pulses are applied. The pulse is reversed, and the stirring is continued. (IV) represents the final product deposited.

The main reason behind using small particles was to ensure that they stayed suspended in the DES. Experimental set up made up by a 100-ml glass beaker filled 65 ml of 0.3 M  $\text{ZnCl}_2$  in 1ChCl: 2EG DES mixture with added 0.05 g of zinc particles, and the mixer was connected to programmable board as shown as small circuit in **Figure 4.20**.

A cathodic pulse of 55 mA, and an anodic pulse of 18 mA were applied for 180 minutes. However, before PRC deposition, DC plating was performed without Zn powder in contact with the working electrode as above to obtain a zinc reservoir on the copper surface, so an initial zinc layer was deposited for 10 minutes (i.e. the before adding the particles).

The pulse sequence uses 1 s for dissolution and 5 s for deposition, to ensure that the solution does not become saturated with zinc. During the plating cycle, the stirrer is stopped to allow the zinc particle to come in to contact with the surface while the zinc metal plates around it.

The pulse profile was different from that used above, so that it was more akin to a DC experiment. After the initial zinc coat, the applied dissolution and deposition currents were the same with horizontal placement experiments. Stirring periods applied as 10 s ON and 5 min. OFF. The total coating time was 180 min. which little longer than the experiment performed in horizontal placement given in **Figure 4.15**. The deposit obtained is shown in **Figure 4.21** was significantly different from those observed above. The zinc coating is very dense, but it is clear to see that each Zn particle has become coated in small zinc crystallites.

The surfaces are rougher than those seen previously due to the very short dissolution pulse length. The samples are also not macro-porous. The layer is approximately 50  $\mu\text{m}$  thick showing that layer on layer growth is occurring.

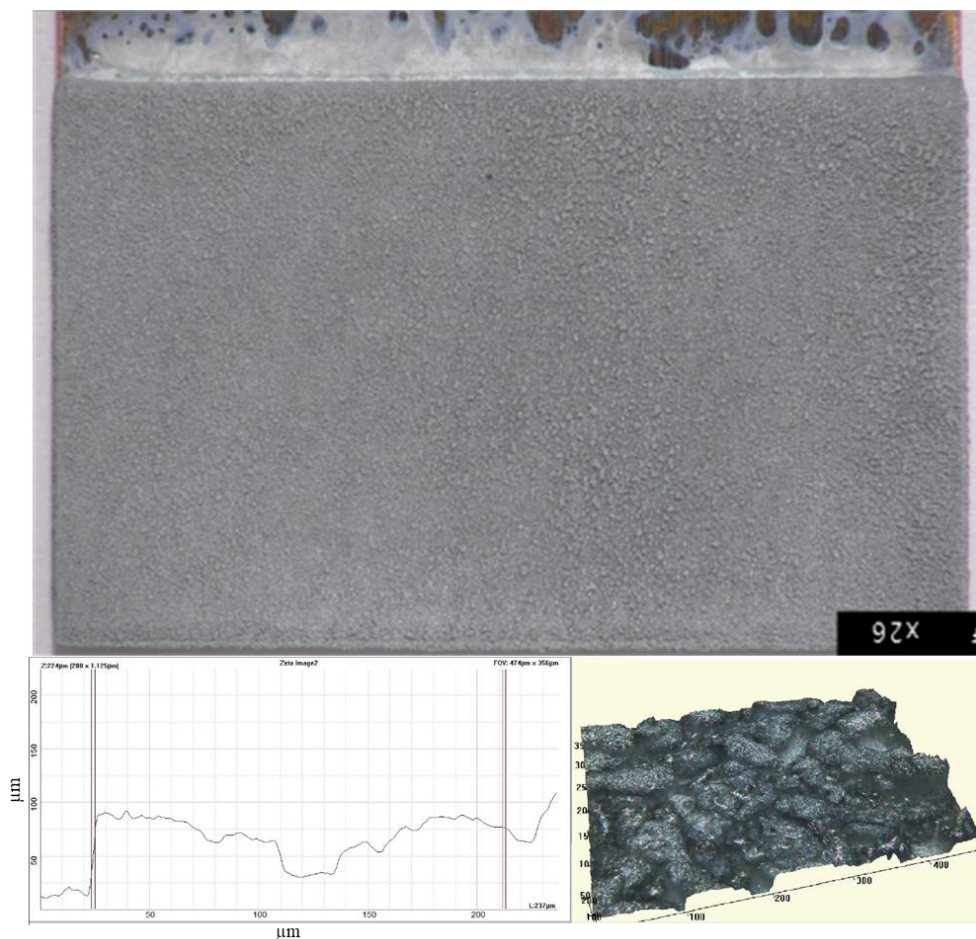


**Figure 4.21** Photograph and SEM image of deposit obtained using 6-9-micron particles by using pulse power supply in 0.3 M ZnCl<sub>2</sub> in 1ChCl: 2EG with a cathodic pulse of 55 mA, and an anodic pulse of 18 mA for 180 minutes.

This is an important result as it demonstrates that it is possible to coat zinc powder into a zinc coating when the electrodes are in a vertical orientation. It is also important to note that the current efficiency was only was c.a 90%. However, it is possible to obtain a thick, homogeneous deposit in three hours. **Figure 4.22** shows the obtained SEM images for vertical-stirrer deposition system. In the experiment, completed with a vertical orientation in the cell given in **Figure 4.15**, the thickness of the deposit was between 40 to 90  $\mu\text{m}$ . **Figure 4.22** shows that the structure is more macro porous, and very different from that seen in **Figure 4.17**. This is due mostly to the zinc particle size.

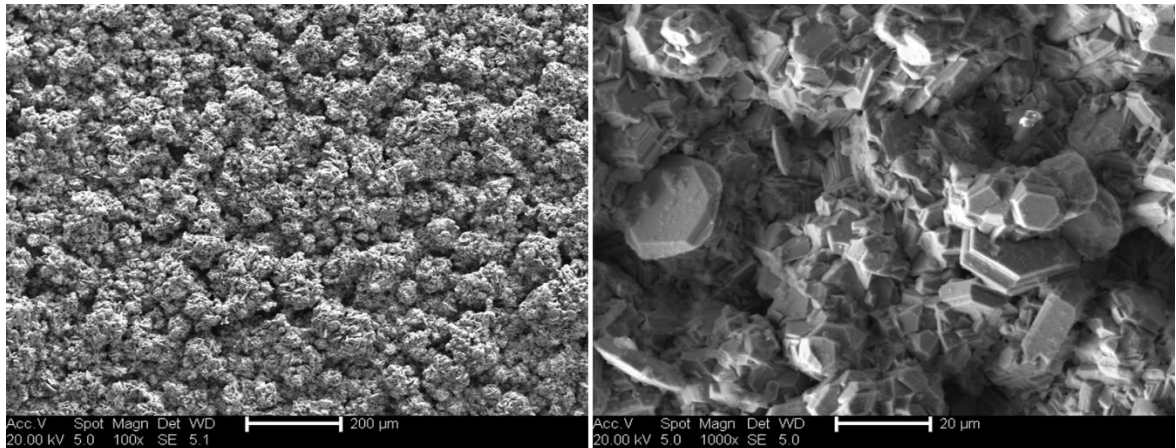


**Figure 4.22** SEM image of the deposit morphology obtained using 6-9-micron particles by using pulse power supply in 0.3 M ZnCl<sub>2</sub> in 1ChCl: 2EG with a cathodic pulse of 55 mA, and an anodic pulse of 18 mA for 180 minutes.

On a macroscopic scale, the deposit obtained with smaller particles is denser and better fused together which is what would be expected. **Figure 4.22** shows that the surfaces of the microparticles have been engineered into hexagonal zinc crystals. As shown in Chapter 3 this could be due to both the anodic and cathodic steps. Imaging the cross section is problematic zinc and the surfaces are friable, but also because they are very soft the material smears when it is polished. It is, however possible to see from **Figure 4.23** that the zinc coatings are microporous.

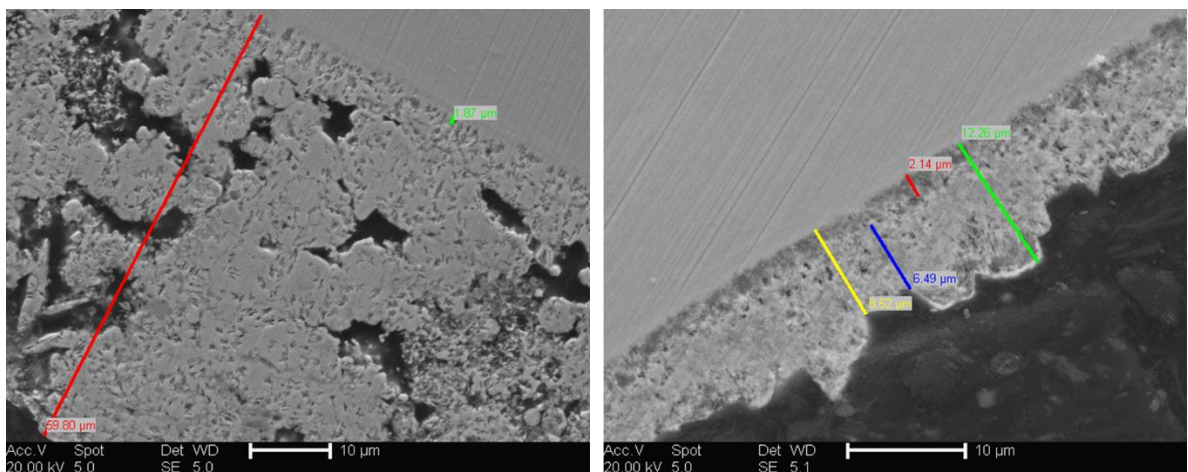


**Figure 4.23** Cross section comparisons of experiments performed with PRC in the vertically-stirred system (left), and an analogous experiment performed with just DC (no particles) for 3 h in 0.3 M ZnCl<sub>2</sub> in 1 ChCl: 2 EG with current density c.a. 6 mA.cm<sup>2</sup>.

As shown in *Figure 4.23* also shows a zinc deposit obtained using the same conditions but from a normal DC experiment with the same electrolyte but without and suspended zinc particles in solution. It can be seen that the suspended particles give a much thicker deposit (approximately 6 times thicker).

#### 4.4.4 Current Efficiency

The current efficiency was determined gravimetrically using a 5 dp balance and the change in mass was compared with that calculated from Faraday's Law given in *Equation 4.4*. Sequential experiments were performed for each method of deposition, and it was found the only super-efficient system were from samples which were horizontally oriented and deposited with 80-150  $\mu\text{m}$  size particles by PRC as described in *Table 4.5*.

$$m = \frac{QM_{RMM}}{nF} \quad \text{Equation 4.4}$$

where  $m$  is the mass deposited  $Q$  is the charge passed,  $M_{RMM}$  is the relative molar mass of the metal being deposited  $n$  is the number of electrons (2 for Zn) and  $F$  the Faraday constant (96484 C mol<sup>-1</sup>).

The results in *Table 4.5* show for the first time that super-efficient deposition (> 100% current efficiency) is possible powder pulse plating. It should be noted that this was only possible for big particles, (80-150  $\mu\text{m}$ ) with the electrode in a horizontal configuration.

*Table 4.5 current efficiency for the electrodeposition of zinc from various plating systems*

Conditions	ZnCl <sub>2</sub> / mol dm <sup>-3</sup>	Added mass/ g	Charge/ C	Efficiency/ %
PRC horizontal	0.3	0.28317	499	165
PRC vertical	0.3	0.16908	520	96
DC no particles	0.3	0.09625	324	87

Comparing the deposition with a standard DC electrodeposition of zinc without particles added to it shows that the current efficiency is significantly higher. An additional issue that has been observed with the deposition of metals from DESs is that the deposition of

very thick coatings is often difficult by DC deposition. Once the deposit is  $> 20 \mu\text{m}$  the morphology changes and a black friable deposit is obtained. This is thought to be due to the nature of insulating films described in Chapter 3. Powder pulse plating allows thick deposits to be obtained comparatively quickly albeit with a porous structure. To see whether these efficiencies are reasonable, it is possible to calculate an ideal super efficiency by considering what the efficiency would be by packing a spherical particle together into a lattice. For a sphere, the packing efficiency in a cubic lattice is approximately 52%  $((4\pi r^3/3)/(8r^3))$ . Using a DC supply to deposit 48 g of Zn would trap a maximum of 52 g of Zn particles so the maximum current efficiency would be 208%  $(100/48)$ . Given that the packing of the zinc particles is relatively dispersed a deposition efficiency of 165 % is quite respectable.

#### 4.5 Electrochemical Quartz Crystal Microbalance

Electrochemical quartz crystal microbalance is a technique that can be applied to measure the in-situ mass changes on an electrode surface with nanogram resolution. EQCM has been extensively used to study electrochemical processes in DESs.<sup>16, 44, 46-53</sup> The traditional EQCM cell used in the laboratory had a hole at the bottom of a glass cell on to which an EQCM crystal was fixed using silicone glue. However, this method did not function with the powder pulse plating as it did not enable the solution to be stirred. Therefore, a new EQCM cell was designed, and printed to perform the experiments as shown in *Figure 4.24*.

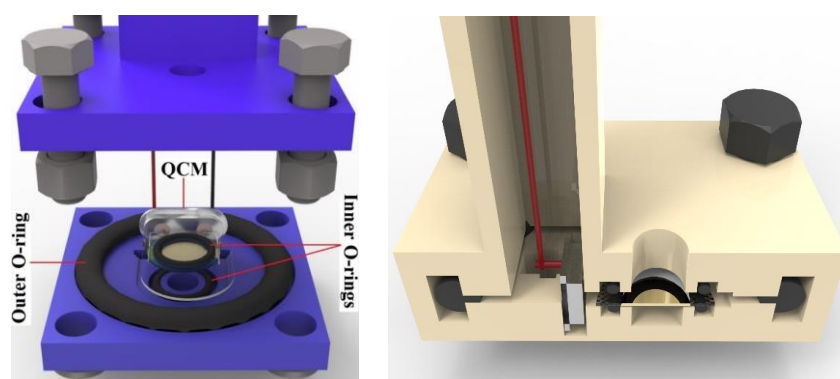


*Figure 4.24* Novel EQCM cell designed to ensure experiments could be carried out at elevated temperatures.

As shown in **Figure 4.24**, the gold coated EQCM crystal is mounted in a horizontal orientation using O-rings above and below the crystal to maintain a seal. Similarly, the leads of EQCM crystal are isolated from liquid contact in rectangular pipe with bigger O-ring. This experiment used 0.0112 g of zinc powder on the exposed gold crystal. As previously,  $0.3 \text{ mol dm}^{-3} \text{ ZnCl}_2$  in 1ChCl: 2EG was used as the electrolyte. A DC potential of -1.2 V was applied for 1300 s.

The admittance data obtained are shown in **Figure 4.25**. As the experiment proceeds the admittance decreases regularly up to 765s where upon there is a large change in admittance. This could indicate the time taken until the zinc particle fuses with the surface. At  $5 \text{ mA.cm}^{-2}$  applied current, the amount of zinc that could be deposited on the gold surface in 765 s would be  $2.73 \times 10^{-4} \text{ g}$  which would equate to a thickness of  $1.8 \text{ }\mu\text{m}$ . Given that the approximate zinc particle size was  $20 \text{ }\mu\text{m}$  this would equate to c.a 10% of the height of the particle which would be in keeping with the results from **Figure 4.25**. Further analysis of the data is not possible as the zinc particles damp the signal and invalidate the conditions needed to apply the Sauerbey equation.

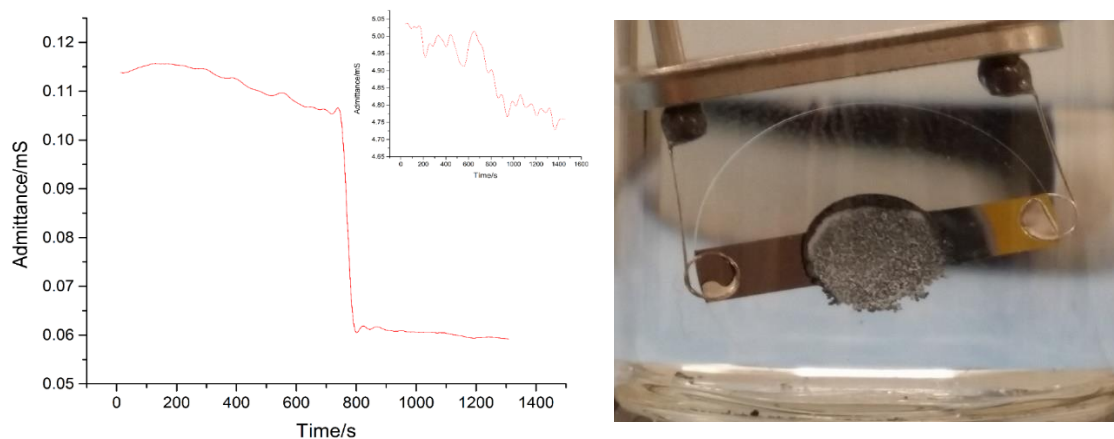


**Figure 4.25** left Powder plating response of QCM crystal for admittance change with respect to time. Inset image shows the response obtained without zinc particles added to the system. Right: Photograph of QCM crystal after the the deposition experiment.

#### 4.6 Electrodeposition of Composite Coatings

As stated at the start of this chapter, one application of this type of approach may be in the deposition of composite coatings. These have been studied for several metals and dispersed phases in the group. Composites coatings are of interest as they have

the ability to modify the coating properties, giving it either increased anti-wear properties or lubricating properties can be introduced by incorporating polymer particles. The particles to be dispersed in the metallic coating are usually small (30-50 nm) so they do not settle out too quickly in the plating solution. The solutions are also stirred vigorously to maintain an even distribution.<sup>54-57</sup> Some studies have been able to achieve alumina loadings of up to 35 wt % in the metal coatings.

Ettaib showed that various particulate materials could be suspended in DESs including Si<sub>3</sub>N<sub>4</sub>, SiC, BN, Al<sub>2</sub>O<sub>3</sub>, and diamond. Even quite large particles (5 μm) formed stable suspensions without the need for stirring. This is because the DESs are very viscous and the high ionic strength of the liquids shields the particles from each other electrostatically. It was shown for example, that 1 μm Al<sub>2</sub>O<sub>3</sub> particles took about 24 hours to settle out whereas 0.05 μm particle suspensions are stable for more than a week.<sup>45</sup> Electrodeposition of copper/Al<sub>2</sub>O<sub>3</sub> composites was achieved but the distribution of the alumina particles was not particularly even. The same was true for PTFE particles. The same study also investigated nickel composites with similar results. Subsequent work by Juma studied the deposition of hard Ni/chrome carbide coatings using the same DES. The chrome carbide particles were scattered on the substrate surface and the nickel was electrodeposited around them.<sup>58</sup> This resulted in a relatively even particle distribution and good adhesion of the dispersed phase to the substrate. The coatings were found to be extremely wear resistant.

In the current study, an alternative approach was attempted: The dispersed phase was mixed with the zinc particles and these were then placed in contact with a smaller printed cell, but same technique performed in section 4.4.2 onto a 2 cm x 2 cm copper substrate. This should ensure an even particle distribution and it should enable highly dispersed phase content to be obtained. The experiment should also be independent of the particle size.

**Table 4.6** Experimental system and procedure is the same given in section 4.4.2.

$T/ ^\circ\text{C}$	$I_a/ \text{mA}$	$t_a/ \text{s}$	$I_c/ \text{mA}$	$t_c/ \text{s}$	$t_{total} / \text{s}$
50	8	2	28	10	13200

Two different dispersed phases were tested  $\text{Al}_2\text{O}_3$  and SiC with zinc particles in two separate experiments. In the experiments 0.01 gram of 320 grit (diameter c.a  $50\ \mu\text{m}$ ) SiC particles were used with 0.05 g of Zn powder (diameter c.a  $40\text{-}60\ \mu\text{m}$ ). A pulse experiment was used, and the deposition conditions are shown in **Table 4.6**. As shown in **Figure 4.26**, SiC particles are relatively evenly distributed throughout the sample but it is clear that zinc is not well adhered to or around the SiC (darker particles).

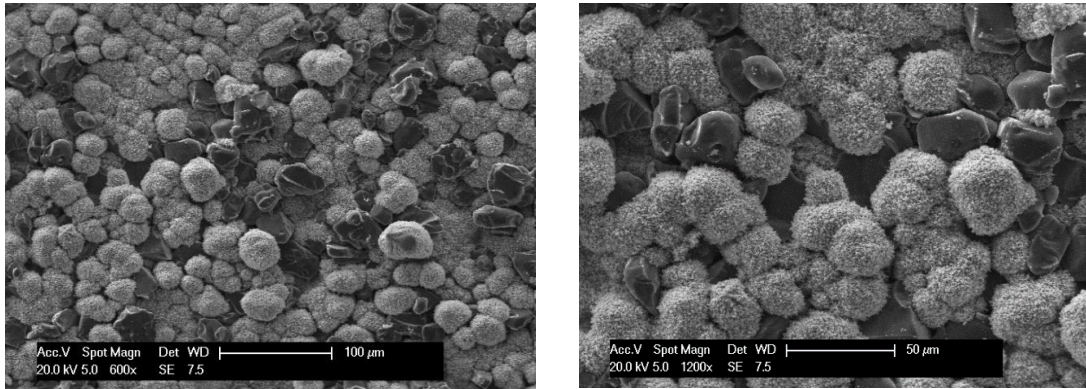


**Figure 4.26** SEM image of a Zn/SiC composite coating obtained using the deposition conditions shown in **Table 4.6** in 0.3 M  $\text{ZnCl}_2$  dissolved in 1 ChCl: 2 EG solution.

There appears to be some entrapment, but the particles are not well adhered to the surface (although they do survive physical washing). The experiment in **Table 4.6** was repeated using the same conditions but using  $\text{Al}_2\text{O}_3$  particles (c.a  $20\ \mu\text{m}$  in diameter). The deposit obtained from this process is shown in **Figure 4.27**. It can again be seen that adhesion to the alumina (darker particles) is poor although fusion has occurred in the zinc particles.

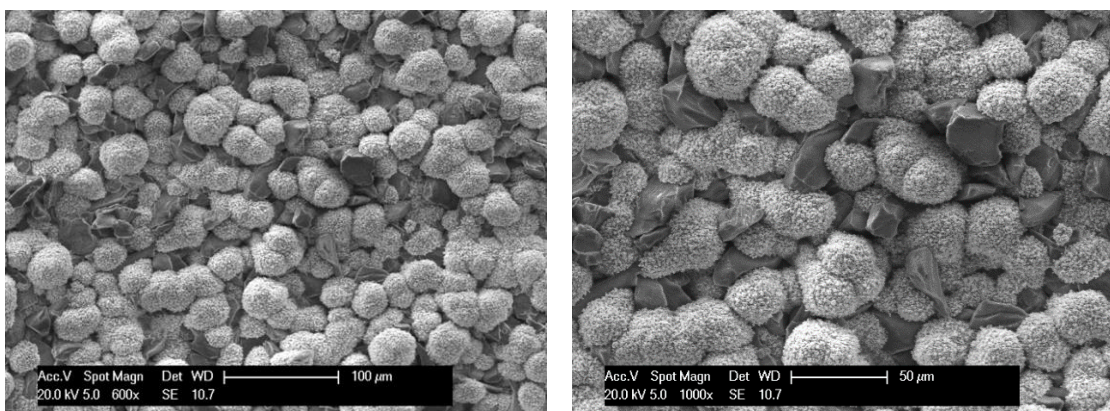


**Figure 4.27** SEM image of a Zn/  $\text{Al}_2\text{O}_3$  composite coating obtained using the deposition conditions shown in **Table 4.6**

## 4.7 Conclusion

In this section of work, it was aimed to adhere zinc particles onto a substrate through cycling the particles via alternating anodic and cathodic charge cycles. Initially the electrochemistry of single zinc particles was studied using cyclic voltammetry and it was found that on small particles gas evolution was an issue that caused the zinc particle to move on the electrode substrate during the cycle. This was less of an issue with larger zinc particles.

Numerous experimental set-ups were attempted using the electrode in both vertical and horizontal configurations to achieve bulk deposition. It was found that for horizontal orientation large zinc particles needed to be used as gravity was needed to ensure the particles retained a good physical contact with the substrate. Cycling the current under these conditions enabled homogeneous zinc layers to be deposited. The anodic cycle was clearly levelling the large zinc particles. The optimal conditions for reduction and oxidation were examined, and it was found that 0.3 M  $\text{ZnCl}_2$  dissolved medium with low frequency, and an effective duty cycle of approximately 75% was needed to ensure fusion of the particles with the surface and with each other.

To enable zinc plating in the vertical orientation an alternative approach was developed. Here zinc chloride was added to the electrolyte and small zinc particles were suspended in the electrolyte. Under these conditions, thick, homogeneous deposits were obtained demonstrating that powder pulse plating is a viable method for coating surface. The current density was calculated for different deposition conditions and it was found that under some conditions, super-efficient deposition could be obtained. This clearly occurs due to zinc being incorporated onto the surface which did not need to be electrochemically reduced. Efficiencies of up to 165% with average of 140% were recorded. This is quite high given the packing density of the zinc particles.

In the final part of this study a composite material was created by mixing alumina and silicon carbide with the zinc particles before the powder pulse plating. These particles are clearly not electroactive, but the zinc was able to pack around the inert particles. It should be noted, however that wetting was not particularly the case, and the dispersed phase was not particularly well adhered to the zinc particles.

## 4.8 References

1. A. P. Popkov, *J. Appf. Chem. USSR*, 1966, **39**, 1630.
2. A. M. Dzerov, N.P. Ivishke, I. N. Vavilina, P. M. Chetvertnov and Y.E. Zhak, *J.Appl. Chem. USSR*, 1967, **40**, 1101.
3. N. V. Mandich, *Metal Finishing*, 2002, **100**, 359-364.
4. R. Olson, *Products Finishing*, 1976, **40**, 68.
5. R. Krishnamoorthi, R. Sundaram and N. Gunasekaran, *Plating and Surface Finishing*, 1974, **74**, 122.
6. D. L. Rehrig, *Plating*, 1974, **61**, 43.
7. C. Raub and A. Knodler, *Gold Bul.*, 1977, **10**, 38.
8. C. Raub and A. Knodler, *Plating*, 1978, **65**, 32.
9. A. Knodler, *Galvano Technique*, 1981, **72**, 1167.
10. L. G. Holmbom and B. E. Jacobsson, presented in part at the AESF, III International Symp., Washington, 1986.
11. T. Yanashika and M. Ito, *J. Metal Finishing Sot. Japan*, 1988, **4**, 214.
12. V. J. Landvay and C. J. Raub, *Metalloberflaeche*, 1975, **29**, 165.
13. Y. Y. Wang, C. S. Tury and C. C. Wan, *Metal Finishingq*, 1980, **78**, 21.
14. J. Puipe, presented in part at the AESF Third International Pulse Plating Symposium, Washington, 1986.
15. M. Ghaemi and L. Binder, *Journal of Power Sources*, 2002, **111**, 248-254.
16. A. Marlot, P. Kern and D. Landolt, *Electrochimica Acta*, 2002, **48**, 29-36.
17. K.-M. Yin, S.-L. Jan and C.-C. Lee, *Surface and Coatings Technology*, 1997, **88**, 219-225.
18. S. Kainuma, S. Ishikura and K. Hisatake, *J. Magn. Soc. Jpn.*, 1995, **21**, 889.
19. T. Houga, A. Yamada and Y. Ueda, *Journal of the Japan Institute of Metals and Materials*, 2000, **64**.
20. Y. Ueda, N. Hataya and H. Zaman, *Journal of magnetism and magnetic materials*, 1996, **156**, 350-352.

21. M. Alper, K. Attenborough, R. Hart, S. Lane, D. Lashmore, C. Younes and W. Schwarzacher, *Applied physics letters*, 1993, **63**, 2144-2146.
22. K. I. Popov, D. N. Keca and B. I. Vuksanovic, *J. Appl. Electrochem.*, 1977, **7**, 185.
23. J. Puipe and N. Ibl., *Plating and Surface Finishing*, 1980, **67**, 68.
24. A. Chinda and O. Yoshika, *J. Metal Finishing Soc. Japan*, 1984, **4**, 221.
25. S. Ghosh and S. Roy, *Surface and Coatings Technology*, 2014, **238**, 165-173.
26. N. Tantavichet and M. D. Pritzker, *Journal of The Electrochemical Society*, 2003, **150**, C665-C677.
27. R. Herdman, *Journal*, 2004, **US20040074775 A1**, USA Patents.
28. M. J. K. Kim, Jae Jeong, *Korean Chemical Engineering Research*, 2014, **52**, 26-39.
29. T. Pearson and J. K. Dennis, *Transactions of the IMF*, 1991, **69**, 75-79.
30. S. Tao and D. Li, *Nanotechnology*, 2005, **17**, 65.
31. H. Y. Cheh, *Journal of The Electrochemical Society*, 1971, **118**, 551-557.
32. K. Saber, C. C. Koch and P. S. Fedkiw, *Materials Science and Engineering: A*, 2003, **341**, 174-181.
33. W. Paatsch, presented in part at the First AES International Pulse Plating Symposium, Boston, 1979.
34. A. E. Saba and A. E. Elsherief, *Hydrometallurgy*, 2000, **54**, 91-106.
35. W. E. and G. Hansal, in *Pulse-Plating*, Eugen G. Leuze Verlag KG, Leuze, E G (Verlag), 2012, ch. 120-182, p. 388.
36. M. Schwartz, in *Handbook of deposition technologies for films and coatings: science, technology and applications*, ed. R. F. Bunshah, Noyes Publications, Los Angeles, California, 2nd edn., 1994, vol. 4, pp. 506-539.
37. M. S. Chandrasekar and M. Pushpavanam, *Electrochimica Acta*, 2008, **53**, 3313-3322.
38. R. Ramanauskas, L. Gudavičiūtė, A. Kaliničenko and R. Juškėnas, *Journal of Solid State Electrochemistry*, 2005, **9**, 900-908.
39. J. Fei, G. Liang and W. Xin, *Journal of Wuhan University of Technology-Mater. Sci. Ed.*, 2007, **22**, 417-421.

40. M. Sajjadnejad, A. Mozafari, H. Omidvar and M. Javanbakht, *Applied Surface Science*, 2014, **300**, 1-7.
41. C. Müller, M. Sarret and T. Andreu, *Electrochimica Acta*, 2003, **48**, 2397-2404.
42. A. P. Abbott, G. Capper, K. J. McKenzie and K. S. Ryder, *Journal of Electroanalytical Chemistry*, 2007, **599**, 288-294.
43. X. Xie, X. Zou, X. Lu, C. Lu, H. Cheng, Q. Xu and Z. Zhou, *Applied Surface Science*, 2016, **385**, 481-489.
44. J. C. Barron, PhD thesis, University of Leicester, 2009.
45. K. E. ttaib, PhD thesis, University of Leicester, 2010.
46. G. Sauerbrey, *Zeitschrift für Physik*, 1959, **155**, 206-222.
47. S. Bruckenstein and M. Shay, *Electrochimica Acta*, 1985, **30**, 1295-1300.
48. W. Vielstich, A. Lamm and H. A. Gasteiger, *Handbook of Fuel Cells*, John Wiley & Sons, Inc., New York, 2003.
49. A. R. Hillman and M. A. Mohamoud, *Electrochimica acta*, 2006, **51**, 6018-6024.
50. S. Zein El Abedin, E. M. Moustafa, R. Hempelmann, H. Natter and F. Endres, *Chemphyschem : a European journal of chemical physics and physical chemistry*, 2006, **7**, 1535.
51. F. Endres, A. Abbott and D. MacFarlane, *Electrodeposition from ionic liquids*, John Wiley & Sons, Weinheim, 2 edn., 2017.
52. N. Borisenko, A. Ispas, E. Zschippang, Q. Liu, S. Zein El Abedin, A. Bund and F. Endres, *Electrochimica Acta*, 2009, **54**, 1519-1528.
53. A. Alhaji, PhD thesis, University of Leicester, 2011.
54. A. Lozano-Morales and E. J. Podlaha, *Journal of The Electrochemical Society*, 2004, **151**, C478-C483.
55. E. J. Podlaha, *Nano Letters*, 2001, **1**, 413-416.
56. E. J. Podlaha and D. Landolt, presented in part at the AESF SUR/FIN Annu. Int. Technol. Conf, 1998, 1998.
57. E. J. Podlaha and D. Landolt, *Journal of The Electrochemical Society*, 1997, **144**, L200-L202.
58. J. A. Juma, PhD thesis, University of Leicester, 2016.

**Chapter-V**  
**Copper Powder Deposition**

## 5.1 Introduction

Copper or its alloys with other metals has been extensively used for processes such as electronic, optic, automobile, and aerospace applications.<sup>1</sup> Copper deposition has a great interest in printed circuit board industry for manufacturing large scale printed circuit boards where it is the interconnect material of choice.<sup>2-4</sup> Although copper is more brittle compared to the aluminium it has a higher electrical conductivity and is intrinsically less susceptibility to electromigration.<sup>4-7</sup>

Copper deposition is often used as a pre-coating for other metals so that it is easier to deposit other metals on top of it. It is often used when the substrate is reactive or when there is a miss-match between the lattice structure of the substrate and the coating e.g. between some steels and nickel.<sup>8</sup> The copper layer can improve the electroplating quality by means of increasing the hardness, decreasing the porosity or smoothing out surface irregularities in the substrate.<sup>9</sup>

Copper electrodeposition has been extensively studied in ionic liquids. It was initially carried out using chloroaluminate based ionic liquids in 1960s and 1970s.<sup>10-13</sup> In the 1990s, copper deposition was studied in ionic liquids with discrete anions such as  $[\text{BF}_4]^-$ .<sup>14, 15</sup>

Abbott et al. studied copper deposition from the mixture of 1ChCl: 2EG<sup>16</sup> and showed that copper has two redox process; the  $\text{Cu}_{(\text{II})}/\text{Cu}_{(\text{I})}$  couple at 0.43 V, and the  $\text{Cu}_{(\text{I})}/\text{Cu}_{(0)}$  couple at -0.45 V. The formed couple was used to determine the diffusion coefficient for  $\text{CuCl}_4^{2-}$  using the Randles-Sevcik relation. This was found to be  $2.42 \times 10^{-7} \text{ cm}^2 \text{ s}^{-1}$  at 25°C.<sup>16</sup> Chronocoulometry experiments carried out using 0.01 M  $[\text{CuCl}_2 \cdot 2\text{H}_2\text{O}]$  in 1ChCl: 2EG revealed a strong linear correlation between deposition charge and  $t^{1/2}$  which indicated the deposition process was diffusion controlled. The current efficiency of the deposition was determined from a charge versus mass plots obtained using an electrochemical quartz crystal microbalance and it was found to be 99.2% at a deposition potential of -0.8 V.<sup>16</sup> Chronoamperometry was also studied to determine the nucleation mechanism of  $[\text{CuCl}_2 \cdot 2\text{H}_2\text{O}]$  in both 1ChCl: 2EG and 1ChCl: 2urea solutions. A conventional Sharifker- Hills approach was used by plotting dimensionless current against time. It was shown that the current data fitted a 3-dimensional instantaneous

mechanism at shorter time scales, and changed to a 3-dimensional progressive nucleation at longer time scales. This was different to aqueous solutions which changed from progressive nucleation to instantaneous nucleation with increasing concentration.<sup>17</sup>

The high viscosity of neat DESs is often perceived as a difficulty with metal plating. It can, however be advantageous for the deposition of composite materials. DESs demonstrate coulombic screening of surface charge which enables them to stabilise colloidal dispersions. Typically, composite materials are deposited by suspending the dispersed phase in the plating solution and maintained in dispersion using vigorous stirring. It was found that in DESs, relatively large particles (1-5  $\mu\text{m}$  in diameter) could be suspended and the colloidal solutions were stable for at least 24 h without stirring.<sup>18</sup>

It was shown with both copper and nickel electrodeposition that these particles could be dragged onto the surface as electroplating took place. Another interesting finding was that suspended particles increased the free volume of the liquid which resulted in an increase in conductivity and a decrease in viscosity as the particles acted as stirrers in the medium creating holes in the liquid.<sup>19</sup> Bulk deposition was performed with  $\text{Al}_2\text{O}_3$  loadings as 3%, 5% and 10% (w/w), and results given and the amount of dispersed phase in the copper layers was found to be proportional to the amount of the particles in solution.<sup>16</sup>

## **5.2 Project Aims and Objective**

The previous chapter on zinc powder pulse deposition showed that one of the issues with the deposition of zinc is the gassing which occurred on the electrode surface and the insolubility of the complex which formed following anodic dissolution. The use of copper should simplify this process as the reduction potential of copper is less negative and copper is less oxophilic than zinc. This section aims to repeat the experiments of the previous chapter to compare and contrast the efficacy of this technique with a less electronegative metal.

## 5.3 Result and Discussion

### 5.3.1 Cyclic Voltammetry Studies

Similar to the zinc deposition, copper powder was placed onto working electrode (Pt) to enable voltammetric studies. With copper, no spring was required because copper dissolution and deposition did not produce gases that could cause a loss in connection between the particle and the substrate as was demonstrated with zinc powder in chapter 4.

**Figure 5.1** shows the cyclic voltammogram for 0.4 M  $\text{CuCl}_2$  in 1ChCl: 2EG on a Pt electrode at  $47.5 \pm 2.5$  °C. It can be seen that the same two redox process as described earlier<sup>20</sup> are observed.

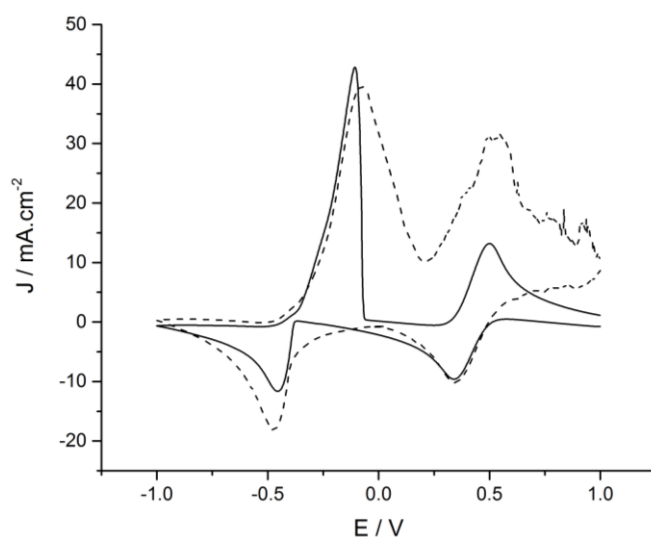


**Figure 5.1** Solid line represents the CV of 0.4 M  $\text{CuCl}_2$  in 1ChCl: 2EG on a Pt working electrode at c.a.  $47.5 \pm 2.5$  °C at  $20 \text{ mV}\cdot\text{s}^{-1}$ . Dashed line represents is the same with a single copper particle ( $150 \mu\text{m}$ ) on the working electrode.

The  $\text{Cu}^{\text{II}}/\text{Cu}^{\text{I}}$  couple was studied as a function of sweep rate and the diffusion coefficient was determined using the Randles-Sevcik equation (See Appendix 7.1).  $D_0$  for the  $\text{Cu}^{\text{II}}/\text{Cu}^{\text{I}}$  was found to be  $8.65 \times 10^{-7} \text{ cm}^2\cdot\text{s}^{-1}$  at 45 °C. This was slightly higher than that previously obtained by Abbott et-al<sup>16</sup>  $2.47 \times 10^{-7} \text{ cm}^2 \text{ s}^{-1}$  which is understandable given the difference in temperature (20 °C) between the two studies.

When the voltammetric experiment was repeated under the same parameters but this time using a copper particle in contact with the working electrode, a slightly different CV was obtained as shown in **Figure 5.1** (dashed line). The copper particle was from a sample classed as ca. 100 mesh sizes, which should be approximately equal to 149  $\mu\text{m}$  in diameter. **Figure 5.2** shows an SEM image of the copper powder and the particle size is quite diverse ranging from 50 to 180  $\mu\text{m}$  although most particles are quite spherical, and the surfaces are quite smooth.

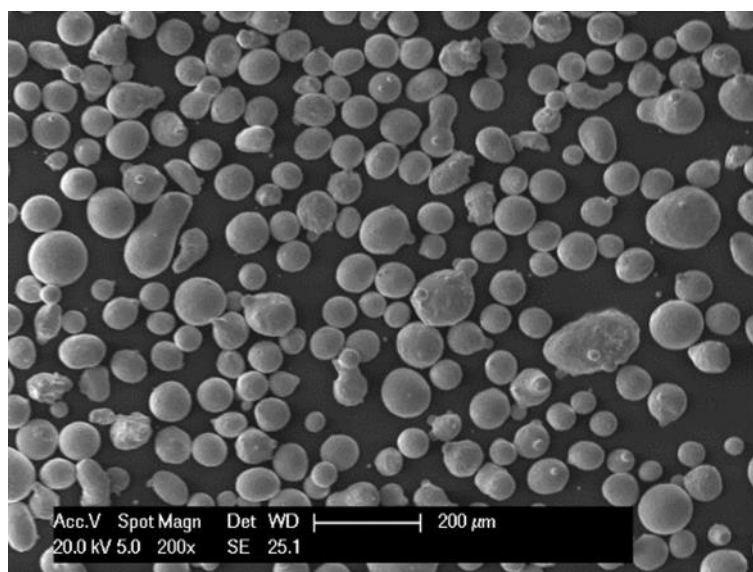


**Figure 5.2** SEM images of the ca. 100 mesh copper powder used in the experiments.

**Figure 5.1** (dashed line) shows a similar response on the reductive cycle with and without the copper particle present. The main difference is that the steady state current at + 1.0 V is higher with the copper particle on the electrode which is due to copper dissolving from the particle. This shows that a good electrical contact is present between the particle and the electrode without the need for external pressure to retain a contact. The deposition current is also larger from the higher local copper concentration resulting from copper dissolution at positive over potentials. On the anodic sweep, the main difference is observed for the  $\text{Cu}^{\text{I}}/\text{Cu}^{\text{II}}$  couple. It would be expected that the large reservoir of copper in the particle would stop the oxidative current reaching a diffusion limited current. The noisy oxidative current suggests that there may be a film forming on the electrode surface. The Pt disc working electrode had an area of  $7.85 \times 10^{-3} \text{ cm}^2$  and the surface area should not change significantly when the Cu particle is placed on the surface. Assuming a particle with radius 75  $\mu\text{m}$  should increase the surface area to  $8.09 \times 10^{-3} \text{ cm}^2$  i.e. a relative

increase in area of only 1.03 times and this is the reason that the currents are relatively similar.

#### 5.4 Anodic Dissolution of Copper

**Figure 5.3** shows the cyclic voltammogram for a Pt electrode in of 50 mM  $\text{CuCl}_2 \cdot 2\text{H}_2\text{O}$  dissolved in 1ChCl: 2EG, and that for an analogous experiment with a copper working electrode.

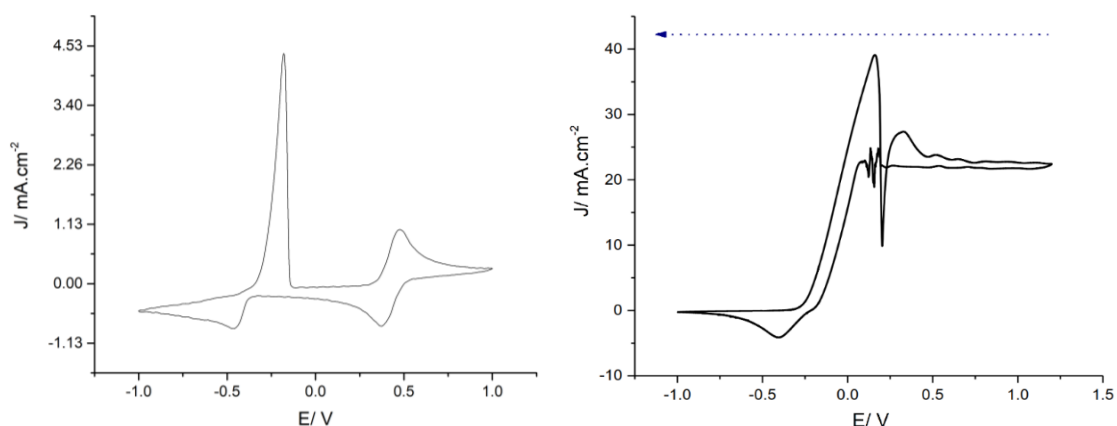


**Figure 5.3** Cyclic voltammogram of 50 mM  $\text{CuCl}_2 \cdot 2\text{H}_2\text{O}$  dissolved in 1ChCl: 2EG, at 20 °C with a scan rate of 20  $\text{mV} \cdot \text{s}^{-1}$  on at Pt electrode (left) and on a Cu electrode (right). In both, Ag/AgCl is RE, and Pt flag is CE.

**Figure 5.3** shows that the copper electrode has a much higher anodic current density. The onset potential for  $\text{Cu}^0$  being oxidised to  $\text{Cu}^{\text{I}}$  occurs at the same potential and the higher current density is clearly due to the copper electrode having a much larger reservoir of copper to dissolve. The current for the anodic dissolution decreases rapidly at approximately +0.2 V before increasing again to a secondary peak at c.a. 0.3 V before levelling off.

On the cathodic sweep, the current remains approximately constant until +0.1 V when there is a noise associated with the process which is perfectly reproducible in successive scans. On the cathodic cycle at potentials more negative than 0 V the current decreases before reaching a peak at -0.4 V due to copper deposition. The passivation on the anodic sweep and noise on the cathodic sweep occur at about the same potential at the  $\text{Cu}^{\text{I}} / \text{Cu}^{\text{II}}$  redox couple on the Pt electrode.

The same process was studied recently by Karim<sup>21</sup> who ascribed the process to passivation and bulk electrolysis in an unstirred electrolyte produced a green coating on the anode surface which was  $\text{CuCl}_2$ . (It should be explained that this part of the study took place at the beginning of the research project at about the same time as Karim's study).

To study these processes linear sweep voltammetry was carried out. Two different linear sweep voltammograms were obtained as shown in **Figure 5.4**, the left one was scanned anodically starting from -0.5 V and ramping the potential to 0.5 V, and right one was scanned cathodically starting from 0.5 V down to -1.0 V.

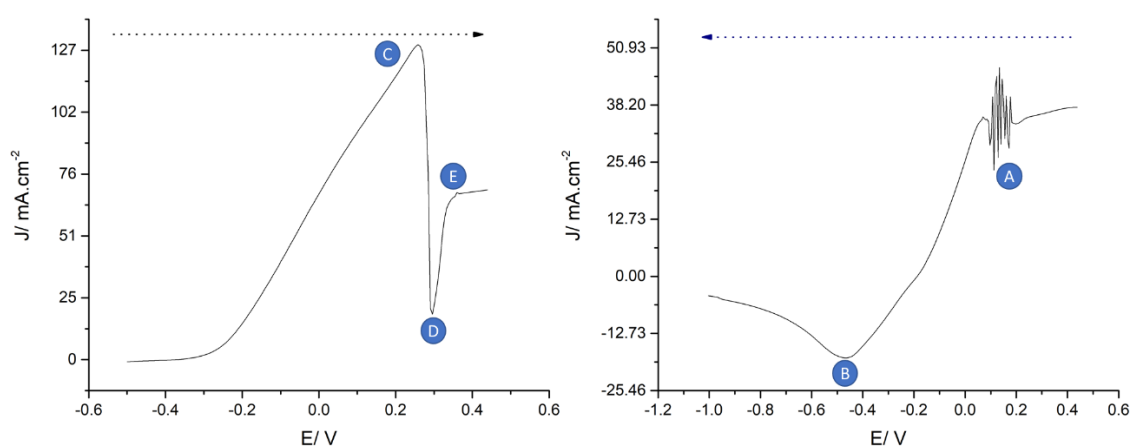


**Figure 5.4** Linear sweep voltammetry of copper disc working electrode (RE is Ag/AgCl and Pt flag is CE) at 20 °C with sweep rate of  $5 \text{ mV}\cdot\text{s}^{-1}$  in bare 1 ChCl: 2 EG solution. Left side represents the anodic scan, and right side represents the cathodic scan as shown dotted arrows at top of graphs.

**Table 5.1** shows the probable processes occurring on the linear sweep voltammograms in **Figure 5.4**. It may seem unusual to suggest that the passivation is due to copper chloride precipitating on the electrode as copper chloride would normally be thought of as having high solubility. It should however be noted that most experiments which have solubilised copper chloride in DESs have used copper chloride dihydrate which has a much lower lattice energy and is therefore easier to dissolve. To dissolve the anhydrous salt required prolonged heating and stirring.

**Table 5.1** Potential assignment of features in the LSVs of copper in 1ChCl: 2EG.

Point	Explanation	Reactions
A	Cu <sup>I</sup> /Cu <sup>II</sup> chloride equilibrium for solid and solution phases	$\text{CuCl}_2(\text{s}) + 2\text{Cl}^- \rightleftharpoons \text{CuCl}_4^{2-}$ $\text{CuCl} \rightleftharpoons \text{Cu}^+ + \text{Cl}^-$
B	Electrodeposition of Cu <sup>I</sup> species	$[\text{CuCl}_2]^- + \text{e}^- \rightleftharpoons \text{Cu}(\text{s}) + 2\text{Cl}^-$
C	Oxidation of Cu <sup>(I)</sup> species	$\text{Cu} \rightleftharpoons \text{Cu}^+ + \text{e}^- / \text{Cu}^+ + 2\text{Cl}^- \rightleftharpoons [\text{CuCl}_2]^-$
D	Salt formation	$[\text{CuCl}_2]^- \rightleftharpoons \text{CuCl}_2 + \text{e}^-$
E	Salt dissolution	$\text{CuCl}_2 + 2\text{Cl}^- \rightleftharpoons [\text{CuCl}_4]^{2-}$

If precipitation is the cause of the “noise” then it should be sweep rate dependent. **Figure 5.5** shows the cathodic LSV as a function of sweep rate with and without CuCl<sub>2</sub>. On the cathodic scan, the noise was obtained at c.a 0.1 V for all sweep rates. It was found that the noise did shift potential slightly in a cathodic direction with increasing scan rate.

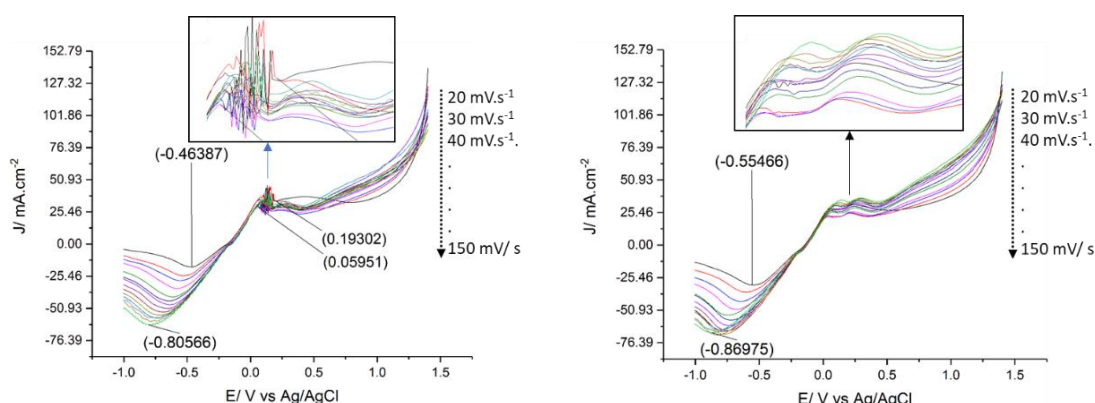


**Figure 5.5** Cu disc working electrode (RE is Ag/AgCl and Pt flag is CE) was scanned from 1.5 V to -1.0 V for different sweep rates ranging from 20 mV.s<sup>-1</sup> to 150 mV.s<sup>-1</sup> (left) in pure 1 ChCl: 2 EG, and (right) in 0.4 M CuCl<sub>2</sub>.2H<sub>2</sub>O in 1 ChCl: 2 EG.

The same experiment was repeated with 0.4 M CuCl<sub>2</sub>.2H<sub>2</sub>O in solution. The aim behind this experiment was to pre-saturate the solution with copper salt. **Figure 5.5**, (right) shows that the noise is lost, and two small peaks are formed at point B. This shows that the feature is probably due to film formation. This means that just like the case for zinc, anodic polarisation leads to a film on the electrode surface which will affect the way in which the electrode can be pulsed.

### 5.4.1 LSV of Copper under 3D Optical Profiler

In chapter 3 it was shown that the optical profiler can be used to image processes in-situ on the electrode surface when it is polarised. Dissolution of the copper disc electrode was performed under the 3D optical profiler using the cell shown in **Figure 3.9**. Dissolution of the Cu disc electrode was carried out at room temperature in 1ChCl: 2EG without CuCl<sub>2</sub> during an LSV experiment under the optical profiler with 100X magnification. The images are shown in **Figure 5.6**. At the start of the experiment a bright copper film is observed. This does not change significantly in appearance until between c.a. 0.22 V when the surface starts to darken.

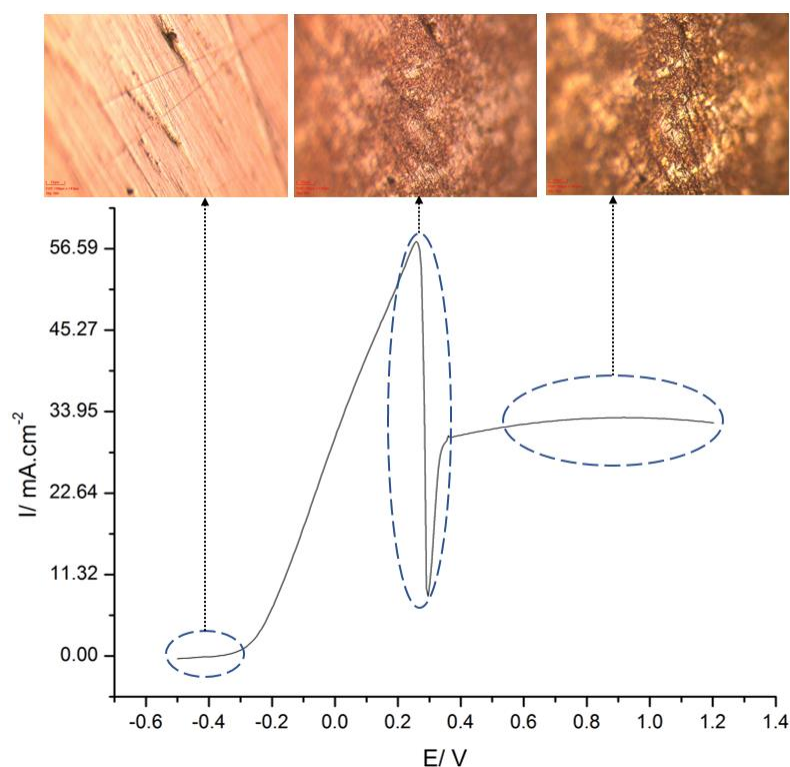


**Figure 5.6** Given Optical images on top shows in situ dissolution of Cu working electrode (Ag/AgCl is RE, and Pt flag is CE) under 3D optical profiler. Potential was scanned anodically from -0.4 V to 1.4 V with sweep rate of  $5 \text{ mV.s}^{-1}$  at room temperature under a 3D optical profiler.

After 0.4 V the current increases again before levelling off. The surface changes colour and becomes a darker brown. This phenomenon clearly shows the formation of the film does occur across the whole electrode. **Figure 5.7** shows that surface roughness plays an important role during this process. It shows a series of images from the potential sweep

which spans 60 mV in less than 1 s. It can be seen how the electrode darkens across the field of view which is approximately 100  $\mu\text{m}$  wide. On the reverse scan, the film takes much longer to redissolve.

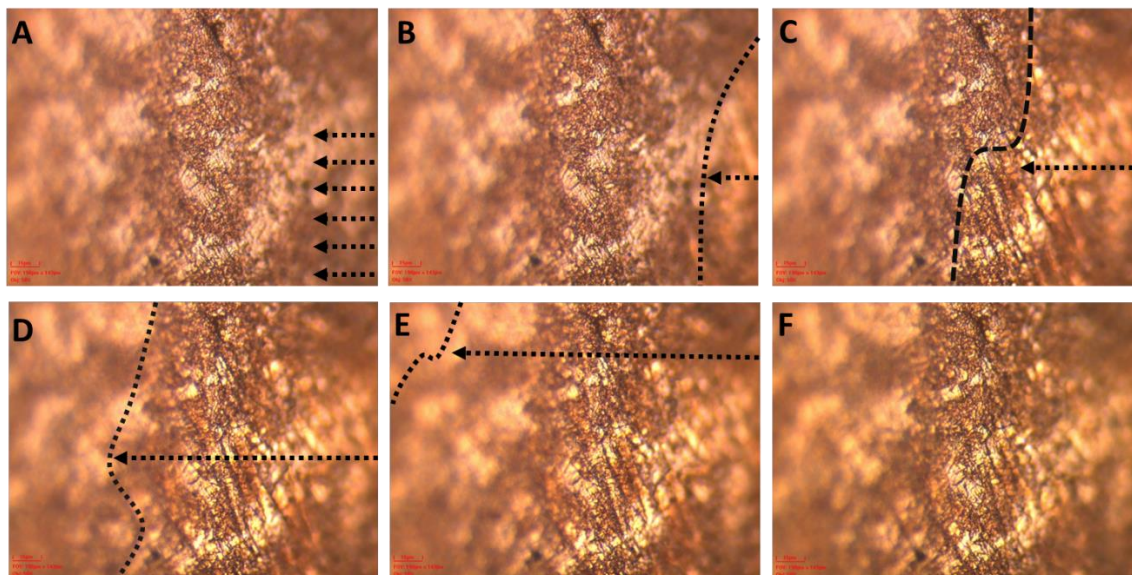


**Figure 5.7** Microscope images of  $\text{CuCl}_2$  film formation with steps of 0.22 V at **A** (0.166 ms) (no film), film formation starts from the bottom edge right at **B** (0.332 ms), film reaches the middle at **C** (0.498 ms), the film covers the 70% at **D** (0.664 ms), and is mostly complete at **E** (0.830ms), and **F** (0.996 ms) at c.a 0.28 V.

To show that the solution would become rapidly saturated on an anodic pulse it is possible to take the diffusion coefficients calculated earlier with the current densities listed above and determine the amount of material that would be dissolved in a unit volume and time. A pulse of 5 s would result in  $1.2 \times 10^{-6}$  moles  $\text{cm}^{-2}$  of Cu being oxidised. Given that the diffusion coefficient of  $\text{CuCl}_4^{2-}$  at 25  $^\circ\text{C}$  is  $2.47 \times 10^{-7}$   $\text{cm}^2\text{s}^{-1}$  the species can diffuse a maximum of 5  $\mu\text{m}$  in that time. ( $\langle x \rangle = (Dt/\pi)^{1/2}$ ). That makes an average concentration of copper of  $2.4 \times 10^{-3}$  mol  $\text{cm}^{-3}$  or 2.4 mol  $\text{dm}^{-3}$ . This exceeds the solubility for anhydrous  $\text{CuCl}_2$  and it is therefore not surprising that after this time the surface layer becomes saturated. Clearly, as the temperature is increased the solubility will increase and the diffusion coefficient will increase. This should mean that anodic pulse lengths could be increased at higher temperatures.

## 5.4.2 Electrochemical Impedance Study of Copper Metal

As in Chapter 3, electrochemical impedance spectroscopy was used to investigate the properties of the film forming on the copper surface. **Figure 5.8** shows the linear sweep voltammetry for 1 ChCl: 2 EG containing 0.1 M  $\text{CuCl}_2$  (top), and the EIS responses at the two potentials marked **A** and **B** (underneath).

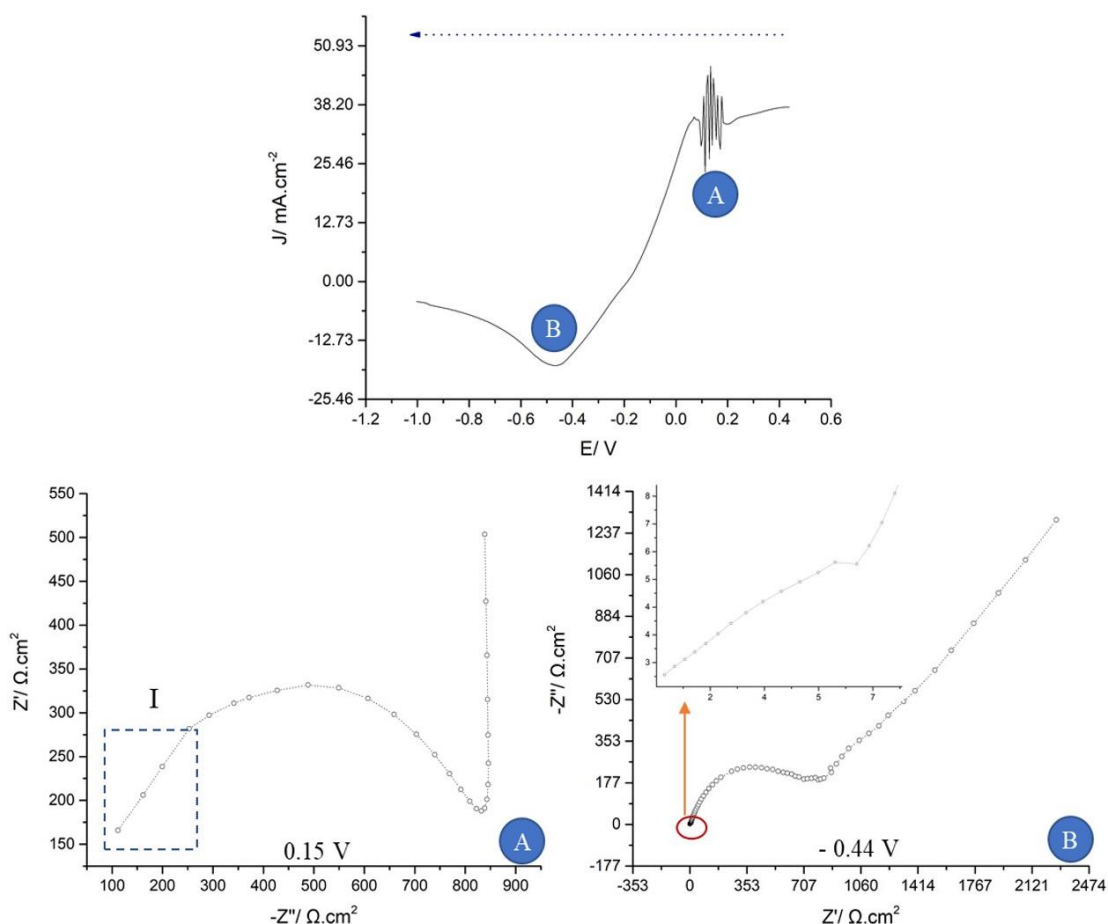


**Figure 5.8** Linear sweep voltammetry during cathodic scan for 1 ChCl: 2 EG containing 0.1 M  $\text{CuCl}_2$  and the EIS responses obtained at points **A** and **B** with Pt flag CE, Pt WE vs Ag/AgCl RE at sweep rate of  $20 \text{ mVs}^{-1}$ .

During the cathodic scan (points **A** and **B**), and anodic scan (points **C**, **D**, and **E**), electrochemical impedance spectroscopy was carried out but in each experiment freshly prepared liquids and clean electrode were used for each experiment.

The EIS measurement performed at point **A** shows a response similar to semi-infinite Warburg line, represented as **I**, just before a complete semi-circle. Although, it is very similar to a Warburg diffusion circuit element, it is known as an *O element*.<sup>22</sup> In the region

of the *O element* diffusion of ionic species is slowed down by the formation of a film or a porous coating.<sup>22-24</sup> It may be ascribed to the formation of a thin copper chloride film which acts as a reflective boundary. In the reflective boundary region, the concentration does not change at the double layer/ film boundary as it acts as an impermeable layer on the electrode surface,<sup>25</sup> and in this case it seems reasonable to explain the source of noise at **A** in LSV experiment.

The EIS at point **B**, (-0.44 V) can be seen in **Figure 5.8**. It shows a 45° semi-infinite line, called as *T element*. If the semicircle has no Warburg response or reflective boundary (i.e. no diffusion anymore), it can be referred as *O element*, but if a Warburg impedance appear after the completion of semi-circle (i.e. diffusion occurs) it can be referred as a *T element*.<sup>22-24</sup> A *T element* is the characteristic of a film which contains a fixed amount of electroactive substance. At point **B**, the electrode surface still has some film from point **A**, and also some diffusion of a Cu<sup>I</sup> species to reduce as metallic copper. As the potential is quite negative, it likely that the copper chloride film is being broken down to deposit metallic copper.

EIS measurements were performed at points **C**, **D**, and **E** in **Figure 5.9** again using fresh liquids, and clean electrodes for each experiment. The EIS data collected at point **C** shows a Randle's circuit with Warburg impedance which is the diffusion controlled oxidation of metallic copper to a Cu<sup>I</sup> species.

At point **D** where there was a sudden decrease in current on the LSV, a semi-circle response is followed by a Warburg impedance, and then a straight, vertical line, which is again a reflective boundary type of behaviour.<sup>25</sup> As described before, in the reflective boundary region concentration does not change on the double layer/ film, and it is assumed that the point **D** is the region that electrode surface is started to be blocked by CuCl<sub>2</sub>.

For the EIS measurement at point **E**, in **Figure 5.9** it is assumed to have some re-dissolution of CuCl<sub>2</sub>. Two semi-circles are observed potentially representing the re-dissolution of the copper salt producing a semi-permeable layer. At lower frequencies a reflective boundary (impermeable layer) is observed which then converts to an apparent

Warburg at even lower frequencies. These data are consistent with the mechanism proposed in *Table 5.1*.

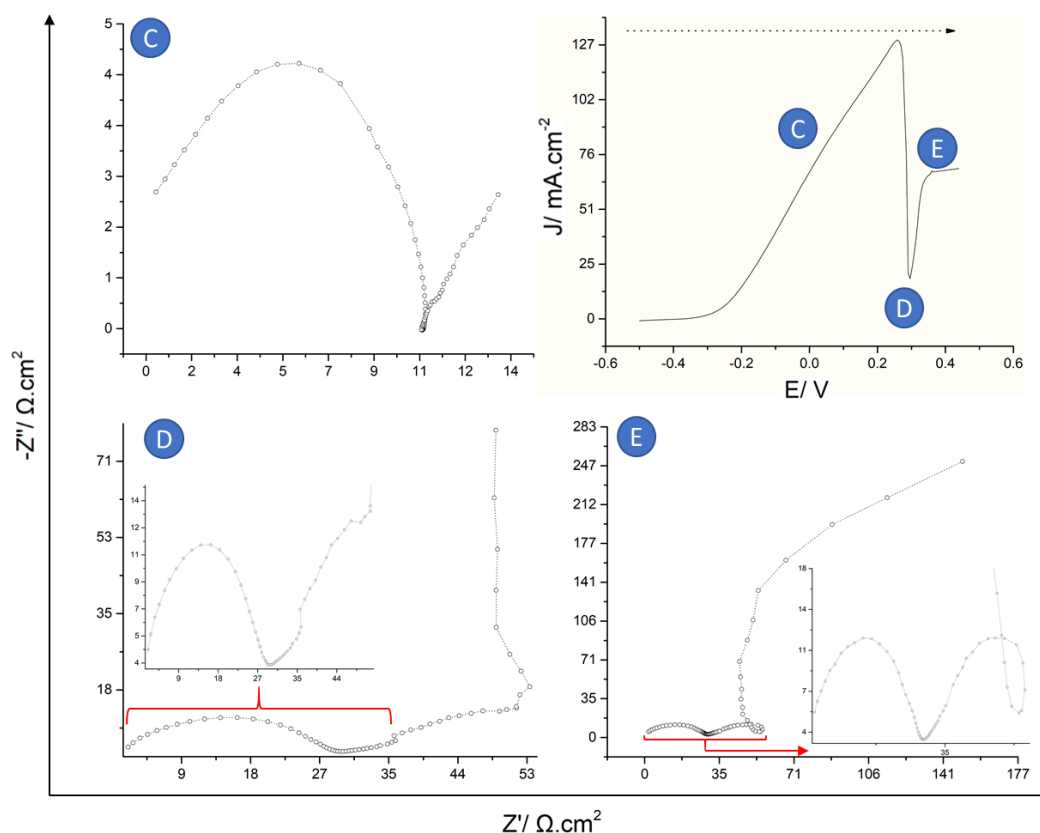


**Figure 5.9** Linear sweep voltammetry for 1ChCl: 2EG containing 0.1 M CuCl<sub>2</sub> and the EIS responses obtained at points C, D and E from Pt working electrode vs Ag/AgCl RE (Pt flag CE) at sweep rate of 20 mVs<sup>-1</sup>.

### 5.4.3 Chronoamperometric Studies of Copper Dissolution and Deposition

In these chronoamperometry experiments, it is aimed to mimic the pulse reverse power supply effect on copper powders and determine the reversibility of the deposition and dissolution processes.

The potential of a copper disc electrode was first stepped to 1 V, which was sufficient for surface oxidation, and this was followed by a step to -1 V for deposition for the same length of time. If a process is fully reversible then the charge on the dissolution pulse should be recoverable on the cathodic step. The charge passed for both processes was measured as a function of the length of the potential step. **Figure 5.10** shows a typical chronoamperometric response and the charge recovery ( $Q_-/Q_+$ ) was calculated.

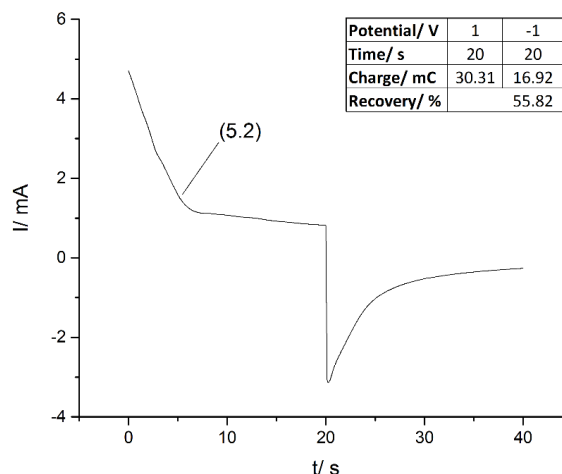


**Figure 5.10** Chronoamperometry of copper disc working electrode vs Ag/AgCl (Pt flag CE) reference electrode in 1 ChCl: 2 EG at room temperature for 20 s dissolution at 1.0 V, and 20 seconds deposition at -1.0 V.

If the dissolution leads to a soluble species which can diffuse to and from the electrode surface, then most the anodic charge should be recoverable on the cathodic pulse. If an insoluble complex is formed, then the dissolved copper will not be immediately recoverable on the cathodic pulse. This will lead to a loss in the recovery rate. **Figure 5.11** shows the same experiment as **Figure 5.10** but for different cathodic and anodic pulse lengths but always the same anodic and cathodic step potentials (1 and -1 V). **Figure 5.11** also shows the recovery rate as a function of the length of the step pulse.

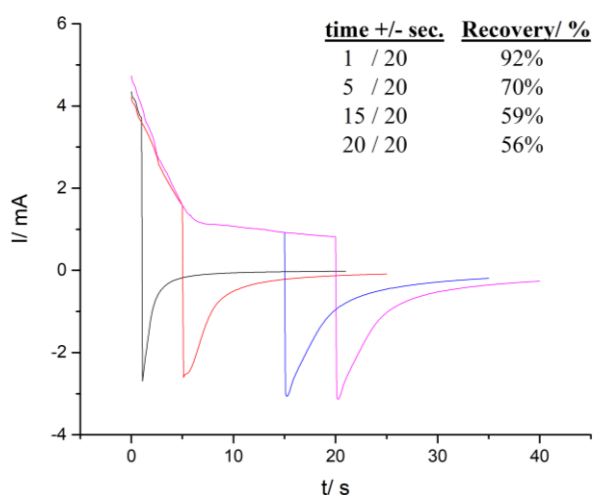


**Figure 5.11** Chronoamperometric steps of copper disc electrode vs Ag/AgCl reference electrode (Pt flag CE) using different cathodic and anodic pulse lengths to determine the recovery rate as a function of the length of the pulse step in 1 ChCl: 2 EG at room temperature.

The process is relatively reversible for short pulse steps (up to 5 s) thereafter, the charge recovery decreases significantly. For example, the recovery rate at a pulse length of 20 s was 56 %. The dissolution rate increases linearly for the first 5 s where after it levels off, presumably because the solution close to the electrode surface is super-saturated with copper chloride.

This ties in with the calculation in the previous section of the local concentration resulting from a 5 s anodic pulse which should super-saturate the solution close to the electrode surface. These results combined show that the anodic pulse should be less than 5 s.

**Figure 5.12** shows a potential step experiment similar to that in **Figure 5.11** using different lengths of anodic pulse length with a semi-infinite (300 s) cathodic pulse. From these the recovery rate was calculated, and the results are given in the legend of the figure.

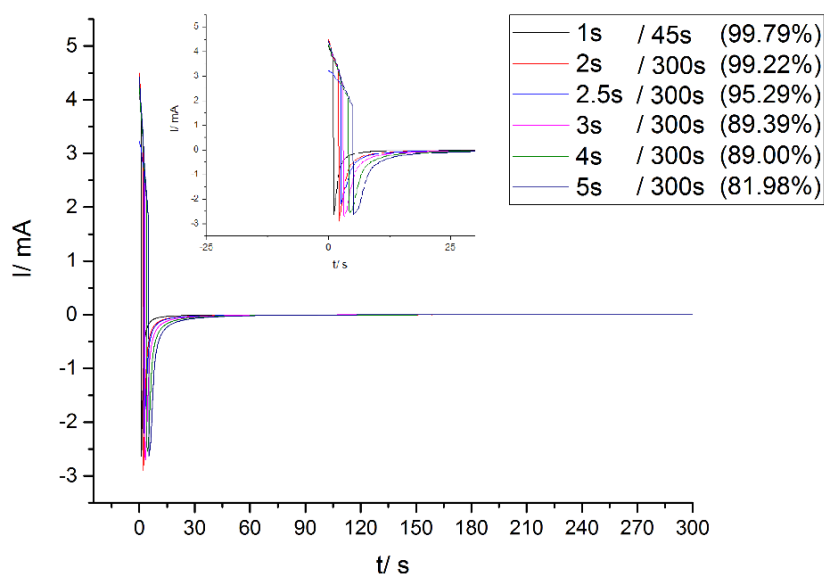


**Figure 5.12** Chronoamperometry study of copper disc working electrode vs Ag/AgCl RE (Pt CE) in 1 ChCl: 2 EG with no added copper for different dissolution and deposition times, at room temperature.

The data in **Figure 5.12** show that for 2 s anodic pulses, almost all the copper can be recovered on the cathodic sweep. For times, greater than 2.5 s there is a slight drop off in recovery rate showing that an increasing amount of copper cannot be recovered on a semi-infinite cathodic pulse. For a 5 s pulse, nearly 20% of the dissolved material is never recovered.

It is possible to calculate a theoretical amount of material which is not recovered if it is assumed that all the unrecovered charge is spent on the formation of  $\text{CuCl}_2$ . It is possible to estimate a theoretical film thickness if it is assumed that a homogeneous film covers the electrode surface.

**Table 5.2** lists the charges and recovery rates for the data in **Figure 5.12**. The film thickness of the  $\text{CuCl}_2$  can be calculated from the unrecovered charge, used during the formation of  $\text{CuCl}_2$ . Surface coverage is given in **Equation 5.1**.

$$\Gamma = \frac{Q}{n * F * A} \quad \text{Equation 5.1}$$

Thickness is a function of the molar volume,  $V$ , and the surface coverage,  $\Gamma$ , as given **Equation 5.2**.

$$V = \frac{m}{\rho}, \quad h = \Gamma * V \quad \text{Equation 5.2}$$

The density and molar mass of the copper chloride are  $3.39 \text{ g.cm}^{-3}$  and  $134.34 \text{ g.mol}^{-1}$  respectively.

**Table 5.2** Chronoamperometry results of Cu disc electrode, dissolution was followed by deposition, and efficiency was calculated by differing charge spent, and gained.

Sample	(-)/ s	(+)/ s	Q+./ mC	Q-./ mC	Recovery/ %	Thickness/ ( $\mu\text{m}$ )
1	1	45	3.92	3.872	98.8	0.00552
2	2	300	7.64	7.580	99.2	0.00692
3	2.5	300	7.43	7.080	95.3	0.04070
4	3	300	10.37	9.270	89.4	0.12792
5	4	300	12.54	11.160	89.0	0.16048
6	5	300	15.01	12.305	82.0	0.31456

The thicknesses listed in **Table 5.2** do not clearly have a physical meaning because all but the first experiment would block the surface and electrically passivate the surface. That does, however show that the copper chloride saturates the area close to the electrode surface and the contacting of the insoluble copper chloride particles with the electrode surface is probably what forms the noise which is observed for the voltammograms in

**Figure 5.8.** The coatings will also be uneven as can be seen on **Figure 5.7** where parts of the grain turn dark and parts remain bright during anodic polarisation. This could be the origin of some of the anisotropic effects which are discussed below. Blocking some parts of the surface while others remain unblocked means that copper deposited on the cathodic pulse will only be able to grow in certain regions.

## **5.5 Deposition with Copper Powder**

### **5.5.1 Single Powder Deposition**

Deposition of copper powder was performed in the same method as that performed with the zinc particle in section **4.2.2** using an O-ring glued to the substrate. The copper powder was 270 – 400 mesh sizes (30-50  $\mu\text{m}$ ). A single powder deposition was tried for different pulse reverse current variations as shown in **Table 5.3**.

All experiments were carried out for 120 minutes. When pure 1ChCl: 2EG was used as the electrolyte, no copper deposition was achieved with any of the conditions listed in **Table 5.3**. This is probably because the copper concentration was too low as the copper was too slow to dissolve and too quick to deposit back on the copper particle.

It was decided to add 0.3 M  $\text{CuCl}_2 \cdot 2\text{H}_2\text{O}$  to the solution and repeat the experiments. It would have seemed logical that copper should be deposited under all conditions as this is just like bulk pulse deposition. As in the zinc chapter, different pulse times, (frequencies) were applied. The starting current pulse was chosen as 50 mA for deposition, and 10 mA for dissolution because copper and zinc had similar deposition current values in DC plating, and so similar pulse values were chosen.

The powder used was smaller than in the zinc case as there was no vigorous bubble formation to break the electrical contact with the electrode.

**Table 5.3** Applied pulse currents and periods to the Ni electrode in 0.3 M CuCl<sub>2</sub> dissolved 1 ChCl: 2EG mixture with calculated duty cycle and frequency values.

<b>Exp.</b>	<b><math>I_c</math> / mA</b>	<b><math>t_c</math> / s</b>	<b><math>I_d</math> / mA</b>	<b><math>t_d</math> / s</b>	<b><math>t_{total}</math> / s</b>	<b><math>T</math> / %</b>	<b><math>f</math> / Hz</b>
<b>I</b>	50	0.001	10	0.001	0.002	50.00	500.00
<b>II</b>	40	0.02	15	0.002	0.022	91	45.45
<b>III</b>	30	0.01	10	0.004	0.014	71	71.43
<b>IV</b>	25	0.01	10	0.004	0.014	71	71.43
<b>V</b>	25	2	10	1	3	67	0.33
<b>VI</b>	25	4	10	1	5	80	0.20
<b>VII</b>	25	5.5	10	0.5	6	92	0.17
<b>VIII</b>	25	7	10	1	8	88	0.13
<b>IX</b>	25	9	10	1	10	90	0.10
<b>X</b>	25	11	7	2	13	85	0.08
<b>XI</b>	25	20	10	4	24	83	0.04
<b>XII</b>	25	30	10	6	36	83	0.03

Experiments **I** and **II** used 50 mA and 40 mA deposition current pulses but these did cause ion depletion and only very sparse copper deposition was observed on the nickel surface with no fusion of the copper particles onto the substrate. An example of the deposit obtained in experiment **II** is given in **Figure 5.13**.

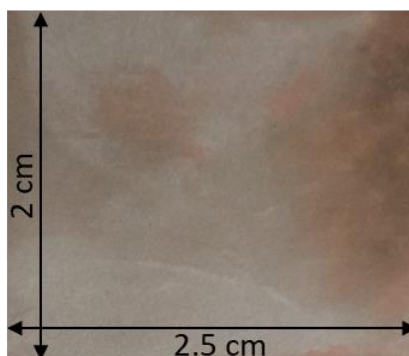


**Figure 5.13** Example of copper deposition onto nickel using the conditions in **Table 5.3** for experiment **II**, 120 min duration in 1 ChCl: 2 EG containing 0.4 M CuCl<sub>2</sub>·2H<sub>2</sub>O at 47.5 ± 2.5 °C.

The conditions used in these experiments were typical of those used in aqueous solutions. The fact that no copper (in the case of **I**) or not much copper (in the case of **II**) were

deposited is probably due to the higher viscosity of the DES compared to aqueous solutions.

Lower current loadings of 30 mA and 25 mA for cathodic deposition with 10 times longer deposition periods were applied for experiments *III* and *IV*. It can be seen in **Figure 5.14** that the copper colouration of the surface is more noticeable although the deposit is not homogeneous and where deposition has occurred it is less than about 5  $\mu\text{m}$  thick. The deposition appears to occur in islands which are about 5  $\mu\text{m}$  across. This is clearly not fusion of the 30-50  $\mu\text{m}$  sized particles but could be localised from copper dissolving in a spot and then depositing.

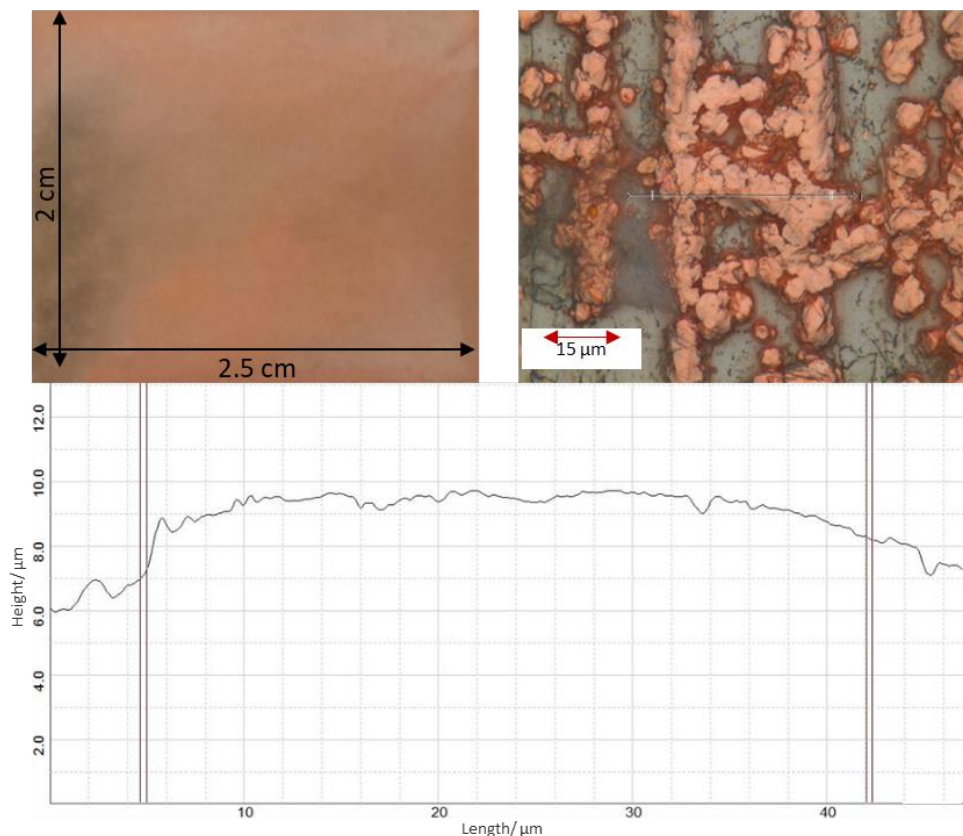


**Figure 5.14** Optical photograph (top left), and 3D profiler image (top right) with cross section (bottom) for the deposit obtained by 25 mA, 2 s, 10 mA 1 s for 3 h as presented at *V* given in **Table 5.3**.

It is also clear from this that a 5  $\mu\text{m}$  thick layer is insufficient to fuse a particle, which is approximately 10 times larger, to the electrode surface. This is in keeping with the results

from Chapter 4. Thus, it is thought that copper deposition is similar to zinc where deposition and dissolution timescales need to be performed on the second timescale. Extending the deposition and dissolution timescale in experiments *V* to *XII*, to the second-time scale deposition resulted in different types of deposits with clear evidence of particle fusion.

For these experiments the dissolution periods were in the frequency range 0.33 to 0.30 Hz with a 90% duty cycle ratio. The best ratio for deposition was found to be 5.5 s for deposition with an applied current of 25 mA, and 0.5 s for dissolution with an applied current of 10 mA. This was performed in experiment *VII* and the result is shown in *Figure 5.15*.

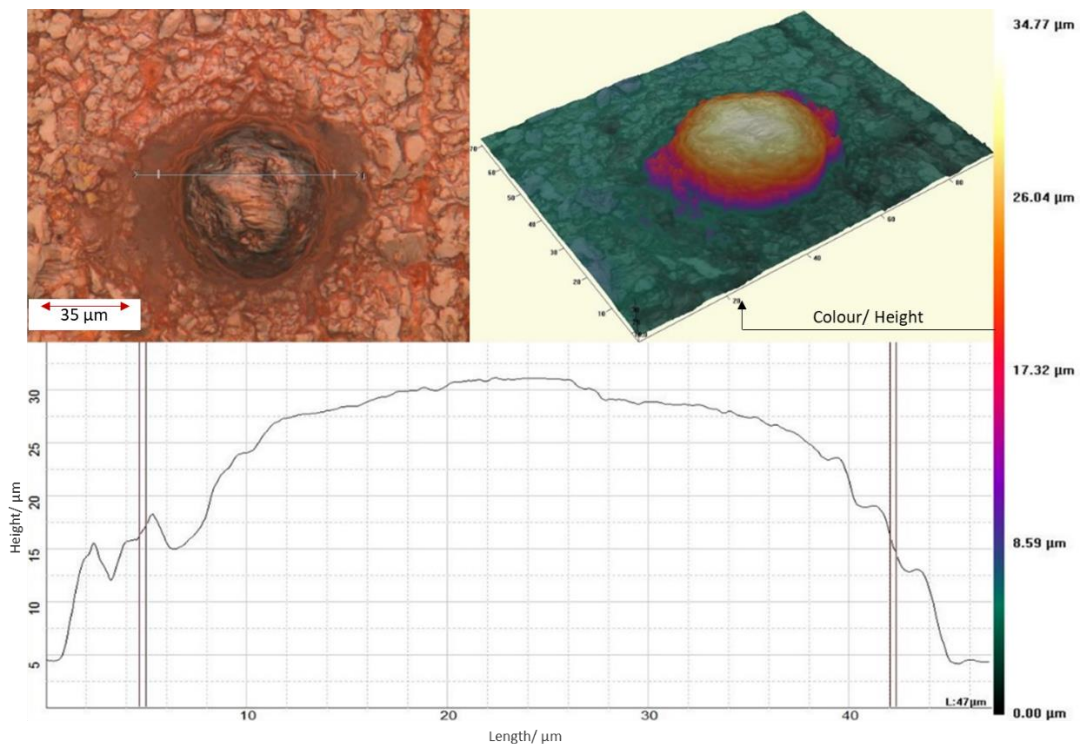


**Figure 5.15** 3D profiler image (top) with cross section (bottom) for the deposit obtained by 25 mA, 5.5 s, 10 mA 0.5 s as presented at *VII* given in *Table 5.3*.

### 5.5.2 Bulk Deposition of Copper Powder

Following the determination of the optimum condition for fusing copper particles to the electrode, bulk deposition studies were carried out in the same manner as those in Chapter

4. Initially the experiment using the filter paper separated cell was repeated using copper powder. This should have been slightly different to the zinc case as there was no bubble formation with copper deposition. The first experiment was performed with the same cell as shown in *Figure 4.12* with a 3 x 3 cm square Ni substrate and 0.3 M  $\text{CuCl}_2 \cdot 2\text{H}_2\text{O}$  dissolved in 1 ChCl: 2 EG at  $47.5 \pm 2.5$  °C. The cell conditions are listed in *Table 5.4*.

*Table 5.4* Experimental conditions used for the sample in *Figure 5.16*.

$T / ^\circ\text{C}$	$I_c / \text{mA}$	$t_c / \text{s}$	$I_a / \text{mA}$	$t_a / \text{s}$	$t_{\text{total}} / \text{h}$	$T / \%$	$f / \text{Hz}$
$47.5 \pm 2.5$	45 mA	5.5	18	0.5	3	91	0.17

Following this time, the cell was dismantled and analysed, and the images of the various sections are shown in *Figure 5.16*.

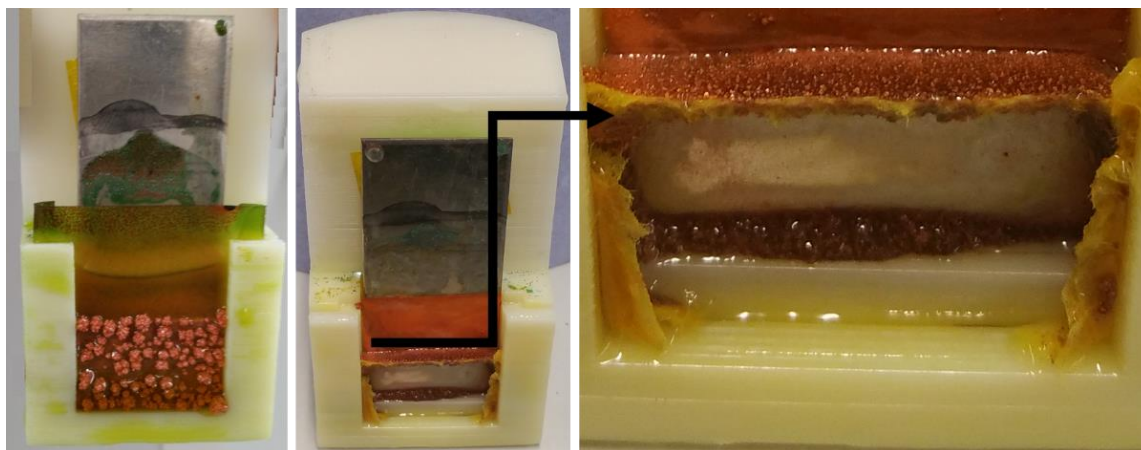


*Figure 5.16* Deposition of 30-50  $\mu\text{m}$  copper powder onto vertically oriented electrode in 0.3 M  $\text{CuCl}_2 \cdot 2\text{H}_2\text{O}$  in 1 ChCl: 2 EG DES at  $47.5 \pm 2.5$  °C. (Left) view of filter paper membrane from that anodic cell side, (centre) Ni cathode (right) close up of cathode.

*Figure 5.16* shows a photograph of the filter paper membrane from that anodic cell side. It can clearly be seen that copper has nucleated on the paper surface to form nodules which are 2 - 4 mm in diameter. There are no copper particles on this side of the membrane and so the filter paper must be acting as a reducing agent in a medium of high copper concentration. Exactly the same behaviour was observed by Hartley<sup>26</sup> when electro-purifying copper-indium-gallium scrap using the same DES. It was concluded in the previous study that the easily oxidisable cellulose structures could act as nucleation

centres for copper in solution. The central image of **Figure 5.16** shows the Ni cathode after electrolysis.

Unlike the case with zinc, there is clear evidence of copper deposition on the cathode but there is little evidence of particles fusing to the nickel substrate. The close-up image of the cathode shows that at the base of the cell is a thick layer of copper *c.a.* 3 mm thick which demonstrates clearly that the particles have fused together. Clearly the particles are settling to the base of the cell and there is enough electrical contact with the Ni cathode to allow particle pulse plating to occur in the densely packed particles. The white fibres attached to the base are where the electrode has fused to the filter paper. **Figure 5.17** shows close up images and 3DM images of the back and base of the plate.

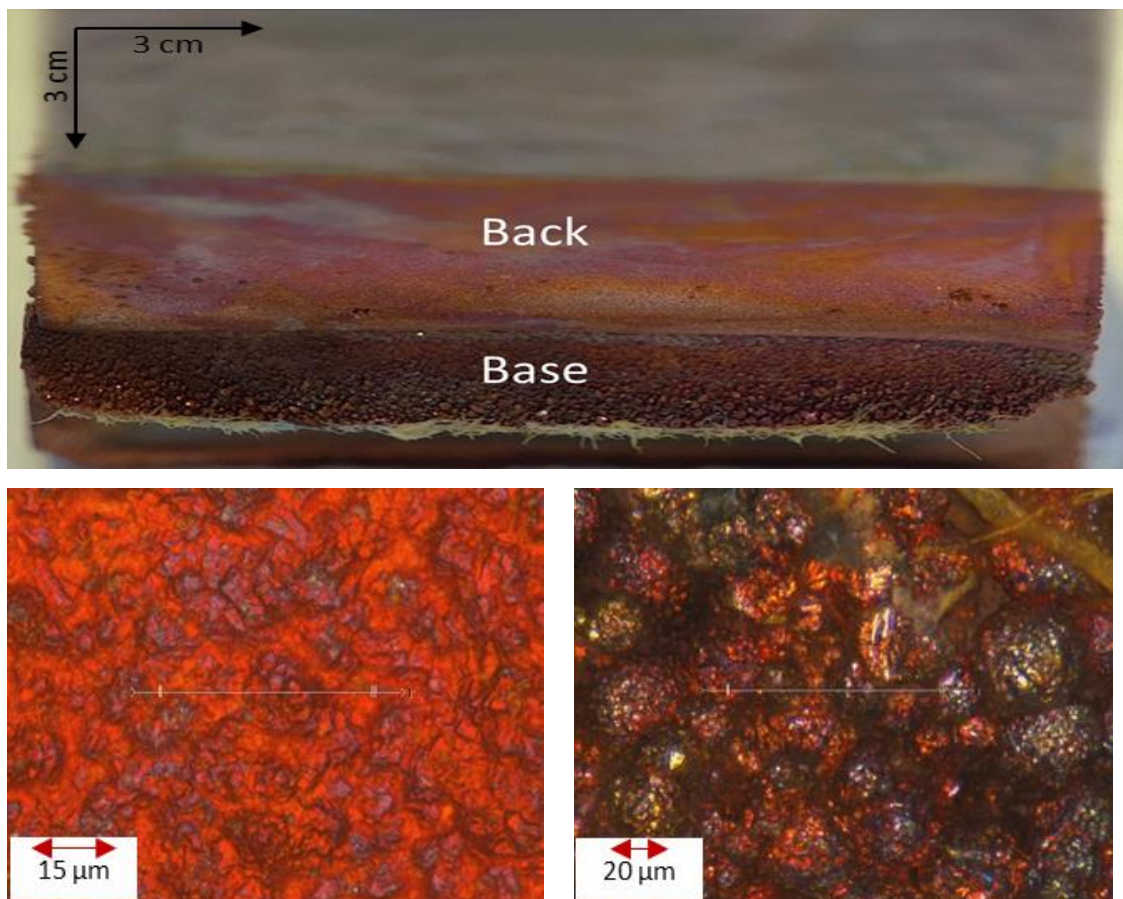


**Figure 5.17** Photograph and 3DM images of plate observed in **Figure 5.16** (below left) back, and (below right) base.

These confirm that the back contains copper deposited from copper in solution whereas the base is made up of fused copper particles.

### 5.5.3 Horizontal Powder Pulse Plating

With the success of depositing copper at the base of the electrolysis cell it was decided to repeat the experiment using the cathode in the horizontal orientation. To achieve this, a slightly different cell was designed so that the samples could be placed directly in the XRD analysis chamber after deposition. The cell design is shown in **Figure 5.18**. The experimental procedure was the same with the used cell in zinc powder deposition in **Figure 4.16**. After deposition of an initial copper layer using a DC current pulse, 30-50  $\mu\text{m}$  particles were added to the solution, and mixed for 5 s. The particle was left to settle on the electrode and this was generally completed within 5 to 10 minutes. The electrodes were then attached to the power pulse supply.

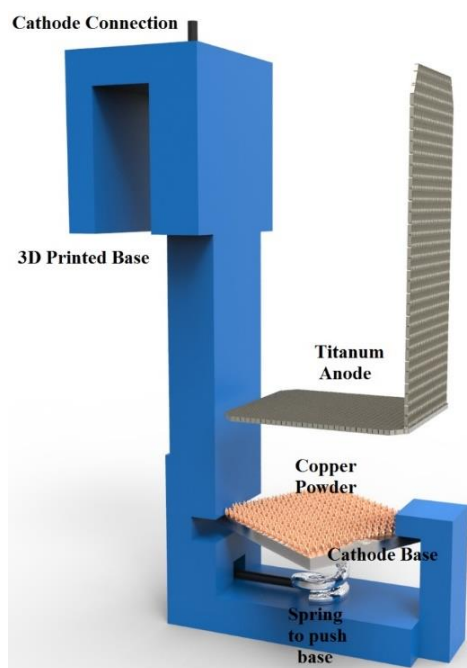


**Figure 5.18** Schematic representation of the printed cell used for copper powder deposition

The cell in **Figure 5.18** was electrolysed on nickel for 180 minutes with the conditions described in **Table 5.5**.

**Table 5.5** Experimental conditions used for the sample in **Figure 5.19**.

$T / ^\circ\text{C}$	$I_c / \text{mA}$	$t_c / \text{s}$	$I_a / \text{mA}$	$t_a / \text{s}$	$t_{total} / \text{s}$	$T / \%$	$f / \text{Hz}$
$47.5 \pm 2.5$	45 mA	5.5	18	0.5	6	91	0.17

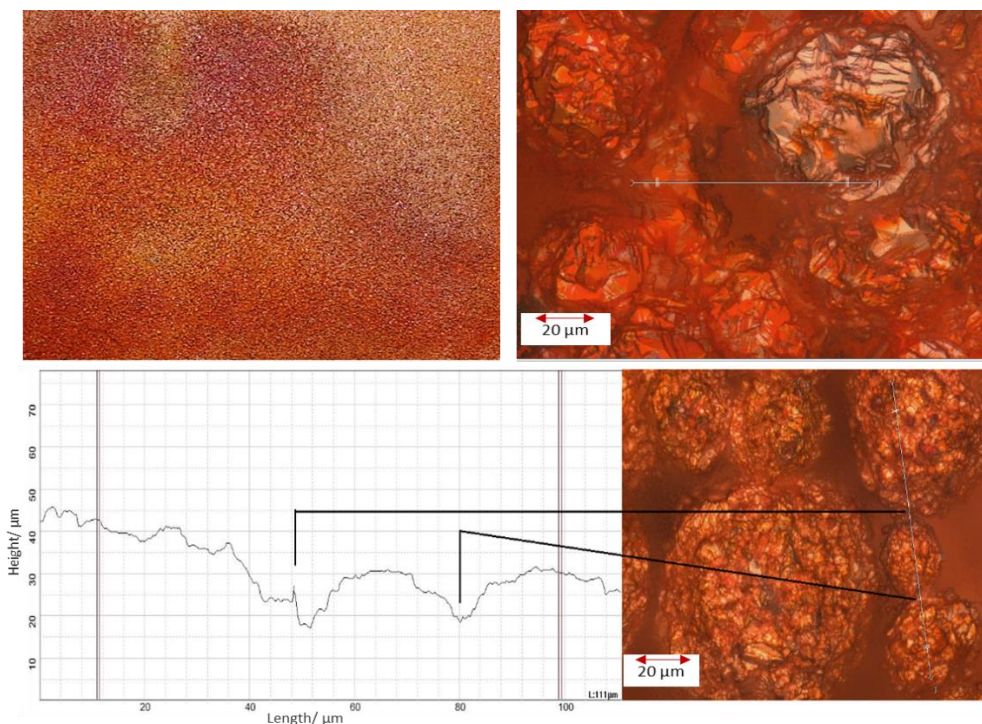


**Figure 5.19** Photograph (top left) and 3DM images of the deposit formed on a nickel electrode using the pulse conditions listed in **Table 5.5** using 0.3 M  $\text{CuCl}_2 \cdot 2\text{H}_2\text{O}$  dissolved in 1 ChCl: 2 EG DES at  $47.5 \pm 2.5$  °C.

**Figure 5.19** shows that under the pulse conditions listed in **Table 5.5** the copper particles fuse together to make a dense, thick copper layer. The individual grains can clearly be resolved, and the smooth grains shown in **Figure 5.2** are transformed into rough surfaces with clear facets etched and deposited into the surface.

Comparing the deposit obtained with copper to that obtained with zinc in **Figure 4.22** it can be seen that both deposits retain a macroporous structure which is governed by the particle size, but the surface structure of the particles is governed by the DES and the etch/ deposit morphology which that liquid imparts. Changing the DES can change the deposit morphology as shown in Chapter 3.

In the performed deposition on the nickel substrate a bright, dense copper deposit is obtained. The deposition efficiency was calculated from the mass of the film (0.138 g) and the total charge passed (461.7C). The theoretical charge required to deposit this mass was 419.55 C. This means that the deposition efficiency was 91 % which is not dissimilar from that obtained for bulk DC deposition without particles so clearly efficiency is being

lost in the process. A likely cause for this the fact that the copper was probably fused at much shorter time-scales and continued pulses are just re-dissolving and redepositing material which has already fused copper particles together. The deposit obtained in **Figure 5.20** was also analysed using SEM so that the macroscopic voids could be observed, and these images are shown in **Figure 5.20**.

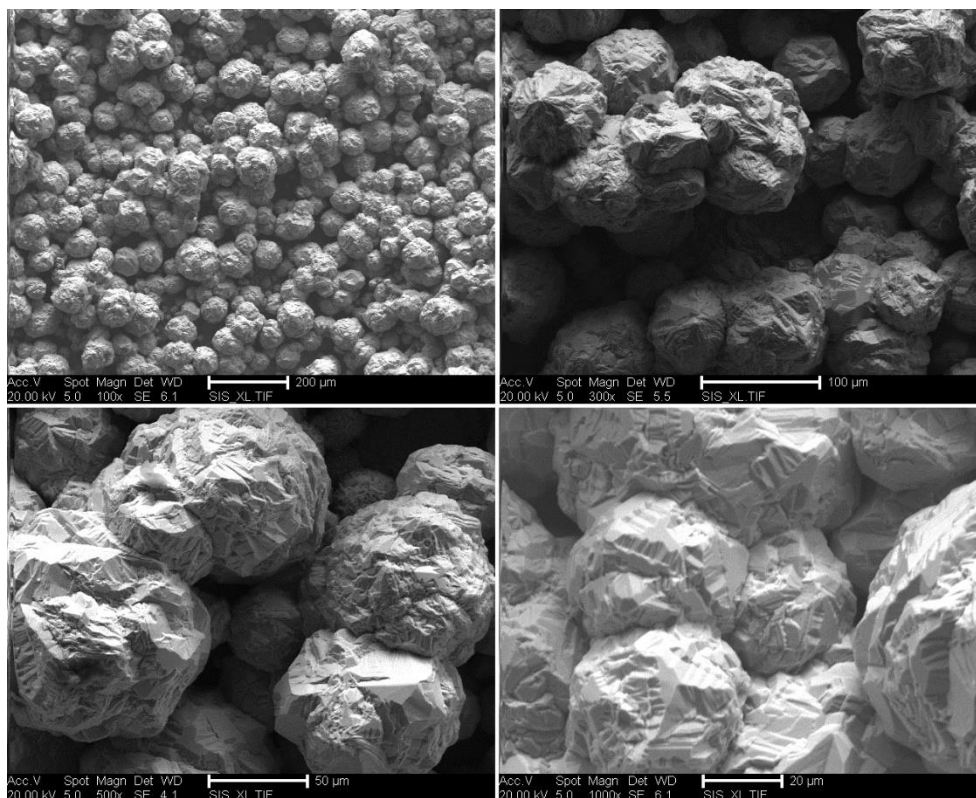


**Figure 5.20** SEM images of deposited nickel samples given in **Figure 5.19** obtained applied conditions given in **Table 5.5**.

The gains have very clear facets deposited or etched onto the surface. As will be shown below, the electrodeposition of copper appears to display some anisotropic behaviour with certain crystal faces preferred.

#### 5.5.4 Electroforming of a Copper Film

Electroforming is a process by which a material is electrodeposited around a form which is easily separated from the deposited layer. The electrodeposited later needs to be thick enough to support and retain its shape once it is separated from the template (known as a

mandrel). This is often carried out by coating a non-conductive mandrel such as a glass, plastic, or ceramic with a metallic layer by electroless deposition. The issue with this approach is that the deposition times to obtain thick deposits are many hours.<sup>27</sup>

Al-Haji studied the electroforming of copper in 1 ChCl: 2 EG containing 0.3 M  $\text{CuCl}_2 \cdot 2\text{H}_2\text{O}$  dissolved in it. It was found that copper could be electroformed into sheets and tubes, but it was very dependent on the substrate.

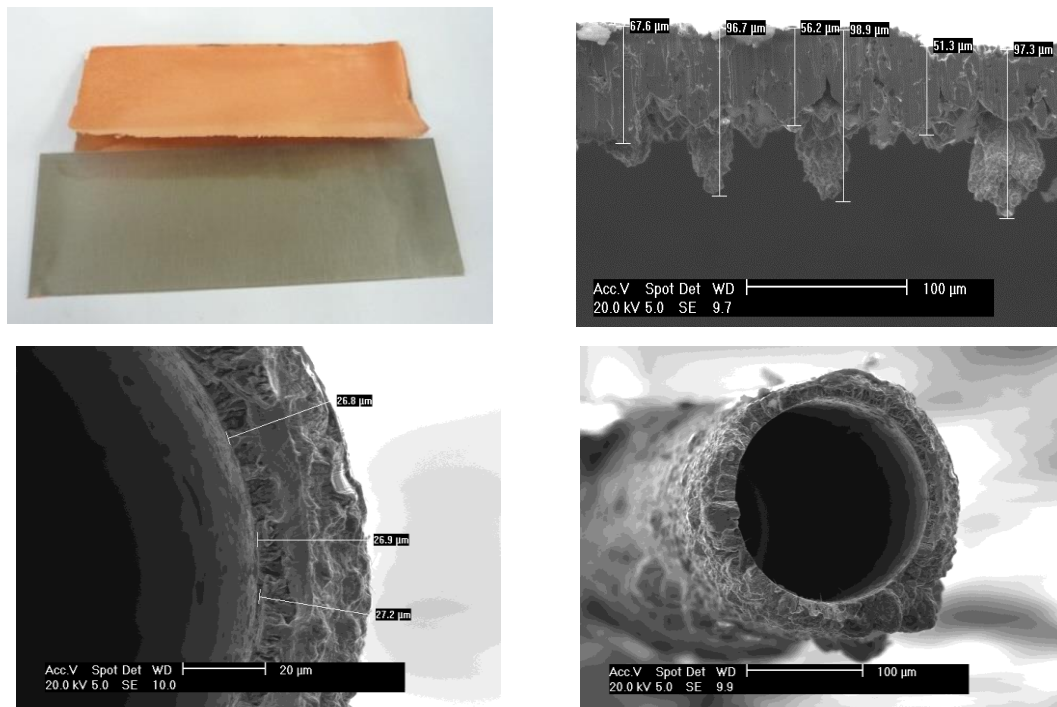


**Figure 5.21** (above) photograph and SEM image of a Cu-P alloy film after removal from the Ti substrate (below) SEM images of Cu deposition on Ni-Cr wire after removal from substrate.<sup>28</sup>

It was found that dense deposits could be obtained which were about 30 to 50 μm thick. These were relatively slow to grow and took up to 24 hours to deposit due to the low current densities that were needed to achieve dense deposits. The sheets could only be separated from metals which had a thick metal oxide coating on the surface. It was possible to peel the copper layers from the substrates when either titanium or nichrome were used as the mandrel.

To see if this would work with powder pulse plating a mandrel was formed using a stainless-steel contact. A new cell was designed and constructed from ABS formed around a stainless-steel contact. This is shown schematically in

**Figure 5.22.** To form the cell a stainless-steel shape was cut into a rectangular frame shape before being embedded in the ABS plastic. The whole shape was then polished using glass paper of different grades followed by polishing with 0.3  $\mu\text{m}$  alumina to create a smooth surface.

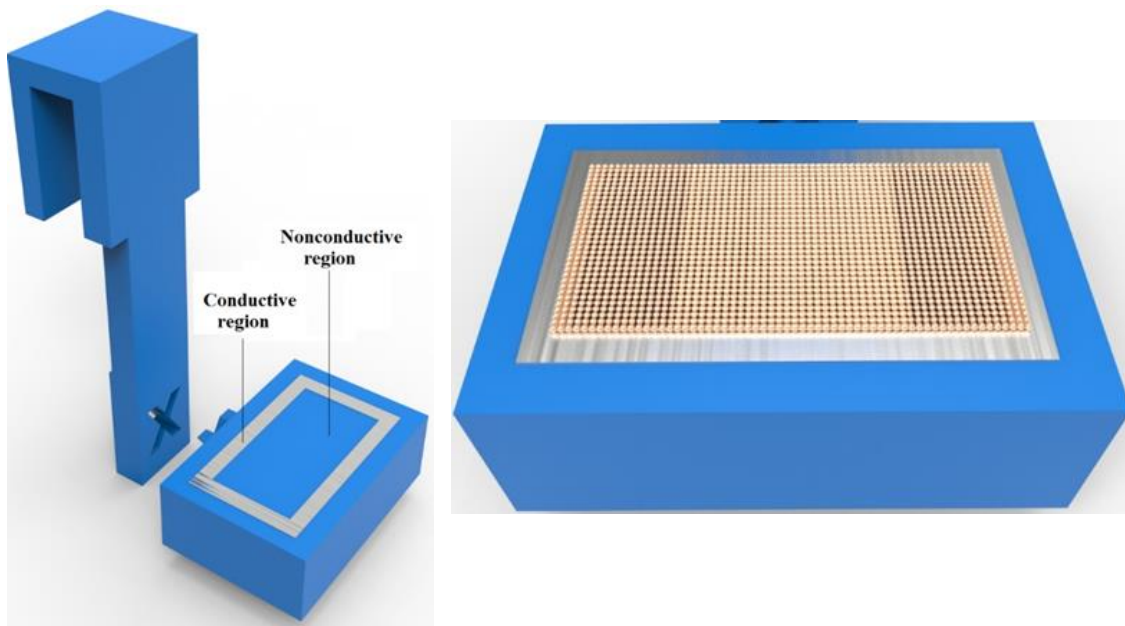


**Figure 5.22** Cell designed for copper electroforming. The conductive stainless-steel region is represented in grey, and the ABS - nonconductive region is blue, and electroforming surface area is 4  $\text{cm}^2$ .

The only difference with the previous experiments was the cleaning procedure which was using a proprietary cleaner, Anapol-C which is commonly used for stainless steel, followed by laboratory grade acetone. The deposition conditions needed to be changed slightly from those used above, to obtain fusion of the particles. The conditions used are listed in **Table 5.6** with 0.4 M  $\text{CuCl}_2$  dissolved in 1 ChCl: 2 EG. The particle size was between 80 and 140  $\mu\text{m}$ .

**Table 5.6** Experimental conditions used for the sample in **Figure 5.23**.

$T / ^\circ\text{C}$	$I_c / \text{mA}$	$t_c / \text{s}$	$I_a / \text{mA}$	$t_a / \text{s}$	$t_{total} / \text{h}$	$T / \%$	$f / \text{Hz}$
----------------------	-------------------	------------------	-------------------	------------------	------------------------	----------	-----------------

$47.5 \pm 2.5$	28 mA	5.5	10	0.5	3	91	0.17
----------------	-------	-----	----	-----	---	----	------

Normally with electroforming, the whole mandrel needs to be conductive, but as seen in **Figure 5.23** as long as one point is in contact with the metallic powder and the rest of the powder is in continuous electrical contact the whole area can fuse together. As shown in **Figure 5.23** the copper powder was distributed onto the ABS platform such that it was densely packed and ensured the copper particles were in constant contact with each other.

What was slightly different about this experiment was when the sample was pre-plated with copper it only formed a contact layer on the stainless-steel contact. When the experimental conditions listed in **Table 5.6** were used the powder grains fused to each other, but not onto the stainless-steel frame. Photographs of the sample holder before and after the experiment are shown in **Figure 5.23**. What should be noted is the thickness of the copper film which was between 0.3 and 1 mm thick which was deposited within ca. 220 minutes. This was much thicker (about c.a. 4 times) than anything that could be deposited using zinc. Approximating the deposition rate for the experiment and comparing it to the electroforming achieved by Al-Haji<sup>28</sup> for the same system without particles it can be seen that the rate is much faster.

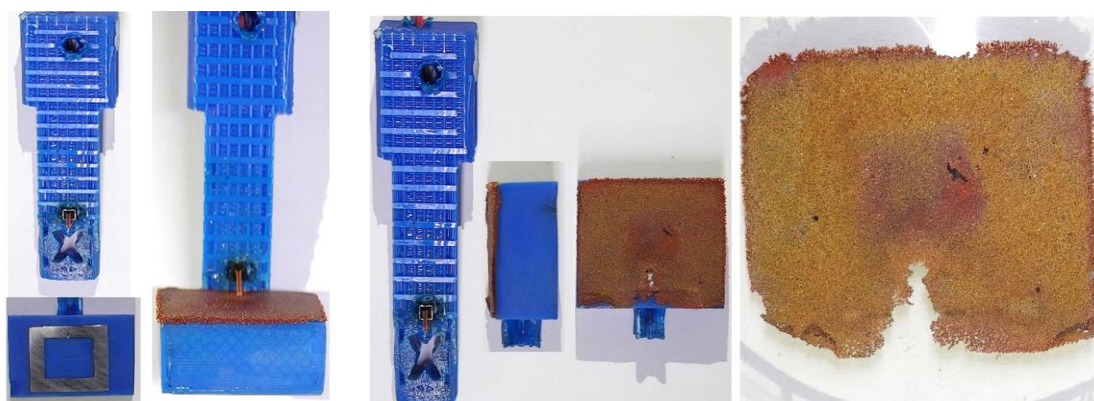


**Figure 5.23** Sample holder before (left) and after (right) copper powder pulse deposition in 0.3 M  $CuCu_2$  1 ChCl: 2 EG with applied conditions given in **Table 5.6**.

It should, however be noted that the deposits are not exactly comparable as the powder pulse plating produces a porous deposit whereas the direct electroforming produces a dense material. After film formation, the cell was dismantled as shown in **Figure 5.23**. The copper sheet peeled easily from the stainless steel sheet. This is different to the work

of Al-Haji where thermal shock (dipping in liquid nitrogen then heating rapidly) had to be used to release the film from the substrate.

There was a V-shaped section of copper missing from the deposit, but this was because of the electrical contact between the support column and the stainless steel frame. The two copper wires precluded copper particles settling on to the base of the sample holder. The film was imaged using a 3D optical profiler, an image of which is shown in **Figure 5.24**. It can clearly be seen that the copper particles are well fused together but the individual particles can still be discerned. The deposition efficiency was calculated from the mass of the film (0.079325 g) and the total charge passed (286.2 C). The theoretical charge required to deposit this mass was 240.8 C. This means that the deposition efficiency was 84 %.

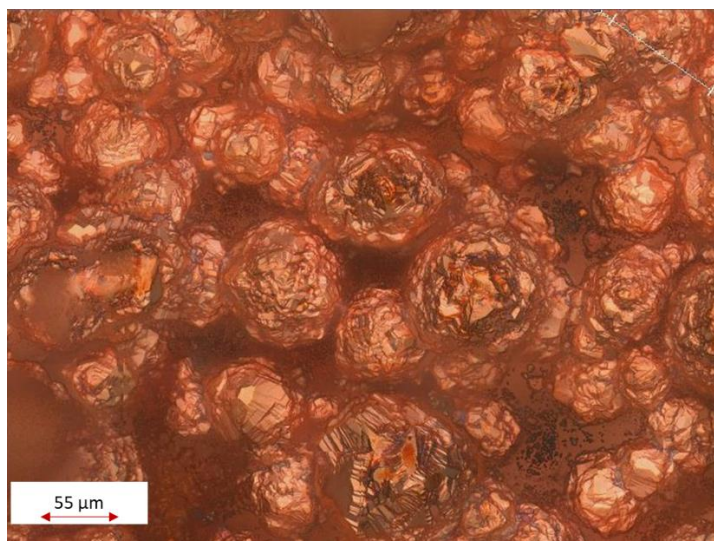


**Figure 5.24** 3D optical images of the obtained copper film by applied conditions and optical images shown in **Table 5.6** and **Figure 5.23** respectively.

This is significantly lower than the efficiency for DC plated copper without particles and certainly lower than the powder pulse plating observed with zinc in the previous chapter.

## 5.6 XRD Analysis

XRD is a well-known applied technique to analyse and characterize coated surfaces. The XRD analysis was carried out on samples deposited by straight DC deposition and by

pulsed deposition on powder coated samples. By doing so, it is aimed to obtain information about the preferred crystal orientations.

By using XRD data, it is also possible to calculate crystallite size of the grains by use of the Scherrer *Equation 5.3*<sup>29</sup> and the Williamson-Hall method *Equation 5.4*.<sup>30</sup>

$$\tau = \frac{K\lambda}{\beta \cos\theta} \quad \text{Equation 5.3}$$

$$\text{where } \beta_L = \frac{K\lambda}{L \cos\theta}, \quad \beta_e = C\epsilon \tan\theta \quad \text{Equation 5.4}$$

The Scherrer equation depends on the inverse relation between the integral breadth (peak width  $\beta$ ), and crystallite size ( $L$ ) which only affects the line broadening caused by size effects.  $K$  and  $\lambda$  represents the Scherrer constant, and wavelength respectively. Similarly, the Williamson-Hall method is a combination of Scherrer equation with an interpretation for the apparent strain retained by differentiating Bragg's law.<sup>31</sup>

These formula can be used to make a quick estimation of the average size of the crystallites (coherently scattering domains) along with the lattice strains.<sup>31</sup> Crystallites which make up the grains are not in coherence as they do not have the same shape and size in general. This situation makes it difficult to evaluate the apparent size as we assumed in integral breadth methods. As a result, using the expressions found by Scherrer and Williamson carries certain degree of arbitrariness, and these expressions should be used with knowledge of the errors and limitations as they do not consider the strain anisotropy and some other additional effects.<sup>31</sup> The Scherrer and Williamson-Hall method is suitable to use for general calculation due to the Cu crystallite sizes being less than 200 nm.<sup>32</sup>

Although the accuracy of the calculated crystallite sizes is out of scope in this study, a clarification with the reason for evaluated crystallite sizes will be referred here. The average crystallite sizes found for zinc and copper deposited from aqueous acidic solutions are typically less than 70 and 30 nm respectively.<sup>33-36</sup> In the current study, the calculated crystallite sizes for copper are often over 100 nm and generally more than 50

nm. The main reason for the crystal sizes being larger than those seen in aqueous solutions is probably due to use of the powders being used together with the use of a pulse power supply.

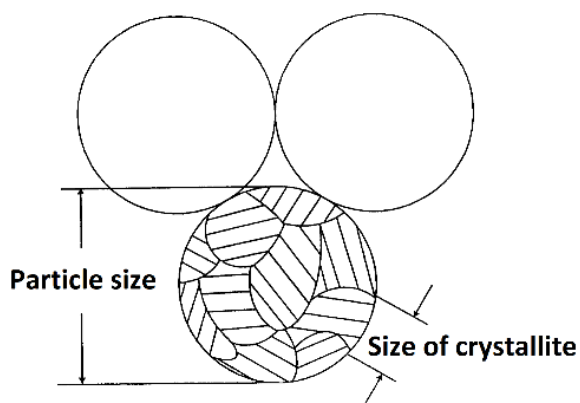


**Figure 5.25** Schematic diagram to show how different crystallites are arranged on a grain.<sup>37</sup>

**Figure 5.25** shows the arrangement of crystallites on a single particle grain. As shown in **Figure 5.2** the copper powder used in the experiment was generally spherical with approximately 150 micron size scale. The question could be asked why crystallites of c.a. 50 nm are not visible under SEM. Although a single virgin zinc powder appears as one contiguous single grain, XRD may reveal the crystallite size if the particle comprise of more than one of crystallite oriented in different directions.<sup>37</sup> The crystallite facets may only become visible once the surface of the particle is etched or built upon. As mentioned above, the following analysis gives a semi-quantitative analysis rather than an absolute analysis of the crystal sizes.

In this study, the deposition of copper onto a variety of substrates was determined for both direct current deposition and using powder pulse plating. In both cases the same electrolyte and temperature were used 0.4 M  $\text{CuCl}_2$  in 1ChCl: 2EG at 50 °C.

**Figure 5.26** shows the XRD analysis of the copper powder shown in **Figure 5.2** before any chemical or physical processing. As it is seen, that the (111) plane is preferred, and this is followed by, in decreasing abundance; (200), (220) and (311). This result was used as a reference because all powders used came from the same sample.

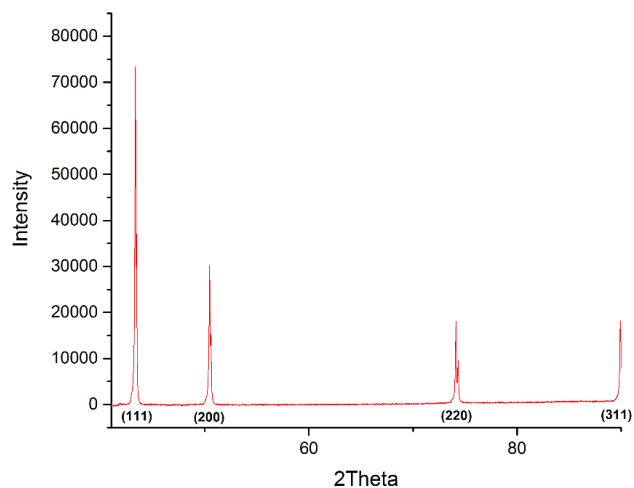


**Figure 5.26** XRD analysis of the pure copper powder without any physical or chemical processing

**Figure 5.27** (left) shows the XRD spectra for layers of copper deposited using a single DC current step of c.a.  $4 \text{ mA cm}^{-2}$  for 180 min onto  $1.5 \text{ cm} \times 1.5 \text{ cm}$  substrates. All the layers were approximately  $17 \mu\text{m}$  thick so no signal for the metal substrate was observed. It is clear that the same crystallite faces grow on each surface but the abundance of each face changes depending on the substrate. This substrate effect is well known.<sup>38</sup> **Figure 5.27**, (right) also shows a similar experiment for copper deposited using a powder pulse technique.

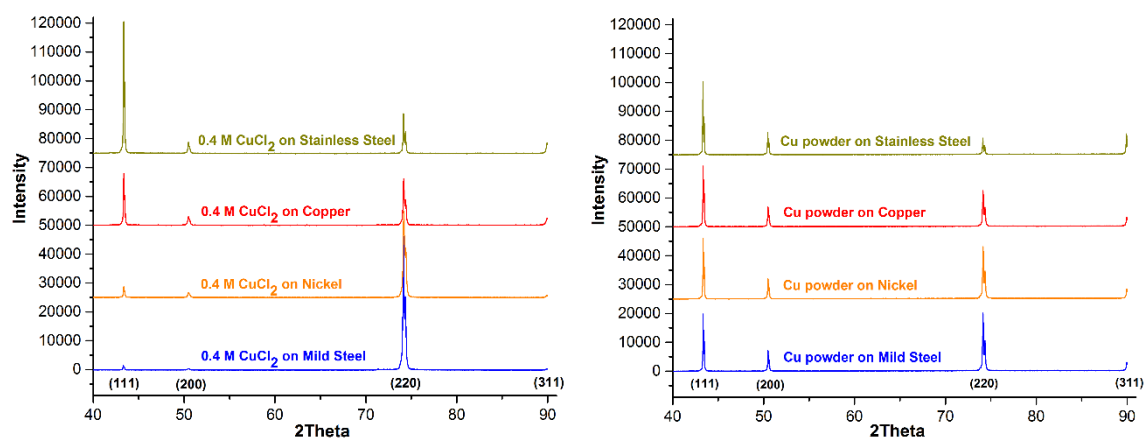


**Figure 5.27** XRD analysis of the deposits obtained from (left) DC deposition and (right) powder pulse deposition.

For each substrate, a seed layer of copper was deposited using a DC step for 10 min. This was followed by an anodic pulse of 12 mA for 5500 s followed by a cathodic pulse of 3

mA for 0.5 s for a total deposition time of 180 min using the same electrolyte and temperature as for the DC experiment. The XRD results for deposition onto four substrates; stainless steel, copper, nickel, and mild steel are shown in *Figure 5.27*. For the DC deposition, the copper layer was around 20 microns thick, whereas that deposited by the powder pulse plating was typically 70-micron thick.

With DC plating (111) is most prevalent on stainless steel and least prevalent on mild steel. The trend for the (220) are the opposite. The (111) face remain constant and small in all samples. In the powder deposited samples there is less of a change in the orientation with the substrate as may be expected since the powder particles act as the template and it is the etching of the powder which is the major influence of the crystallites observed. Accordingly, the (111) is the dominant face in all cases. What is surprising is that there is any difference at all in the samples. The (220) face does change with the substrate in the same way as that observed with the bulk deposited phase. It is clear therefore that some “memory” exists in the copper deposited from the seed layer which is put down first in the experiment and either the layer is so porous that the response of this is seen for the average of the material or the seed layer acts as a template for material which grows around the particles. The powder fusing technique may have an interest in catalyst preparation as it allows some capability to control the crystal faces of a material. For instance, the results obtained from powder deposition reveals that the planes in the direction of (200) and (311) were suppressed. Copper powders will have different crystallite intensities due to differences in production processes or post-processing steps such as heating, cooling, cutting or ball milling.<sup>31</sup> Each different sub processes cause the change on the distribution and predominance of the certain crystallites due to occurring defects which ended up in 1D, 2D and 3D defects of the crystallites. *Figure 5.28* is an SEM image taken from powder coating onto nickel, and preferential etching is clearly visible after re-coloured some part of the SEM picture.

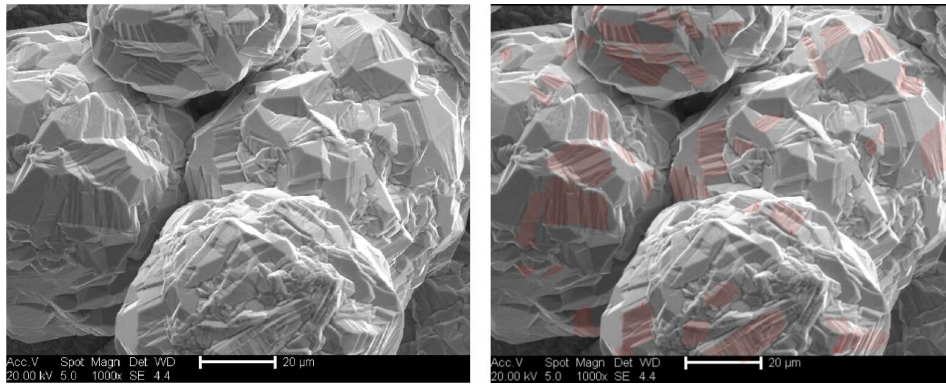


**Figure 5.28** Preferentially etched powder particles are highlighted in red colour to show how crystallites can exist on a copper particle.

In the last part of the XRD section, the size distributions of crystallites were analysed. An example of the size calculation for pure copper is shown in **Figure 5.29**. Fourier smoothing, and K-Alpha 2 stripping were applied before calculation. Then, strain and size analysis were done using the Scherrer equation from FWHM values of the peaks for (111) and (200).

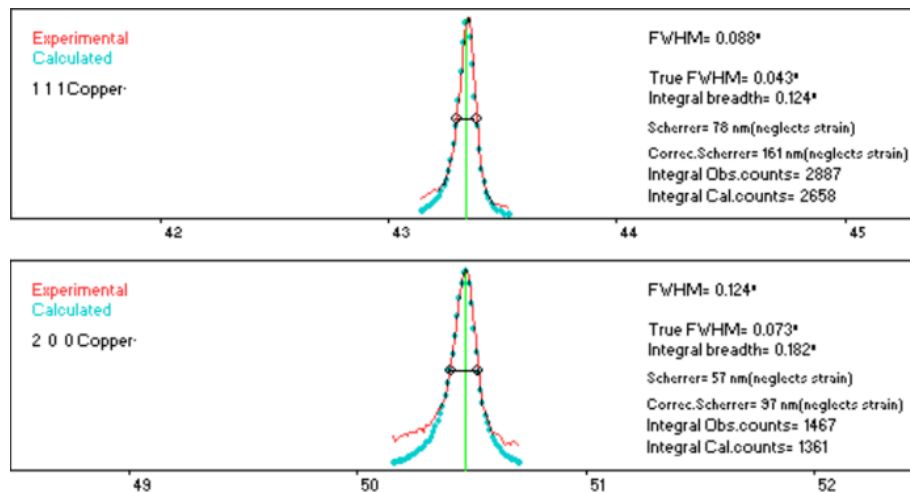


**Figure 5.29** Pure copper powder size analysis using the Scherrer equation

All the size calculations were performed with same method and the crystal sizes are summarised in **Table 5.7**. It can be seen that for the DC deposition experiments the (200) faces are relatively small, generally < 50 nm whereas those for (111) and (220) are somewhat larger (40 - 130 nm).

*Table 5.7 Average crystallite size analysis (in nm) for the copper deposits*

Planes	Cu on Cu	Cu on MS	Cu on SS	Cu on Ni
(1 1 1)	73	132	40	53
(2 0 0)	27	56	27	16
(2 2 0)	51	94	78	48

	Pow on Cu	Pow on MS	Pow on SS	Pow on Ni	Pure Powder
(1 1 1)	75	131	130	87	98
(2 0 0)	58	105	100	68	83
(2 2 0)	56	106	94	62	87

For the pure copper powder before powder pulse plating the particle size is in the range 80 - 100 nm. The crystallite sizes do not stay the same with the different substrates. For copper and nickel substrates the crystallite sizes are intermediate between those of the pure powder and those plated using a DC source. This would seem logical as the sizes will be an average and the XRD will see signals from the powder and the seed layer. What is somewhat unusual, and cannot be explained currently, is that the crystallite sizes for powder pulse plating on mild steel and stainless steel which are in all cases significantly larger than either the powder or the seed layer

This study has shown an alternative method to change the orientation of crystallites in metal plating. There are hundreds of studies in the literature developing different methods to control deposit morphology.<sup>39, 40</sup> The surface structure can affect corrosion resistance, catalytic behaviour etc.<sup>41, 42</sup> Scull et al. showed that the energy required to break the bonds on a surface depended on the number of nearest neighbour atoms which in turn depends on the crystal orientation. The dissolution of metal atoms is superior for close packed planes and low-index planes, such as the (111) orientation in the case of copper.<sup>43</sup>

## 5.7 Electrodeposition of Composite Coatings

As stated in the previous chapter composites coatings are of interest as they have the ability to modify the coating properties, giving it either increased anti-wear properties or lubricating properties. The results for composite deposition using powder pulse plating of zinc showed that the metal did not adhere well to either silicon carbide or alumina particles. However, the zinc did fuse together in a matrix which trapped the dispersed phase particles. The experiment from chapter 4 were repeated using copper particles in

this study. In the experiments 0.01 g of the dispersed phase (50  $\mu\text{m}$  SiC particles or 20  $\mu\text{m}$   $\text{Al}_2\text{O}_3$  particles) were mixed with 0.05 g of copper powder (40-60  $\mu\text{m}$  diameter) separately in different experiments. A pulse experiment was used, and the deposition conditions are shown in **Table 5.8**.

**Table 5.8** Experimental conditions used for mixture of copper powder with both SiC and  $\text{Al}_2\text{O}_3$  as the dispersed phase.

$T/^\circ\text{C}$	$I_a/\text{mA}$	$t_a/\text{s}$	$I_c/\text{mA}$	$t_c/\text{s}$	$t_{\text{total}}/\text{s}$
$47.5 \pm 2.5$	8	0.5	18	5.5	13200

Unlike the study with zinc, in neither of the composite powder pulse plating experiments did the SiC or  $\text{Al}_2\text{O}_3$  adhere to the copper particles. At the end of the experiments only pure copper was observed. This could be because copper does not wet the surface of the particles well however the previous work by Ettaib shows that this is not the case (albeit on smaller particles). Just to prove this the experiments were repeated the same SiC and  $\text{Al}_2\text{O}_3$  particles but this time with no copper particles but using a DC plating protocol with a current density of 12-15  $\text{mA cm}^{-2}$ .

**Figure 5.30** shows that the SiC particles are relatively evenly distributed throughout the sample but it is clear that, the copper is not well adhered to or around the SiC (darker particles) but it is better in some cases than was seen with zinc.

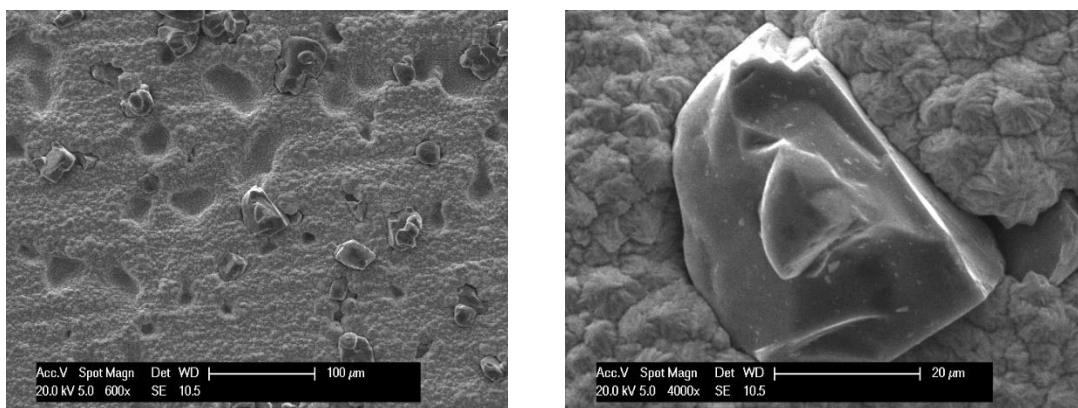


**Figure 5.30** SEM image of a Cu/SiC composite coating obtained using DC plating for 200 minutes at 14  $\text{mA.cm}^{-2}$  at  $47.5 \pm 2.5$  in 0.3 M  $\text{CuCl}_2$  1ChCl: 2EG mixtures.

Same experiment was repeated using the same conditions but using  $\text{Al}_2\text{O}_3$  particles (c.a. 20  $\mu\text{m}$  in diameter). The deposit obtained from this process is shown in **Figure 5.31**. Unlike the previous cases the coating of the alumina particles areas to be good and the close up shows that one particle is almost totally enveloped. This shows that copper does wet the surface of the alumina. The reason why powder pulse plating does not appear to work with copper will need to be studied in more detail.

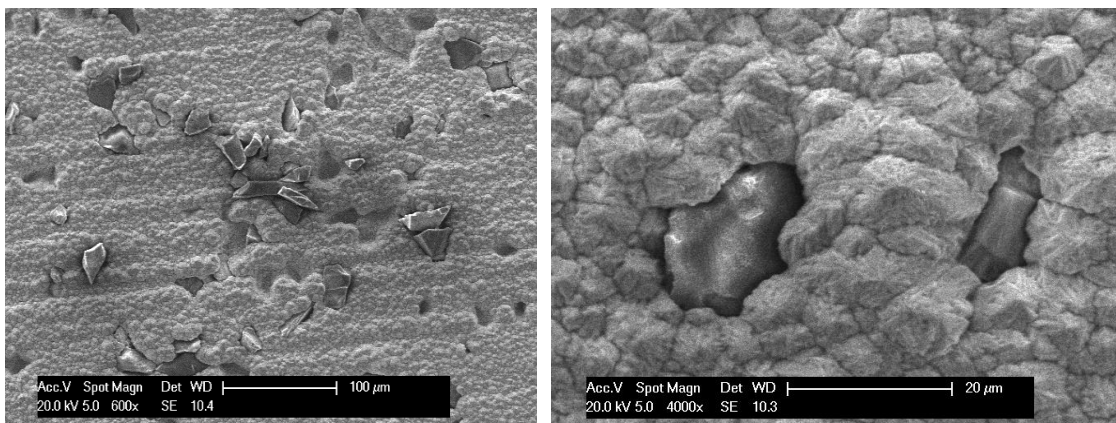


**Figure 5.31** SEM image of an  $\text{Al}_2\text{O}_3$  composite coating, conditions were same used in the SiC experiment in **Figure 5.30**.

## 5.8 Conclusions

In this chapter, the deposition and dissolution of copper was studied in the DES 1ChCl:2EG. It was shown that while the deposition and dissolution appear to progress by two simple one electron transfer processes the dissolution was in fact quite complex. Anodic pulses can lead to super-saturation of the solution close to the electrode surface due to the high viscosity of the liquid and the relatively low ligand concentration. This results in a layer of insoluble copper chloride forming on the electrode surface which limits the reversibility of the deposition process. The properties of the passivating film were studied using electrochemical impedance spectroscopy and profilometry. The dissolution process leads to insoluble films which form within 2-3 s of an anodic pulse which means that the duration of the pulses needs to be relatively short.

Single copper grain fusion was studied, and it was found to be impossible without a reservoir of copper chloride in the solution. Even with this, it was difficult to get copper deposition without deposition and stripping pulses which were about 1-5 s long. A copper

layer of  $> 5 \mu\text{m}$  in thickness was required to enable the copper particle to fuse to the surface. This was in keeping with the experiments performed for zinc.

Bulk powder pulse experiments were attempted with the electrode in both the vertical and horizontal orientation and as in the previous chapter, it was found that much greater success could be achieved with the electrode in a horizontal orientation. In contrast to the zinc chapter, it was possible to deposit very thick copper layers ( $> 1 \text{ mm}$ ) relatively quickly. Because of this, electroforming of copper was attempted using a stainless-steel contact. It was possible to form a porous sheet of copper relatively quickly which could easily be detached from the substrate.

XRD analysis was carried out on the deposits obtained using direct DC deposition and powder pulse deposition. It was found that the substrate had a significant effect on the deposit morphology and the orientation of the crystallites when DC deposition was used. This was in keeping with other studies in the area. Powder pulse deposition showed that the orientation of the crystallites was less affected by the substrate but there was still an effect.

## 5.9 References

1. A.-M. Popescu, A. Cojocaru, C. Donath and V. Constantin, *Chemical Research in Chinese Universities*, 2013, **29**, 991-997.
2. P. C. Andricacos, C. Uzoh, J. O. Dukovic, J. Horkans and H. Deligianni, *IBM Journal of Research and Development*, 1998, **42**, 567-574.
3. P. Andricacos, *Interface*, 1998, **7**, 23-25.
4. Q. Zhang, Y. Hua, Y. Ren and L. Chen, *Journal of Central South University*, 2013, **20**, 2096-2102.
5. M. Kang and A. A. Gewirth, *Journal of The Electrochemical Society*, 2003, **150**, C426-C434.
6. S. Miura and H. Honma, *Surface and Coatings Technology*, 2003, **169**, 91-95.
7. R. Bernasconi, M. Zebarjadi and L. Magagnin, *Journal of Electroanalytical Chemistry*, 2015, **758**, 163-169.
8. B. Tromans, in *The Canning Handbook: Surface Finishing Technology*, Kluwer Academic Publishers, New York, 23rd edn., 1982, ch. 430-442, p. 1094.
9. L. N. Schoenberg, *Journal of the Electrochemical Society*, 1972, **119**, 1491-1493.
10. R. T. Carlin, C. Hugh, J. Fuller and P. C. Trulove, *Journal of The Electrochemical Society*, 1998, **145**, 1598-1607.
11. B. J. Tierney, W. R. Pitner, J. A. Mitchell, C. L. Hussey and G. R. Stafford, *Journal of The Electrochemical Society*, 1998, **145**, 3110-3116.
12. C. Nanjundiah and R. Osteryoung, *Journal of The Electrochemical Society*, 1983, **130**, 1312-1318.
13. F. Endres and A. Schweizer, *Physical Chemistry Chemical Physics*, 2000, **2**, 5455-5462.
14. P.-Y. Chen and I.-W. Sun, *Electrochimica Acta*, 1999, **45**, 441-450.
15. K. Murase, K. Nitta, T. Hirato and Y. Awakura, *J Appl Electrochem*, 2001, **31**, 1089-1094.
16. A. P. Abbott, K. El Ttaib, G. Frisch, K. J. McKenzie and K. S. Ryder, *Physical Chemistry Chemical Physics*, 2009, **11**, 4269-4277.
17. C. S. Barin, A. N. Correia, S. A. Machado and L. A. Avaca, *Journal of the Brazilian Chemical Society*, 2000, **11**, 175-181.
18. K. E. ttaib, PhD thesis, University of Leicester, 2010.

19. A. P. Abbott, R. C. Harris and K. S. Ryder, *The journal of physical chemistry. B*, 2007, **111**, 4910-4913.
20. A. P. Abbott and K. J. McKenzie, *Physical chemistry chemical physics : PCCP*, 2006, **8**, 4265-4279.
21. W. O. Karim, PhD thesis, University of Leicester, 2016.
22. M. Boillot, S. Didierjean and F. Lopicque, *J Appl Electrochem*, 2004, **34**, 1191-1197.
23. B. Boukamp, *Equivalent Circuit (version 3.97) 'Computer program for MS-Dos computers and Users Manual', 2nd revised edition*, University of Twente, 1989.
24. T. Jacobsen and K. West, *Electrochimica Acta*, 1995, **40**, 255-262.
25. Andrzej Lasia, in *Electrochemical Impedance Spectroscopy and its Applications*, Springer, New York, USA, 2014, vol. 4, pp. 94-106.
26. J. M. Hartley, PhD thesis, University of Leicester, 2013.
27. M. J. Sole, *JOM Journal of the Minerals, Metals and Materials Society*, 1994, **46**, 29-35.
28. A. Alhaji, PhD thesis, University of Leicester, 2011.
29. P. Scherrer, *Math-Phys Kl.*, 1918, **2**, 98-100.
30. G. K. Williamson and W. H. Hall, *Acta Metallurgica*, 1953, **1**, 22-31.
31. P. Scardi, M. Leoni and R. Delhez, *Journal of Applied Crystallography*, 2004, **37**, 381-390.
32. U. Holzwarth and N. Gibson, *Nat Nano*, 2011, **6**, 534-534.
33. H. B. Muralidhara and Y. Arthoba Naik, *Bulletin of Materials Science*, 2008, **31**, 585-591.
34. A. Gomes and M. I. da Silva Pereira, *Electrochimica Acta*, 2006, **51**, 1342-1350.
35. M. Li, S. Luo, Y. Qian, W. Zhang, L. Jiang and J. Shen, *Journal of The Electrochemical Society*, 2007, **154**, D567-D571.
36. K. O. Nayana, T. V. Venkatesha, B. M. Praveen and K. Vathsala, *J Appl Electrochem*, 2010, **41**, 39-49.
37. Y. Waseda, K. Shinoda and E. Matsubara, in *X-Ray Diffraction Crystallography*, Springer Heidelberg Dordrecht London New York, 2011, DOI: DOI 10.1007/978-3-642-16635-8, ch. 4, p. 123.

38. S. B. Ogale, P. G. Bilurkar, N. Mate, S. M. Kanetkar, N. Parikh and B. Patnaik, *Journal of Applied Physics*, 1992, **72**, 3765-3769.
39. L. Bonou, M. Eyraud, R. Denoyel and Y. Massiani, *Electrochimica Acta*, 2002, **47**, 4139-4148.
40. N. D. Nikolić, G. Novaković, Z. Rakočević, D. R. Đurović and K. I. Popov, *Surface and Coatings Technology*, 2002, **161**, 188-194.
41. N. D. Nikolić, Z. Rakočević and K. I. Popov, *Journal of the Serbian Chemical Society*, 2001, **66**, 723-727.
42. J. D. Kiely and D. A. Bonnell, *Journal of Vacuum Science & Technology B*, 1997, **15**, 1483-1493.
43. M. Niwa, H. Iwasaki, Y. Watanabe, I. Sumita, N. Akutsu and Y. Akutsu, *Applied Surface Science*, 1992, **60-61**, 39-44.

**Chapter-VI**  
**Future Work**

## 6.1 Conclusions

This study investigated the fundamental aspects of deposition and dissolution in DESs. It was shown that similar DESs could produce different deposit morphologies depending upon the composition of the liquid. The morphology can range from large nodular grains through flat, planar, hexagonal structures to small, almost amorphous, structures. It was shown that film formation appears to be a significant issue when oxygen containing ligands are available to react with the zinc surface. It is probable, although not proven in this thesis, that most oxophilic metals e.g. Co, Fe, Ni all grow a film on the surface when the liquid is not free from all moisture or oxygen containing ligands.

The thesis also studied the reversibility of the electrodeposition processes and it found that in  $\text{ChCl}: 2 \text{ZnCl}_2$ , deposition was reversible as was the case for the  $\text{ZnCl}_2: 4 \text{urea}$  eutectic. Both eutectics produced large, granular deposits with a prevalence of the (002) crystal phase. Both of the type 3 eutectics produced significantly different deposit morphologies. The  $1\text{ChCl}: 2 \text{EG}$  system produced large, flat, hexagonal crystals and the reason for this was shown to be due to the formation of zinc glycolate films on the growing surface with the (101) phase dominating and almost no (002) phase present. The morphology is strongly affected by the temperature and this is thought to be due to changes in the film solubility. Increasing the temperature increases the (002) phase with respect to the (101) phase and results in a change in the size and shape of the crystallites. The zinc nitrate based eutectics had a different type of passivating film which is much thicker, resulting in an irreversible deposition.

In pulse plating the response of the electrode in both anodic and cathodic polarisation pulses was found to be important. Anodic polarisation of a zinc electrode showed that zinc dissolves readily, but the high viscosity of the liquid means that the solution close to the electrode surface rapidly becomes saturated in zinc. It had previously been assumed that the zinc complex would be very soluble since it forms eutectics with both  $\text{ChCl}$  and  $\text{EG}$  where the concentration of  $\text{ZnCl}_2$  is in the region of 2 to 5 mol dm<sup>3</sup>. This assumption had originally affected the interpretation of the voltammetric data. Very slow scan linear sweep voltammetry suggests that the film is soluble, however moderate potential scan rates clearly show that the electrode surface is passivating and this was confirmed with impedance spectroscopy. An insoluble complex forms on the electrode surface which

passivates the zinc surface. Optical microscopy shows that the solution becomes saturated in less than 5 s. This will clearly depend upon the operating temperature and any forced mass transport in the liquids. This will affect the reversibility of the pulse and the morphology of the deposit.

In Chapter 4 the technique of powder pulse plating was successfully demonstrated for the first time. Zinc particles were fused onto a copper substrate by applying alternating anodic and cathodic current pulses. By studying the cyclic voltammetry under an optical microscope, it was noted that gas evolution resulted in moving the zinc particle on the electrode surface which stopped it from sticking to the electrode. This was less of an issue with larger zinc particles.

The size of the particle was found to be an important factor with the experimental set up. The length of the pulses was found to be critical in being able to fuse the zinc particles to the electrode. Anodic cycles of less than 1 s were insufficient to dissolve enough material but more than 5 s resulted in super-saturation of the liquid such that the particles would not fuse due to a passivating layer forming on the zinc surface. On the cathodic cycle the deposition time had to be in the order of 5 to 7 s to enable the zinc to diffuse around the particle to the site where it had to either fuse the particle to the electrode or fuse the particle to neighbouring particles. It was found that a horizontal orientation of the working electrode worked well when large zinc particles were used as gravity kept them on the electrode surface and ensured they did not lift during gas evolution. Cycling the current under these conditions enabled homogeneous zinc layers to be deposited. Efficiencies of up to 140% were recorded which is probably the first demonstration of super-efficient deposition of this type. This is quite high given the packing density of the zinc particles.

To allow zinc plating with the electrode in a vertical orientation an alternative approach was used. Small zinc particles were suspended in the electrolyte and the electrolyte was vigorously stirred. Under these conditions, thick, homogeneous deposits were obtained demonstrating that powder pulse plating is a viable method for coating surfaces. The current efficiency for this form of powder pulse plating was lower than for larger particles due probably to the lower efficiency of getting the particles to stick. The efficiency was nevertheless significantly higher than without particles and was still close to 100%.

Another advantage of powder pulse plating is that significantly thicker deposits could be obtained than using conventional DC plating.

It was also demonstrated that composite materials could be produced using particles of alumina and silicon carbide which were mixed with the zinc particles before the powder pulse plating. The zinc could pack around the inert particles although they did not wet the dispersed phase particularly well so adherence to the zinc particles was poor.

In the final part of the study copper was used as the particulate phase. It was thought that the deposition would be more reversible and, because copper is not very oxophilic, there would be less issues with film formation. It became clear during the study that while gassing was not prevalent during pulses, fusing the particles together was difficult under some pulse conditions. It was found that copper dissolution was the issue due to film formation. In this case the film appeared to be  $\text{CuCl}_2$  which formed during the anodic pulse. The timescale for this process was like that observed for zinc. Maintaining the anodic pulse to less than 5 s enabled copper fusion to be obtained. The copper films were more dense than those obtained using copper and as previously, it was shown that super-efficient deposition could be obtained and it was possible to get thick deposits very quickly.

## **6.2 Suggestions for Future Work**

### **6.2.1 Metal Deposition and Electropolishing**

While this study has demonstrated a novel method for producing thick, porous metallic deposits quickly and with high current efficiency some of the most important results are in the fundamental aspects of metal deposition and dissolution. The study suggests that film formation is common to many metals in DESs and potentially to all ionic liquids. This appears to change the mechanism metal growth. One factor that may be related to this is that film growth appears to me limited to about 30-50  $\mu\text{m}$  in these media. If the metal is growing through reduction of an oxide/glycolate film, then if that film gets too thick it will become too resistive and the metal will stop growing. Film formation could be studied as a function of time during the growing process using electrochemical

impedance spectroscopy. Film formation could also be studied using Raman spectroscopy.

Recent studies within the group have found that some brighteners work effectively to change the surface morphology. It was proposed by Juma,<sup>1</sup> that these function by forming a hydrophobic film at the electrode-solution interface although this process has not been studied in depth. Some of the additives function at relatively low concentrations and do not affect speciation or mass transport so that is why they are probably surface active. EIS could once again be used to see if a film forms with and without the additives.

As well as metal deposition, film formation has been shown to be important in metal dissolution. It has previously been shown that glycolate films are important for the electropolishing of metals such as stainless steel, cobalt, nickel and nickel based alloys.<sup>2-4</sup> This study has shown that glycolate films form with most metals and it would be interesting to see whether the electrolyte conditions could be changed, particularly with temperature, to optimise the thickness and density of the films such that other metals could be electropolished. Karim<sup>5</sup> has recently shown that to achieve electropolishing in DESs a certain Warburg impedance is essential to obtain the correct migration of metal ions through the glycolate film.

### **6.2.2 Powder Pulse Plating**

It was evident from chapter 3 that the deposit morphology obtained for zinc could be modified by choice of the DES and, to some extent, through changes in temperature. Porous materials are important for the development of supercapacitors, catalysis and filters. The choice of the particle size appears to change the porosity of the zinc matrix. It is probable that the length and size of the current pulse will also change the amount of material that is deposited between the grains. This could be quantified and modelled to optimise the porosity of the material. The real advantage of these materials would be for the deposition of ultra-high surface area materials. For this the morphology of the surface would need to be changed. It would be useful to study powder pulse plating from the other DESs studied in Chapter 3 to determine the effect of mass transport, concentration and speciation on the deposit morphology. Also, if films do not form during anodic polarisation then the pulse lengths and magnitudes to be varied more. It would be

interesting to note whether the dissolution and deposition cycles would have to be lengthened in more viscous DESs.

Chapter 3 showed that increasing the temperature can lead to high surface area, amorphous materials. Work by Hsieh et al.<sup>6</sup> showed that various nano-structured materials could be obtained for the electrodeposition of zinc from imidazolium based chlorozincate ionic liquids. It was further shown that zinc nano-rods could be exchanged for other, more catalytic, metals such as gold.

Recent work by Zhang et al. has focussed on the use of DESs to produce nano-templated coatings. They showed that nano-porous copper could be deposited by an immersion process onto zinc.<sup>7</sup> The same group also showed that nano-nickel and nano-NiS could be deposited by an immersion process onto copper, the latter by adding thiourea to the DES.<sup>8</sup> These materials were found to be excellent catalysts for producing hydrogen from the electrolysis of water. The ability to coat these materials onto a microporous substrate would increase the effective surface area of the material. The material would need to be constructed such that gas bubbles could not get trapped in the materials.

Ultimately it would be interesting to see if water sensitive metals such as aluminium could be electrodeposited by this method. There is a need for materials like this in the next generation of battery materials particularly for an aluminium air battery.<sup>9</sup>

### 6.3 References

1. J. A. Juma, PhD thesis, University of Leicester, 2016.
2. A. P. Abbott, G. Capper, K. J. McKenzie and K. S. Ryder, *Electrochimica Acta*, 2006, **51**, 4420-4425.
3. A. P. Abbott, G. Capper, K. J. McKenzie, A. Glidle and K. S. Ryder, *Physical Chemistry Chemical Physics*, 2006, **8**, 4214-4221.
4. A. P. Abbott, N. Dsouza, P. Withey and K. S. Ryder\*, *Transactions of the IMF*, 2012, **90**, 9-14.
5. W. O. Karim, PhD thesis, University of Leicester, 2016.
6. Y.-T. Hsieh, T.-I. Leong, C.-C. Huang, C.-S. Yeh and I. W. Sun, *Chemical Communications*, 2010, **46**, 484-486.
7. Q. B. Zhang, A. P. Abbott and C. Yang, *Physical Chemistry Chemical Physics*, 2015, **17**, 14702-14709.
8. C. Yang, Q. B. Zhang and A. P. Abbott, *Electrochemistry Communications*, 2016, **70**, 60-64.
9. S. Yang and H. Knickle, *Journal of Power Sources*, 2002, **112**, 162-173.

**Chapter-VII**  
**APPENDIX**

## 7 Appendix

### 7.1 Nucleation Mechanism

#### 7.1.1 Zinc

All nucleation studies were performed with a Ag/AgCl reference electrode (0.1 M AgCl dissolved in 1ChCl: 2EG and filled in glass tube with a frit at the tip). The nucleation mechanism of zinc deposition with and without a Zn particle was studied to determine whether the nucleation depended upon the substrate. Both systems used a Pt working electrode, in the second case a large zinc particle was chosen which largely obscured the Pt surface.

The well-known theoretical model proposed by Scharifker and Hills was used. The model fits the chronoamperometric data an instantaneous and progressive nucleation mechanism. <sup>1</sup>

Dimensionless plots of  $I^2/I_m^2$  versus  $t/t_m$  for actual nucleation data are compared to two theoretical models derived from Scharifker and Hills equations. The Scharifker and Hills model for instantaneous nucleation followed by 3D-diffusion-limited growth, assuming hemi-spherical nuclei, is defined as given in **Equation 7.1**.

$$\frac{I_m}{I_m^2} = \frac{1.9542}{\frac{t}{t_m}} \left[ 1 - \exp \left[ -1.2654 \left( \frac{t}{t_m} \right) \right] \right]^2 \quad \text{Equation 7.1}$$

Accordingly, the Scharifker and Hills model for a progressive nucleation followed by 3D-diffusion limited growth of hemi-spherical nuclei is defined as given in **Equation 7.2**.

$$\frac{I_m}{I_m^2} = \frac{1.2254}{\frac{t}{t_m}} \left[ 1 - \exp \left[ -2.3367 \left( \frac{t}{t_m} \right) \right]^2 \right]^2 \quad \text{Equation 7.2}$$

Where  $I$  represent the current density, and  $I_m$  is the maximum current density,  $t$  represents the time, and  $t_m$  represents the time at  $I_m$ .

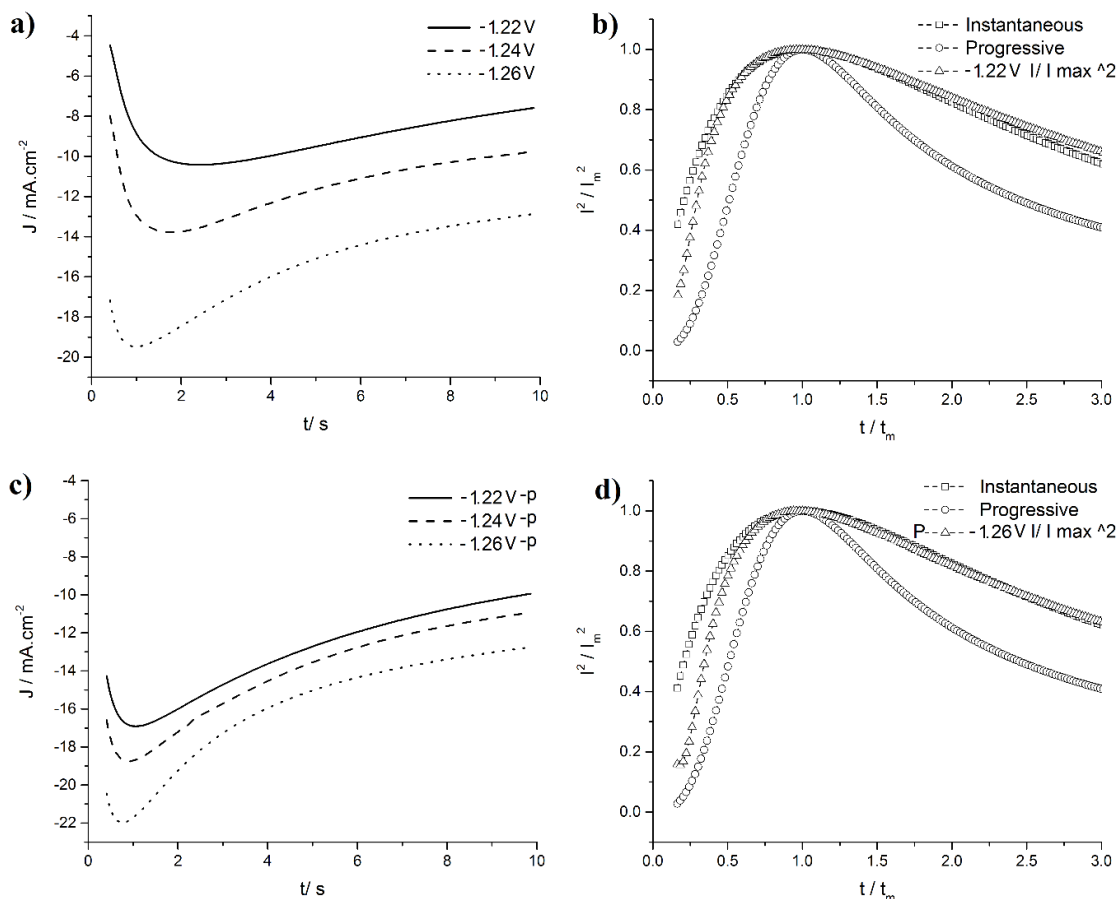


**Figure 7.1** The experimental  $I$ - $t$  curves for the electrodeposition of Zn from (a) 0.5 M  $ZnCl_2$  in 1: 2  $ChCl$ : EG and (c) with a  $150\ \mu m$  Zn particle placed on the WE. The potential was stepped from o.c.p. to cathodic potentials indicated. Dimensionless Scharifker and Hills plots for (b) corresponding to the data in (a) and (d) corresponding to the data in (c).

**Figure 7.1** shows a comparison of the experimental  $I$ - $t$  curves with the theoretical models for 3D instantaneous and progressive nucleation for Zn deposition from 0.5 M  $ZnCl_2$  in 1  $ChCl$ : 2 EG in (a), and same conditions with (a), but on a single  $150\ \mu m$  particle placed onto working electrode in (c). The behaviour of  $I$ - $t$  traces for both (a) and (c) are compared to the standard models calculated from *Equation 7.1* and *Equation 7.2*. When an over potential is applied, the current rises due to charging of the double layer (these current spikes are omitted from **Figure 7.1** for clarity). When the current rises to a maximum this indicates that nucleation occurs due to an increase in the surface area. The plots in **Figure 7.1** (b) and (d) show that nucleation and growth is similar in both systems suggesting that it is independent of the substrate. Initially nucleation is intermediate between instantaneous and progressive but growth follows closely an instantaneous mechanism. A similar study was performed (albeit with a silver wire reference electrode, at a lower temperature and in 0.3 M  $ZnCl_2$ ),<sup>2</sup> however poor fits to the theoretical models proposed

by Scharifker and Hills were obtained. The authors could not explain this phenomenon but suggested that it may be due to a secondary process.<sup>3</sup>

### 7.1.2 Copper

The same experiments were carried out to determine the nucleation behaviour of copper in 0.3 M CuCl<sub>2</sub> dissolved in 1ChCl: 2EG at 45 ± 5 °C on a platinum electrode. The copper particle was spherical and 149 μm diameter.

**Figure 7.2** shows the I-t transients obtained as a function of potential with and without the particle present. The current increases when the particle is present as the surface area is slightly higher and nucleation of copper on copper is easier than copper on Pt. The current also increases as expected with increasing over-potential.

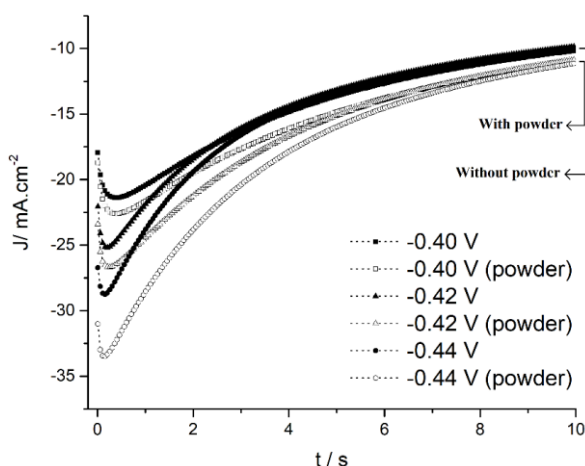


**Figure 7.2** Chronoamperograms obtained at a Pt disc, and a powder placed onto the same working electrode at 45 ± 5 °C in 0.3 M CuCl<sub>2</sub>.2H<sub>2</sub>O in 1 ChCl: 2EG DES at 15 mV.s<sup>-1</sup>.

**Figure 7.3** shows the fitted data for comparison theoretical and instantaneous nucleation mechanisms for both Pt working electrode (left), and the same experiment with a copper particle placed on the Pt working electrode (right). **Figure 7.3** shows that nucleation is 3D instantaneous without a copper particle on the electrode surface and becomes more progressive with the metal particle present. The growth phase after the peak system does not fit either model well.

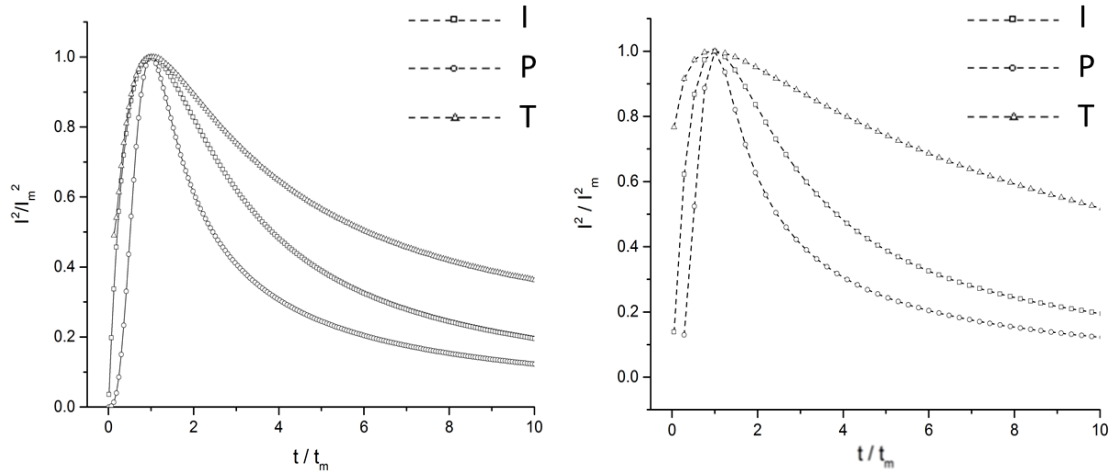


**Figure 7.3** Dimensionless Scharifker and Hills plots for the data in **Figure 7.2** without (left) and with (right) a copper particle on the working electrode.

## 7.2 Mass Transport Modelling

It was decided to make a more in-depth analysis to understand the reason why particle deposition in the cell with a filter paper membrane was unsuccessful. To do this it was decided to model the current and potential across the cell shown in **Figure 7.4**.

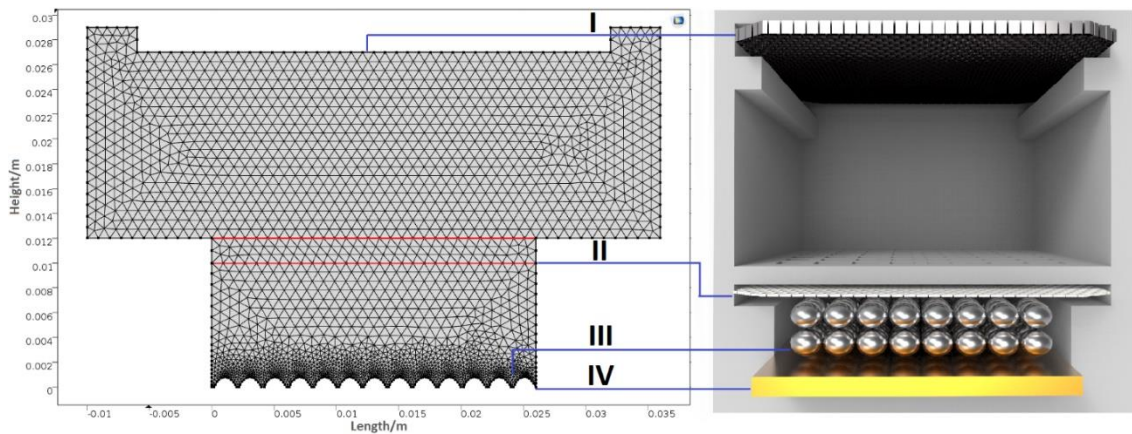


**Figure 7.4** Left 2D, and in the right 3D representation of the modelled cell. This model is based on secondary current-distribution. Composition of the electrolyte in subdomains is taken as constant. Electron dependence is highly related to the local potential.

The cell was divided into four domains for ease of analysis. The plating area is represented as domain-**IV**; a copper plate. The space between filter paper and copper substrate which holds the zinc particles is domain-**III**. The filter paper is domain-**II**, and the region between the filter paper and anode is represented as domain-**I**.

While the filter paper kept the zinc particles in contact with the copper electrode, it also acted as a salt bridge between the two halves of the cell. Domain-*I* had an iridium oxide coated titanium dimensionally stable anode. The hypothesis was that the filter paper was causing a low current distribution on the cathode surface. Thus, the process was becoming insufficient to sustain ion exchange due to resistivity between domain-*II* and domain *III*. This resistance was likely preventing ion transfer across the double layer where deposition takes place.

To check the effect of filter paper on plating process, a mathematical model was prepared in COMSOL multi physics program. At first sight, it is not reasonable to claim that a filter paper with 10-20  $\mu\text{m}$  pore size could slow down ion transfer as the ions are only a few angstroms in diameter. The main aim of this study was to determine whether the filter paper caused a decrease in plating efficiency when compared to the system without filter paper. One of the main parameter was to calculate conductivity. Conductivity values were determined by measuring resistivity of 1ChCl: 2EG with and without filter paper for applied cell, and thus; a relative data was acquired. Surface area of the filter paper was measured as 4  $\text{cm}^2$  and the distance between electrodes was taken as 2 cm. The conductivity of 1ChCl: 2EG at 60  $^\circ\text{C}$  was measured as 16.2  $\text{mS}\cdot\text{cm}^{-1}$ , and for a filter paper placed system was 4.1  $\text{mS}\cdot\text{cm}^{-1}$ . So clearly the filter paper decreases the conductivity by a factor of 4. Using the conductivity data, the COMSOL program was run to obtain current and potential distributions across the cell. The cathode was covered with half spherical zinc particles, but everything was calculated for a two-dimensional system because three-dimensional system requires far more computer power and may end up with mesh errors. In the deposition of zinc particles in 1ChCl: 2EG, cathode is the electrode which reduction occurs and anode is the electrode which oxidation occurs. The prepared model was set up with several assumptions, and it is shown in two-dimensional system in **Figure 7.4**.

In the model, regions *I* and *III* are assumed to be the same, and so, the electrolyte is taken as being fixed for both regions. Butler-Volmer kinetic expressions were used as given in **Equation 7.3**.

$$i_{loc} = i_0 \left( \exp\left(\frac{\alpha a F \eta}{RT}\right) - \exp\left(\frac{(-\alpha) c F \eta}{RT}\right) \right) \quad \text{Equation 7.3}$$

The local anodic potential of the system was taken as zero, and the current flow was set from cathode to anode. The reaction process at the anode was assumed to be very fast which results in high fluctuation in current density with respect to small changes in potential gradient. At the cathode, zinc deposition occurs, while at the anode an electron transfer occurs but no physical change is assumed to occur on the anode. It is assumed that the process occurring at the cathode is much slower than the anode.

One of the important parameters in the design of electrochemical cells is the current-density distribution on the electrode surfaces. It is important to have current density on the electrode frontal surfaces as uniform as possible. The applied model is a secondary current-distribution model which implies a dependence of the electron transfer on the local potential, and it is assumed a constant composition in the subdomains.<sup>4</sup> The possible electron transfer reactions at the anode and cathode are given in chapter 3.

Along with this information it is possible to simplify the model by neglecting the concentration gradients in the anolyte and catholyte. By doing so, migration will be the primary transport mechanism of ionic current inside the cell in which the electric field induces a flux of ions. Thus, it is not required to design a complex model which counts internal free convection.

To model the current in the cell, the electrolyte domains are used for secondary current distribution interfaces. In this way, two different values for electrolyte conductivity for the case of filter based system and filter free system are applied as given in *Equation 7.4*. It is assumed that the anode reaction is faster than the cathode reaction in which ionic metallic species form at the solid interface, but the anode behaviour is expected to be an electron exchange mechanism, and small changes in potential provide large changes in current density. In this way, the over potential becomes negligible so errors in the potential calculations will be very small (typically a few millivolts).<sup>5</sup>

$$E_{eq, a} = \phi_{s, a} - \phi_{l, c} \qquad \text{Equation 7.4}$$

Thus, the anode and cathode potentials can be written as  $E_{cell}$  as given in *Equation 7.5*.

$$E_{cell} = \phi_{s,a} - \phi_{s,c} \quad \text{Equation 7.5}$$

As the cell potential is based on the equilibrium potentials, and the cell polarization potential, be described as given in **Equation 7.6**.

$$E_{cell} = E_{eq,a} - E_{eq,c} + E_{pol} \quad \text{Equation 7.6}$$

When the **Equation 7.5**, and **Equation 7.6** are combined, **Equation 7.7** is obtained.

$$\phi_{s,c} = \phi_{l,c} + E_{eq,c} - E_{pol} \quad \text{Equation 7.7}$$

If it is assumed that formation of local anodic charge throughout the reaction is zero, **Equation 7.8** can be obtained.

$$\phi_{s,c} = E_{eq,c} + E_{pol} \quad \text{Equation 7.8}$$

When the cathode is used as a reference potential ( $E_{q,c} = 0$ ), and the relation is used to define the kinetics in **Equation 7.9**.

$$\phi_{s,c} = -E_{pol} \quad \text{Equation 7.9}$$

Using the above expressions a map of electrolyte potential can be obtained for the cell shown in **Figure 7.4** with and without the presence of the filter paper membrane. These two models are shown in **Figure 7.5**.

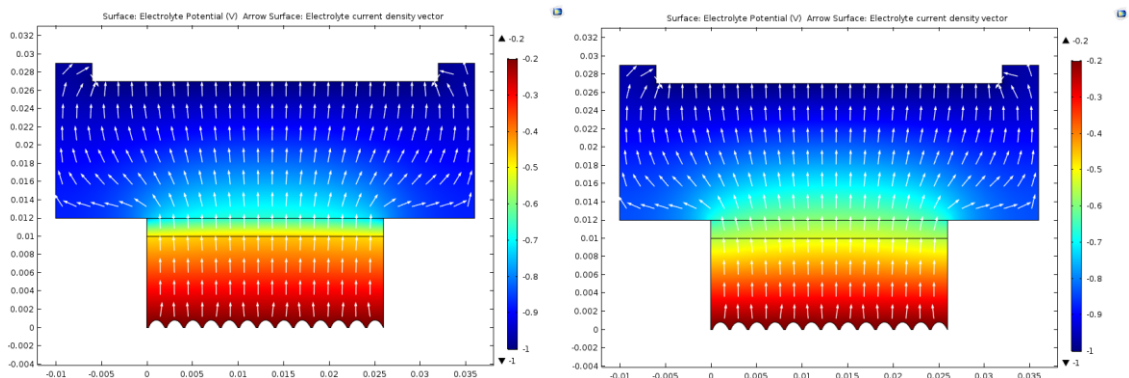


**Figure 7.5** Change in electrolyte potential in the presence of (left) and absence of a filter paper separator (right).

The change in electrolyte potential shows a clear border of the electrolyte potential limits near the filter paper which likely causes the deficiency in exchange of charged species between the anode and cathode, especially from the domain-*I* which carries most of the electrolyte. However, in the filter paper free system, domain-*I* is actively accessible, and the transfer of charged species are clearly much easier, and this phenomenon creates less depletion of ions at region *III* when compared the filter based system. In an analogous manner, the current distribution was calculated and the results are shown in **Figure 7.6**.

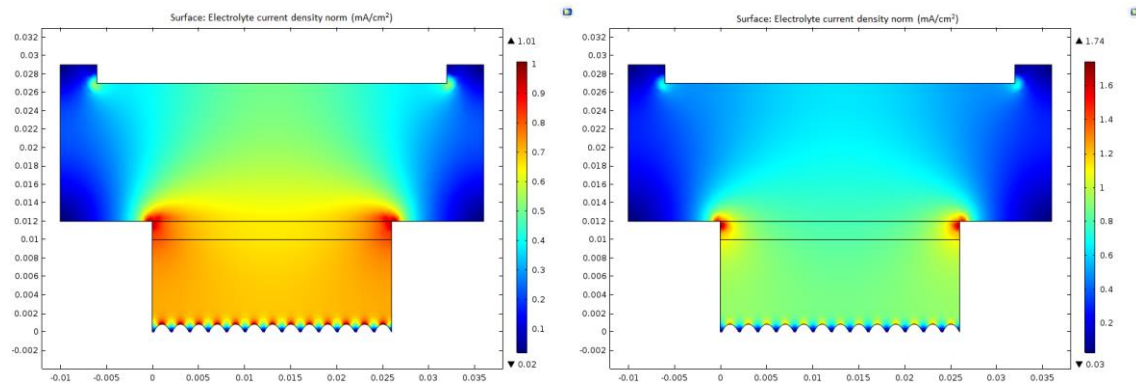


**Figure 7.6** Current distribution across surface of cathode and the anode in the presence of (left) and absence of a filter paper separator (right).

As it is known, if the exchange current density is much faster than replenishing time of charge carriers in the double layer, depletion of charge carriers is inevitable. Inversely, if the exchange current density is too low, either potential difference or the conductivity of the electrolyte can be increased. However, if the potential increases more than the kinetics of charged species exchange, depletion of available charge carriers will occur. Filter paper placed in domain-*II* prevents the ion migration between domain-*I*, and domain-*III*. If the current density is set to  $3 \text{ mAcm}^{-2}$  for both cells, the real current density in local areas differs significantly on the anode, cathode, and cell geometry. If the whole cell is investigated, the current density distribution through the anode and cathode is quite uneven when a filter paper is placed in the cell as shown in **Figure 7.4**. When the filter paper is missing, the current distribution is more evenly distributed. Additionally, there is a notable decrease in current density on the particles and cathode in the filter placed system.

The above analysis shows that the decrease in performance of deposition when a filter paper is used is due to the uneven current distribution in the cell. In hindsight, the packing

of the zinc powder in the cell was sub-optimal and probably not sufficient to maintain contact of the particles with the electrode. An alternative may have been to pack the powder into the cavity in the dry form and then fill it up with DES. This may, however have had the disadvantage of trapping air bubbles or gas bubbles in during electrolysis making the above situation even worse.

### 7.3 References

1. G. Gunawardena, G. Hills, I. Montenegro and B. Scharifker, *Journal of Electroanalytical Chemistry and Interfacial Electrochemistry*, 1982, **138**, 225-239.
2. L. Vieira, Schennach, R, Gollas, B., *Electrochimica Acta*, 2016, **197**, 344-352.
3. J. C. Barron, PhD thesis, University of Leicester, 2009.
4. J. Newman and K. E. T. Alyea, in *Electrochemical Systems*, John Wiley & Sons, Inc., New Jersey, 3 edn., 2004, vol. 18, pp. 419-456.
5. P. Bosander, P. Byrne, E. Fontes and O. Parhammar, *Proc Electrochemical Society*, 1999, **99-21**.